

CRANFIELD UNIVERSITY

NURHANA MOHMAD ROUYAN

MODEL SIMULATION SUITABLE FOR AN AIRCRAFT AT  
HIGH ANGLES OF ATTACK

SCHOOL OF ENGINEERING

MPhil Thesis  
Academic Year: 2014/2015

Supervisors: Dr. Alastair K. Cooke & Dr. James F. Whidborne  
January 2016



CRANFIELD UNIVERSITY

SCHOOL OF ENGINEERING  
MPhil in the School of Engineering

MPhil THESIS

Academic Year: 2014/2015

NURHANA MOHMAD ROUYAN

Model Simulation Suitable for an Aircraft at High Angle of Attack

Supervisors: Dr. Alastair K. Cooke  
Dr. James F. Whidborne

January 2016



# Abstract

Simulation of a dynamic system is known to be sensitive to various factors and one of them could be the precision of model parameters. While the sensitivity of flight dynamic simulation to small changes in aerodynamic coefficients is typically not studied, the simulation of aircraft required to operate in nonlinear flight regimes usually at high angles of attack can be very sensitive to such small differences. Determining the significance and impact of the differences in aerodynamic characteristics is critical for understanding the flight dynamics and designing suitable flight control laws. This thesis uses this concept to study the effect of the differences in aerodynamic data for different aerodynamic models provided for a same aircraft which is F-18 HARV combat aircraft. The aircraft was used as a prototype for the high angles of attack technology program. However modeling an aircraft at high angles of attack requires an extensive aerodynamic data which are usually difficult to access. All aerodynamic models were collected from open literature and implemented within a nonlinear six degree of freedom aircraft model. Inspection of aerodynamic data set for these models has shown mismatches for certain aerodynamic derivatives, especially at higher angles of attack where nonlinear dynamics are known to exist. Nonlinear simulations are used to analyse three different types of flight dynamic models that use look-up-tables, arc-tangent formulation and polynomial functions to represent aerodynamic data that are suitable for high angles of attack application. To achieve this, a nonlinear six degree of freedom Simulink model was developed to accommodate these aerodynamic models separately. The trim conditions were obtained for different combinations of angles of attack and airspeed and the models were linearized in each case. Properties of the resulting state matrices such as eigenvalues and eigenvectors were studied to determine the dynamic behaviour of the aircraft at various flight conditions.

**Keywords:** NASA F-18 HARV, high angles of attack, aerodynamic model, aircraft simulation.

This page is intentionally left blank.

# Contents

<b>Abstract</b>	<b>i</b>
<b>Content</b>	<b>v</b>
<b>List of Figures</b>	<b>ix</b>
<b>List of Tables</b>	<b>xii</b>
<b>Nomenclature</b>	<b>xiii</b>
<b>Abbreviations</b>	<b>xvii</b>
<b>1 Introduction</b>	<b>1</b>
1.1 Research Background . . . . .	1
1.2 F-18 HARV Description . . . . .	2
1.3 Aim and Objectives . . . . .	3
1.4 Thesis Outline . . . . .	4
<b>2 Literature Review</b>	<b>5</b>
2.1 High Angles of Attack Aerodynamics . . . . .	5
2.2 Nonlinear Flight Dynamic Analysis . . . . .	7
2.2.1 Bifurcation: Investigating Critical Flight Regime . . . . .	8
2.2.2 Other Approaches to Nonlinear Analysis . . . . .	12
2.3 Simulation Model for High Angles of Attack Flight . . . . .	13
2.3.1 Mathematical Modeling . . . . .	13
2.3.2 Aerodynamic Representation . . . . .	14
2.4 Conclusion . . . . .	15

<b>3</b>	<b>F-18 HARV Aerodynamic Models</b>	<b>19</b>
3.1	Introduction . . . . .	19
3.2	Aerodynamic Modelling: Source of Models . . . . .	19
3.2.1	Cao Model . . . . .	20
3.2.2	Chakraborty Model . . . . .	20
3.2.3	NASA Model . . . . .	21
3.2.4	Modified Cao Model . . . . .	22
3.2.5	Summary . . . . .	25
3.3	Analysis of Different F-18 HARV Aerodynamic Models . . . . .	25
3.3.1	Extraction of the Derivatives from the Cao Model . . . . .	25
3.3.2	Graph Comparison of the Aerodynamic Derivatives . . . . .	27
3.4	Conclusion . . . . .	35
<b>4</b>	<b>Pole Map for Longitudinal Dynamics</b>	<b>37</b>
4.1	Trimming and Linearization . . . . .	37
4.2	Analytical Linearized Model . . . . .	41
4.3	Eigenvalue Trajectories . . . . .	43
4.3.1	Longitudinal Modes . . . . .	44
4.3.2	Lateral-Directional Modes . . . . .	56
4.4	Conclusion . . . . .	57
<b>5</b>	<b>Nonlinearity Assessment on the F-18 HARV Aerodynamic Data</b>	<b>65</b>
5.1	Introduction . . . . .	65
5.2	Nonlinearity Index: Theoretical Background . . . . .	66
5.2.1	Static Non-linearity Indices . . . . .	67
5.2.2	Dynamic Non-linearity Indices . . . . .	68
5.3	Non-linearity Index within a Region of Flight Envelope . . . . .	69
5.4	Non-linearity Index with respect to Different Input Excitation Shape . . . . .	73
5.5	Conclusion . . . . .	75
<b>6</b>	<b>Conclusion</b>	<b>81</b>
6.1	Summary . . . . .	81
6.2	Contributions to Knowledge . . . . .	82
6.3	Recommendations for Future Study . . . . .	83



---

<b>References</b>	<b>84</b>
<b>A Mathematical Model Development</b>	<b>93</b>
A.1 Generalized Nonlinear Model of Aircraft . . . . .	93
A.2 Aerodynamic Modeling . . . . .	96
A.3 Thrust Modeling . . . . .	96
A.4 Actuator Dynamics . . . . .	99
A.5 Nonlinear Simulink Model of F-18 HARV . . . . .	99
<b>B F-18 HARV Aerodynamic Data</b>	<b>101</b>
B.1 Cao Aerodynamic Data . . . . .	101
B.2 Chakraborty Aerodynamic Data . . . . .	129
B.3 NASA Aerodynamic Data . . . . .	135
<b>C Linearized Matrix</b>	<b>139</b>
C.1 State Matrix from the Cao Model . . . . .	139
C.2 State Matrix from the Chakraborty Model . . . . .	140
C.3 State Matrix from the NASA Model . . . . .	140

This page is intentionally left blank.

# List of Figures

1.1	Schematic view of F-18 HARV . . . . .	2
2.1	Wing terminology . . . . .	5
2.2	Variation of lift coefficient with $\alpha$ . . . . .	6
2.3	Flow characteristics transition . . . . .	6
2.4	The Birhle-Weissman chart . . . . .	8
2.5	Saddle-node bifurcation. . . . .	10
2.6	Hopf bifurcation. . . . .	10
2.7	Bifurcation diagram with elevator deflection as the continuation parameter showing the behaviour of (a) angle of attack, (b) roll rate, (c) yaw rate, and (d) pitch angle . . . . .	11
2.8	Effect of positive pitch rate on the aerodynamic coefficients . . . . .	15
2.9	Effect of negative pitch rate on the aerodynamic coefficients . . . . .	16
3.1	Domain of the arctangent function of $\alpha$ . . . . .	22
3.2	Mach no. effect on the Cao Model . . . . .	26
3.3	Stabilator effect on lift coefficient at different Mach no. . . . .	26
3.4	Distribution for drag coefficient and its derivative. . . . .	28
3.5	Distribution for lift coefficient and its derivative at $M = 0.6$ . . . . .	29
3.6	Distribution for pitch moment coefficient and its derivative at $M = 0.6$ . . . . .	30
3.7	Distribution for side force coefficient and its derivative. . . . .	31
3.8	Distribution for roll moment coefficient and its derivative. . . . .	33
3.9	Distribution for yaw moment coefficient and its derivative. . . . .	34
3.10	Flowchart of the arodynamic models presented in the chapter. . . . .	35
4.1	Flight envelope trim conditions. . . . .	39
4.2	Example of trim simulation for the Cao model at $V_T = 300$ m/s. . . . .	39
4.3	Example of trim simulation for the Chakraborty model at $V_T = 300$ m/s. . . . .	40

4.4	Example of trim simulation for the NASA model at $V_T = 300$ m/s. . . . .	40
4.5	Simple schematic diagram showing the s-plane. . . . .	43
4.6	Typical complex roots on the s-plane. . . . .	45
4.7	Plot of eigenvalues trajectory as $\alpha$ is changed for Cao model showing longitudinal modes at $h = 15000ft$ . . . . .	46
4.8	Variation of $m_w$ with $\alpha$ for the Cao model. . . . .	47
4.9	Refined low frequency response of Cao model showing migration of eigenvalues crossing the imaginary axis. . . . .	47
4.10	Nonlinear simulation of the state variables for Cao model at $\alpha = 22.66^\circ$ . . . . .	48
4.11	Plot of eigenvalues trajectory as $\alpha$ is changed for Chak model showing longitudinal modes at $h = 15000ft$ . . . . .	50
4.12	Plot of eigenvalues trajectory as $\alpha$ is changed for NASA model showing longitudinal modes at $h = 15000ft$ . . . . .	51
4.13	Variation of $x_w$ with $\alpha$ for the NASA model. . . . .	52
4.14	High frequency eigenvalue trajectories for all models. . . . .	53
4.15	Low frequency eigenvalue trajectories for all models. . . . .	54
4.16	Response of the Cao and the NASA models to stabilator deflection for (a) high frequency, (b) low frequency, and (c) poles in s-plane. . . . .	55
4.17	Gap showed by the $C_{L\delta_h}$ and $C_{m_q}$ for each model. . . . .	56
4.18	Lateral-directional eigenvalues trajectories as $\alpha$ is changed for the Cao model. . . . .	58
4.19	Lateral-directional eigenvalues trajectories as $\alpha$ is changed for the Chakraborty model. . . . .	59
4.20	Lateral-directional eigenvalues trajectories as $\alpha$ is changed for the NASA model. . . . .	60
4.21	Eigenvalue trajectories showing dutch roll mode for all models. . . . .	61
4.22	Numerical eigenvalue trajectories showing (a) roll mode and (b) spiral mode for all models. . . . .	62
5.1	Schematic Diagram showing the worst case variations . . . . .	68
5.2	Interpretation of dynamic non-linearity. . . . .	69
5.3	Non-linearity index algorithm within the trimming and linearization processes. . . . .	70
5.4	Plots of the nonlinearity index for all the models numerically and analytically. . . . .	72
5.5	Sudden change in input matrix across the sub-region. . . . .	73
5.6	Input shapes used to excite the model aircraft. . . . .	74
5.7	Simulation with time of the non-linearity index for input 1. . . . .	76

5.8	Simulation with time of the non-linearity index for input 2. . . . .	77
5.9	Simulation with time of the non-linearity index for input 3. . . . .	78
A.1	Variation of the thrust with Mach no. and altitude (a) Without afterburner and (b) With afterburner . . . . .	97
A.2	Example of thrust response as a function of throttle setting with account to the afterburner effect. . . . .	98
A.3	Thrust line and orientation. . . . .	98
A.4	(a) Maximum jet turning envelope for HARV and (b) Jet turning model for the study. . . . .	99
A.5	Open loop simulink model of HARV. . . . .	100
B.1	Lift coefficient for (a) basic airframe and (b) stabilator deflection. . . . .	129
B.2	Drag coefficient for (a) basic airframe and (b) stabilator deflection. . . . .	130
B.3	Pitching moment coefficient for (a) basic airframe, (b) stabilator deflection and (c) pitch rate. . . . .	131
B.4	Side force coefficient for (a) basic airframe, (b) aileron deflection and (c) rudder deflection. . . . .	132
B.5	Rolling moment coefficient for (a) basic airframe, (b) aileron deflection, (c) rudder deflection, (d) yaw rate and (e) roll rate. . . . .	133
B.6	Yawing moment coefficient for (a) basic airframe, (b) aileron deflection, (c) rudder deflection, (d) yaw rate and (e) roll rate. . . . .	134
C.1	Variations of the state matrix's elements with AoA for the Cao model. . . . .	139
C.2	Variations of the state matrix's elements with AoA for the Chakraborty model. . . . .	140
C.3	Variations of the state matrix's elements with AoA for the NASA model. . . . .	140

This page is intentionally left blank.

# List of Tables

1.1	Physical characteristics of the NASA F-18 HARV . . . . .	3
2.1	Typical Flight Regimes for General Aviation (GA), Jet Transport (JT), and Fighter (F) Aircraft . . . . .	7
3.1	Demonstration on the chosen modified curve. . . . .	23
3.2	Summary of the modified analytical formulation . . . . .	25
3.3	Basic information about the different aerodynamic models for F18 HARV. . . . .	25
3.4	Summary of effects from Mach number, sideslip angle and control deflec- tions as supplied by Cao. . . . .	26
3.5	Summary of variables affecting the aerodynamic formulations for different F-18 HARV models aircraft longitudinally. . . . .	35
3.6	Summary of variables affecting the aerodynamic formulations for different F-18 HARV models aircraft lateral-directionally. . . . .	36
4.1	Initial value and variables setting for speed trimming purpose. . . . .	38
4.2	Trim data for the various models at different trim speed taking the altitude at 15000 $ft$ . . . . .	38
4.3	Dimensionless derivatives of aerodynamic coefficients for longitudinal motion. . . . .	42
4.4	Dimensionless derivatives of aerodynamic coefficients for lateral-directional motion. . . . .	42
4.5	Weight and inertia. . . . .	43
5.1	Trim speeds in each $i$ and $j$ loop as $\alpha$ is increased. . . . .	73
5.2	Summary of the influence of aerodynamic data to the highest nonlinearity index for each input shape. . . . .	75
A.1	F18 HARV control surface position and rate limits. . . . .	100
B.1	Drag coefficients, $C_D$ , notation. . . . .	101
B.2	Compared formulation from Cao's report: Drag Coefficients. . . . .	101

---

B.3	Lift coefficients, $C_{L_0}$ , notation. . . . .	102
B.4	Compared formulation from Cao's report: Lift Coefficients. . . . .	103
B.5	Notation used for the pitch moment coefficients, $C_{M_0}$ . . . . .	104
B.6	Compared formulation from Cao's Report: Pitching Moment. . . . .	104
B.7	Notation used for side force coefficient, $C_{Y_0}$ . . . . .	111
B.8	Compared formulation from Cao's report: Side Force. . . . .	111
B.9	Notation used for rolling moment coefficient, $C_{l_0}$ . . . . .	113
B.10	Compared formulation from Cao's report: Rolling Moment. . . . .	114
B.11	Notation used for yawing moment coefficient, $C_{n_0}$ . . . . .	117
B.12	Compared formulation from Cao's report: Yawing Moment. . . . .	117
B.13	List of some curves which have been modified. . . . .	123



# Nomenclature

## General

$\bar{c}$	Mean aerodynamic chord (ft)
$\mathbf{I}$	Identity matrix
$a$	Installed full throttle lapse
$A, B, C, D$	Linear state space matrices
$a_1$	Tailplane lift curve slope
$a_{max}$	Installed full throttle lapse with afterburner
$a_{mil}$	Installed full throttle lapse without afterburner
$b$	Wing span (ft)
$C_D$	Drag coefficient
$C_L$	Lift coefficient
$C_l$	Roll moment coefficient
$C_m$	Pitch moment coefficient
$C_n$	Yaw moment coefficient
$C_Y$	Side force coefficient
$C_{D_0}$	Basic airframe for drag coefficient
$C_{D_{\delta_h}}$	Drag coefficient due to horizontal stabilator deflection, (1/°)
$C_{L_0}$	Basic airframe for lift coefficient
$C_{l_0}$	Basic airframe for roll moment coefficient
$C_{l_\beta}$	Roll moment coefficient due to sideslip angle, (1/°)
$C_{l_{\delta_a}}$	Roll moment coefficient due to aileron deflection, (1/°)
$C_{L_{\delta_h}}$	Lift coefficient due to horizontal stabilator deflection, (1/°)
$C_{l_{\delta_r}}$	Roll moment coefficient due to rudder deflection, (1/°)
$C_{L_{\dot{\alpha}}}$	Lift coefficient due to rate of angle of attack, (s/°)
$C_{l_p}$	Roll moment coefficient due to roll rate, (s/°)

$C_{L_q}$	Lift coefficient due to pitch rate, (s/°)
$C_{l_r}$	Roll moment coefficient due to yaw rate, (s/°)
$C_{m_0}$	Basic airframe for pitch moment coefficient
$C_{m_{\delta_h}}$	Pitch moment coefficient due to horizontal stabilator deflection, (1/°)
$C_{m_{\dot{\alpha}}}$	Pitch moment coefficient due to rate of angle of attack, (s/°)
$C_{m_q}$	Pitch moment coefficient due to pitch rate, (s/°)
$C_{n_0}$	Basic airframe for yaw moment coefficient
$C_{n_\beta}$	Yaw moment coefficient due to sideslip angle, (1/°)
$C_{n_{\delta_a}}$	Yaw moment coefficient due to aileron deflection, (1/°)
$C_{n_{\delta_r}}$	Yaw moment coefficient due to rudder deflection, (1/°)
$C_{n_p}$	Yaw moment coefficient due to roll rate, (s/°)
$C_{n_r}$	Yaw moment coefficient due to yaw rate, (s/°)
$C_{Y_0}$	Basic airframe for side force coefficient
$C_{Y_\beta}$	Side force coefficient due to sideslip angle, (1/°)
$C_{Y_{\delta_a}}$	Side force coefficient due to aileron deflection, (1/°)
$C_{Y_{\delta_r}}$	Side force coefficient due to rudder deflection, (1/°)
$C_{Y_p}$	Side force coefficient due to roll rate, (s/°)
$C_{Y_r}$	Side force coefficient due to yaw rate, (s/°)
$h$	Altitude (ft)
$I_x, I_y, I_z$	Moment of inertia with respect to x, y, and z body axes (lb)
$I_x, I_y, I_z$	Moment of inertia with respect to x, y, and z body axes (lb)
$I_{xz}$	Product of inertia with respect to $x$ and $z$ body axes
$I_{xz}$	Product of inertia with respect to $x$ and $z$ body axes (lb)
$l, m, n$	Roll, pitch and yaw moment (lbft)
$M$	Mach no.
$m$	Mass of aircraft (lb)
$m$	Mass of aircraft (lb)
$p, q, r$	Roll, pitch and yaw rate about x, y and z body axes (°/s)
$u$	Input vector
$u, v, w$	Component of linear perturbed velocity along the x, y and z body axes (ft/s)
$V_T$	Total velocity, (ft/s)
$x$	State vector

---

$X, Y, Z$	Forces in x, y, and z body axes (lb)
$y$	Output vector

**Greek Symbols**

$\alpha$	Angle of attack ( $^{\circ}$ )
$\beta$	Sideslip angle ( $^{\circ}$ )
$\delta_a$	Aileron deflection ( $^{\circ}$ )
$\delta_h$	Horizontal stabilator deflection ( $^{\circ}$ )
$\delta_r$	Rudder deflection ( $^{\circ}$ )
$\gamma$	Flight path angle( $^{\circ}$ )
$\lambda(t)$	State dynamic matrix
$\lambda$	Eigenvalue : Scheduling parameter
$\omega_n$	Natural frequency ( $s^{-1}$ )
$\phi$	Roll angle ( $^{\circ}$ )
$\psi$	Yaw angle ( $^{\circ}$ )
$\sigma$	Static density ratio
$\tau$	Throttle (%)
$\mathbf{v}$	Eigenvector
$\theta$	Pitch angle ( $^{\circ}$ )
$\zeta$	Damping ratio

**Subscripts**

$aero$	Aerodynamics
$L$	Left
$R$	Right
$th$	Thrust
$TV$	Thrust vectoring

This page is intentionally left blank.

# Abbreviations

AoA	Angle of attack
BACTM	Bifurcation and Catastrophe Theory Method
DoF	Degree of freedom
EBCM	Extended Bifurcation and Continuation Method
EoM	Equations of motion
GTM	Generic Transport Model
HARV	High Alpha Research Vehicle
HATP	High Alpha Technology Programme
HHIRM	Hypothetical High Incidence Research Model
LCDP	Lateral control departure parameter
LEX	Leading Edge Extensions
LUT	Look up table
MTS	Multiple time scale
NASA	National Aeronautics and Space Administration
ODEs	Ordinary Differential Equations
SPPO	Short period oscillation
UAV	Unmanned aerial vehicle
VISTA	Variable-Stability In Flight Simulator Test Aircraft

This page is intentionally left blank.

# Chapter 1

## Introduction

### 1.1 Research Background

Flying at high angles of attack (AoA) is potentially risky. Flying beyond this region is limited by maximum lift coefficient and can be dangerous due to the drastic changes in the aircraft dynamics that are introduced by nonlinearities in the aerodynamic characteristics. As the aircraft enters this region, it can end up in a critical flight condition such a stall, a spin or an autorotation. The nonlinear dynamics of the aircraft beyond this region can be hard to tackle especially when conventional control is implemented.

To improve the effectiveness of flight at high AoA, much research has been undertaken regarding design control so the non-linearity possessed by the aircraft can be overcome [1, 2, 3]. Besides, additional controllers such as vectored thrust and actuated forebody vortex control have been effective in extending the flight envelope [4]. However, prior to the design of a proper control technique combining either these two approaches, it is necessary to understand the dynamic behaviour of aircraft at high AoA.

Research regarding high AoA, High Alpha Technology Program (HATP) had been developed by the National Aeronautics and Space Administration (NASA). This programme was intended to deal with the problems that arose when the F-16 and F-18 experienced deep stall and lateral-directional departure susceptibility, respectively [5]. The programme involved three aircraft: X-31A research aircraft, F-16 Variable-Stability In Flight Simulator Test Aircraft (VISTA), and F-18 High Alpha Research Vehicle (HARV). Each aircraft was specifically employed for different sets of objectives in the HATP but overall, the aim was to enhance fighter manoeuvrability at high AoA [6]. During the HATP, extensive wind tunnel tests and flight tests were carried out. The programme ended in the mid 1990s when all the flight tests for F-18 HARV were completed.

Nonetheless, research into high AoA flight is still active. It has currently evolved towards understanding the nonlinear behaviour as a means towards an evaluation of safe flight [7, 8]. New methods such as bifurcation analysis was applied quantitatively and reconfigurable control designs were proposed as guidelines to improve flight safety. In addition, a more robust analysis method was proposed for use in validating the flight control design.

In conjunction with the basic objectives of the F-18 HARV, the aircraft model was found to be the most acceptable model to aid understanding of nonlinear flight behaviour. This behaviour can be captured through simulation. Therefore, a mathematical model that represents the aircraft, is a priority for all of the analysis intended in the future

tasks. However, developing simulation model for high AoA such as F-18 HARV is a formidable task. An issue exists concerning incorporating the aerodynamic models into computer simulation. The data for the aerodynamic characteristics at high AoA are not widely available in the public domain since confidentiality is involved when dealing with technology of a fighter aircraft.

## 1.2 F-18 HARV Description

The NASA F-18 HARV was a modified F/A-18 Hornet used for about ten years from 1987 onwards. The purpose of the program was to study the issues associated with flight at high AoA and to investigate control and manoeuvring propulsive control concepts and advanced aerodynamic control concepts. It had three phases [6, 9, 10];

- *Phase 1:* A research technique was developed to understand the airflow pattern at high AoA by measurement of the aircraft and comparison with wind tunnel data.
- *Phase 2:* Three vanes were mounted around the engine's exhaust to provide pitch (up and down) and yaw (right and left) control of the aircraft as an alternative when the aerodynamic controls become ineffective at high AoA thereby enhancing manoeuvrability.
- *Phase 3:* Nose strakes were installed on the forebody to influence the vortices and separation lines in order to enhance roll control at high  $\alpha$ .

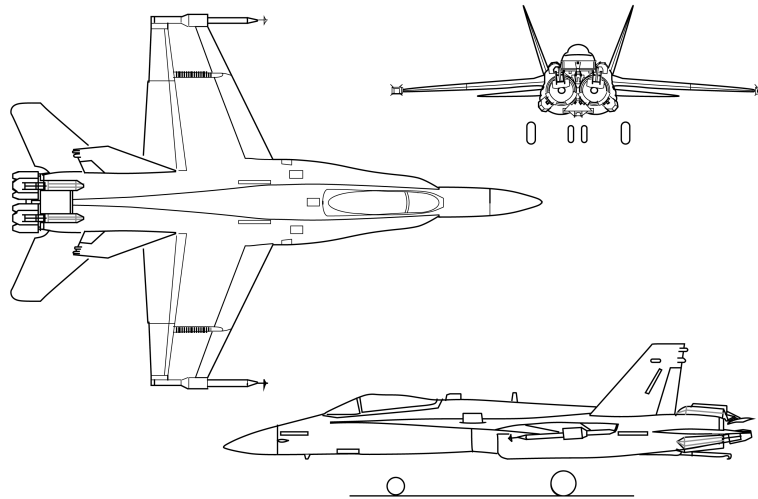


Figure 1.1: Schematic view of F-18 HARV extracted from [6].

The aircraft was a single seat fighter aircraft powered by two F404-GE-400 afterburning turbofan engines. It has a midwing which is moderately swept, canted with twin vertical fins and an extended wing root which forms the leading edge root extension (LEX). The control features include stabilators, rudders, ailerons, leading edge flaps, trailing edge flaps and a speed brake. The flaps adjust the wing camber for maximum performance while manoeuvring throughout the flight envelope whilst, the use of an all moveable horizontal tail or stabilator is intended to increase the longitudinal stability of the aircraft at high AoA.



Table 1.1: Physical characteristics of the NASA F-18 HARV extracted from [6].

Parameter	Value
<i>Wing:</i>	
Area, $S$ ( $ft^2$ )	400
Span, $b$ ( $ft$ )	37.42
Aspect ratio, $AR$	3.5
Mean aerodynamic chord, $\bar{c}$ ( $ft$ )	11.5
<i>Stabilator:</i>	
Span, $b_{tail}$ ( $ft$ )	21.6
Area, $S_{tail}$ ( $ft^2$ )	88.1

One of the outcomes of the programme was the capability of stable flight up to  $70^\circ$  AoA and manoeuvring at high rates at AoA of  $65^\circ$  [10].

### 1.3 Aim and Objectives

The aim of the thesis is to determine the significance and impact of differences shown in the modelled aerodynamic characteristics of the same aircraft especially in the nonlinear high AoA region. There can be many aerodynamic models available in the domain provided for the same aircraft. They can be varied from a simple model to a complex model based on the approaches with which they were formulated, or dependency of the model to certain flight parameters, for example control surfaces and angular rates. But how different are the aerodynamic models and why do differences exist? It is important to quantify the differences as the model should suit the objective of any research before being implemented as the end results might be influenced by the model's characteristics.

The nonlinear high AoA region is pursued due to the rapidly changing aerodynamic properties in this region. Therefore, it needs to be clarified whether the differences in the characteristics will influence the nonlinear simulation of the aircraft when the models are considered for similar flight conditions. How does the model response to these changes?

Therefore, to answer questions such as those raised above, several objectives are set as follows:

1. A review of the high AoA aerodynamic models available in the open literature.
2. Evaluation of the aerodynamic coefficients from the collected models to identify the differences presented in each model.
3. Evaluation and characterization of dynamics behaviour of all the models in order to check if the models predict instabilities at the same flight condition from the eigenvalues determination.
4. Assessment using the non-linearity index to quantify the source of the non-linearity of the all models and to identify if the non-linearity originates from the same source for each model.
5. Implementation of nonlinear simulation to confirm the responses of each model based on the eigenvalue analysis and non-linearity index assessment.

## 1.4 Thesis Outline

This thesis consists of six chapters. The first chapter serves as an introduction which details the research background and expresses the statement of the thesis aim and objectives.

Chapter 2 summarises the literature review regarding the topic of aircraft simulation at high AoA. It starts by discussing basic aerodynamics theory pertinent to high AoA aerodynamics, tools for solving nonlinear flight dynamics, and lastly criteria for modelling the aircraft at high AoA.

Chapter 3 details the compilation of the aerodynamic data for the F-18 HARV models used in this thesis. The data was collected from three different sources available in the open literature. Each model was compared analytically to detail the differences.

In Chapter 4, the different data sets are analysed by evaluating the eigenvalues in order to determine the dynamic behaviour by applying the numerical and analytical approaches. The poles were mapped which produced a trajectory in the S-plane as the AoA was varied from low to high AoA. This is to check if the models predict the same instabilities or dynamics behaviour at the same flight condition.

The content of the thesis is expanded in Chapter 5 by use of the non-linearity index theory to identify the source of the nonlinear aerodynamic data. The background theory is explained further in this chapter. Application of the non-linearity index was conducted within a region of flight envelope and different input excitation shapes.

Finally, Chapter 6 concludes this thesis and provides statements regarding contribution to knowledge as well as recommendations for other work that may be useful to approach in future if similar cases are considered.

## Chapter 2

# Literature Review

### 2.1 High Angles of Attack Aerodynamics

“Angle of attack” (AoA) is an aerodynamic term used to represent the inclination of a wing’s chord line relative to the direction in which the aircraft is moving through the air. The chord line is the reference line connecting the leading edge and trailing edge of the wing.

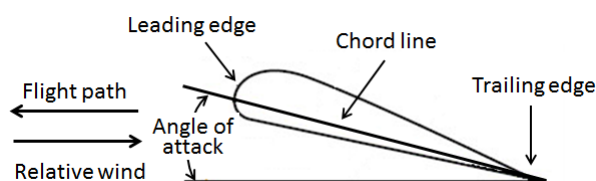


Figure 2.1: Wing terminology

The relationship between lift and AoA typically shows a linear relationship at lower AoA up to a certain point, when the wing no longer producing enough lift it started to reverse the relationship (see Figure 2.2). This point of turn in lift is associated with the maximum lift,  $C_{Lmax}$ . Having a negative slope beyond this point is indicative of stall occurrence due to flow separation on the upper side of the airfoil. There are likely to be changes in pitching and roll moment characteristics as well as increases in drag. Depending on the severity of the stall effects, it may limit the manoeuvring capabilities of the aircraft.

The characteristics of the flow is illustrated in Figure 2.3 and shows a smooth flow attached to a streamlined body but as AoA is increased, it starts to detach and finally the flow separates, inducing a complicated vortex. The consequence of the separation in the flow is a loss of lift.

The variation of aerodynamic behaviour with AoA is classified as either prestall, stall, or poststall. These domains reflect different stability tendencies. In prestall, the behaviour is usually linear, but in the stall regime, the aerodynamics can be strongly nonlinear. In the poststall domain, the behaviour can also be nonlinear.

Aircraft at high AoA present a diverse set of nonlinear motions including stall, post-stall gyration, departure and different types of spin, all of which are considered as critical flight regimes. Different types of aircraft tend to have different characteristics due to their design and shape, especially wing section and tailplane position [14]. Table 2.1

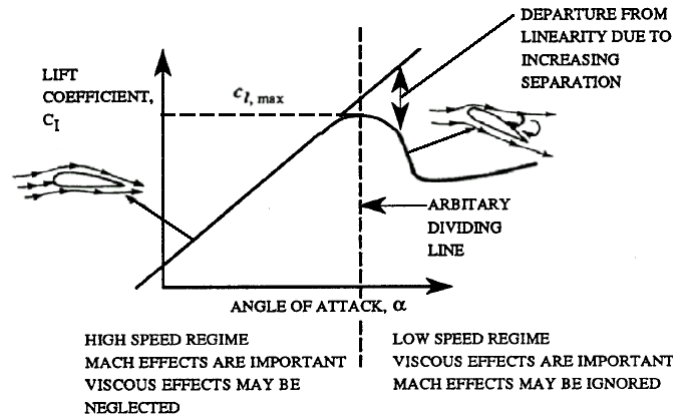


Figure 2.2: Variation of lift coefficient with  $\alpha$  (modified from [11, 12]).

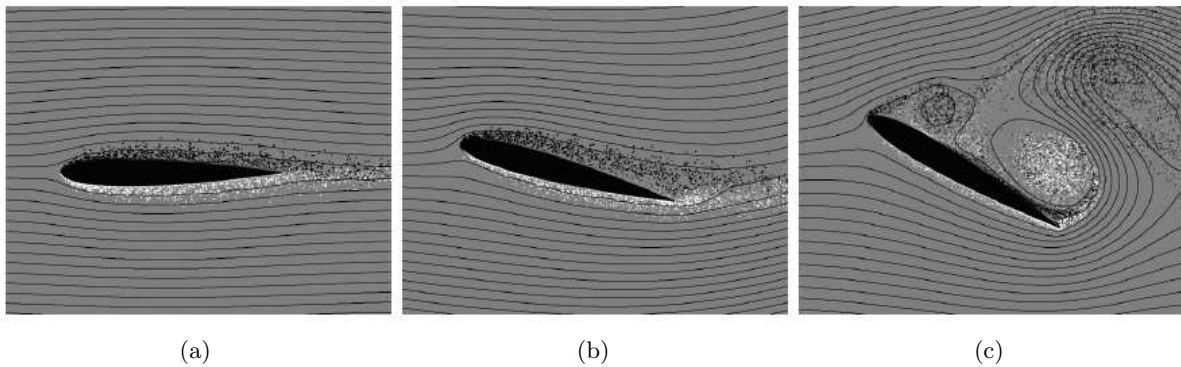


Figure 2.3: Flow characteristics at low AoA in (a), moderate AoA in (b) and high AoA in (c) with separated flow, creating low pressure pockets behind the wing.[13]

categorizes the flight regime associated with AoA for different types of aircraft with the possible flight attributes that they might encounter.

These attributes are:

- *Buffeting* - caused by the turbulent airflow moving rearwards around the fuselage and tail. It may be important to understand the characteristics as it affects the airframe of the aircraft.
- *Wing rock* - involves lightly damped rolling oscillations. It has two types; a lateral unsteadiness with intermittent oscillations in roll of small amplitude and an AoA dependent limit cycle due to periodically changes of rolling moments with larger amplitude [16]. This is typically associated with the involvement of separated flow and time dependent effects.
- *Departure* - defined as the initial state before the aircraft enters a spin, post-departure gyration or deep stall. It is considered as large amplitude (changes in yaw, roll or pitch  $> 20^\circ$ ) and continuously increases to a divergent motion.
- *Deep stall* - happens beyond the stall region occurred when the aircraft is in a very high AoA. Recovery may be possible depending on the pitching moment coefficients though it comprises an out of control flight condition.
- *Post-stall gyration* - a non-repeatable and irregular motion such as the falling leaf motion which happens at high AoA and high side slip angle.

Table 2.1: Typical Flight Regimes for General Aviation (GA), Jet Transport (JT), and Fighter (F) Aircraft [15].

Aerodynamic Region	Angle of Attack Range (deg)	Possible Flight Attributes
Low Angle of Attack	0 - 15 (GA, F) 0 - 10 (JT)	Conventional flight
Pre-stall	15 - 20 (GA) 10 - 15 (JT) 15 - 25 (F)	Unsteady effects (buffet, wing drop, wing rock)
Stall, Stall Break	20 - 30 (GA) 15 - 25 (JT) 25 - 35 (F)	First lift peak, loss of lift, porpoising, loss of longitudinal and directional stability, adverse yaw
Post-stall	30 - 40 (GA) 25 - 40 (JT) 35 - 50 (F)	Departure, post-stall gyrations, incipient spin
Super-stall	40 - 90 (GA, JT) 50 - 90 (F)	Second lift peak, deep stall, spin, supermanoeuvrability

- *Spin* - a complicated manoeuvre involving simultaneous roll, pitch and dominantly yaw rate at high AoA. The spin mode can be defined in three phases, incipient phases, developed phases and fully developed phases.

Further characterization of these attributes can be achieved by approximating the stability derivatives parameters as seen in Figure 2.4. The approach is particularly convenient as the derivatives can be calculated from static aerodynamic data. This method has been applied with a high degree of reliability [17]. The chart indicates susceptibility of the aircraft to departure, spin and roll reversal. The chart consists of two important parameters which are:

1. Directional departure parameter,  $C_{n\beta_{dyn}}$ : convenient departure predictor;

- $C_{n\beta_{dyn}} = C_{n\beta} \cos(\alpha) - (I_z/I_x) C_{l\beta} \sin(\alpha)$ ,
- at least  $C_{n\beta_{dyn}} > 0$  to avoid departure.

2. Lateral control departure parameter (LCDP): tendency to roll reversal;

- $LCDP = C_{n\beta} - C_{l\beta}(C_{n\delta_a}/C_{l\delta_a})$ ,
- must be positive to avoid departure.

## 2.2 Nonlinear Flight Dynamic Analysis

The dynamics of aircraft can be modelled using the equations of motion (EoM) consisting of the forces and moments due to weight, aerodynamics and thrust for a given rigid body. Non-linearities are due to kinematic coupling, inertia coupling, aerodynamic characteristics and trigonometric functions of the Eulers angles [18]. Specific methods are utilized to analyze a nonlinear system. The following subsections present a review of the contributions from researchers in the field of flight dynamics analysis.

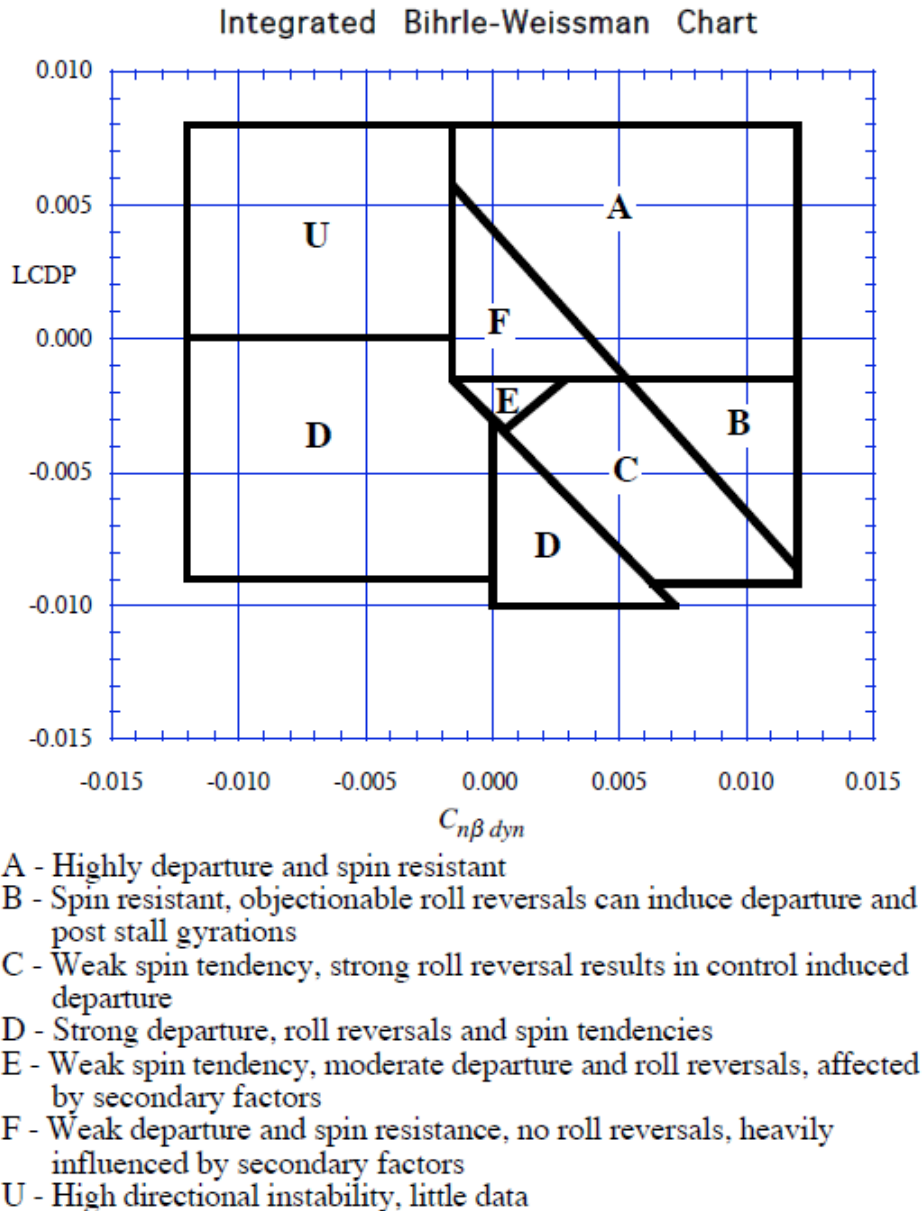


Figure 2.4: The Bihrl-Weissman chart extracted from [17].

### 2.2.1 Bifurcation: Investigating Critical Flight Regime

Much effort has been undertaken to understand aircraft dynamics by using different methods associated with nonlinear system analysis. One of the most recognized methods is bifurcation analysis which is the study of a system of equations with several solutions that ‘bifurcate’ (branch out) from some known solution [19, 20]. The analysis records all the critical points in a dimensional state parameter space where equilibrium and periodic solutions are either created, destroyed, or undergo a change in stability.

#### 2.2.1.1 Bifurcation and Catastrophe Theory Method

Flight dynamic analysis using the Bifurcation and Catastrophe Theory Method (BACTM) was introduced by Carroll and Mehra [21] in the 1980s. They managed to quantify the

main types of instabilities of an aircraft by generating bifurcation and equilibrium surfaces. Then Zagaynoz and Goman [22] varied the method by calculating and analyzing periodic solution stability using Poincare mapping. Jahnke and Culick [23] used an F-14 model to predict the nature of the instabilities caused by bifurcations and the responses of the aircraft once bifurcation was encountered.

Ananthkrishnan and his team [24, 25] have extended the usage of the BACTM method into the Extended Bifurcation and Continuation Method (EBCM). The new approach allows more than one control parameter to be simultaneously varied in a set of equations which is more realistic in evaluating the dynamic behaviour of highly agile aircraft such as the F-18 HARV.

EBCM had also been applied in the aircraft design process by reviewing the deep stall characteristics of four different configurations of T-tail aircraft with various pitching moment curves [26]. From the analysis, the study concluded that the design requirement for the tail is important in determining the aerodynamics characteristics. Moreover, Liaw and Song [27] utilized the bifurcation-theoretic approach to study the longitudinal dynamics of the F-8 and found that bifurcation behaviour changed with aircraft mass.

Bifurcation investigation has been proven to be successful as the predictions obtained theoretically correlate with flight test results. In [28], an Alpha jet was used to perform transient analysis to understand the immediate behaviour and the influence of speed variations on the control of motion in the spin problem. Jahnke and Culick [29] also proved the efficiency of the method when analyzing the roll coupling instability.

### 2.2.1.2 Continuation Method to Find Equalibria

However, bifurcation analysis cannot stand alone. It needs to be coupled with the continuation technique to provide a comprehensive view of dynamic response from parameter variation. The continuation technique extends the space of state variables by making other control parameters constant while one selected parameter is varied in time. It uses predictor and corrector steps to search for the nearest solution point in the curve. Thus, it maps out how the equilibrium condition changes as a function of the parameters as well as the periodic solution [30, 31, 32]. Continuation technique has been accepted widely as a catalyst to begin the bifurcation analysis.

The stability limit of a nonlinear system can be defined using attraction estimation as a basin. This is considered the hardest region to establish. However, Goman and Khramtsovsky [33], designed a nonlinear control for wing rock suppression for the Hypothetical High Incidence Research Model (HHIRM) based on the domains of attraction for the closed loop system. To employ such a complicated analysis, they created a tool to find the solution branches, systematically combining robust continuation method and basin of attraction techniques.

### 2.2.1.3 Bifurcation Diagram for Control Design

Bifurcation analysis was used to produce a ‘reference map’ or bifurcation diagram to indicate the source of undesirable flight behaviours. Information provided from the diagram can detect the type of bifurcation occurring in the condition, thus predicting the discontinuity in the equilibrium of the system which may lead to the stall of the aircraft. Two common types of bifurcation dealt within flight dynamics [19];

- Saddle - Node Bifurcation (one zero eigenvalue) - One stable steady state (node) and one unstable steady state node (saddle) which cause jump phenomena when node is destroyed.

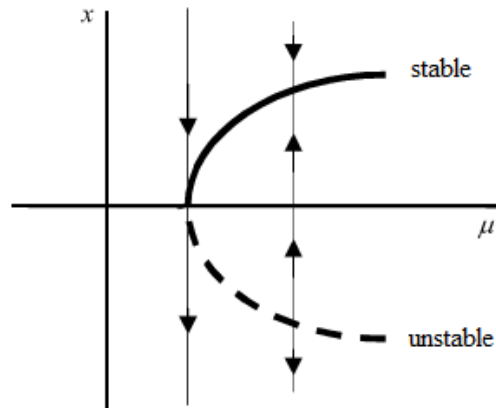


Figure 2.5: Saddle-node bifurcation (taken from [34]).

- Hopf Bifurcation (complex eigenvalue with zero real part) - Creation or destruction of periodic orbit (limit cycle) encircling the equilibrium point.

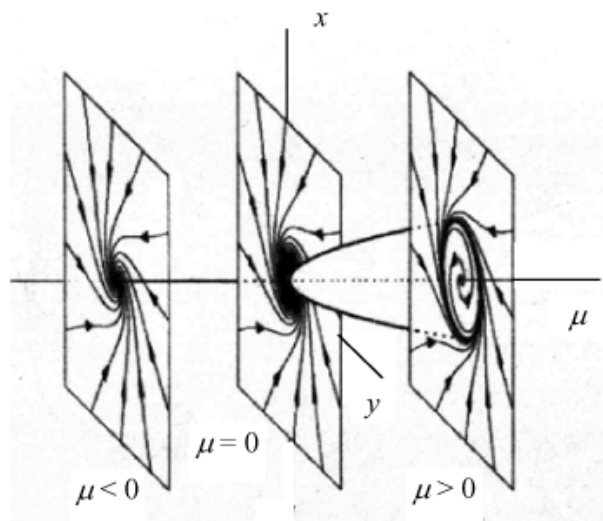


Figure 2.6: Hopf bifurcation (taken from [34]).

An example of application of the bifurcation diagram showing the bifurcation points appears in the work of Rhagavendra et. al. [35]. The authors had used the information from the bifurcation diagram to identify level flight trim states before triggering the spin phenomena. Then, a nonlinear dynamic inversion was applied to determine the control inputs to recover to a level trim flight condition. Several Hopf bifurcations (H1 and H2) were identified at high AoA in Figure 2.7 where limit cycles started to develop. On the bifurcation diagrams, a solid line denotes stable equilibria while dashed lines indicate unstable equilibria. However, it was found that the direct recovery process was restricted because of saturation of the primary control. Thus, two alternate solutions were proposed using vectored thrust.



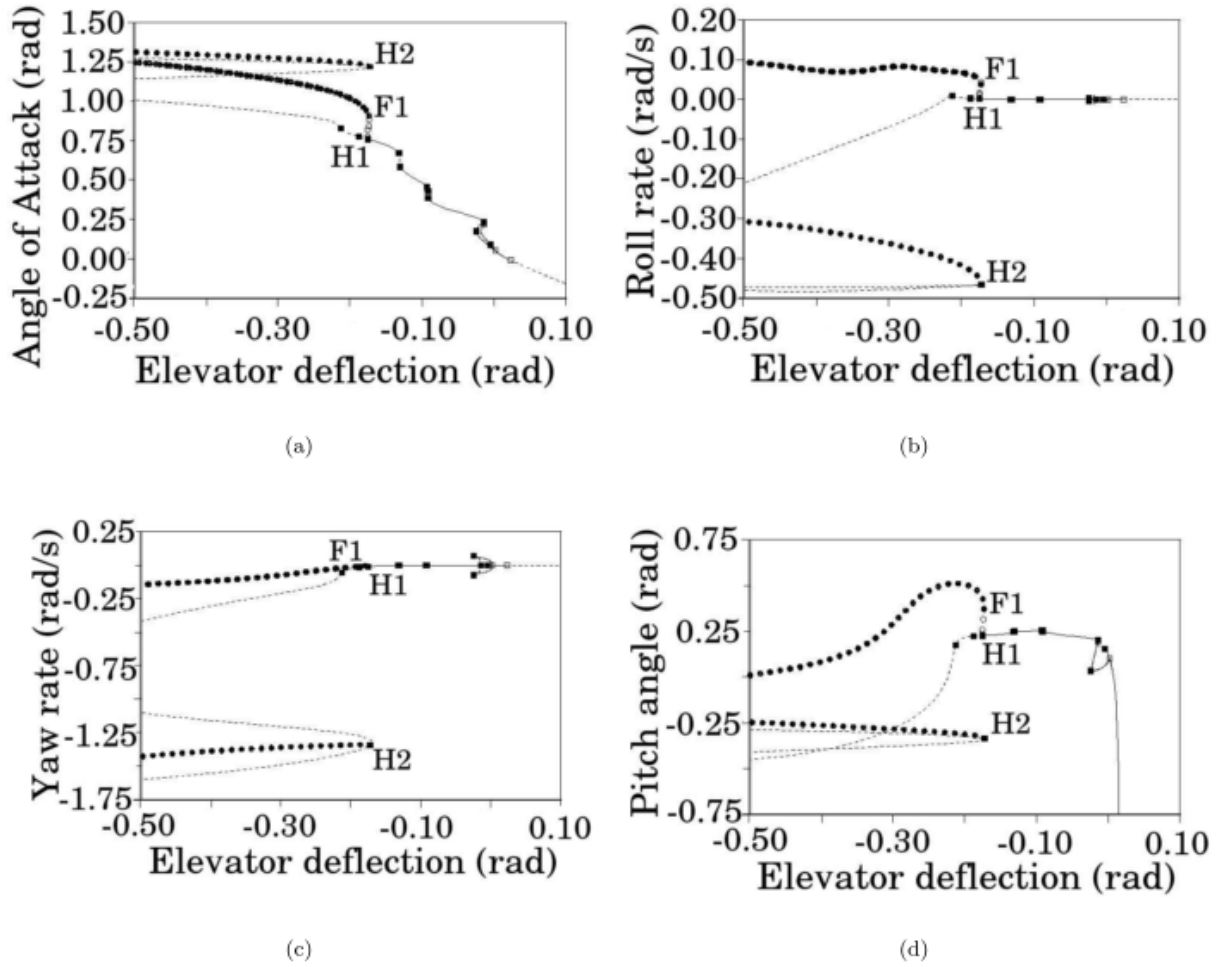


Figure 2.7: Bifurcation diagram with elevator deflection as the continuation parameter showing the behaviour of (a) angle of attack, (b) roll rate, (c) yaw rate, and (d) pitch angle extracted from [35].

The bifurcation diagram can be used to suggest the control required to achieve stable flight assuming no spin takes place. The map proved very useful as a guideline in designing control laws where Thomas et. al.[36] used a bifurcation diagram to design a reconfigurable control for the F-16. Limitations in the stability were identified as the effect from actuator failure to design reconfiguration controller formulated as a nonlinear regulator problem.

#### 2.2.1.4 Expanding the Application of Bifurcation Analysis

The application of bifurcation analysis to the solution of the nonlinear dynamics of fighter aircraft has been widely accepted. For example, Liebst [37] examined the wing rock on the F-15. However, rather than solve the problem nonlinearly, the author used linear analysis. At each bifurcation point, the eigenvalues were analysed to identify the effect of longitudinal and lateral - directional modes on the wing rock onset by varying the AoA. He then used a different technique to predict the wing rock which is simplistic approach.

Recently, the application of bifurcation theory has been extended to a Generic Transport Model (GTM) [38, 39] to aid the understanding of upset scenarios. Though in Reference[38], it focused more on the technical method of applying the bifurcation analysis on the GTM detailing the approaches to tackle the feasibility of the model representa-

tion with bifurcation analysis. As the author remarked, the look up table representation on the GTM model with a linear interpolation has yielded unacceptable results and was hence modified to use cubic spline interpolation.

While the nature of the bifurcation analysis is numerical, an effort to approach the problem analytically has been attempted [40, 41]. However, the conditions are restricted to lower AoA with a weaker coupling effect, thus limiting its application to flight dynamics. Also the calculations involve a heavy computational load with large symbolic expression which is not conducive to the use of tabular data.

#### 2.2.1.5 Software Tools

The bifurcation method has gained wide acceptance as more open source software has been developed, such as AUTO[42], XPPAUT[42], and MATCONT[43]. AUTO and XPPAUT are used interchangeably in analyzing the dynamics of a system. First, a set of ordinary differential equations is integrated in the phase plane provided in the XPPAUT environment until a steady state has been reached and then it is passed to AUTO for continuation and bifurcation analysis.

MATCONT is a graphical MATLAB package for the interactive numerical study of bifurcation analysis of dynamical systems. Compared to AUTO and XPPAUT, MATCONT is still a new tool in bifurcation world, as it has recently been developed. The latest bifurcation software developed by a group of researchers from Bristol University has integrated AUTO into MATLAB and Simulink interfaces the application of bifurcation techniques in engineering problem-solving [44].

### 2.2.2 Other Approaches to Nonlinear Analysis

There was an attempt to investigate the nonlinear behaviour of aircraft at high AoA by modelling the system using Volterra series. The series comprises output generalized power series containing multiple convolution integrals of products of the input variables evaluated at different times [45]. Results from this approach showed good correlation with the simplified nonlinear aircraft model for the longitudinal limit cycle and wing rock. It was found that higher order Volterra series predicted the limit cycle period and magnitude.

Omran and Newman [46] improved the method by characterizing the flight attributes according to pre-stall, stall, and post-stall using a piecewise Volterra kernel. To simplify the problem, the aircraft was modelled in a reduced order form applicable only to longitudinal flight. The method produced information for limit cycle amplitude and frequency as well as transient oscillation frequency and rate decay.

A study of the physical characterization of the limit cycle has been attempted by Abdulwahab and Hongquan in order to tackle the problem of periodic oscillation using the Lyapunov stability criterion [47, 48]. A numerical investigation was conducted on different aircraft to characterize both the limit cycle in longitudinal and lateral-directional modes which might lead to chaos.

Multiple Time Scale (MTS) analysis was applied to assess the longitudinal dynamics of a small agile Unmanned Aerial Vehicle (UAV) at high AoA [49]. The MTS method

was applied together with linear dynamics and bifurcation theory to capture the non-asymptotic stability behaviour analytically. It was found that the interaction between the cubic non-linearity in lift and thrust together with the loss of pitch damping caused the limit cycle to occur.

Last but not least, an index to represent a degree of system non-linearity has been suggested in [50]. The concept has been applied in orbital mechanics [51, 52], in which a different theories had been tested to capture the non-linearity effects based on the sensitivity of the state space matrices to the initial conditions. Recently, the method has been extended in the application of flight mechanics as found in [53, 54, 55] and [56] where the index was not only sought based on initial value problem but also on the sensitivity of the input excitation.

## 2.3 Simulation Model for High Angles of Attack Flight

Simulation is a widely used and accepted tool in flight operations research and aircraft systems analysis due to its capability to decrease flight evaluation cost. Simulation uses a model which describes the aircraft in a mathematical form in order to generate the dynamic performance and to explore modes of interaction between the system, the operators, and the environment [57].

In constructing the simulation model, two major elements are needed; the EoM for the vehicle and a representation of the vehicle aerodynamics [58].

### 2.3.1 Mathematical Modeling

An aircraft simulation consists of different subsystems, for example; aerodynamics, propulsion, structure, dynamics, and other mechanical, electrical and hydraulic systems which are assembled together to predict the complete system responses to control and external disturbances. These responses are measured in terms of displacement, velocity, and acceleration variables presented in the Equations of Motion (EoM) [59]. It relates the translational and rotational accelerations of an aircraft to the resultant forces and moments acting on it.

The EoM usually take the form of a set of Ordinary Differential Equations (ODEs) in five different ways, nonlinear fully coupled, nonlinear semi-coupled, nonlinear decoupled, linear coupled, and linear decoupled. For each representation, the EoM determines the precision, accuracy, complexity and credibility of the system to be studied [60].

However, the aircraft is usually nonlinear and fully coupled. Depending on the purpose of the simulation, the EoM can be simplified into a linear system by assuming small perturbations and decoupled between the longitudinal and lateral-directional dynamics into a three DoF system for a simple flight operation. These simplifications can be applied individually or simultaneously.

In a recent study, a polynomial vector field was implemented to approximate the longitudinal EoM of an aircraft. The study analysed the falling leaf mode of the F/A-18 using nonlinear simulation [8]. A region of attraction was estimated as a means to validate the revised control law which is less susceptible to loss of control phenomena. It was observed that this control law significantly increased the performance of the aircraft. Similarly,

Zhongke and Li [61] transformed the EoM into polynomial expressions to avoid linear approximation method at high AoA and to apply the bifurcation theory analytically.

Sadraey [60] has suggested some guidelines to suit the purpose of a simulation. Generally, a linear decoupled model is reliable enough for a simulation not involving a large bank angle that is less than  $30^\circ$  though he agrees that an accurate dynamic model for a full envelope flight simulation requires nonlinear fully coupled EoM.

In related work regarding the divergence of a linear solution from the nonlinear solution [62], the results showed that the nonlinear solution caused a large difference in amplitude and frequencies of oscillations as the control input deflections were increased. However, Ozdemir noted that the accuracy of the nonlinear solutions was limited to the accurate determination of the aerodynamic model.

### 2.3.2 Aerodynamic Representation

Aerodynamic force and moment representation for a high AoA model requires sufficiently comprehensive data to cover the wide range of parameter variation and must accurately represent all the complex aerodynamic phenomena [58]. The aerodynamics in this region are characterized by nonlinear effects due to unsteady flow and inertial coupling [63]. Usually, the data is limited as advanced acquisition methods are required during wind tunnel testing or risky flight test manoeuvres.

Specifying a universal aerodynamic model requires it to be defined statically and dynamically. The contributing static effect can be determined from standard wind tunnel test while the dynamic effects from unsteady aerodynamics can be modelled by combining the derivative values collected from forced oscillation and rotary balance tests conducted in the wind tunnel [64]. Otherwise, it can be determined from flight tests using the parameter estimation technique discussed by Napolitano [65, 66].

Generally, the mathematical formulation is expressed as a function of several effects, such as [67];

$$\begin{aligned}
 C_i = & f(\alpha, \beta, \delta) && \text{measured static data} \\
 & + f(M) && \text{Mach number effect} \\
 & + f(Re) && \text{Reynolds number correction} \\
 & + f(\Omega/V) && \text{rotary balance data} \\
 & + f(pl/V, ql/V, rl/V) && \text{forced oscillation data}
 \end{aligned} \tag{2.1}$$

An example of forced oscillation data for the F-18 HARV is shown in Figure 2.8 and 2.9. The data was published by Brandon [68] to visualize the unsteadiness of the aerodynamic flow. A wind tunnel test was conducted on the F-18 HARV model to investigate the effects of the pitch rate and motion time history. The test was done at AoA range from  $5^\circ$  to  $75^\circ$  for  $0^\circ$  and  $10^\circ$  sideslip angles. The aircraft was configured with flap setting at  $34^\circ$  at the leading edge and  $0^\circ$  at the trailing edge while reference gravity center was located at 24%.

The conventional method is to represent each coefficient in Equation 2.1, in tabulated form. However, this method can be problematic if extrapolation is used to cover large arbitrary rotations. On the other hand, the large database required to store the aerodynamic characteristics raises concern over slow computation time and the amount of

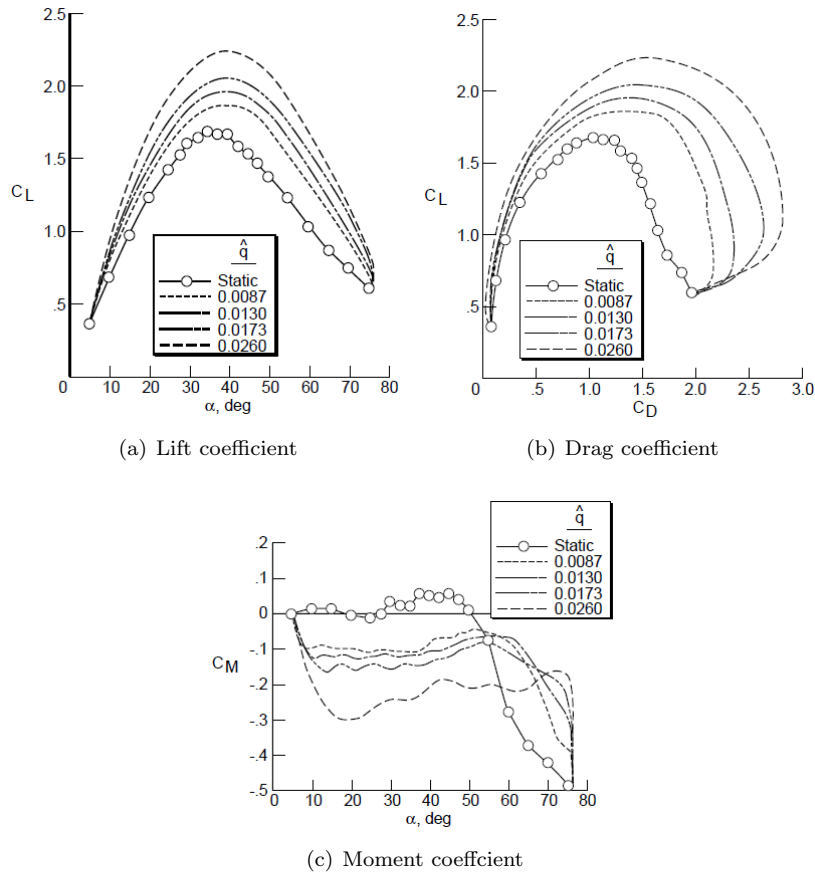


Figure 2.8: Effect of positive pitch rate on the aerodynamic coefficients extracted from [68].

space for memory storage. This approach has been found to be ineffective when used in bifurcation analysis [69, 38].

Attempts to formulate a global model of the aerodynamic forces and moments covering a large portion of the flight envelope by function approximation has been undertaken. In order to generate a compact model that still has adequate complexity to capture the non-linearities, certain mathematical formulations were introduced using multivariate orthogonal functions [70] and B-splines [71], taking advantage of the properties of numerical computation. Alternatively, multivariable Chebyshev polynomials have been used to describe the dominant trends in the variation of AoA and sideslip angle [72].

Another approach to represent the data is by a polynomial expansion which is widely applied in parameter estimation techniques. This is because it provides a concise description of the aerodynamic characteristics. However, the polynomial formulation can be disordered in describing the nonlinear data typically when higher order functions are considered [73].

## 2.4 Conclusion

Bifurcation theory may have been proven a reliable tool in understanding the nonlinear dynamics of aircraft. However, to analyse the nonlinear model is not straight forward but may involved a computationally tedious approach. There also has existed a trend of

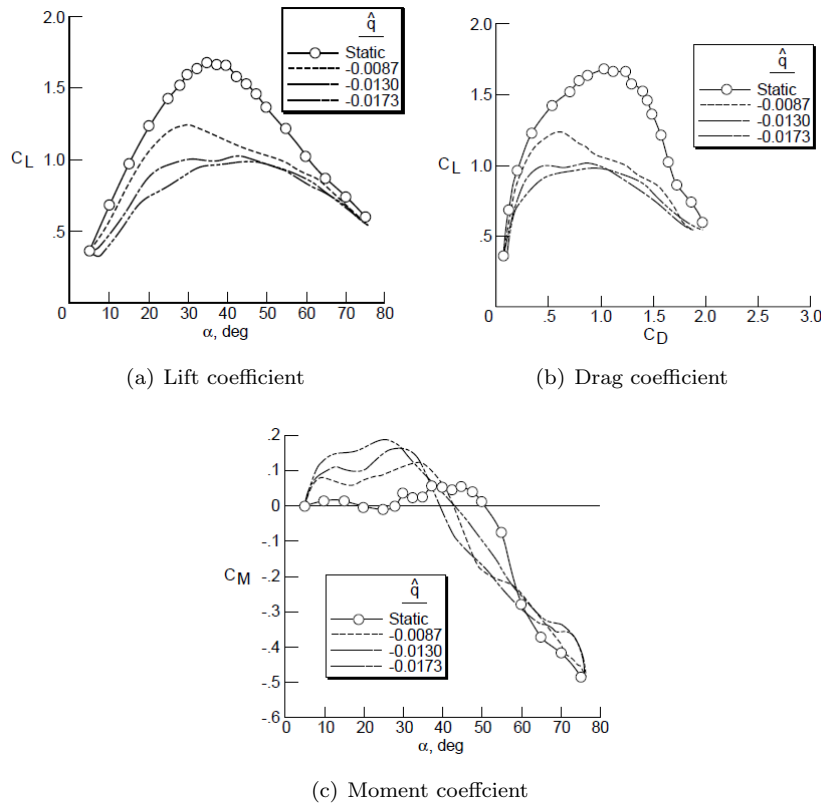


Figure 2.9: Effect of negative pitch rate on the aerodynamic coefficients extracted from [68].

performing the bifurcation analysis analytically in solving problems for flight dynamics. While flight dynamics is a nonlinear system, it is often linearized with some simplification or assumptions applied to the system. Otherwise, whenever a linear approach fails to predict or identify nonlinear behaviour, the nonlinear analysis such as bifurcation should be utilised. Therefore, understanding the non-linearity of a system is worthwhile, so it is known how well the system could be regarded as a linear system prior the system analysis, as has been examined in [54, 55].

Dynamics of aircraft are dominated by the aerodynamic forces. In order to study the behaviour of the aircraft at high AoA, careful selection on appropriate aerodynamic models and evaluation of the aerodynamic coefficients which represent the full scale aircraft flight should be considered. The aerodynamic characteristics can be based on data from wind tunnel experiments and flight testing which depend on the reduced scale of the model and data reduction. Data from both methods are often used to comprehend each other.

The flight data for the F-18 HARV can be found in technical reports or in public domain published by NASA. The data was presented in various forms such as plotted graphs from flight test result or wind tunnel experiments and also look up table [68, 65, 66, 9]. However, the data collected from the published reports were applicable only to certain flight conditions. For example, the aerodynamic model published by [68] is suitable for high AoA model development, but is limited to the longitudinal flight only, which may not be sufficient to develop a comprehensive model. The effect of the flaps also may not be very promising if a blended model is to be developed.

There was significant effort to regenerate some of the experimental data from wind tunnel test and flight test into mathematical representation, to allow it to be easily embedded into

the aircraft model. For example, arc-tangent formulation to describe each coefficient at different flight conditions as resulting from wind tunnel experiment [74] and a polynomial function coefficients [73, 75] of AoA to match the original flight test result. It is noted nonlinear region at high AoA results in the model being complex. In view of this, it raised questions regarding how the data should be presented to represent the general model of the aircraft.

In this thesis, the different sources of the aerodynamic data will be reviewed to quantify the differences from an analytical perspective. The study also will try to discover if the differences in the the model representations affect the nonlinear simulation. Then, a series of non-linearity assessments were carried out to quantify the non-linearity in the models when certain flight conditions are considered and if it might be related to a bifurcation behaviour when certain index is reached. The assessment also will be used in identifying the source of the non-linearity.

This page is intentionally left blank.



## Chapter 3

# F-18 HARV Aerodynamic Models

The purpose of this chapter is to discuss and present several aerodynamic models for the F-18 HARV used in this thesis. The source for each model was investigated while the data were compared in order to identify any type of irregularity that might affect the dynamics of the aircraft.

### 3.1 Introduction

Aerodynamics simulates the forces and moments that shape the flight trajectory. For each aircraft, the characteristics are unique depending on the aerodynamic model. The representation of the aerodynamic data can be as simple as the linear terms of the Taylor-series expansion or as complicated as tables with various independent variables.

Estimation of the aerodynamic characteristics for an aircraft can be determined from wind tunnel experiments, simulation of Computational Fluid Dynamics (CFD), and a computer program developed by United State Air Force (USAF) called Digital DATCOM, or sometimes from the flight test evaluation [59]. Determination of the aerodynamic characteristics is important for early design process of the aircraft for control and performance estimation as well as for parameter identification process using the flight test data. The aerodynamic characteristics are usually presented in dimensionless coefficient form with respect to the flight control settings and can be built up by combining all respective derivatives for a full representation of the forces and moments coefficients.

However, it is not always easy to get aerodynamic data from the open literature, mostly the primary sources. As for the F-18 HARV, several papers exist that describe the aerodynamic characteristics. One that might be very useful is from the manufacturer itself [76], which some of the research papers on F-18 HARV refer to [77, 74]. On the other hand, there have been efforts to determine the aerodynamic model using published flight data [65, 66, 78]. Some papers refer to these efforts [8, 79] where the stability and control derivatives of the aircraft are fitted in a polynomial form with varying alpha.

### 3.2 Aerodynamic Modelling: Source of Models

The diverse models of the F-18 HARV as available in the public domain can be varied from linear simple models as presented in state space to full nonlinear models. As for

the thesis development, three sets of aerodynamic data were collected from the literature though there would be other data that may have not been considered due to limited access. These various sources of the aerodynamic data are discussed and presented in the following subsection.

### 3.2.1 Cao Model

The aerodynamic model developed by Cao et al [74] contains a continuous function of the coefficients depending on the AoA for various flight conditions. Though the curves reflect nonlinear behaviours with respect to AoA, it has been assumed that the intermediate flight conditions depending on  $\beta$ ,  $M$ ,  $\delta_h$ ,  $\delta_r$ , and  $\delta_a$  may be predicted by linear interpolation.

The analytical formulations as contained in the report were developed in order to implement optimal control analysis at high AoA. A function approximation was established based on the wind tunnel data [77] using the arc-tangent function for several flight conditions covering the extreme deflections of stabilator,  $\delta_h$ , ( $+10.5^\circ, -24^\circ$ ), rudder,  $\delta_r$ , ( $\pm 30^\circ$ ) and aileron,  $\delta_a$ , ( $\pm 25^\circ$ ) for the range of  $\alpha$  between  $0^\circ$  to  $90^\circ$ ,  $\beta$  from  $-20^\circ$  to  $20^\circ$  and Mach number from  $0.3 - 0.9$ .

The derived formulations are nonlinear functions of  $\alpha$  with other variables such as  $\beta$ ,  $M$ , control surfaces deflections,  $\delta_h$ ,  $\delta_r$  and  $\delta_a$ , and angular velocity,  $p, q$ , and  $r$ , kept constant accordingly. In addition, the effect of unsteady aerodynamics was considered for lift coefficient and pitch moment coefficient in the mathematical structure for both coefficients by the inclusion of  $\dot{\alpha}$ . All the data from wind tunnel tests corresponded to  $15000ft$  altitude.

The equations were formulated based on aerodynamic coefficients from wind tunnel tests reported by McDonnell Aircraft Company [76, 80] and a technical report published by NASA [77]. Though the developed formulation was reported to decrease the storage requirement of the wind tunnel data to one tenth with a faster simulation time, no further work on the same author was traced in the public domain. Even so, [81] and [82] have used the Cao model in order to design adaptive controllers and to study the dynamics of vectored thrust aircraft in the post stall region respectively. Both papers mention only the longitudinal model motion which is described by angles of attack, pitch rate, and total speed.

It was noted that some of the curves which produced by the analytical expressions did not match with the wind tunnel data as published in the report. Therefore, the model has been modified taking into account the contribution of each arc-tangent effect on the curves' properties (refer to the following section).

### 3.2.2 Chakraborty Model

In analysing the falling leaf mode for F/A-18 Hornet, Chakraborty developed a comprehensive six DoF mathematical model for the aircraft based on several papers available publicly. The aerodynamic data of the F/A-18 HARV is used to formulate the aerodynamic model for the F/A-18 Hornet. In the model, the flight test data from [65, 66, 78] had been extracted to generate an aerodynamic model based on polynomial function as a function of AoA. However, the data only covered the AoA range from  $10^\circ$  to  $60^\circ$ .

Therefore, an artificial data has been introduced between the range of  $0^\circ < \alpha < 10^\circ$  by extrapolation. This is to ensure realistic fit for estimating the closed form expression of the aerodynamic coefficients [8]. The assumption is that for a conventional aircraft, the aerodynamic characteristics do not change significantly at lower AoA. On another precautions, the data is unavailable for nonzero sideslip flight conditions which is one of the basic criteria that one must considered in analysing the falling leaf mode. In order to include the effect, an approximation based on Steven and Lewis [83] approach was adapted to be considered for the side force coefficient, rolling moment coefficient and yawing moment coefficient models.

The functional form for the aerodynamic coefficients can be expressed as a sum of terms that model the aerodynamic effects of the basic airframe, control inputs and angular rate damping. In general, Chakraborty aerodynamic model is given as follow:

$$C_D = C_{D_0} + \sum_{i=1}^4 C_{D_{\alpha_i}} \alpha^i \cos \beta + \sum_{i=0}^3 C_{D_{\delta_{h_i}}} \alpha^i \delta_h \quad (3.1a)$$

$$C_L = \sum_{i=1}^3 C_{L_{\alpha_i}} \alpha^i \cos\left(\frac{2\beta}{3}\right) + \sum_{i=0}^3 C_{L_{\delta_{h_i}}} \alpha^i \delta_h \quad (3.1b)$$

$$C_Y = \sum_{i=1}^2 C_{Y_{\beta_i}} \alpha^i \beta + \sum_{i=0}^3 C_{Y_{\delta_{a_i}}} \alpha^i \delta_a + \sum_{i=0}^3 C_{Y_{\delta_{r_i}}} \alpha^i \delta_r \quad (3.1c)$$

$$C_l = \sum_{i=1}^2 C_{l_{\beta_i}} \alpha^i \beta + \sum_{i=0}^3 C_{l_{\delta_{a_i}}} \alpha^i \delta_a + \sum_{i=0}^3 C_{l_{\delta_{r_i}}} \alpha^i \delta_r + \frac{b}{2V} \left[ \sum_{i=0}^1 C_{l_{p_i}} p + \sum_{i=0}^2 C_{l_{r_i}} r \right] \quad (3.1d)$$

$$C_m = \sum_{i=1}^2 C_{m_{\alpha_i}} \alpha^i + \sum_{i=0}^2 C_{m_{\delta_{h_i}}} \alpha^i \delta_h + \frac{\bar{c}}{2V} \sum_{i=0}^3 C_{m_{q_i}} \alpha^i \quad (3.1e)$$

$$C_n = \sum_{i=1}^2 C_{n_{\beta_i}} \alpha^i \beta + \sum_{i=0}^4 C_{n_{\delta_{a_i}}} \alpha^i \delta_a + \sum_{i=0}^3 C_{n_{\delta_{r_i}}} \alpha^i \delta_r + \frac{b}{2V} \left[ \sum_{i=0}^1 C_{n_{p_i}} p + \sum_{i=0}^1 C_{n_{r_i}} r \right] \quad (3.1f)$$

Due to lack of available data the rate damping effect on the aerodynamic force coefficients ( $C_D$ ;  $C_L$ ;  $C_Y$ ) is ignored in the model formulation.

### 3.2.3 NASA Model

NASA model is traceable via [84], which is a link to NASA's website describing previous F18 projects. The link provides raw MATLAB coding for the application of dynamic inversion control. From one of the files, a description on the aerodynamic model consisting of an aerodynamic database containing of 33 aerodynamic coefficients and derivatives as a function of AoA between  $-14^\circ$  to  $90^\circ$ . However, the source is nonlinear with respect to AoA and is linear with respect to all other state variables and control surface deflections

in a similar manner to Cao model.

$$C_{D_{NASA}} = C_{D_0} + C_{D_{\delta_{h_l}}} \delta_{h_l} + C_{D_{\delta_{h_r}}} \delta_{h_r} + \frac{\bar{c}}{2V} C_{D_q} q \quad (3.2a)$$

$$C_{L_{NASA}} = C_{L_0} + C_{L_{\delta_{h_l}}} \delta_{h_l} + C_{L_{\delta_{h_r}}} \delta_{h_r} + \frac{\bar{c}}{2V} C_{L_q} q \quad (3.2b)$$

$$C_{m_{NASA}} = C_{m_0} + C_{m_{\delta_{h_l}}} \delta_{h_l} + C_{m_{\delta_{h_r}}} \delta_{h_r} + \frac{\bar{c}}{2V} C_{m_q} q \quad (3.2c)$$

$$C_{Y_{NASA}} = C_{Y_\beta} \beta + C_{Y_{\delta_a}} \delta_a + C_{Y_{\delta_r}} \delta_r + \frac{b}{2V} [C_{Y_p} p + C_{Y_r} r] \quad (3.2d)$$

$$C_{l_{NASA}} = C_{l_\beta} \beta + C_{l_{\delta_a}} \delta_a + C_{l_{\delta_r}} \delta_r + \frac{b}{2V} [C_{l_p} p + C_{l_r} r] \quad (3.2e)$$

$$C_{n_{NASA}} = C_{n_\beta} \beta + C_{n_{\delta_a}} \delta_a + C_{n_{\delta_r}} \delta_r + \frac{b}{2V} [C_{n_p} p + C_{n_r} r] \quad (3.2f)$$

The data was presented in non-analytical components such as LUTs embedded within. Though NASA model provide a nearly complete model with a relatively simple approach as compared to Cao, traceability of the data is remains questionable. However, several publications in the public domain exist referencing the model to be used in their works such as [35, 85, 86, 18].

### 3.2.4 Modified Cao Model

This subsection describes the method used to improve the matching of the analytical formulations from [74] to the published wind tunnel data. All the curves were regenerated in a MATLAB environment and compared with the original curves from the same source. The curves which did not match the wind tunnel data were then adjusted to improve the condition so the deviations were reduced.

The arc-tangent of a variable  $x$  returns the inverse tangent function of  $x$  when  $x$  is in the real domain. However, in the Cao formulation, the  $x$  is taken to be the  $\alpha$  which is in a degree unit ranging from  $0^\circ < x < 90^\circ$ . This has the effect of adding an increment over a narrow range of angles. The graph of basic arc-tangent is illustrated in Figure 3.1.

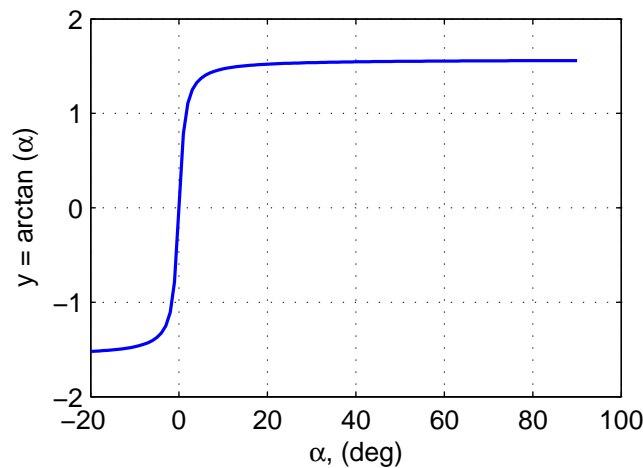


Figure 3.1: Domain of the arctangent function of  $\alpha$ .

In general, formulation can be generalized as:

$$f(\alpha) = a \arctan((\alpha \pm b)c) \pm d \quad (3.3)$$

where

- $a$ : scales the magnitude of the curves.
- $b$ : shifts the curves horizontally.
- $c$ : increases or decreases the vertical slope of the curve.
- $d$ : shifts the curves vertically.

This is demonstrated as in Table 3.1 which shows the method applied to improved the fit of those functions that do not match the published curve in Cao et. al. [74].  $Cy0XXB2$  is the original curve whereas the subscript  $E$  represents the modification.

Table 3.1: Demonstration on the chosen modified curve.

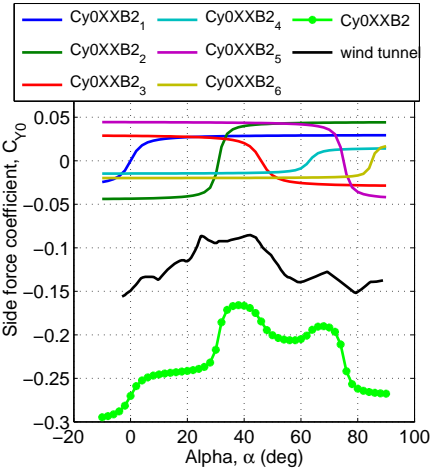
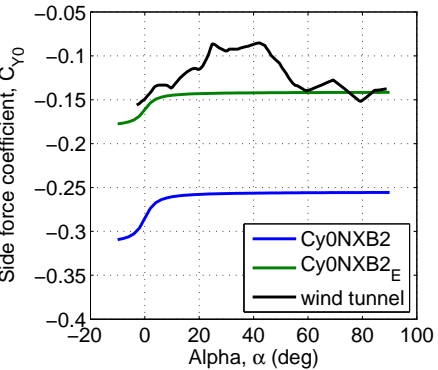
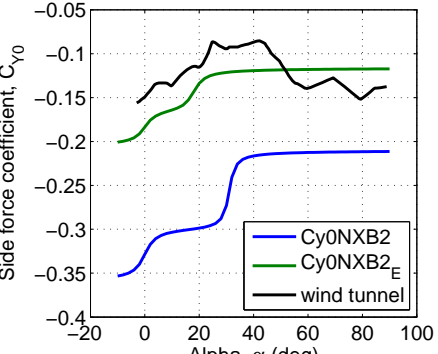
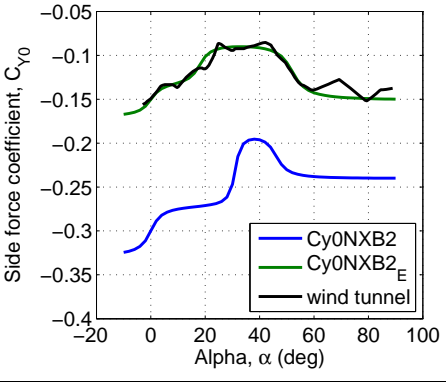
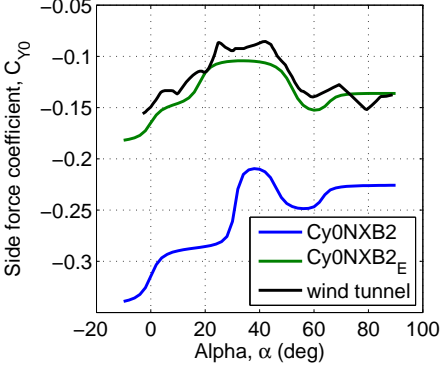
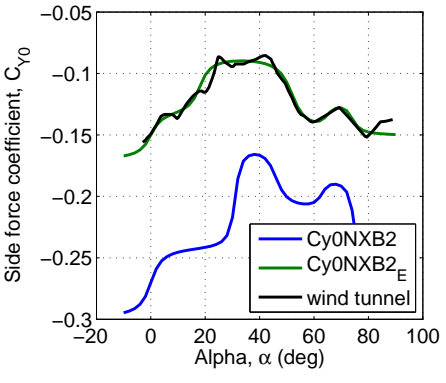
Curve	Step
	<p><b>Step 1:</b> Showing the effect of each element:</p> $Cy0XXB2_1 = (.06/\pi) \arctan((\alpha/3))$ $Cy0XXB2_2 = (.09/\pi) \arctan((\alpha - 31)5/8)$ $Cy0XXB2_3 = (.06/\pi) \arctan(-(\alpha - 46)3/10)$ $Cy0XXB2_4 = (.03/\pi) \arctan((\alpha - 65)3/7)$ $Cy0XXB2_5 = (.09/\pi) \arctan((75 - \alpha)3/5)$ $Cy0XXB2_6 = (.04/\pi) \arctan((\alpha - 85)4/5) - .285$ $Cy0XXB2 = Cy0XXB2_1 + Cy0XXB2_2 + Cy0XXB2_3 + \dots$ $Cy0XXB2_4 + Cy0XXB2_5 + Cy0XXB2_6 - .285$ <p><math>Cy0XXB2</math> is the original curve from Cao.</p>
	<p><b>Step 2:</b> Shifting the curve and tuning the first element.</p> $Cy0XXB2_{S2} = Cy0XXB2_1 - .2850$ $= (.06/\pi) \arctan((\alpha/3) - .2850)$ $Cy0XXB2_E = (.04/\pi) \arctan((\alpha/3) - .1612)$
	<p><b>Step 3:</b> Tuning the second element to capture second rise.</p> $Cy0XXB2_{S3} = Cy0XXB2_{S2} + Cy0XXB2_2$ $= (.06/\pi) \arctan((\alpha/3) + \dots$ $+ (.09/\pi) \arctan((\alpha - 31)5/8) - .285$ $Cy0XXB2_E = (.04/\pi) \arctan((\alpha/3) + \dots$ $+ (.05/\pi) \arctan((\alpha - 18)5/15) - .1612$

Table 3.1 – Continued from previous page

Curve	Step
	<p><b>Step 4:</b> Tuning the third element to capture the peak between <math>20^\circ &lt; \alpha &lt; 45^\circ</math>.</p> $Cy0XXB2_{S4} = Cy0XXB2_{S3} + Cy0XXB2_3$ $= (.06/\pi) \arctan((\alpha/3) + \dots$ $(.09/\pi) \arctan((\alpha - 31)5/8) + \dots$ $(.06/\pi) \arctan(-(\alpha - 46)3/10) - .2850$ $Cy0XXB2_E = (.04/\pi) \arctan((\alpha/3) + \dots$ $(.05/\pi) \arctan((\alpha - 18)5/15) + \dots$ $(.07/\pi) \arctan(-(\alpha - 52)3/12) - .1612$
	<p><b>Step 5:</b> Tuning the fourth element to match peak at <math>\alpha = 70^\circ</math>.</p> $Cy0XXB2_{S5} = Cy0XXB2_{S4} + Cy0XXB2_4$ $= (.06/\pi) \arctan((\alpha/3) + \dots$ $(.09/\pi) \arctan((\alpha - 31)5/8) + \dots$ $(.06/\pi) \arctan(-(\alpha - 46)3/10) + \dots$ $(.03/\pi) \arctan((\alpha - 65)3/7) - .2850$ $Cy0XXB2_E = (.04/\pi) \arctan((\alpha/3) + \dots$ $(.05/\pi) \arctan((\alpha - 18)5/15) + \dots$ $(.07/\pi) \arctan(-(\alpha - 52)3/12) + \dots$ $(.03/\pi) \arctan((\alpha - 65)3/9) - .1612$
	<p><b>Step 6:</b> Replacing of fifth element to match reduction beyond <math>\alpha = 70^\circ</math>.</p> $Cy0XXB2_{S6} = Cy0XXB2_{S5} + Cy0XXB2_5$ $= (.06/\pi) \arctan((\alpha/3) + \dots$ $(.09/\pi) \arctan((\alpha - 31)5/8) + \dots$ $(.06/\pi) \arctan(-(\alpha - 46)3/10) + \dots$ $(.03/\pi) \arctan((\alpha - 65)3/7) + \dots$ $(.09/\pi) \arctan((75 - \alpha)3/5) - .2850$ $Cy0XXB2_E = (.04/\pi) \arctan((\alpha/3) + \dots$ $(.05/\pi) \arctan((\alpha - 18)5/15) + \dots$ $(.07/\pi) \arctan(-(\alpha - 52)3/12) + \dots$ $(.03/\pi) \arctan((\alpha - 65)3/9) + \dots$ $(.03/\pi) \arctan((74 - \alpha)3/7) - .1612$

The method was used to provide a good match to the wind tunnel data given in [74]. No further explanation is given discussed about size of the coefficients.

A summary of the formulations which have been corrected is given in Table 3.2.

All the graphs have been redrawn and are given in Appendix B and the list of modified curves are referred to Table 3.2. The adjusted formulations are also highlighted with some marked text to notify the variable changes from the original formulations wherever it is applicable.

Table 3.2: Summary of the modified analytical formulation

<b>Aerodynamic Characteristics</b>	<b>Modified Formulation</b>
Lift	CL0X6
Pitch moment	CM0X29
Side force	Cy0XNB2, Cy0NNB2, Cy0XXB2, CyP, CyR
Roll moment	Cl0XN2, Cl0XX2, Cl0NX2, Cl0XNB0, HC1P, ClR, ClB
Yaw moment	CnXXX2, CnNXX2, CnXXN2, CnNXN2, CnXNX0, CnXXN0, CnR, CnB

### 3.2.5 Summary

In short, the important features of the F-18 HARV aerodynamic models as discussed previously are summarized in Table 3.3.

Table 3.3: Basic information about the different aerodynamic models for F18 HARV.

	<b>Cao</b>	<b>Chakraborty</b>	<b>NASA</b>
<b>Source</b>	Wind tunnel test	Various literatures on estimation of aerodynamic parameters from flight data	No information
<b>Type of formulation</b>	Arctangent	Least square polynomial	Table look up
<b>Flight condition</b>	$h = 15000ft$ $M = 0.3 - 0.9$	$h = 25000ft$ No specification on $M$	No specification on $h$ $M < 0.6$
<b>Limitation</b>	$0^\circ < \alpha < 90^\circ$ $-20^\circ < \beta < 20^\circ$	$0^\circ < \alpha < 60^\circ$	$-14^\circ < \alpha < 90^\circ$
<b>Center of gravity</b>	$x_{cg} = 0.250\bar{c}$	$x_{cg} = 0.238\bar{c}$	$x_{cg} = 0.250\bar{c}$

## 3.3 Analysis of Different F-18 HARV Aerodynamic Models

### 3.3.1 Extraction of the Derivatives from the Cao Model

The aerodynamic model as given in Cao et. al. [74] presents various coefficients as a function of angle of attack considering the effects of Mach no., sideslip angle and control deflections. These conditions are summarized in Table 3.4. The effect of Mach no. is not large unless a high speed flight is considered. The example in Figure 3.2 shows no difference in the zero lift pitching moment coefficient for a change in Mach no. from 0.3 to 0.6. However this effect can be neglected as flying at high  $\alpha$  requires a low speed.

The aerodynamic model for Cao has been generalized to provide stability and control derivatives considering the effects from sideslip angle and control deflections only. These derivatives are obtained by assuming that the intermediate flight conditions are predicted from linear interpolation and the effect of each control deflection could be eliminated for

Table 3.4: Summary of effects from Mach number, sideslip angle and control deflections as supplied by Cao.

	$C_D$	$C_L$	$C_m$	$C_Y$	$C_n$	$C_l$
$\beta$ (deg)				✓	✓	✓
Mach no.		✓	✓		✓	✓
$\delta_h$ (deg)	✓	✓	✓			✓
$\delta_r$ (deg)				✓	✓	✓
$\delta_a$ (deg)				✓	✓	✓

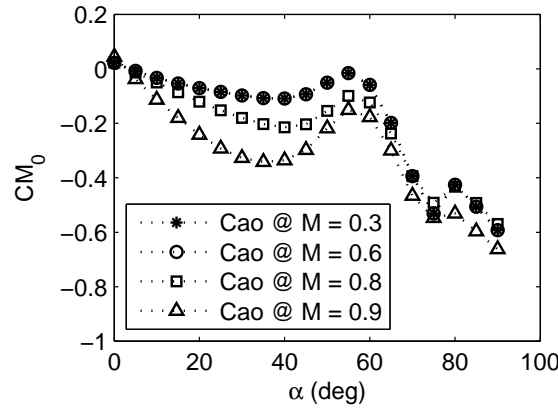


Figure 3.2: Mach no. effect on the Cao Model

the various flight conditions given. For example, considering the analytical model for lift coefficients as listed in Table B.3, the coefficient of lift due to the horizontal stabilator deflections  $C_{L_{\delta_h}}$  are calculated by applying the linear interpolation within the range of maximum and minimum deflections given. This is written as:

$$C_{L_{\delta_h}} = \frac{C_L @ \delta_{h_{max}} - C_L @ \delta_{h_{min}}}{\delta_{h_{max}} - \delta_{h_{min}}} \quad (3.4)$$

Figure 3.3 showed the control derivatives of  $C_{L_{\delta_h}}$  at different flight condition of Mach no. at 0.6 and 0.9. The same method has been applied in all control and dynamic stability derivatives for other aerodynamic coefficients.

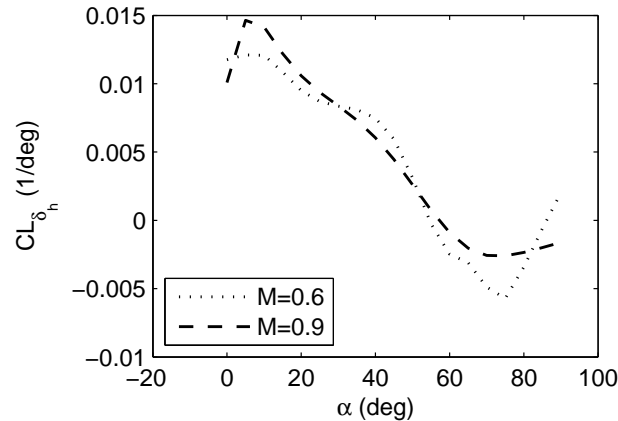


Figure 3.3: Stabilator effect on lift coefficient at different Mach no.



### 3.3.2 Graph Comparison of the Aerodynamic Derivatives

The aerodynamic forces and moments are presented in nondimensional form and are characterized as a function of state and control variables as follows:

$$C_i = C_{i_o}(\alpha, \beta) + C_{i_\omega}(\alpha) \frac{\omega l}{2V} + C_{i_\delta}(\alpha) \delta \quad (3.5)$$

where

- $i$  is the lift,  $L$ , drag,  $D$ , side force,  $Y$ , roll moment,  $l$ , pitch moment,  $m$ , or yaw moment,  $n$ ,
- $\omega$  is the rate damping term for roll,  $p$ , pitch,  $q$  or yaw,  $r$ ,
- $l$  can be the mean aerodynamic chord,  $\bar{c}$ , for longitudinal coefficients or wing span,  $b$ , for lateral-directional coefficients.

Equation 3.5 shows that an aerodynamic coefficient is built up from a sum of components that consist of a static part plus an increment from rate damping and from the control. These components provide a physical insight into the aerodynamic coefficients and can be studied independently as required.

In this subsection, it is aimed to present the modification effects on the original Cao's formulation previously discussed in Section 3.2.4. A review of the distribution of all the collected aerodynamic data to identify differences in the representation of the aerodynamics characteristics is also provided.

#### Drag Coefficients

The mathematical structure for drag coefficient for all the models are given in Equation 3.6. By eliminating the effects of control deflection in the Cao model and sideslip angle in Chakraborty model, the contribution from the basic airframe shows that all the models agree as plotted in Figure 3.4(a). On another distribution, Cao and NASA models almost possess identical behaviours except for  $\alpha$  range from  $55^\circ$  to  $80^\circ$  for  $C_{D_{\delta_h}}$ . Though Chakraborty model is said to be applicable for angle of attack range up to  $60^\circ$ , it seems that the model shares same distribution with the other two models at least for angle of attack up to  $35^\circ$ .

$$C_{D_{Cao}} = C_{D_{0Cao}}(\alpha, M, d_h) \quad (3.6a)$$

$$C_{D_{Chak}} = C_{D_{0Chak}}(\alpha, \beta) + C_{D_{\delta_h}}(\alpha) \delta_h \quad (3.6b)$$

$$C_{D_{NASA}} = C_{D_{0NASA}}(\alpha) + C_{D_{\delta_{hr}}}(\alpha) \delta_{hr} + C_{D_{\delta_{hl}}}(\alpha) \delta_{hl}(\alpha) + \frac{\bar{c}}{2V_T} C_{D_q} q \quad (3.6c)$$

#### Lift Coefficients

The mathematical structure for lift coefficient is given in Equation 3.7.

$$C_{L_{Cao}} = C_{L_0}(\alpha, M, d_h) + \frac{\bar{c}}{2V_T} [C_{L_q}(\alpha) q + C_{L_{\dot{\alpha}}}(\alpha) \dot{\alpha}] \quad (3.7a)$$

$$C_{L_{Chak}} = C_{L_0}(\alpha, \beta) + C_{L_{\delta_h}}(\alpha) \delta_h \quad (3.7b)$$

$$C_{L_{NASA}} = C_{L_0}(\alpha) + C_{L_{\delta_{hl}}}(\alpha) \delta_{hl} + C_{L_{\delta_{hr}}}(\alpha) \delta_{hr} + \frac{\bar{c}}{2V_T} C_{L_q}(\alpha) q \quad (3.7c)$$

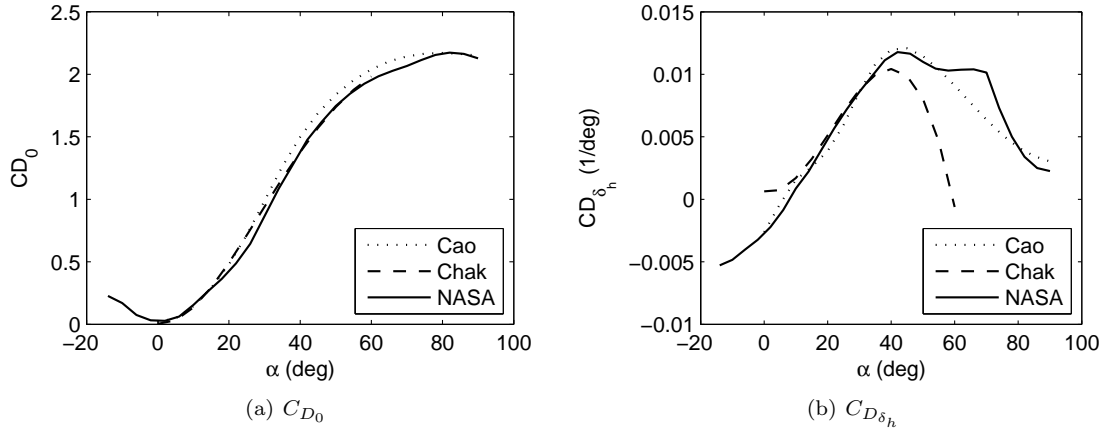


Figure 3.4: Distribution for drag coefficient and its derivative.

It is seen that the Cao formulation has included the effect of the rate change of  $\alpha$  or  $\dot{\alpha}$ . This derivative is due to slow adjustment of the wing and tail pressure to its equilibrium value when  $\alpha$  is suddenly changed. The contribution of this derivative only appears in the lift and moment coefficients and usually its effect is considered to be combined together with the pitch rate effect [87].

The basic airframe value for the lift coefficient exhibits a good agreement among all the models, as depicted in Figure 3.5(a). The modification to the original Cao formulation has improved with the match with the data from Chakraborty and NASA. However, the plotted data for the control derivative shows a different value but generally similar trend for angle of attack between  $0^\circ$  and  $40^\circ$ . Referring to the graph in Figure 3.5(b), the horizontal stabilator deflection derivatives can be approximately represented by a linear relation with the  $\alpha$ . Figure 3.5(c) shows a large deviation of the plotted data in the area of  $40^\circ \leq \alpha \leq 50^\circ$ . The NASA model showed a maximum peak of  $0.16 \text{ sdeg}^{-1}$  at  $\alpha = 40^\circ$  whereas Cao model only reached half of the value for the same  $\alpha$  condition.

### Pitch Moment Coefficients

The mathematical structures for the pitch moment coefficients are as follows:

$$C_{m_{Cao}} = C_{m_0}(\alpha, M, d_h) + \frac{\bar{c}}{2V_T} [C_{m_q}(\alpha)q + C_{m_{\dot{\alpha}}}(\alpha)\dot{\alpha}] \quad (3.8a)$$

$$C_{m_{Chak}} = C_{m_0}(\alpha) + C_{m_{\delta_h}}(\alpha)\delta_h + \frac{\bar{c}}{2V_T} C_{m_q}(\alpha)q \quad (3.8b)$$

$$C_{m_{NASA}} = C_{m_0}(\alpha) + C_{m_{\delta_{h_l}}}(\alpha)\delta_{h_l} + C_{m_{\delta_{h_r}}}(\alpha)\delta_{h_r} + \frac{\bar{c}}{2V_T} C_{m_q}(\alpha)q \quad (3.8c)$$

Similar to the lift coefficient, the Cao formulation has included the effect from the rate of change of  $\alpha$  in the equation.

The distributions of the data for moment coefficients considering all the variables from control derivatives and rates damping effect shows a reasonable similarity between all the models. Except for basic airframe effect, the Chakraborty model shows some consistency at the range of  $\alpha$  between  $10^\circ \leq \alpha \leq 30^\circ$  before it deviates from the other two models. Based on the plotted data for Cao and NASA models in Figure 3.6(a), F-18 HARV is statically stable aircraft as  $C_{m_\alpha}$  is negative for  $\alpha$  between  $0^\circ$  to  $40^\circ$ . Whereas, the

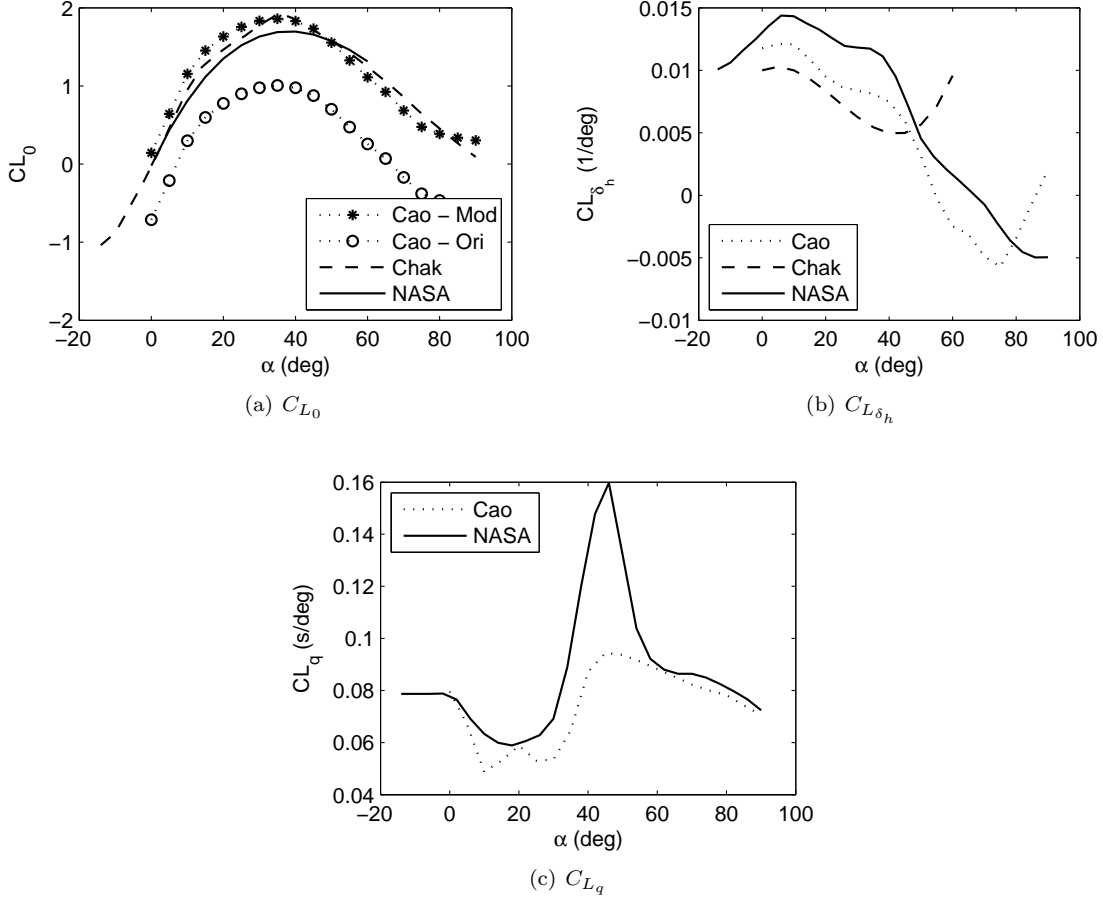


Figure 3.5: Distribution for lift coefficient and its derivative at  $M = 0.6$ .

Chakraborty model particularly not very well predicted for  $\alpha < 10^\circ$  due to the lack of data availability.

### Side Force Coefficients

The side force coefficient arises from sideslip, roll and yaw rate. The mathematical form of the side force coefficients for all the models are given in the following equation:

$$C_{Y_{Cao}} = C_{Y_0}(\alpha, \beta, M, d_a, d_r) + C_{Y_\beta}(\alpha)\beta + \frac{b}{2V_T}[C_{Y_p}(\alpha)p + C_{Y_r}(\alpha)r] \quad (3.9a)$$

$$C_{Y_{Chak}} = C_{Y_0}(\alpha, \beta) + C_{Y_{\delta_a}}(\alpha)\delta_a + C_{Y_{\delta_r}}(\alpha)\delta_r \quad (3.9b)$$

$$C_{Y_{NASA}} = C_{Y_\beta}(\alpha)\beta + C_{Y_{\delta_a}}(\alpha)\delta_a + C_{Y_{\delta_{h_l}}(\alpha)}\delta_{h_l} + C_{Y_{\delta_{h_l}}(\alpha)}\delta_{h_l} + \dots \quad (3.9c)$$

$$C_{Y_{\delta_r}}(\alpha)\delta_r + \frac{b}{2V_T}[C_{Y_p}(\alpha)p + C_{Y_r}(\alpha)r]$$

The distributions of all the data for the side force coefficients are shown in Figure 3.7. The first figure compares the given formulation of side force derivative due to sideslip angle,  $C_{Y_\beta}$ , with the extracted effects based on various flight conditions as specified in the Cao formulation. It is seen that the modified formulation of the Cao model shifts the

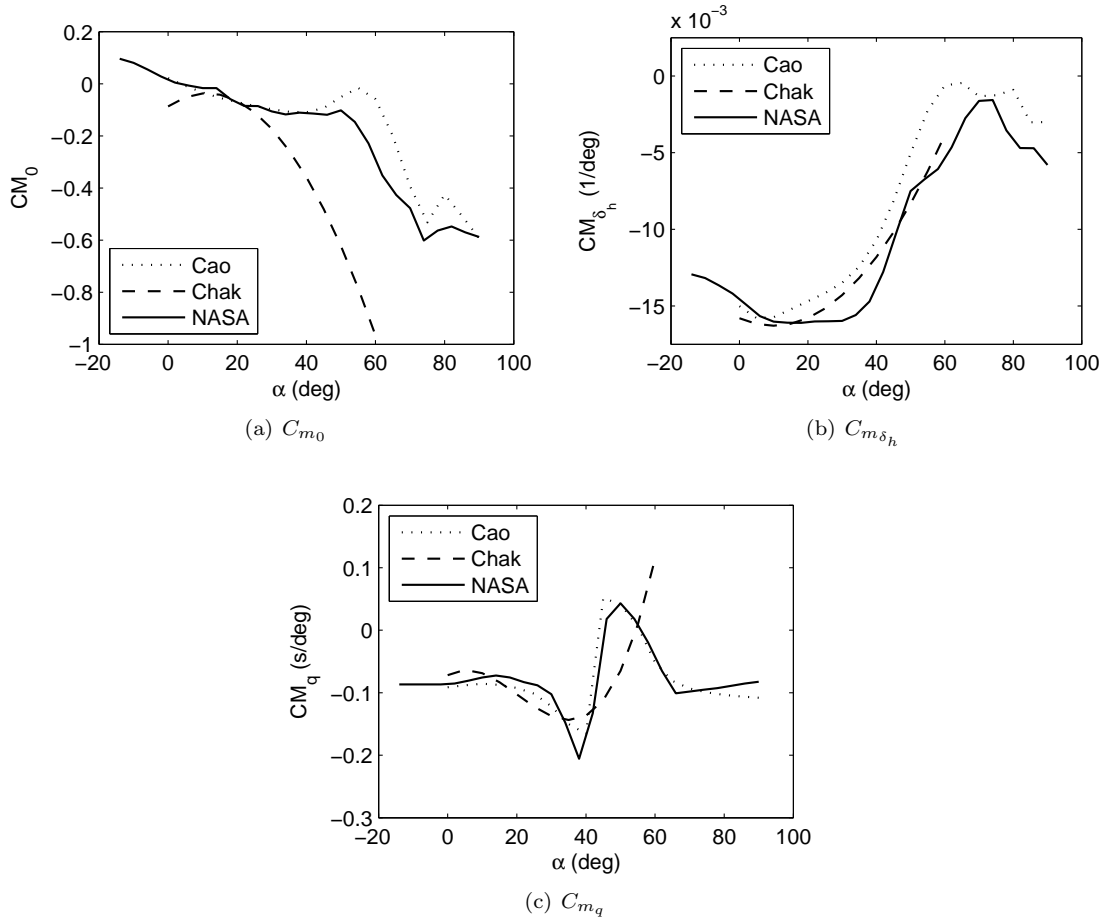


Figure 3.6: Distribution for pitch moment coefficient and its derivative at  $M = 0.6$ .

curve upwards slightly. The given formulation has shown a constant positive value as  $\alpha$  varies.

However, the modification of the original Cao model are seen not to have common tendency as expected from previous distribution on account of the effect from the sideslip angle,  $\beta$ . This is reflected in Figure 3.7(b), where the extracted derivative from the original formulation appears to have similar behaviour rather than the modified curve. Still, the modification of Cao formulation predicts same derivative values at low  $\alpha$  when compared with Chakraborty model. Relative to the roll rate,  $p$ , and yaw rate,  $r$ , the distribution from the modified formulations do not contribute to a major impact on the curves though they seemed to have close estimation to the NASA model. The lack of data for the rate damping effect on the side force did not allow Chakraborty to include those effects in his model.

On the other hand, the distribution of the data on the effect from control derivatives,  $\delta_a$  and  $\delta_r$ , shows a resemblance for the Cao and NASA models but diverse tendency for the Chakraborty model. The diversion is clearly depicted in Figure 3.7(c) for the derivative due to the aileron deflection, for which there is no region along the curve that similarly predicts a same distribution except for the point of intersection at  $\alpha$  approximately  $25^\circ$ . But, the derivative due to the rudder deflection depicted in Figure 3.7(d) at least showed a similarity in the distribution of the data for  $\alpha$  region between  $0^\circ \leq \alpha \leq 30^\circ$ .

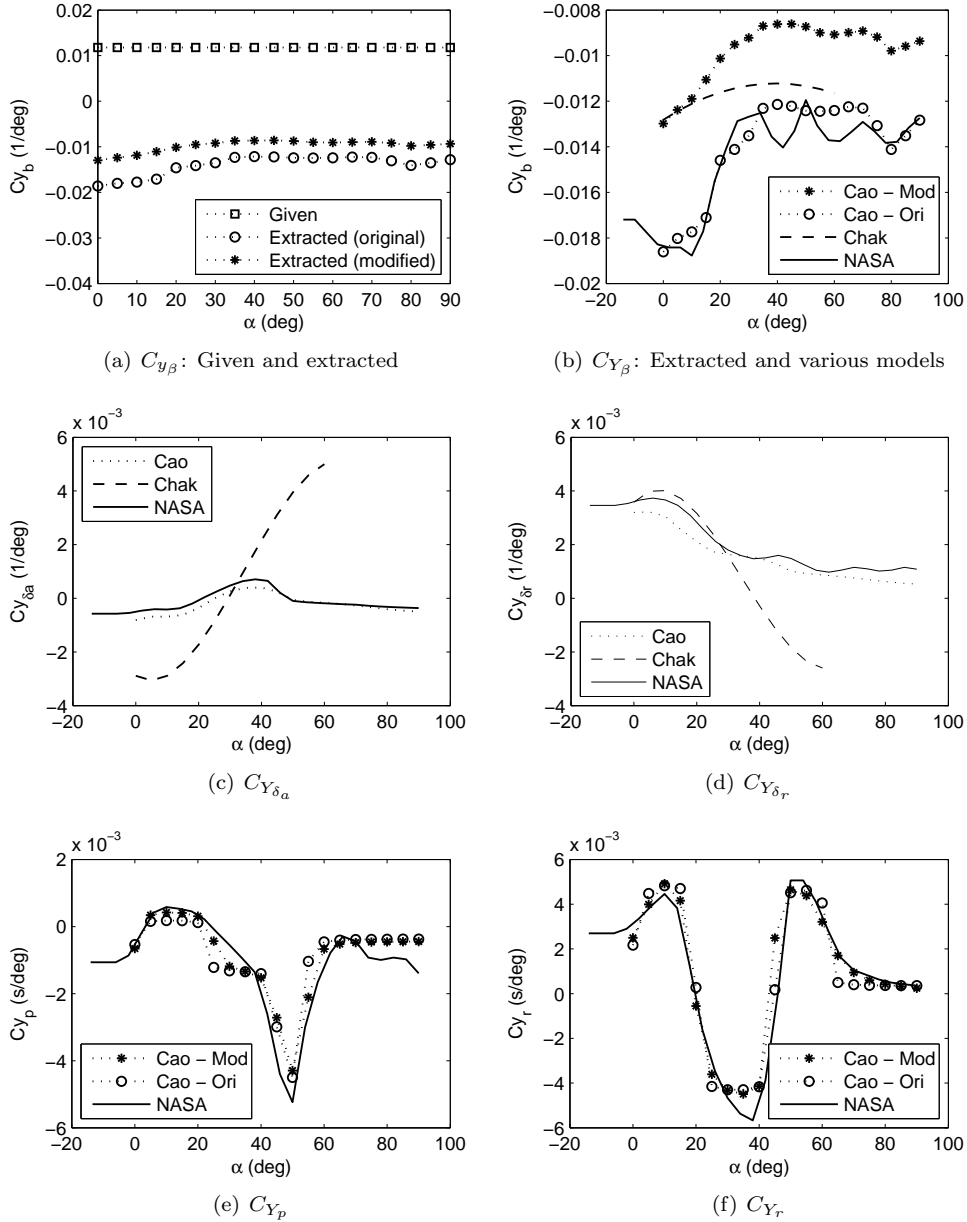


Figure 3.7: Distribution for side force coefficient and its derivative.

### Rolling Moment Coefficients

Rolling moments can result from sideslip, control action of the ailerons and the rudders, and rate damping resisting the rolling and yawing motion. The mathematical structures for the coefficient depending on each model are given as follows:

$$C_{l_{Cao}} = C_{l_0}(\alpha, \beta, M, d_a, d_r) + C_{l_\beta}(\alpha, M)\beta + \frac{b}{2V_T} [C_{l_p}(\alpha, M)p + C_{l_r}(\alpha)r] \quad (3.10a)$$

$$C_{l_{Chak}} = C_{l_0}(\alpha, \beta) + C_{l_{\delta_a}}(\alpha)\delta_a + C_{l_{\delta_r}}(\alpha)\delta_r + \frac{b}{2V_T} [C_{l_p}(\alpha)p + C_{l_r}(\alpha)r] \quad (3.10b)$$

$$C_{l_{NASA}} = C_{n_\beta}(\alpha)\beta + C_{l_{\delta_a}}(\alpha)\delta_a + C_{l_{\delta_{h_i}}}(\alpha)\delta_{h_i} + C_{l_{\delta_{h_r}}}(\alpha)\delta_{h_r} + C_{l_{\delta_r}}(\alpha)\delta_r + \dots \quad (3.10c)$$

$$\frac{b}{2V_T} [C_{l_p}(\alpha)p + C_{n_r}(\alpha)r]$$

The effect of sideslip angle on the rolling moments,  $C_{l_\beta}$ , is one of the most important parameters for lateral-directional stability and handling qualities. This derivative is called dihedral effect, which determines the lateral static stability of the aircraft. A negative sign of the derivative indicates a stabilizing effect that causes the aircraft roll away from the sideslip. The contributing factors to the dihedral effect are from the wing geometric dihedral, wing sweep, the vertical tail and the wing-fuselage interaction.

However, the Cao formulation for  $C_{l_\beta}$  did not support the data presented in the report. This is clearly showed in Figure 3.8(a). The formulation has a very small magnitude when compared to the extracted data.

The distribution of dihedral derivative for all the models as in Figure 3.8(b) has shown a similar trend at least for  $\alpha \leq 20^\circ$ . It is also seen that the modification on the Cao formulation did not affect the overall sideslip angle distribution on the original Cao formulation. Both of the formulations closely predict the distribution of the dihedral derivative with the NASA model at low and high  $\alpha$ . The approximation of Chakraborty model using the fourth order polynomial of flight test data has shown that it is not applicable to high  $\alpha$ .

The control derivatives from aileron and rudder effect on the roll moments coefficients have shown a close approximation for all the models. In Figure 3.8(d), the modified the Cao formulation matched the distribution data from the NASA model almost precisely but not as close for the aileron effect on the rolling moments. The curve is depicted to match the NASA model at higher  $\alpha$  as well as the Chakraborty model as plotted in Figure 3.8(c).

The Cao and NASA models have exhibited a common distribution data for rate damping derivatives which can be seen in Figure 3.8(e) and 3.8(f). Chakraborty has presented the rate damping derivatives in the first order polynomial function for the roll damping derivative,  $C_{l_p}$ , and second order polynomial function for the yaw rate effect on the rolling moment coefficient,  $C_{l_r}$ , which showed the distribution data were poorly conditioned if they are to compare with Cao and NASA models.

### Yawing Moment Coefficients

The mathematical formulations for the yawing moment coefficients for each model are given as follows:

$$C_{n_{Cao}} = C_{n_0}(\alpha, \beta, M, d_h, d_a, d_r) + C_{n_\beta}(\alpha, M)\beta + \frac{b}{2V}[C_{n_p}(\alpha)p + C_{n_r}(\alpha)r] \quad (3.11a)$$

$$C_{n_{Chak}} = C_{n_0}(\alpha, \beta) + C_{n_{\delta_a}}(\alpha)\delta_a + C_{n_{\delta_r}}(\alpha)\delta_r + \frac{b}{2V}[C_{n_p}(\alpha)p + C_{n_r}(\alpha)r] \quad (3.11b)$$

$$C_{n_{NASA}} = C_{n_\beta}(\alpha)\beta + C_{n_{\delta_a}}(\alpha)\delta_a + C_{n_{\delta_{h_l}}}(\alpha)\delta_{h_l} + C_{n_{\delta_{h_r}}}(\alpha)\delta_{h_r} + C_{n_{\delta_r}}(\alpha)\delta_r + \dots \quad (3.11c)$$

$$\frac{b}{2V}[C_{n_p}(\alpha)p + C_{n_r}(\alpha)r]$$

The yaw stiffness is represented by the yawing moment derivative due to the sideslip angle,  $C_{n_\beta}$ , which suggests the stability of the aircraft to restore to its original flight path due to sideslipping or “weathercock” stability. In Figure 3.9(a), the given formulation for the yaw stiffness is so small as compared to the extracted data for the same Cao model. But, when the distributions of the yaw stiffness from the v Chakraborty and NASA models are plotted, the extraction data appeared to have similar effect on the yawing moment coefficient.

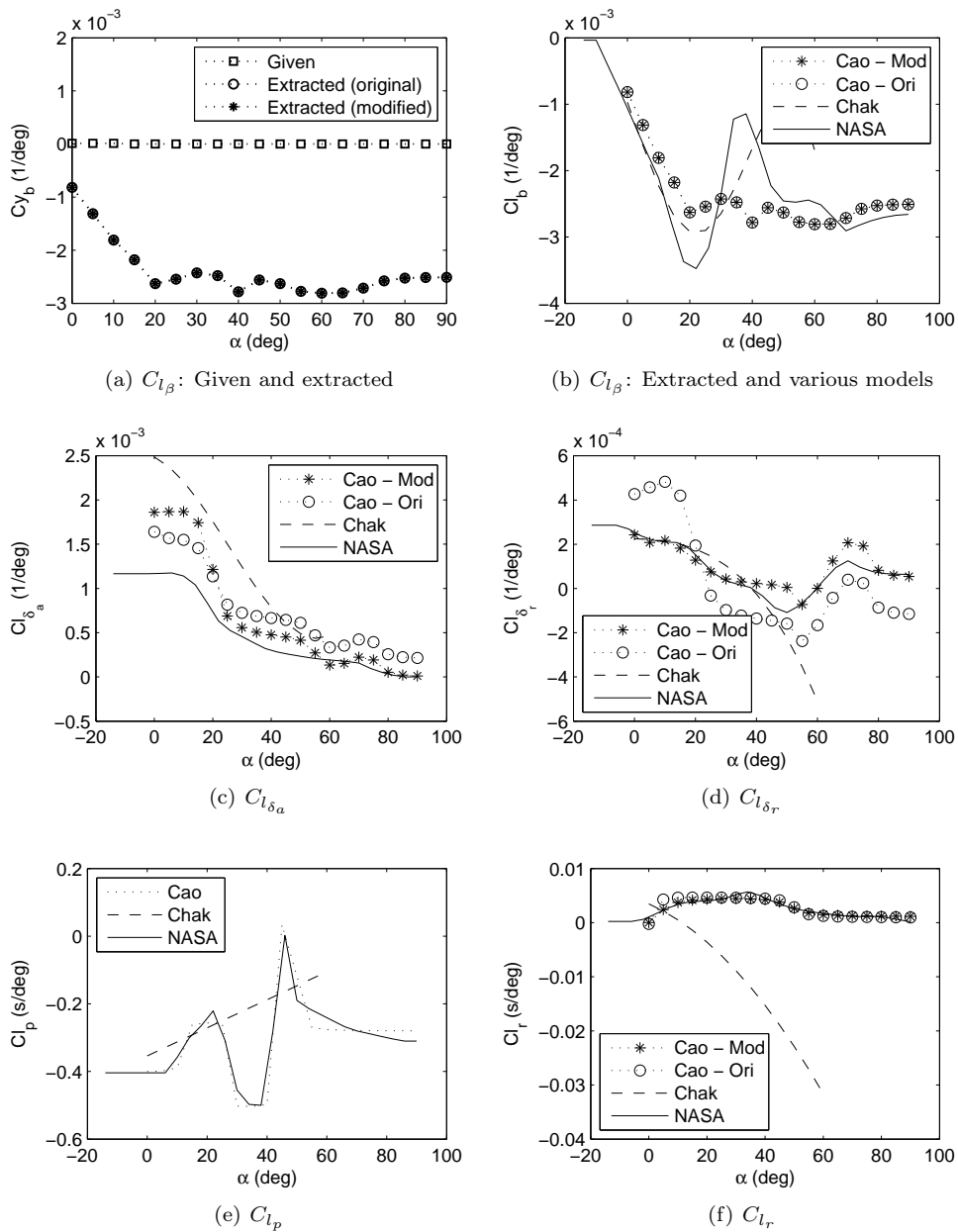


Figure 3.8: Distribution for roll moment coefficient and its derivative.

The modified formulation of Cao model does not have a significant effect on most of the yaw moment coefficient, as depicted in Figure 3.9. This is because most of the effected curves for the modified formulations, listed in Table 3.2, involved of the coefficients at Mach number 0.9. Since a lower Mach number is interested at high  $\alpha$ , thus, the effect of modification is not presented in this section. However, the modification on the derivative due to the rudder deflection has shown a close estimation to the NASA model as seen in Figure 3.9(f).

The comparison of the Cao and NASA models have also shown a close distribution between each other with most of the curves displaying a resemblance in the pattern of the curves. Whereas the Chakraborty model showed a diverse distribution with the basic airframe and rudder deflection effects almost predicting similar distribution at lower  $\alpha$  with the Cao and NASA models.

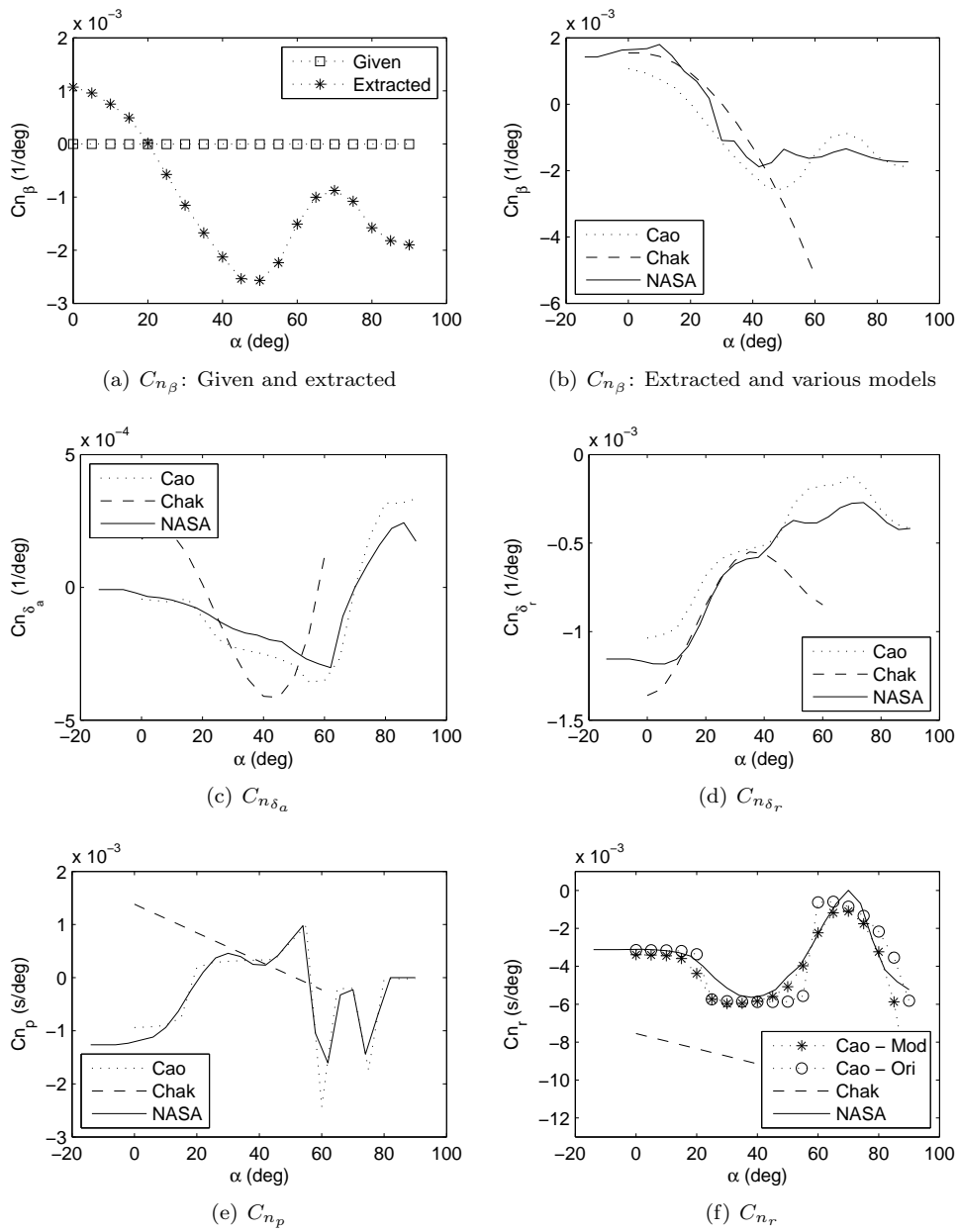


Figure 3.9: Distribution for yaw moment coefficient and its derivative.



### 3.4 Conclusion

In summary, a simple flowchart of the existing F-18 HARV aerodynamic models discussed in this chapter is illustrated in Figure 3.10. Basically, there are three difference models which are available in the public domain. Further investigation of the models showed that there are some discrepancies in Cao formulation which have been corrected.

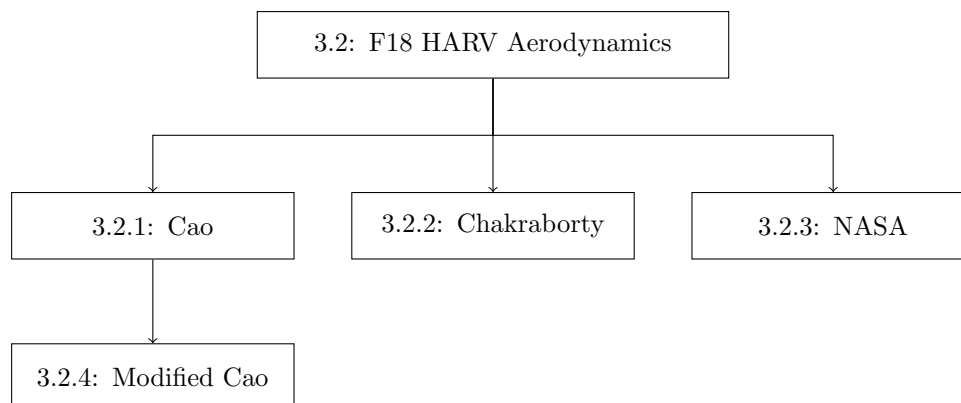


Figure 3.10: Flowchart of the aerodynamic models presented in the chapter.

Though all the models showed variation in difference state and control variables dependency, the effects of each variable as presented in Section 3.3 mostly exhibited a similar projection of the curves, especially for Cao and NASA models. However, the Chakraborty model has shown a close prediction of the longitudinal coefficients compared to the Cao and NASA models for the range of  $\alpha$  from  $10^\circ$  to  $40^\circ$  for certain curves. Tables 3.5 and 3.6 summarize the various effects of each variable that are considered in each models.

Table 3.5: Summary of variables affecting the aerodynamic formulations for different F-18 HARV models aircraft longitudinally.

Coefficient	Model	$\alpha$	$\beta$	M	$\delta_h^*$	$q$	$\dot{\alpha}$
$C_D$	Cao	✓		✓	✓		
	Chakraborty	✓	✓		✓		
	NASA	✓			✓	✓	
$C_L$	Cao	✓		✓	✓	✓	✓
	Chakraborty	✓	✓		✓		
	NASA	✓			✓	✓	
$C_m$	Cao	✓		✓	✓	✓	✓
	Chakraborty	✓			✓	✓	
	NASA	✓			✓	✓	

\* NASA's model considers left and right stabilator deflection angle.

The effect of  $\dot{\alpha}$  on the aerodynamic model may be substantial in simulating the non-linearity dynamics at high  $\alpha$  [88]. Though the formulation provided by Cao looks complex, it includes the unsteady effects due to the rate of change of the angular deflection making the model suitable for analysis of the high  $\alpha$  problem.

Mainly, the Cao original formulation has shown a close approximation with the NASA model. Though the modifications to the Cao original formulation were made due to

Table 3.6: Summary of variables affecting the aerodynamic formulations for different F-18 HARV models aircraft lateral-directionally.

Coefficient	Model	$\alpha$	$\beta$	M	$\delta_h^*$	$\delta_a$	$\delta_r$	$p$	$r$
$C_Y$	Cao	✓	✓	✓		✓	✓	✓	✓
	Chakraborty	✓	✓			✓	✓		
	NASA	✓	✓		✓	✓	✓	✓	✓
$C_l$	Cao	✓	✓	✓		✓	✓	✓	✓
	Chakraborty	✓	✓			✓	✓	✓	✓
	NASA	✓	✓		✓	✓	✓	✓	✓
$C_n$	Cao	✓	✓	✓	✓	✓	✓	✓	✓
	Chakraborty	✓	✓			✓	✓	✓	✓
	NASA	✓	✓		✓	✓	✓	✓	✓

\* NASA's model considers left and right stabilator deflection angle.

the unmatched data from the generated formulation and wind tunnel data, it appears a more likely match than the NASA model in the majority of the aerodynamic derivatives as presented in Section 3.3. But the condition may not be applied on the derivative due to sideslip angles for the side force coefficient,  $C_{Y\beta}$ . The extracted derivative from the original formulation is more likely to resemble the distribution data from the NASA model which contradicts with the condition for most of the derivatives extracted from the modified Cao formulation.

Even though Chakraborty claimed that his model was valid for  $\alpha$  range from  $0^\circ$  up to  $60^\circ$ , most of the plotted curves showed that the data is approximately behave in the same way as the Cao and NASA models at least for  $\alpha$  up to  $40^\circ$ . It is also noted that the longitudinal aerodynamic data by Chakraborty has introduced variations to the longitudinal aerodynamic data with the sideslip angle. The approximation of the damping rate for the lateral-directional coefficients using the second order polynomial formulation also has shown a poor condition as compared to the Cao and NASA models.

## Chapter 4

# Pole Map for Longitudinal Dynamics

The purpose of this chapter is to report on the analysis of the open loop characteristics of each model in steady flight. It was shown in Chapter 3 that the models have some differences in the distribution of aerodynamic characteristics. The key differences are the use of look-up-tables by NASA, the arc-tangent function by Cao and the least square polynomial by Chakraborty in the representation of aerodynamic derivatives. Here, effects of these differences on the aircraft's modes of motion together with time domain simulations will be studied to identify the impact of small changes in aerodynamic derivatives on nonlinear flight dynamics.

### 4.1 Trimming and Linearization

For an initial value problem such as aircraft simulation, it is important to define an operating point where the behaviour of the aircraft is known. Usually, this point is chosen within a flight envelope which will then comprise the initial state for a nonlinear simulation as well as operating point to extract the linearized model. The process involves finding an equilibrium point for the aircraft during steady flight that satisfies the input, output and state conditions. The state vector  $\mathbf{x}$ , input vector  $\mathbf{u}$  and output vector  $\mathbf{y}$  for the aircraft model can be chosen as:

$$\mathbf{x} = [u \quad v \quad w \quad h \quad p \quad q \quad r \quad \phi \quad \theta \quad \psi]^T \quad (4.1)$$

$$\mathbf{u} = [\delta_h \quad \delta_a \quad \delta_r \quad \tau]^T \quad (4.2)$$

$$\mathbf{y} = [V_T \quad \beta \quad h \quad \gamma]^T \quad (4.3)$$

Mathematically, all state derivatives are fixed to a zero to ensure that a steady state condition is obtained. MATLAB's `trim` routine starts from a guessed initial starting point for  $x_0$ ,  $y_0$  and  $u_0$  and searches for the equilibrium condition by iterating about all states until steady state condition is satisfied or some close proximity to equilibrium is found by solving the steady-state parameters that satisfy certain input, output and state conditions.

For example, the syntax `[x,u,y,dx] = trim('sys',x0,u0,y0,ix,iu,iy)` in MATLAB attempts to find nearest trim point for  $\mathbf{x}$ ,  $\mathbf{u}$  and  $\mathbf{y}$  of the initial guess  $\mathbf{x}_0$ ,  $\mathbf{u}_0$ , and  $\mathbf{y}_0$  respectively that set the state derivatives,  $\mathbf{dx}$ , of the Simulink system 'sys' to zero. The integer value `ix`, `iu` and `iy` select the values in  $\mathbf{x}_0$ ,  $\mathbf{u}_0$  and  $\mathbf{y}_0$  that must be satisfied.

If no solution to this problem can be found then `trim` will attempt to find values that minimize the maximum deviation from the intended values.

The trim problem is also used to find the control settings that yield a steady flight condition. In the case of trimming for steady horizontal flight, the variables of the aircraft in lateral-directional plane and angular rates are restricted to zero. These include sideslip angle, roll angle and yaw angle. Meanwhile, the level flight is assured by setting the flight path angle as zero, while the remaining state variables are allowed to be freely tuned to the intended trim condition from initial guess or guided values. The input variables are freed allowing the control surfaces deflection and throttle level to be tuned to suitable configurations for the required steady states. Some of the output variables are fixed for the trimming process to achieve the given condition. All the settings used in this study are summarized in Table 4.1.

Table 4.1: Initial value and variables setting for speed trimming purpose.

State variable	Initial value	Status	Input variable	Initial value	Status	Output variable	Initial value	Status
$u$	Guess	Free	$\delta_h$	Guess	Free	$V_T$	Trim	Fixed
$v$	0	Fixed	$\delta_a$	Guess	Free	$\beta$	0°	Fixed
$w$	Guess	Free	$\delta_r$	Guess	Free	$h$	15000ft	Fixed
$h$	15000ft	Fixed	$\tau$	Guess	Free	$\gamma$	0°	Fixed
$p$	0°/s	Fixed						
$q$	0°/s	Fixed						
$r$	0°/s	Fixed						
$\phi$	0°	Fixed						
$\theta$	Guess	Free						
$\psi$	0°	Fixed						

The initial values of the free variables for the state, input and output variables were guessed to any approximate value that in turn returned the close trim value in the searching of zero derivatives for the states. The variables setting shown in Table 4.1 were used to find the trim condition at a given trimmed airspeed,  $V_T$ . If the model needs to be trimmed at a specific AoA condition, the output variables for  $V_T$  should be freed and  $\theta$  in the state variable should be fixed to allow the reverse condition to be achieved. All the trim values at different speed settings are presented in Table 4.2.

Table 4.2: Trim data for the various models at different trim speed taking the altitude at 15000ft.

$V_T$ (ft/s)	$\theta_{trim}/\alpha_{trim}(deg)$			$\delta_{h_{trim}}(deg)$			$\tau_{trim}$		
	Cao	Chak	NASA	Cao	Chak	NASA	Cao	Chak	NASA
200	37.3	NA	40.7	-5.1	NA	-3.2	0.93	NA	0.96
250	22.6	24.4	26.1	-4.9	-3.0	-3.0	0.83	0.86	0.85
300	13.1	15.7	14.3	-1.0	-0.4	0.4	0.56	0.78	0.67
350	9.0	11.1	10.0	-0.2	-0.6	0.2	0.41	0.56	0.52
400	6.9	8.3	7.7	0.1	-1.2	0.2	0.34	0.41	0.45
450	5.5	6.6	6.2	0.2	-1.8	0.3	0.29	0.31	0.37
500	4.5	5.4	5.1	0.3	-2.3	0.4	0.28	0.25	0.37

The plot in Figure 4.1 shows that as the AoA is varied, the trim for speed gives common value for all the models. But the variation in trim condition is seen to be significantly diverse in the trim stabilator deflection but slightly common in the trim throttle level. Though in a previous chapter we have seen how close the aerodynamic properties were for both the Cao and the NASA models, but at least both models have displayed a similar

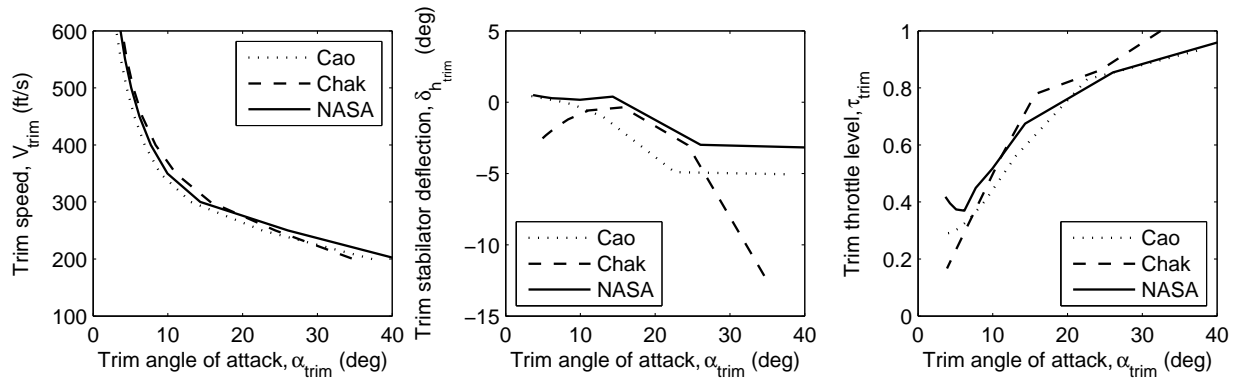


Figure 4.1: Flight envelope trim conditions.

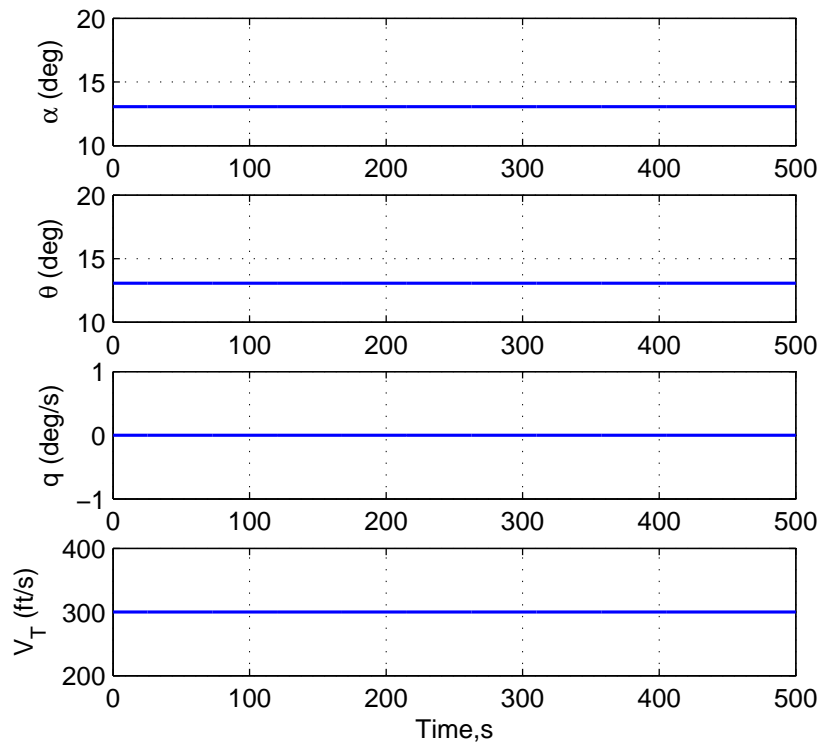


Figure 4.2: Example of trim simulation for the Cao model at  $V_T = 300$  m/s.

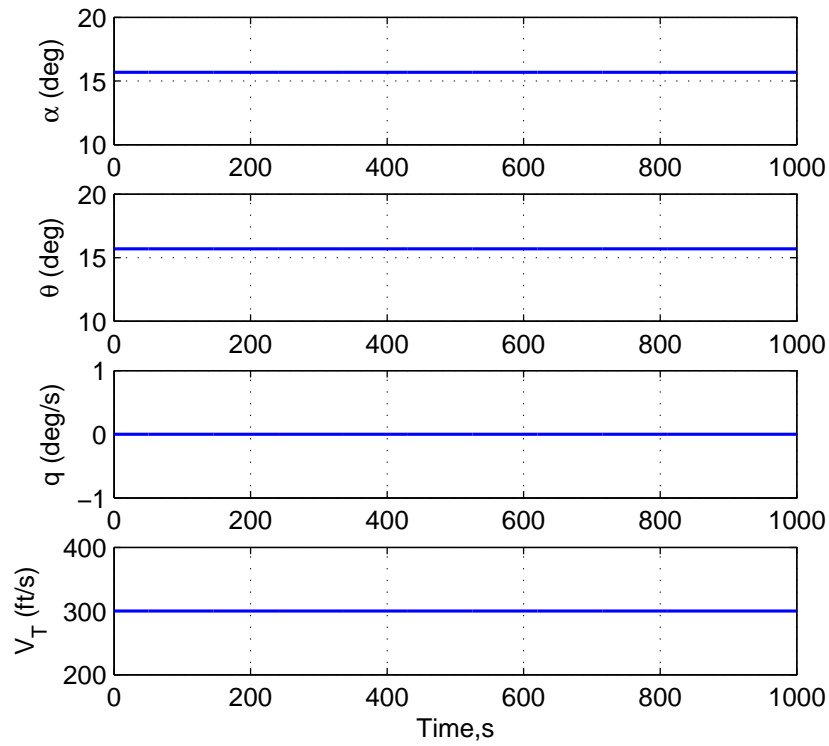


Figure 4.3: Example of trim simulation for the Chakraborty model at  $V_T = 300$  m/s.

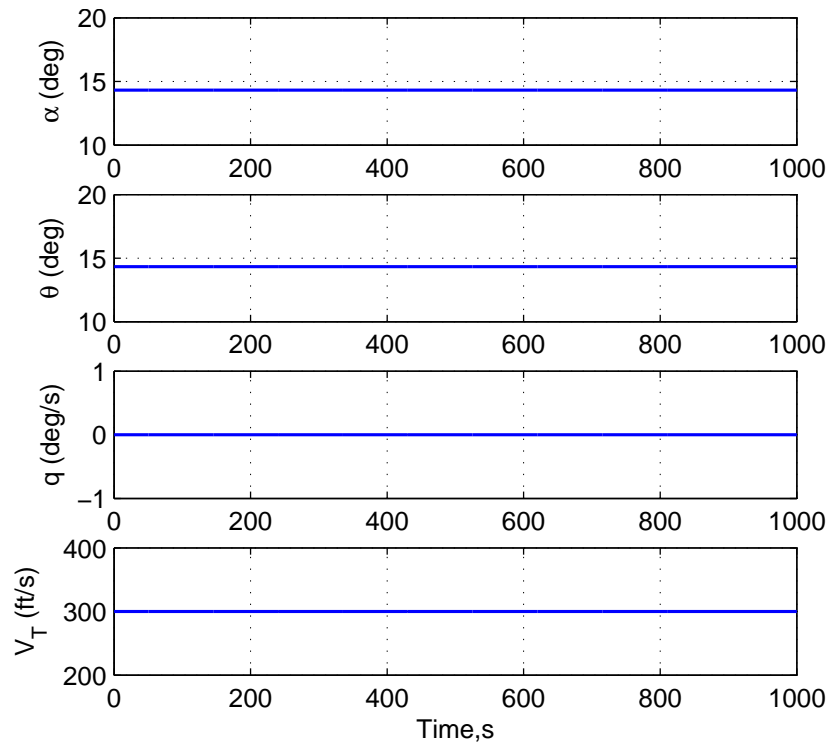


Figure 4.4: Example of trim simulation for the NASA model at  $V_T = 300$  m/s.

projection for the trim stabilator deflection though not sharing trim deflection at the same value.

From the trim values defined for each model, a linearized state-space model is determined using the MATLAB routine `linmod`. The aircraft models were linearized around the trim conditions to produce the four state space matrices, ( $A, B, C$  and  $D$ ) defined as follows:

$$\dot{\mathbf{x}} = \mathbf{A}\mathbf{x} + \mathbf{B}\mathbf{u} \quad (4.4)$$

$$\mathbf{y} = \mathbf{C}\mathbf{x} + \mathbf{D}\mathbf{u} \quad (4.5)$$

The  $A$  matrix characterizes the system's stability. the dynamic modes of a model can be studied by analysing its eigenvalues and eigenvectors. The ten state variables in Equation 4.1 can be reduced to four state variables and two input variables representation of the longitudinal dynamics decoupled from the six DoF model, which are written as:

$$\dot{\mathbf{x}}_{long} = \mathbf{A}_{long}\mathbf{x}_{long} + \mathbf{B}_{long}\mathbf{u}_{long} \quad (4.6)$$

$$\mathbf{y}_{long} = \mathbf{C}_{long}\mathbf{x}_{long} + \mathbf{D}_{long}\mathbf{u}_{long} \quad (4.7)$$

These new reduced state and input vectors are defined as:  $\mathbf{x}_{long} = [u \ w \ q \ \theta]^T$  and  $\mathbf{u}_{long} = [\delta_h \ \tau]^T$ . The output variables are taken to be the state variables, which  $\mathbf{y}_{long} = \mathbf{x}_{long}$ .

Similarly, the lateral-directional dynamics are explained in the reduced form described from:

$$\dot{\mathbf{x}}_{lat} = \mathbf{A}_{lat}\mathbf{x}_{lat} + \mathbf{B}_{lat}\mathbf{u}_{lat} \quad (4.8)$$

$$\mathbf{y}_{lat} = \mathbf{C}_{lat}\mathbf{x}_{lat} + \mathbf{D}_{lat}\mathbf{u}_{lat} \quad (4.9)$$

which the new reduced state, input and output vectors are given as  $\mathbf{x}_{lat} = [v \ p \ \phi \ r \ \psi]^T$  and  $\mathbf{u}_{lat} = [\delta_a \ \delta_r]^T$  taken the output variables to be the state variables, which  $\mathbf{y}_{lat} = \mathbf{x}_{lat}$ .

## 4.2 Analytical Linearized Model

The linearized  $A$  matrix can also be obtained analytically as described in Reference [89]. From the definition, the coefficients of the longitudinal state matrix are the concise form of the aerodynamic stability derivatives which given as follows:

$$A_{long} = \begin{bmatrix} x_u & x_w & x_q & x_\theta \\ z_u & z_w & z_q & z_\theta \\ m_u & m_w & m_q & m_\theta \\ 0 & 0 & 1 & 0 \end{bmatrix} \quad (4.10)$$

These stability derivatives are expressed in terms of the dimensionless aerodynamic coefficient derivatives as summarized in Table 4.3.

The term  $m_u$  was taken to be zero considering that there is no change in the aerodynamics coefficient due to the change in velocity from the data given by Cao at lower  $M$ . Besides, there is not much information regarding the NASA model taken from Reference [84] to suggest that actually it is applicable for  $M < 0.6$ .

For an all moving tail aircraft like HARV, the tailplane lift and drag curve slopes ( $C_{L_{\alpha_t}}$ ,  $C_{D_{\alpha_t}}$ ) are taken directly from the lift and drag due to the change of stabilator deflections ( $C_{L_{\delta_h}}$ ,  $C_{D_{\delta_h}}$ ). However, the value for  $C_{L_{\delta_h}}$  and  $C_{D_{\delta_h}}$  are so small that  $x_q$  and  $z_q$

Table 4.3: Dimensionless derivatives of aerodynamic coefficients for longitudinal motion.

Variable	$u$	$w$	$q$	$\theta$
x	$x_u = \frac{-2C_D}{m'}$	$x_w = \frac{C_L - C_{D\alpha}}{m'}$	$x_q = \frac{-\bar{c}\bar{V}_T C_{D\delta h}}{m'} - W_e$	$x_\theta = -g \cos \theta$
z	$z_u = \frac{-2C_L}{m'}$	$z_w = \frac{-C_D - C_{L\alpha}}{m'}$	$z_q = \frac{-\bar{c}\bar{V}_T C_{L\delta h}}{m'} + U_e$	$z_\theta = -g \sin \theta$
m	$m_u = 0$	$m_w = \frac{C_{M\alpha}}{I'_y}$	$m_q = \frac{-l_T \bar{V}_T C_{L\delta h}}{I'_y}$	$m_\theta = 0$

are dominated by the velocity components. The velocity components are calculated as follows;

$$U_e = V_0 \cos \alpha \quad (4.11)$$

$$W_e = V_0 \sin \alpha \quad (4.12)$$

The term  $m_\theta$  cancels due to close coupled configuration for which downwash effects can be neglected. All the calculated derivatives need to be transformed to the body axes system since the equation of motion are derived using the body axes convention. Therefore, the matrix  $A_{long}$  can be obtained for a given  $V_0$  and  $\alpha$ .

Meanwhile, the coefficients of the lateral-directional of the state matrix are shown as below:

$$A_{lat} = \begin{bmatrix} y_v & y_p & y_\phi & y_r & y_\psi \\ l_v & l_p & l_\phi & l_r & l_\psi \\ 0 & 1 & 0 & 0 & 0 \\ n_v & n_p & n_\phi & n_r & n_\psi \\ 0 & 0 & 0 & 1 & 0 \end{bmatrix} \quad (4.13)$$

The expressions for each term are directly taken from the aerodynamic coefficients for the stability derivatives summarized in Table 4.4.

Table 4.4: Dimensionless derivatives of aerodynamic coefficients for lateral-directional motion.

Variable	$v$	$p$	$\phi$	$r$	$\psi$
y	$y_v = \frac{C_{y\beta}}{m'}$	$y_p = \frac{bC_{y_p}}{2m'}$	$y_\phi = g \cos \theta$	$y_r = \frac{bC_{y_r}}{2m'}$	$y_\psi = g \sin \theta$
l	$l_v = \frac{C_{l\beta}}{Ix'}$	$l_p = \frac{bC_{l_p}}{2Ix'}$	$l_\phi = 0$	$l_r = \frac{bC_{l_r}}{2Ix'}$	$l_\psi = 0$
n	$n_v = \frac{C_{n\beta}}{Iz'}$	$n_p = \frac{bC_{n_p}}{2Iz'}$	$n_\phi = 0$	$n_r = \frac{bC_{n_r}}{2Iz'}$	$n_\psi = 0$

The aircraft constants are referred to Table 4.5. Though both the Cao and NASA models have similar dimensions for the aerodynamic reference length and area, the weight and inertia properties are evidently different.

Each derivative in the matrix are calculated from the aerodynamic coefficients, as defined



Table 4.5: Weight and inertia as collected from [74, 8, 84].

Parameter	Cao	Chakraborty	NASA
Mass, $m$ (lb)	1035.31	1034.5	1111.74
<i>Inertias, (slug-ft<sup>2</sup>):</i>			
Roll, $I_x$	23000	23000	22632.6
Pitch, $I_y$	151293	151293	174246.3
Yaw, $I_z$	169945	169945	189336.4
Cross Product about Y-axis, $I_{xz}$	-2971	-2971	-2131.8

in Table 4.3 and 4.4, where the normalised mass and inertia are defined as;

$$m' = \frac{m}{\frac{1}{2}\rho V_0 S} \quad (4.14)$$

$$I'_x = \frac{I_x}{\frac{1}{2}\rho V_0 S b} \quad (4.15)$$

$$I'_y = \frac{I_y}{\frac{1}{2}\rho V_0 S \bar{c}} \quad (4.16)$$

$$I'_z = \frac{I_z}{\frac{1}{2}\rho V_0 S b} \quad (4.17)$$

### 4.3 Eigenvalue Trajectories

The modes of a dynamical system can be studied through the eigenvalues and eigenvectors obtained from a linearized state matrix at a given trim condition. Eigenvalues can be either real or complex oscillatory mode respectively. As for the complex eigenvalues, a negative real part indicates a stable system while a positive real part indicates an unstable system.

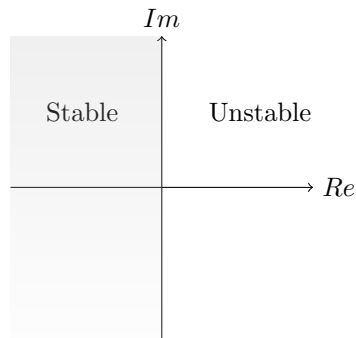


Figure 4.5: Simple schematic diagram showing the s-plane.

These eigenvalues are obtained from the characteristic equation by solving the state equation in Equation 4.4 to determine the responses of the aircraft longitudinally and lateral-directionally. By taking the Laplace transform, it can be restated as follow;

$$s\mathbf{x}(s) = \mathbf{A}\mathbf{x}(s) + \mathbf{B}\mathbf{u}(s) \quad (4.18)$$

so, the solution of the state equation can be written as;

$$\mathbf{x}(s) = [s\mathbf{I} - \mathbf{A}]^{-1}\mathbf{B}\mathbf{u}(s) \quad (4.19)$$

where  $\mathbf{I}$  is the identity matrix with the same order of the state matrix  $\mathbf{A}$ . The characteristic equation is given by equating the characteristic polynomial to zero:

$$\Delta(s) = [s\mathbf{I} - \mathbf{A}] = 0 \quad (4.20)$$

$\lambda_i$  are the eigenvalues of the state matrix  $\mathbf{A}$  by finding the roots of Equation 4.20 only if  $\det(\lambda_i\mathbf{I} - \mathbf{A}) = 0$  which is true if there exists a nonzero eigenvector,  $\mathbf{v}_i$ , for which

$$(\lambda_i\mathbf{I} - \mathbf{A})\mathbf{v}_i = 0 \quad (4.21)$$

such that

$$\mathbf{A}\mathbf{v}_i = \lambda_i\mathbf{v}_i \quad (4.22)$$

If the size of the state matrix  $\mathbf{A}$  is define by  $(n \times n)$ , typically it will give  $n$  eigenvalues/eigenvectors. Assuming that the eigenvectors are linearly independent that the characteristic equation has no repeating roots, it can be understood that;

$$\mathbf{A}[v_1 \cdots v_n] = [v_1 \cdots v_n] \begin{bmatrix} \lambda_1 & & 0 \\ & \ddots & \\ 0 & & \lambda_n \end{bmatrix} \quad (4.23)$$

Its roots can now be written in the suggestive forms, that;

$$\lambda_i = \begin{cases} -\zeta\omega_n \pm \omega_n\sqrt{\zeta^2 - 1}, & \text{for } \zeta > 1 \\ -\zeta\omega_n, & \text{for } \zeta = 1 \\ -\zeta\omega_n \pm i\omega_n\sqrt{1 - \zeta^2}, & \text{for } \zeta < 1 \end{cases} \quad (4.24)$$

where  $\zeta$  is the damping ratio and  $\omega_n$  is the natural frequency of the modes. From the eigenvalues, some interesting properties can be derived. From Equation 4.24, the modes can be categorized into the following:

- overdamped,  $\zeta > 1$  - the characteristic equation has two distinct real roots,
- critically damped,  $\zeta = 1$  - the characteristic equation has repeating real roots,
- underdamped,  $\zeta < 1$  - the roots of the characteristic equation consist of the complex conjugate pair which means it can cause an oscillation.

### 4.3.1 Longitudinal Modes

The classical modes of longitudinal motion can be described by two underdamped oscillatory modes. The longitudinal eigenvalues consist of two well separated complex pairs called the short period mode (stable) and the phugoid mode (marginally stable or unstable). The short period mode is oscillatory and relatively well damped. It affects disturbances in AoA and pitch rate while the phugoid mode is oscillatory and takes a long time to decay or grow. It affects disturbances in component velocity vector in x-axis and angle of attack.

The plotting of the eigenvalue for the Cao model (Figure 4.7) for both high and low frequency modes show deviations in the trajectories for the numerical and analytical methods. The high frequency mode shows reductions in frequency by approaching the real axis as AoA is increased. In contrast, the low frequency mode showed common

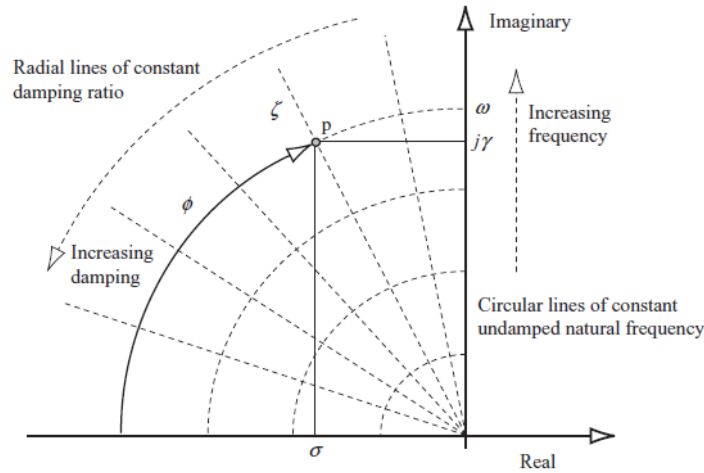


Figure 4.6: Typical complex roots on the s-plane taken from [89].

trajectories for both numerical and analytical results at lower AoA until at certain AoA, the eigenvalues for the numerical result turned towards the imaginary axis and making a cross before turning back towards the imaginary axis. The analytical results on the other hand, continuously showed an increasing frequency as AoA is increased except when AoA reaching  $34^\circ$ , the eigenvalues jumping drastically to the right hand side of the real axis.

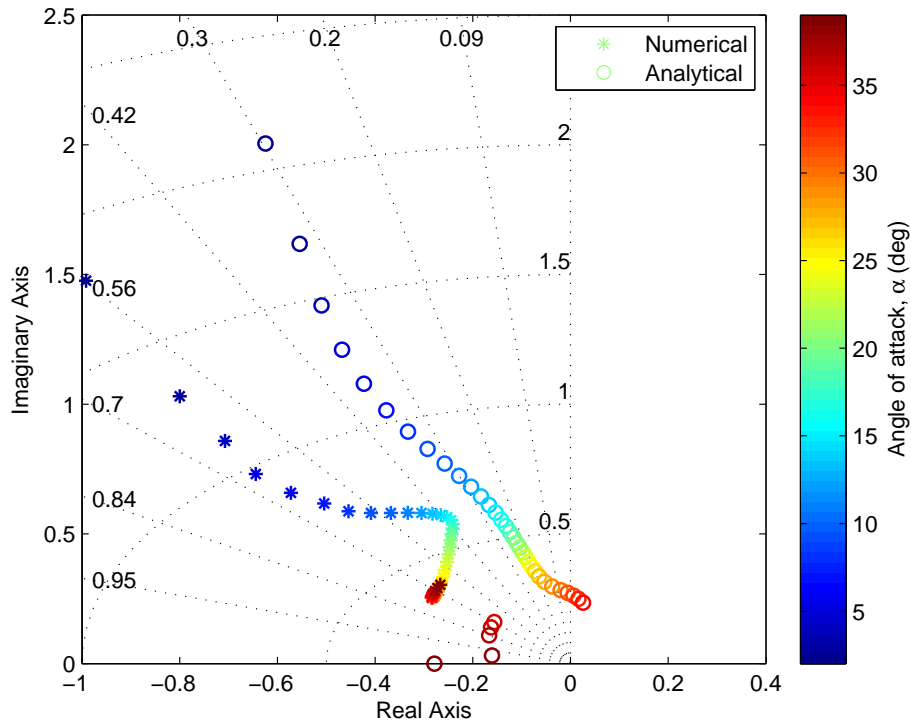
From Figure 4.7, the turnings of the eigenvalue trajectory in the numerical not only shown by low frequency mode but also can be seen for the high frequency mode. These turnings are corresponding to similar AoA for both modes at which  $\alpha = 19^\circ$  and  $\alpha = 34^\circ$ . When variation of each element in the state matrix was plotted for both numerical and analytical values, it was detected that the change of properties in  $m_w$  may be the contributing factor of these turnings. From Figure 4.8, it is seen that both numerical and analytical values coincide between each other at  $\alpha = 19^\circ$  and  $\alpha = 34^\circ$ . Though the projection of both values may not explained fully on how it affected the turnings, but it appeared that the change in the numerical properties of  $m_w$  has influenced the dynamics properties of the state matrix as a whole when the AoA is varied. On the other hand, the analytical expression for  $m_w$  is depending on the  $C_{m_\alpha}$ .

Migration of the low frequency poles to the right hand side of the real axis showed that the longitudinal modes become unstable when  $\alpha > 22^\circ$ . This condition corresponded to  $V_T \leq 250 \text{ ft/s}$ . Though the lower frequency mode is less critical, the migration of the eigenvalues is thought to cause bifurcation [32, 15]. To further understand the dynamics, it should be demonstrated in the nonlinear simulation of the model at this particular flight condition.

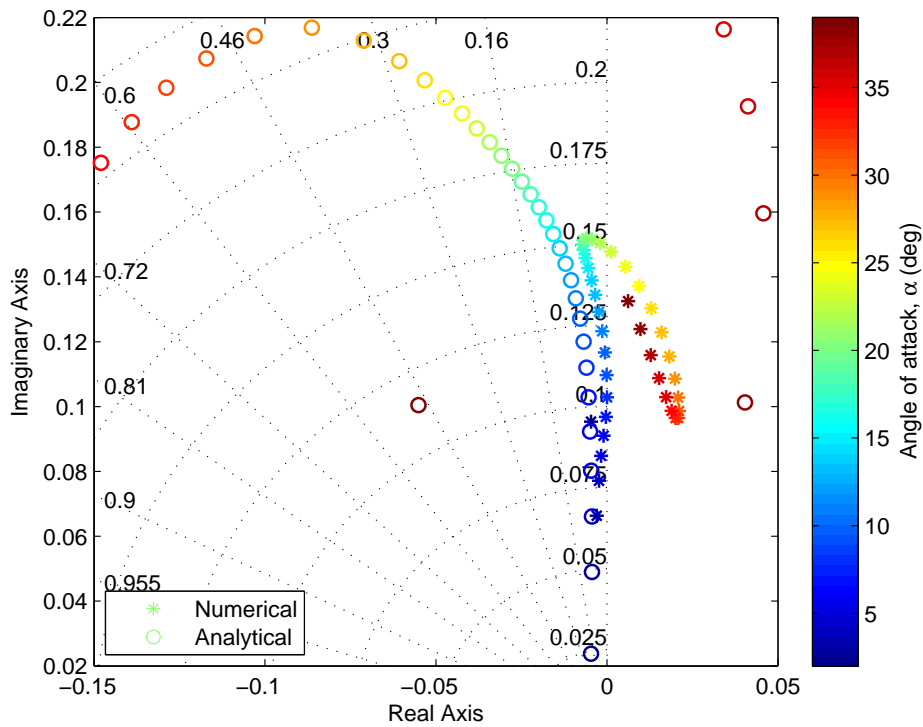
Firstly, trim conditions for the range of AoA between  $22^\circ < \alpha < 23^\circ$  were considered to determine the exact point where the migration of the eigenvalues crossing the imaginary axis. From Figure 4.9, it was seen that about  $\alpha \approx 22.66^\circ$ , the eigenvalue is nearly zero. Then, this value of AoA was taken to simulate the nonlinear model showed in Figure 4.10.

The model is disturbed at the trim condition with a small perturbation from horizontal stabilator. The sinusoidal shape of the state variables responses with time showed almost neutrally stable behaviour. The amplitude of the motion also seen to grow slowly and maintain the magnitude through out the time.

The eigenvalue trajectories for the Chakraborty model (Figure 4.11) for both high and



(a) High frequency



(b) Low frequency

Figure 4.7: Plot of eigenvalues trajectory as  $\alpha$  is changed for Cao model showing longitudinal modes at  $h = 15000ft$ .

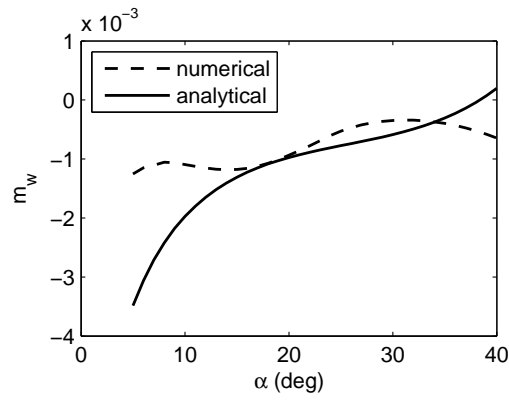


Figure 4.8: Variation of  $m_w$  with  $\alpha$  for the Cao model.

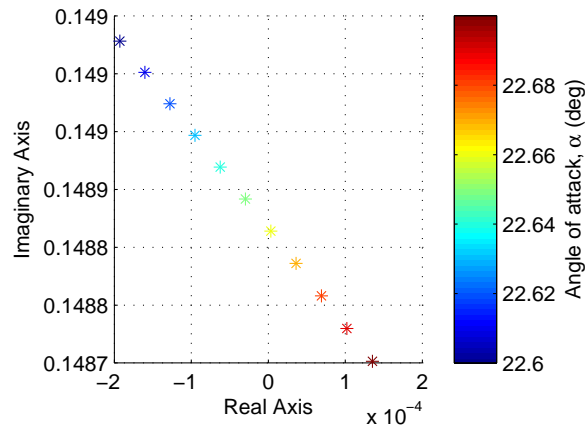


Figure 4.9: Refined low frequency response of Cao model showing migration of eigenvalues crossing the imaginary axis.

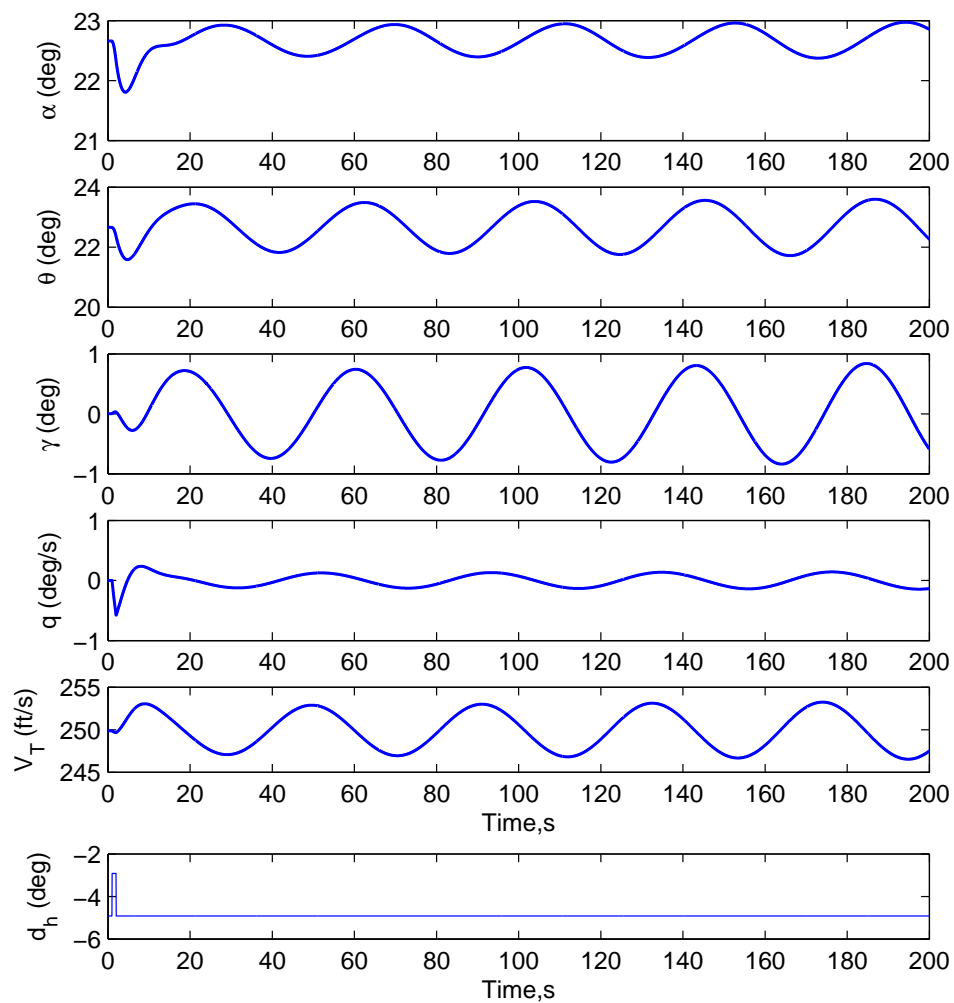


Figure 4.10: Nonlinear simulation of the state variables for Cao model at  $\alpha = 22.66^\circ$ .

low frequency modes have shown separation in both trajectories numerically and analytically. Though both numerical and analytical poles mapped similar trajectories, they did not correspond to similar eigenvalues for each AoA which were slightly shifted. The eigenvalues for higher frequency,  $\alpha < 13^\circ$  numerically and  $\alpha < 11^\circ$  analytically, possessed negative real numbers but suddenly changed the trend by having negative complex numbers as the AoA is increased. Nevertheless, the unexpected behavior at lower AoA is most likely due to the artificial data generated by Chakraborty [8] to cover the lack of data for aerodynamic model at lower  $\alpha$  from the original sources.

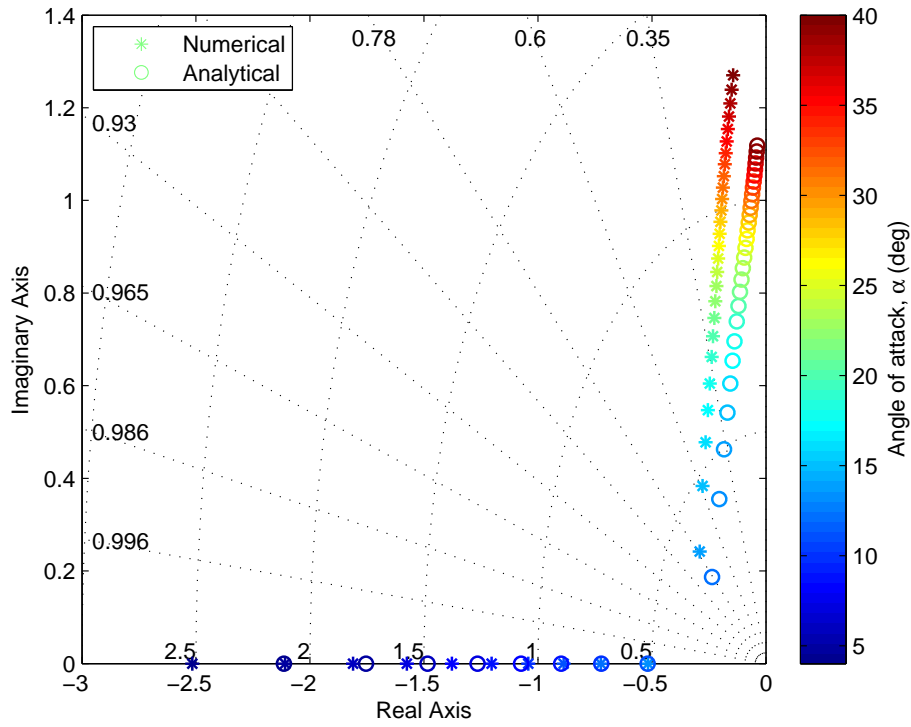
Similarly, when low frequency mode was referred at lower AoA, the eigenvalues mapped between  $4^\circ < \alpha < 13^\circ$  were separated from the smooth trajectory between  $16^\circ < \alpha < 40^\circ$  for numerical trajectory and  $4^\circ < \alpha < 11^\circ$  were separated from the smooth eigenvalue trajectory between  $14^\circ < \alpha < 40^\circ$  for analytical trajectory. The separation creates two layers of eigenvalue trajectories for both the numerical and analytical plots. However, the conditions shown by the Chakraborty model did not support the results shown by the Cao model previously. Rather than became completely unstable at high AoA, the Chakraborty model only showed an unstable mode at certain AoA. The Chakraborty model has shown unstable eigenvalues of the low frequency mode predicted between  $14^\circ < \alpha < 16^\circ$ .

As for the NASA model (Figure 4.12), it is difficult to trace the trajectories of the eigenvalues as AoA is increased for the numerically trimmed models. The distribution of the eigenvalues are clustered within small groups and scattered regardless of the value of AoA. On the other hand, the analytical models show sequenced order of eigenvalues at lower AoA as it is increased. It is not easy to trace the progression of the eigenvalues, especially for the low frequency mode. Some of the eigenvalues lie on the real axis for both high and low frequency modes, which is not seen for the Cao and Chakraborty models.

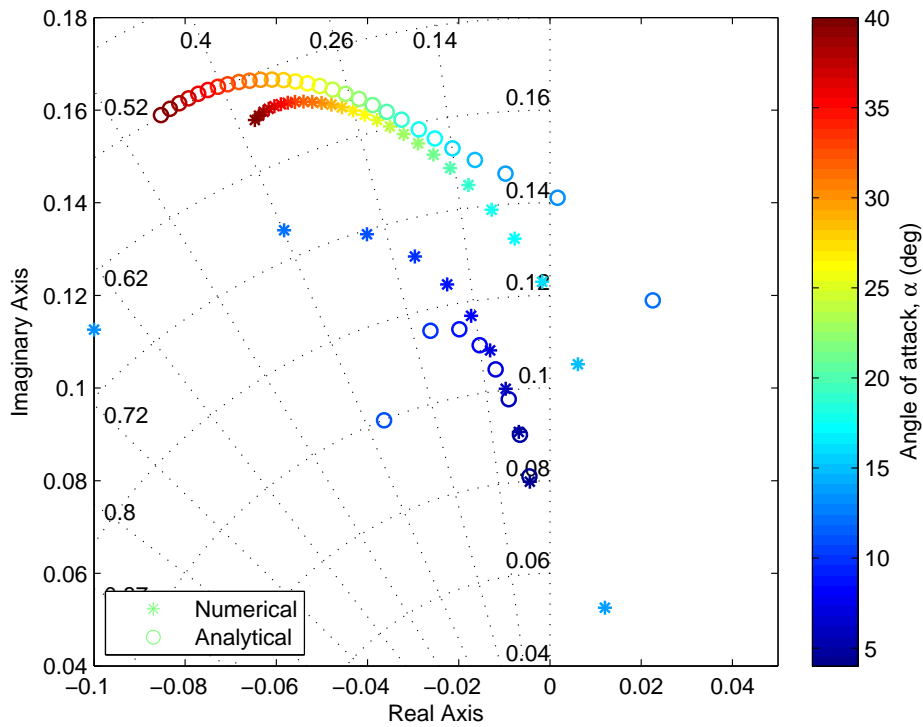
It can be seen in the range of  $7^\circ < \alpha < 14^\circ$  and  $23^\circ < \alpha < 35^\circ$ , there are a large jump in between the eigenvalues especially for the numerical results. The ranges are partitioned on each of the stability derivatives for the NASA model and it is found that the stability derivative of  $m_w$  may have been the contributing factor to jump. In Figure 4.13, the high peaks showed in between the blue dotted lines (showing the previous ranges of  $\alpha$ ), experienced a sudden change in sign value of  $m_w$  which may lead to the large jump of the eigenvalues in between the ranges. Similar to the Cao and Chakraborty models, the low frequency mode for the NASA model has eigenvalues on the right hand side of the imaginary axis. However, the eigenvalues which lie on the right hand side are not in order and mostly involved high AoA.

Previously, it was seen that the Chakraborty and NASA models both yield real eigenvalues at low and at intermediate AoA respectively, especially for the high frequency mode. Having eliminated this range of eigenvalues from both models, the trajectories for all models were replotted. In general, the trajectories do not show close resemblance, but are concentrated in the same areas. It was also noticed that a slight change in the aerodynamic characteristics can affect the trajectory of the eigenvalues for the whole system. This is closely replotted in Figure 4.14 and 4.15 for all the models both in low and high frequencies.

However, it is obvious that for high frequency modes (Figure 4.14), the Chakraborty model does not map the eigenvalues towards the real axis as mapped by the Cao and NASA models. Instead of mapping downward, the trajectory for the Chakraborty model



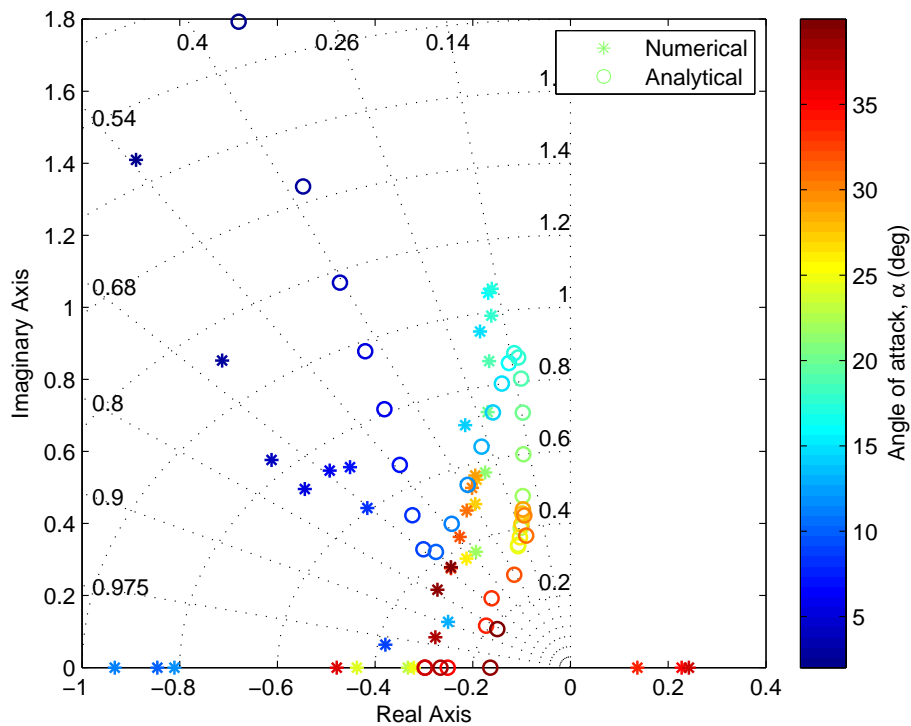
(a) High frequency



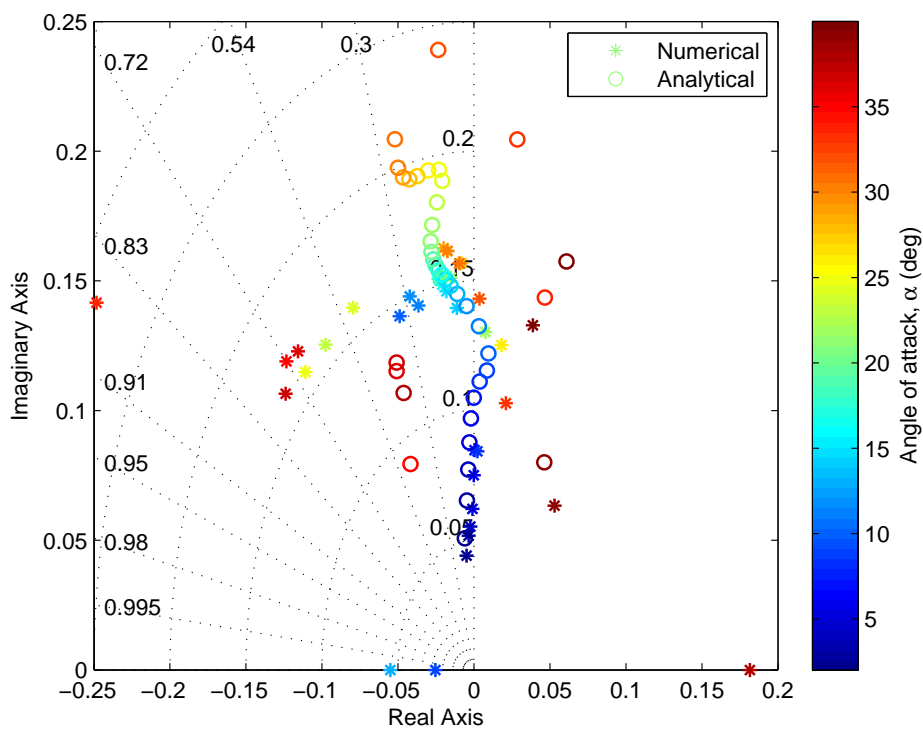
(b) Low frequency

Figure 4.11: Plot of eigenvalues trajectory as  $\alpha$  is changed for Chak model showing longitudinal modes at  $h = 15000ft$ .





(a) High frequency



(b) Low frequency

Figure 4.12: Plot of eigenvalues trajectory as  $\alpha$  is changed for NASA model showing longitudinal modes at  $h = 15000ft$ .

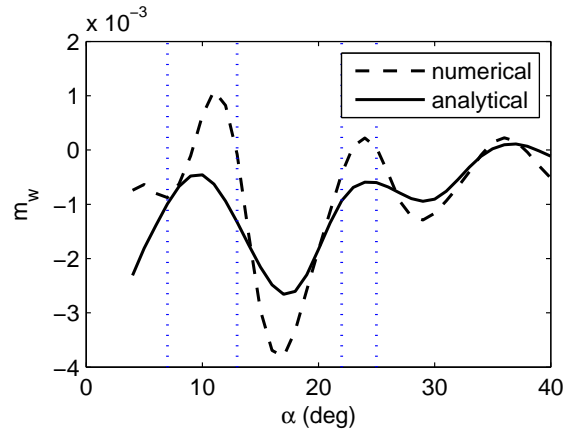


Figure 4.13: Variation of  $x_w$  with  $\alpha$  for the NASA model.

moving upward from the real axis, as AoA is increased showing a decrease in damping ratio.

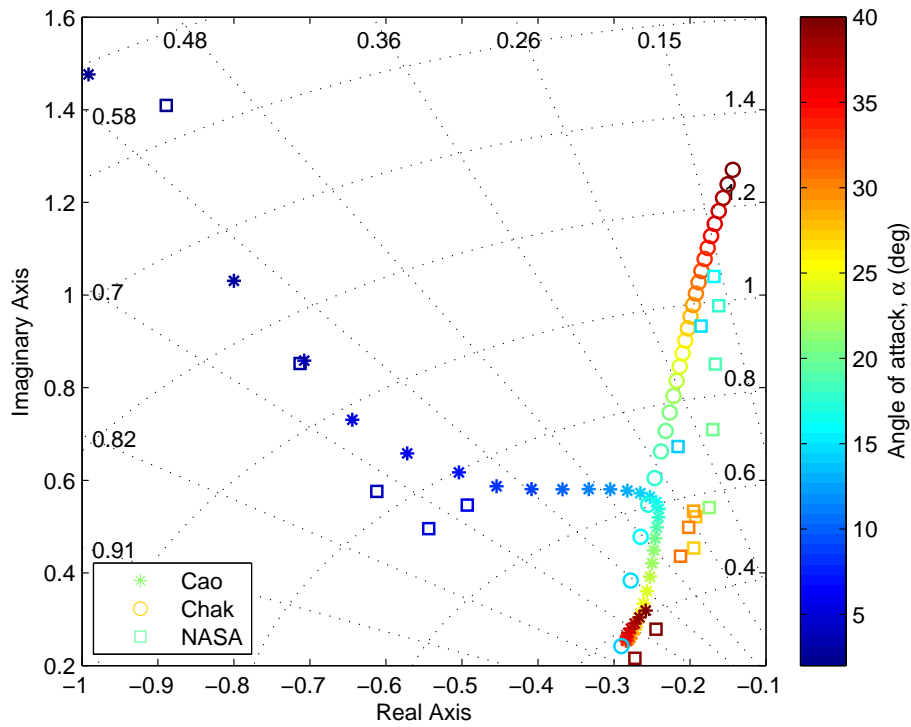
As for the low frequency mode (Figure 4.15), the Cao and NASA models almost predict similar eigenvalues at specified AoA which also clearly reflect in the analytical trajectories. It is also noted that the elimination of the eigenvalues that produced negative real numbers in the high frequency mode from the Chakraborty model (refer Figure 4.11 (a)) also eliminates the first layer of eigenvalue trajectories for the low frequency mode.

Though the eigenvalues for the NASA model are scattered, it can be seen that the mapping of poles at low AoA have almost similar trajectories for both the numerical and analytical approaches with the Cao model. Unfortunately, it cannot be mapped for the Chakraborty model due to the invalid data range of AoA. Figure 4.14 (a) showed that at least at one flight condition, the NASA model has similar eigenvalues with Cao model at high frequency mode, but not for the low frequency mode. However, this point did not correspond to similar flight condition for both models but at  $\alpha = 3^\circ$  for the NASA model which has the eigenvalue of  $\lambda_{SP} = -0.6131 \pm 0.8520$  while the Cao model at  $\alpha = 4^\circ$  which has the eigenvalue  $\lambda_{SP} = -0.7074 \pm 0.8584$ .

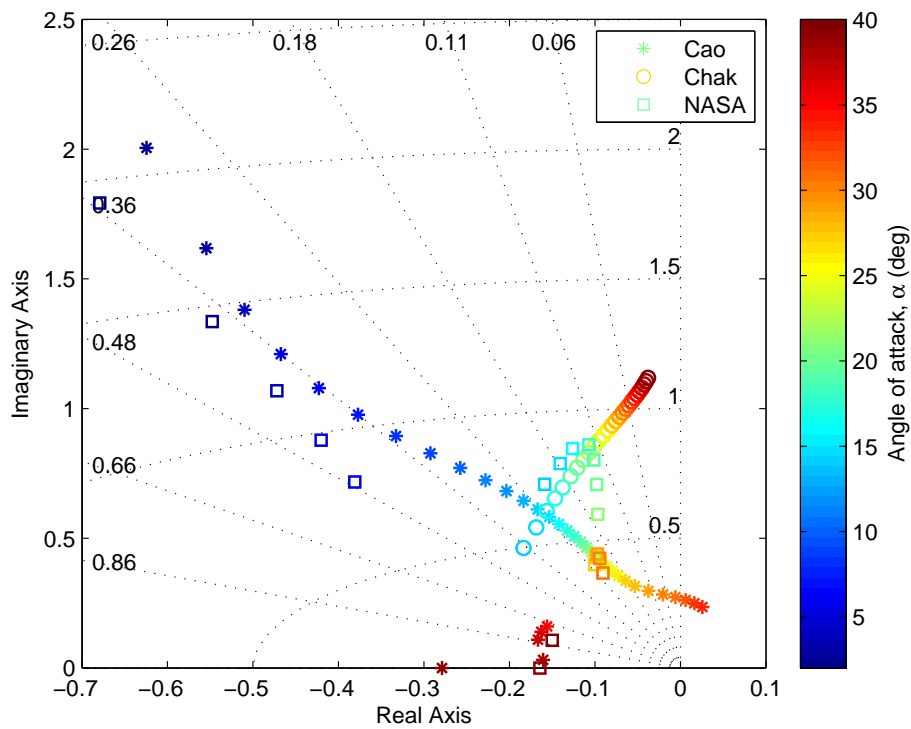
Taken the trim conditions at the respective flight conditions for both the Cao and NASA models, identical disturbance is induced to the horizontal stabilator,  $\delta_h$ , of  $1^\circ$  for  $1s$ . The nonlinear simulation for both the Cao and NASA models is shown in Figure 4.16. The response of AoA is clearly seen to show the major impact from the control surface disturbance which the Cao model reacted with a higher magnitude compared to the NASA model; while other state vectors show almost mutual responses with slight differences.

### Differences in Numerical and Analytical Results

The poles mapping for the eigenvalue as the variation of AoA show that both numerical and analytical trajectories did not share common dynamics behaviour. Elements comparison from the numerical and analytical approaches for the  $A_{long}$  matrix showed large differences in  $m_q$ . The differences in other derivatives are small in comparison. This condition is demonstrated in the following example, which gave the numerical and analytical  $A_{long}$  matrix for the Cao model longitudinal modes at  $\alpha = 5^\circ$  as follows:

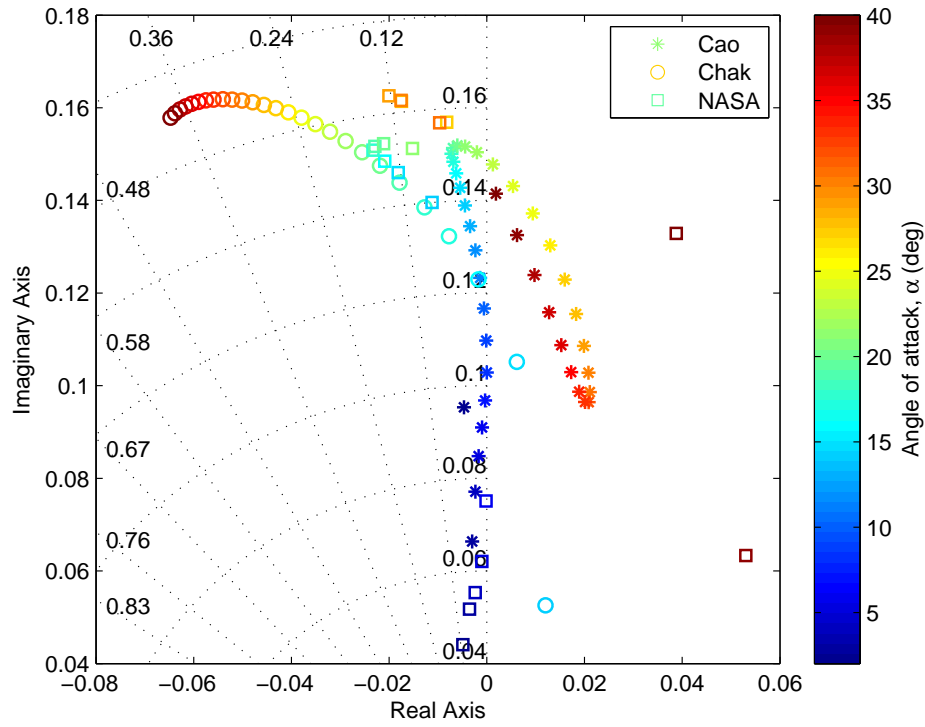


(a) Numerical

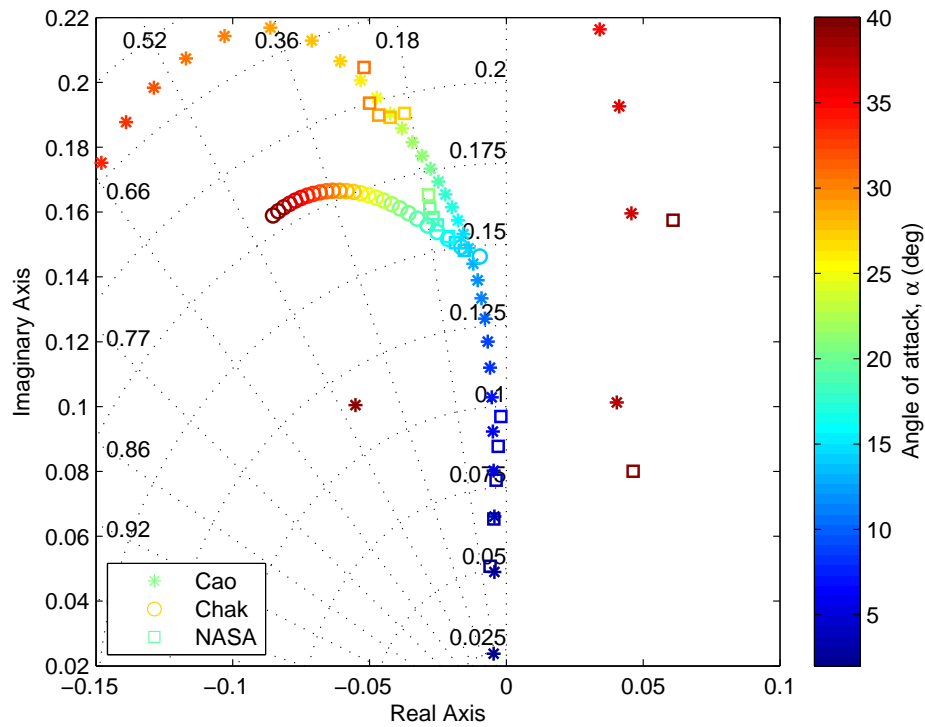


(b) Analytical

Figure 4.14: High frequency eigenvalue trajectories for all models.



(a) Numerical



(b) Analytical

Figure 4.15: Low frequency eigenvalue trajectories for all models.

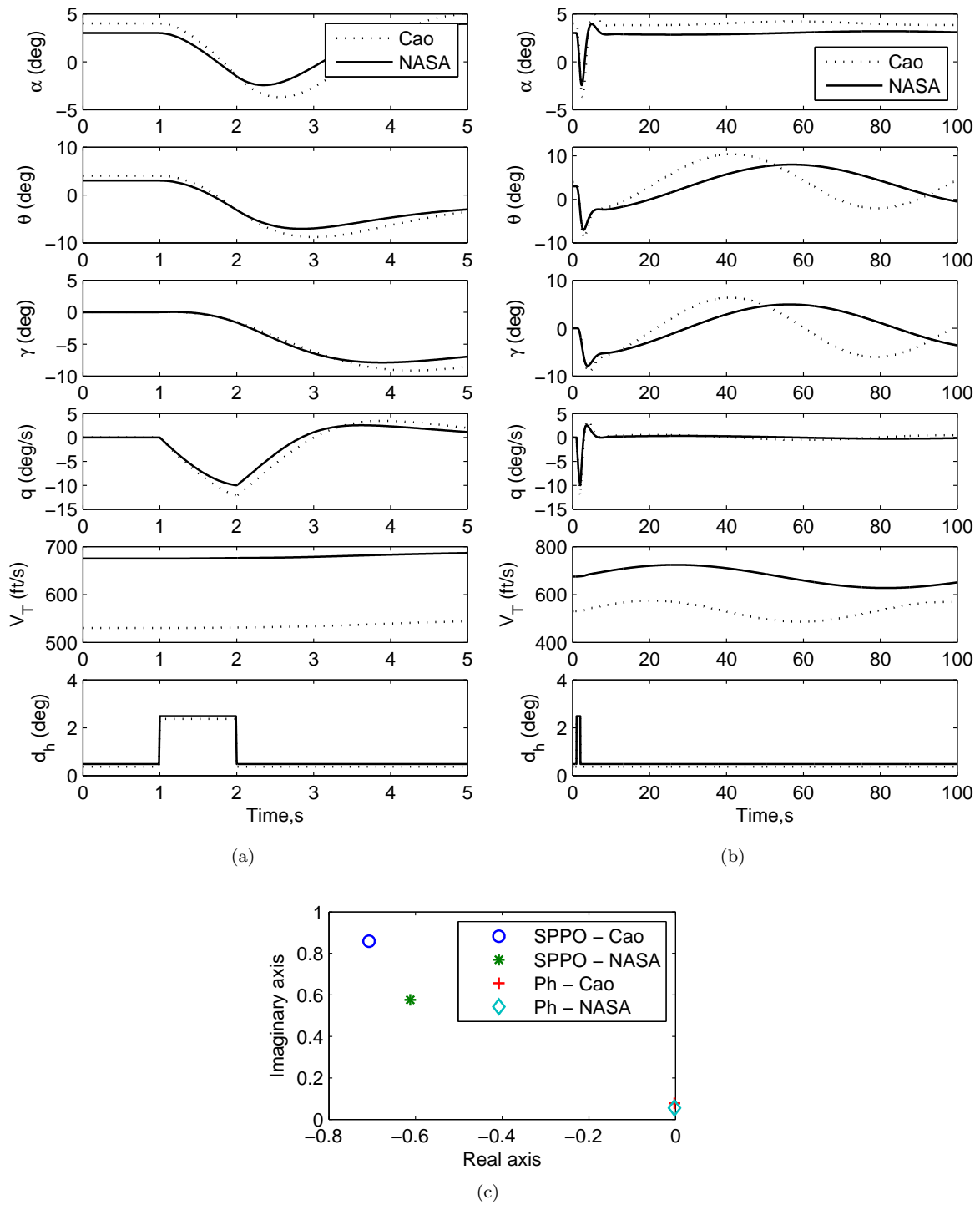


Figure 4.16: Response of the Cao and the NASA models to stabilator deflection for (a) high frequency, (b) low frequency, and (c) poles in s-plane.

$$A_{long_{num}} = \begin{bmatrix} -0.0044429 & 0.039604 & -40.795 & -32.052 \\ -0.69393 & -0.87448 & 466.29 & -2.8041 \\ 0.00014405 & -0.0012546 & -0.41322 & 0 \\ 0 & 0 & 1 & 0 \end{bmatrix} \quad (4.25)$$

$$A_{long_{ana}} = \begin{bmatrix} -0.0065611 & 0.024231 & -41.217 & -32.052 \\ -0.019104 & -0.89722 & 471.24 & -2.8041 \\ 0.00030489 & -0.0034849 & -0.040426 & 0 \\ 0 & 0 & 1 & 0 \end{bmatrix} \quad (4.26)$$

The case also holds for the Chakraborty and the NASA models when close comparison was made between the numerical and analytical approaches in defining the  $A_{long}$  matrix indicate  $m_q$  as the largest deviation in numerical and analytical results for both model. The definition of the  $m_q$  (given in Table 4.3) is taken from Reference [90] which assumes it to arise entirely from the moment of the tailplane given by:

$$M_q = -\bar{V}_0 \frac{l_T}{\bar{c}} a_1 \quad (4.27)$$

where for an all-moving tailplane, the deflection changes the AoA of the whole tail, so;

$$a_1 = C_{L_{\delta_h}} \quad (4.28)$$

From the above equation, the concise derivative  $m_q$  for the F-18 HARV depends on the slope of the lift coefficient of the entire aircraft with respect to the changes in horizontal stabilator deflection,  $C_{L_{\delta_h}}$ . On the other hand, though the calculation is not straightforward numerically, the direct definition can be obtained from the pitching moment coefficient,  $C_{m_q}$ , provided from the mathematical approximation in the Cao and the Chakraborty models, or from the LUT in the NASA model.

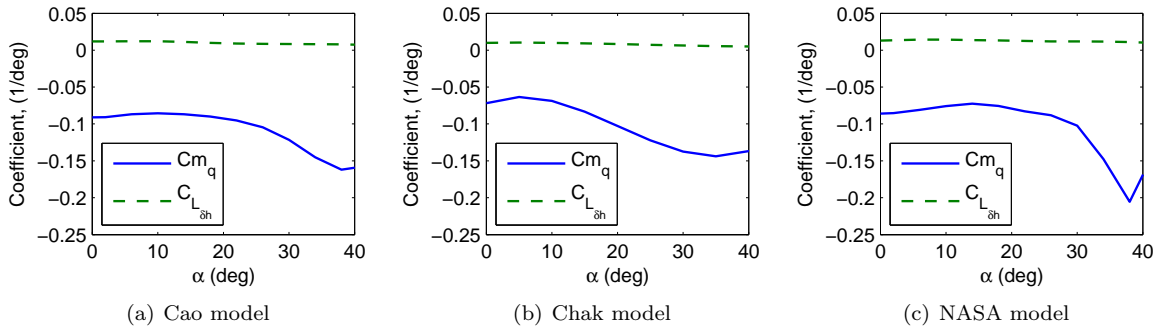


Figure 4.17: Gap showed by the  $C_{L_{\delta_h}}$  and  $C_{m_q}$  for each model.

The differences in both derivatives explain the deviation observed in the eigenvalue trajectories for both the numerical and analytical approaches. However, determination of  $m_q$  from the direct application of  $C_{m_q}$ , should represent a more corrected rather than  $C_{L_{\delta_h}}$ . Therefore, the numerical approach for the eigenvalues determination should be acceptable, rather than the analytical approach.

### 4.3.2 Lateral-Directional Modes

The lateral eigenvalues typically consists of a stable real eigenvalue (roll), a marginally stable or unstable real eigenvalue (spiral), and a stable complex pair (dutch roll). The

roll mode is said to be well damped as it affects roll rate and thus roll angle. On the other hand, the spiral mode affects mainly yaw angle and hence yaw rate. Lastly, the dutch roll is a coupled oscillatory roll-yaw motion.

Figure 4.18 shows the eigenvalue trajectories for the Cao model analytically and numerically. For the dutch roll mode, the analytical trajectory is considerable small when compared with the numerical trajectory. When it is zoomed on the analytical area, the trajectory is actually concentrated on the right hand side of the real axis but very close to the origin of the s-plane, making it an unstable kind of mode. On the other hand, the analytical trajectories for the roll and spiral mode showed a negative real value, which is as expected for a typical model. Nevertheless, the numerical trajectories also show a similar condition except when the AoA goes beyond  $27^\circ$ . This may due to the instability of the spiral mode as AoA is keep increasing.

In the lateral-directional modes for the Chakraborty model, it shows three separated modes as discussed above which is reflected in Figure 4.19. The dutch roll mode consists of complex eigenvalues in which when the AoA is increased, they move towards the imaginary axis. However, for the analytical trajectory, it crossed the imaginary axis and become an unstable mode for  $\alpha > 11^\circ$ .

As for the NASA model, though Figure 4.20 shows three different modes for the lateral-directional motion, the analytical trajectory for dutch roll mode shows a positive eigenvalue, which means unstable mode. As for the numerical trajectory, unlike the Chakraborty model, the numerical trajectory move away the imaginary axis as the AoA is increased.

Interestingly, all the numerical models for the HARV models show unstable roll and spiral modes at higher AoA. The fact can be seen in Figure 4.22, where it shows that the trajectories slightly leave the real axis moving towards the imaginary axis. If both roll and spiral modes are plotted together, they are actually moving towards each other and become pair of complex eigenvalues as they leave the real axis. Whereas, the analytical trajectories for the roll mode and spiral modes for the HARV models predict a stable non oscillatory modes as expected.

## 4.4 Conclusion

In this chapter, pole mapping was applied to the longitudinal dynamics of different HARV models as a way to identify parameter differences in each model. In order to achieve that, linearization was performed so the eigenvalues could be harvested from each model. Numerical and analytical techniques for the linearization have been applied to validate the models and to understand any deviation in between the numerical and analytical results that caused uncommon trajectories in the plots. The mathematical expressions from the analytical technique can be guide in providing explanation on the numerical results.

The trajectories for the high frequency and low frequency modes were individually plotted for all the models. The mathematical formulation used to replace the aerodynamic data in LUT has shown smooth trajectories of the eigenvalues for both the Cao and the Chakraborty models. On the other hand, LUT presentation of aerodynamic data in the NASA model did not possess the same attributes but a showed scattered eigenvalues in small precision.

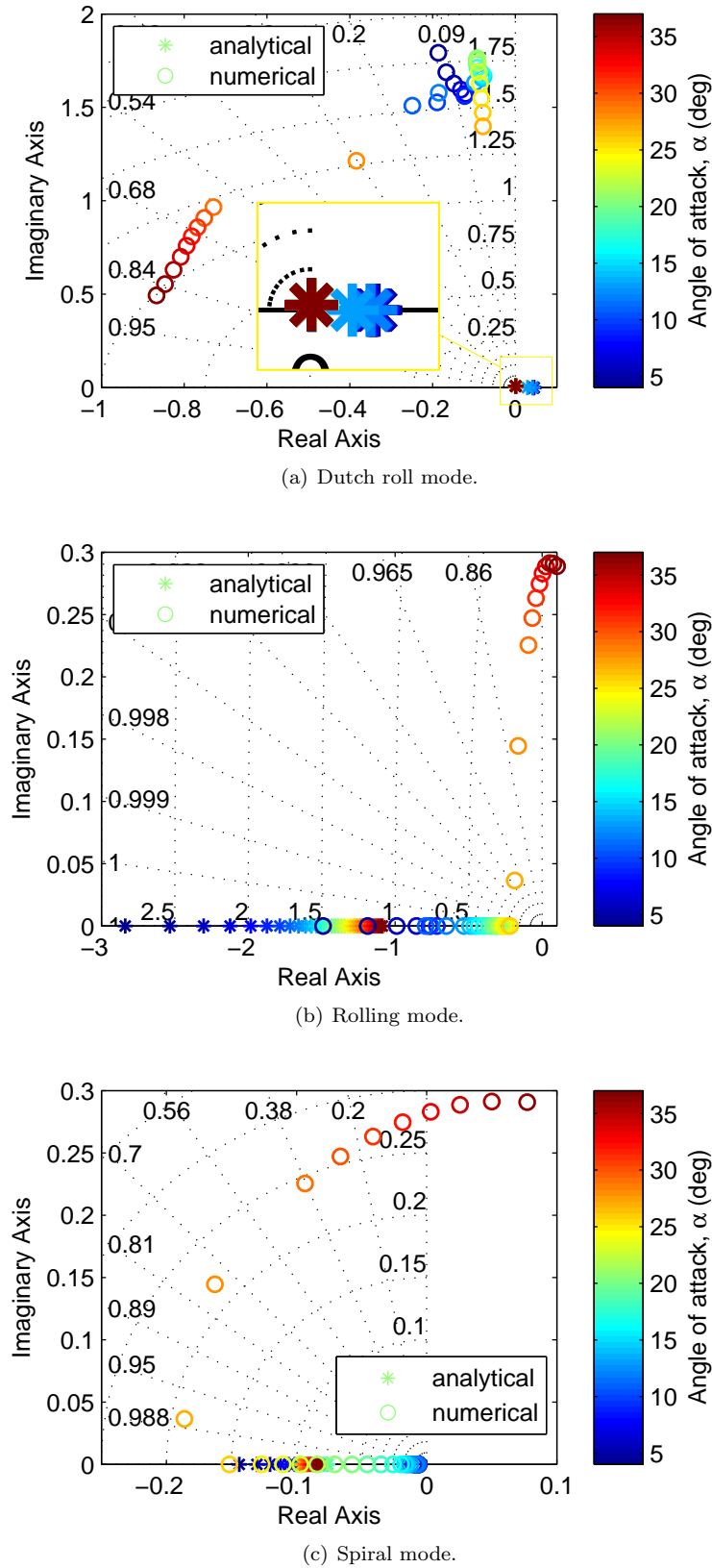


Figure 4.18: Lateral-directional eigenvalues trajectories as  $\alpha$  is changed for the Cao model.



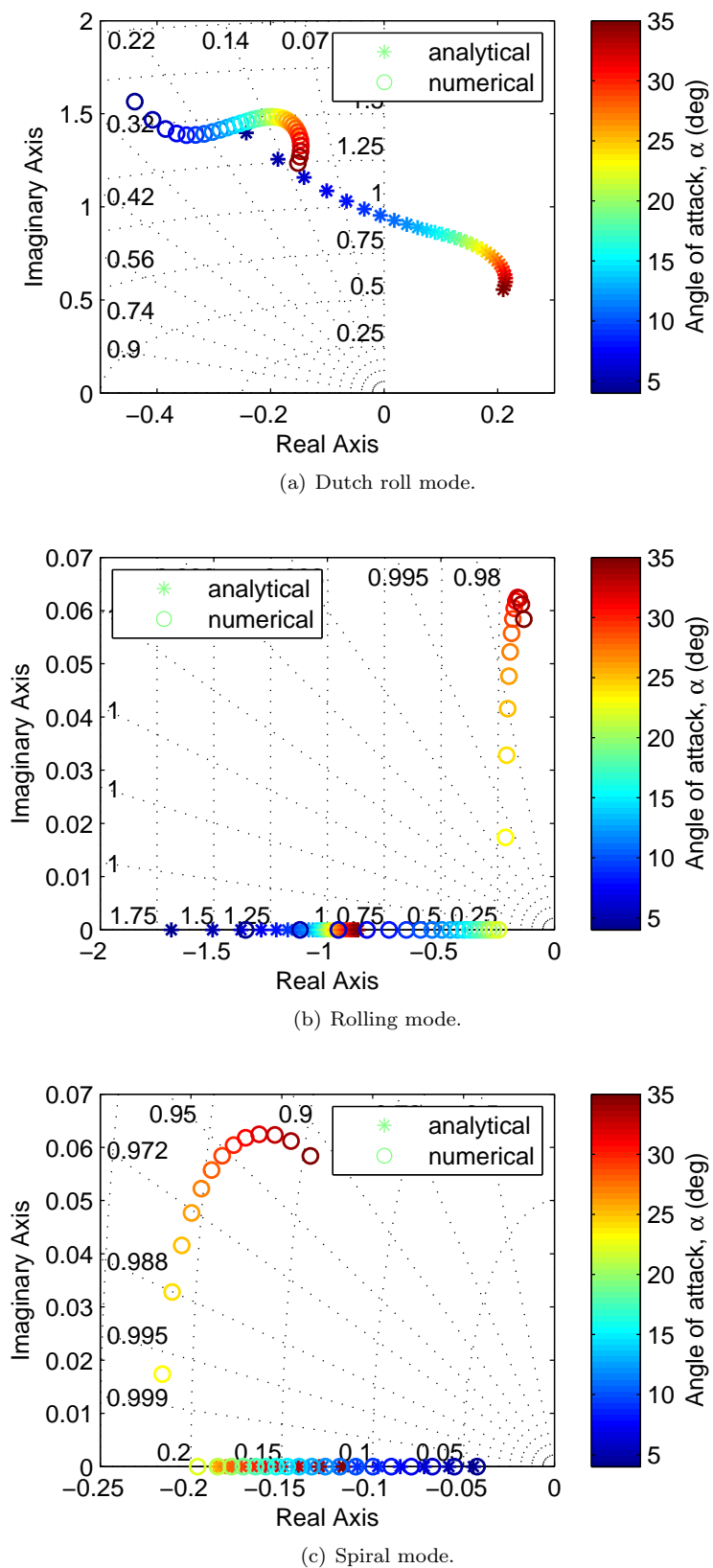


Figure 4.19: Lateral-directional eigenvalues trajectories as  $\alpha$  is changed for the Chakraborty model.

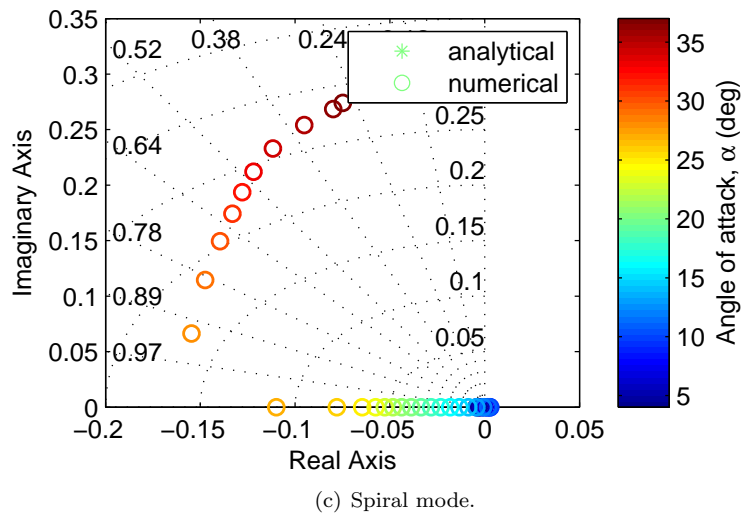
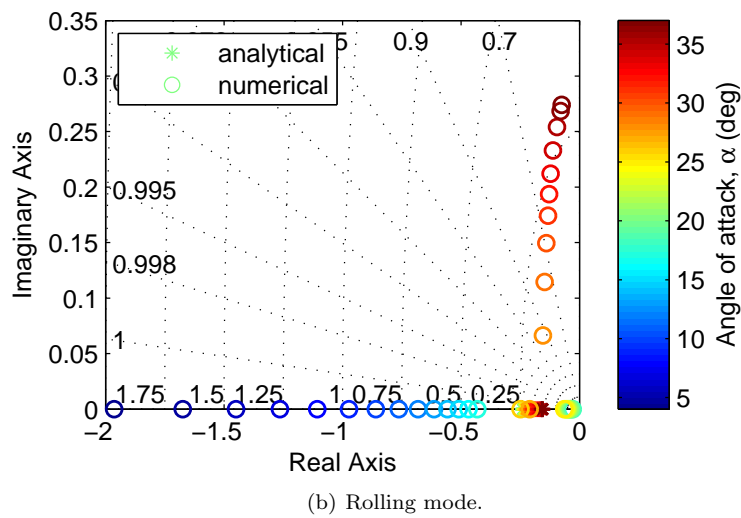
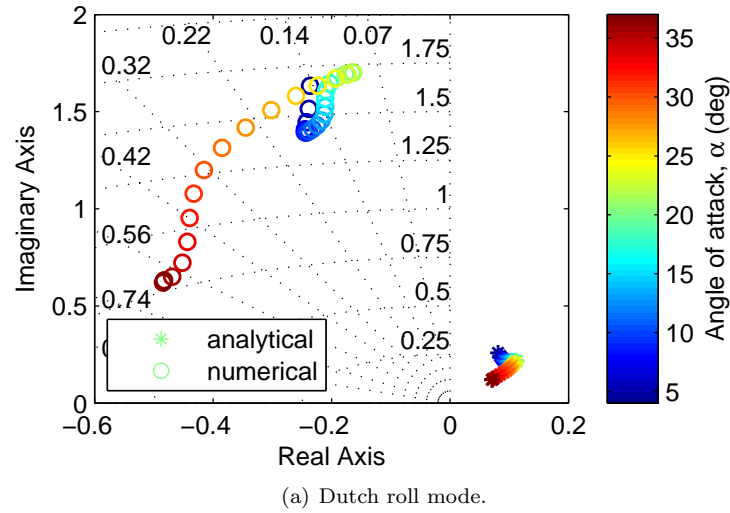
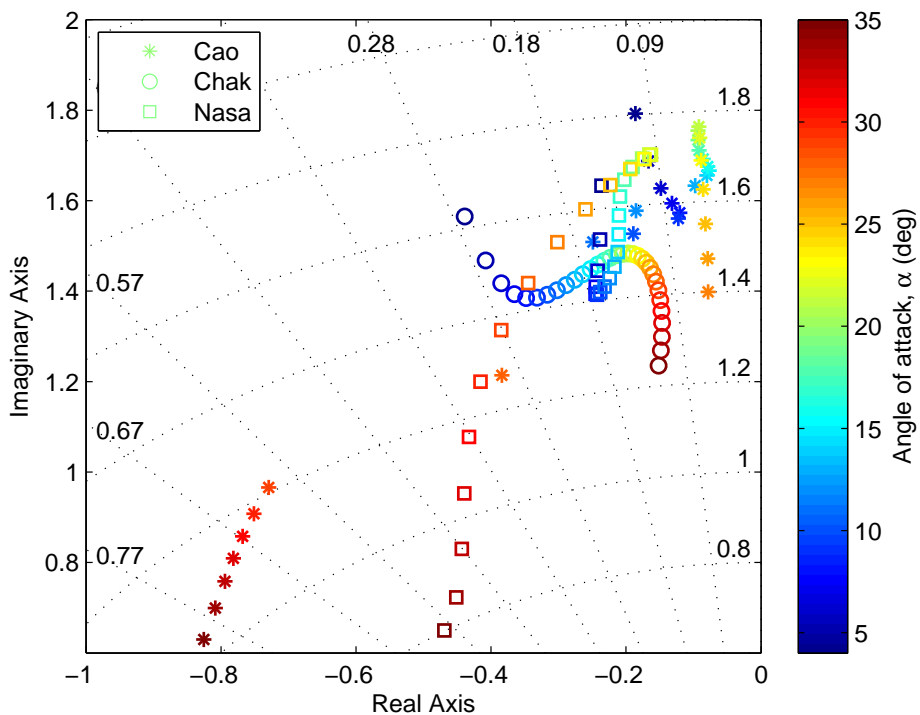
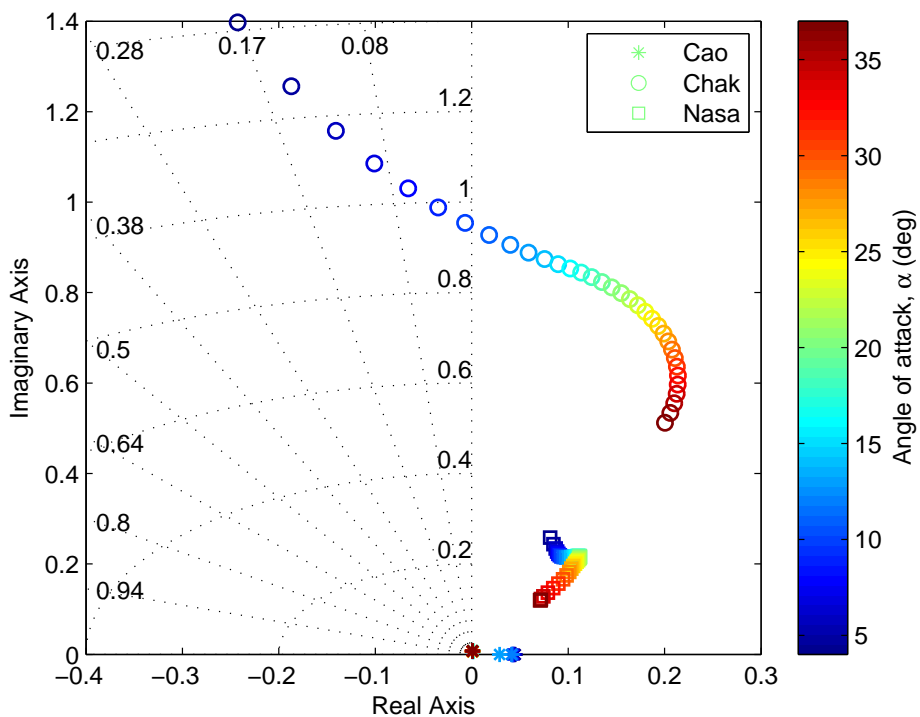


Figure 4.20: Lateral-directional eigenvalues trajectories as  $\alpha$  is changed for the NASA model.

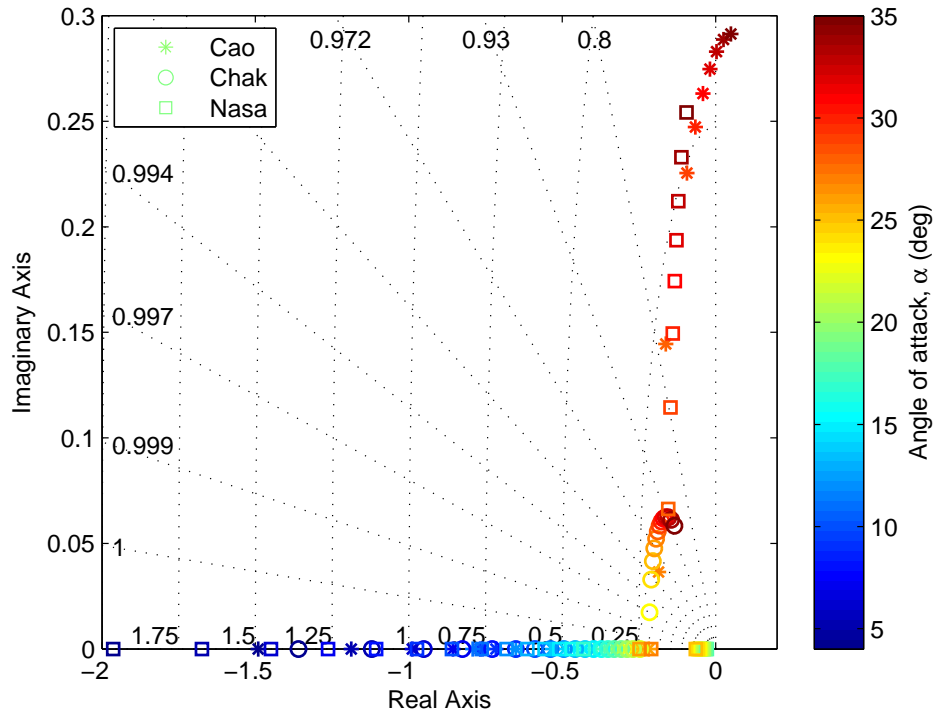


(a) Numerical.

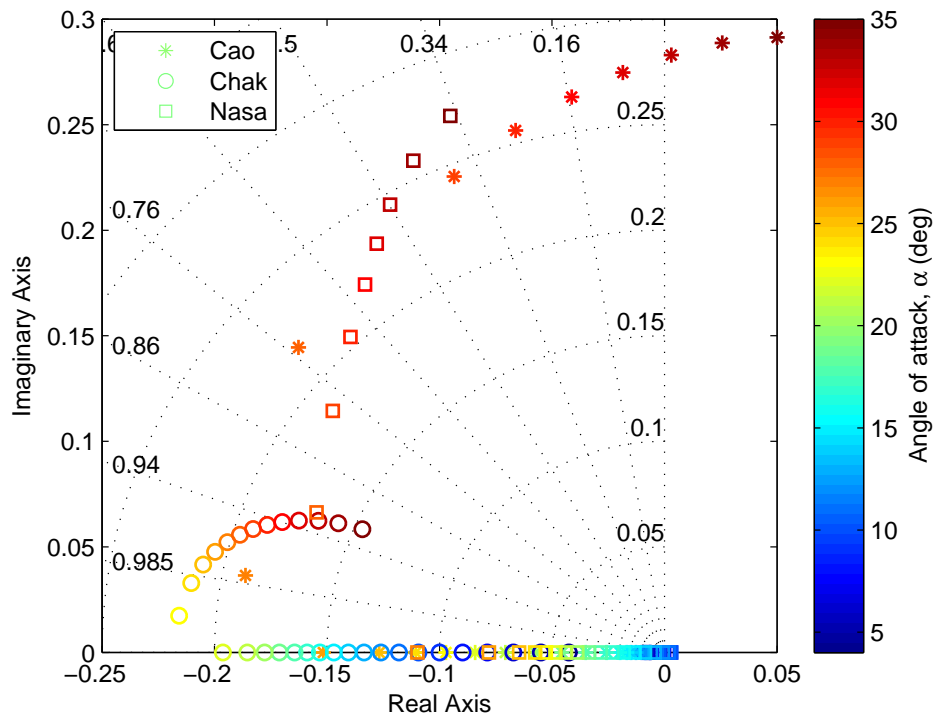


(b) Analytical.

Figure 4.21: Eigenvalue trajectories showing dutch roll mode for all models.



(a) Rolling mode.



(b) Spiral mode.

Figure 4.22: Numerical eigenvalue trajectories showing (a) roll mode and (b) spiral mode for all models.

Based on the poles mapping, the smooth trajectory produced by the Cao and the Chakraborty models are considered more systematic than the scattered mapping as a result from the NASA model. While at some flight conditions, the poles evaluated for the NASA model did not behave as expected for a conventional type aircraft like the F-18 HARV where some of the eigenvalues yield real eigenvalues. Nevertheless, the projections as showed by both the Cao and the Chakraborty models were contrast to each other especially in the high frequency domain. According to Nelson [91], the damping ratio for short period is characterized by  $m_q$  and  $m_{\dot{\alpha}}$  which may not be accessible for the Chakraborty model. Therefore, it is not applicable to conclude which aerodynamic model is more correct as each model may have different factors contributing to each. However, the diverse eigenvalue trajectories for all the models may be due to the methods of selection in presenting the model either in mathematical formulation or LUT.

From the results of the time domain responses, it is noted that despite of the differences found in the aerodynamic characteristics of each model, the nonlinear simulation for all the models did not shown a significant deviation between each other when small perturbation where excited in to the models. However, the eigenvalue trajectories for all the models did not show similarity in the projection of the poles which indicated that the models should have different dynamics behaviour. Therefore, similar approach will proceed in next chapter, applying the concept of propagation of linearized model in assessing the non-linearity strength of each model. Based on the information regarding the strength of non-linearity for each model, it will be utilized to signify the differences in the aerodynamic properties of the models.

This page is intentionally left blank.

## Chapter 5

# Nonlinearity Assessment on the F-18 HARV Aerodynamic Data

The objective of this chapter is to apply the non-linearity index theory in studying the differences in nonlinear models of the same aircraft, but represented by different aerodynamic models. The index is applied to the F-18 HARV models to signify the differences by identifying the source of the non-linearity in the models which are represented in the nonlinear aerodynamics thus determine the impact on nonlinear simulation.

### 5.1 Introduction

System analysis involves developing a model describing the system and solving for the model's response in order to understand the behaviour of the system towards a disturbance or to study the effects on the system's behaviour from different components. The system is usually modelled in terms of a set of equations which can take various forms. The most common form is the differential equation relating the input and output as a result of the direct application of a physical law.

Solving the system involves a complete investigation into the differential equations and their solution. This usually requires a numerical method if the equations are complex; otherwise an analytical method can be opted. But before further analysis can be done on the dynamic system, it is better to understand the principal categorization of the various mathematical models. They are either linear or nonlinear, time invariant or time varying, continuous time or discrete time, and deterministic or stochastic [87]. In this chapter, the intention is to focus on the effect of any non-linearity in a system.

Flight simulations are basically carried out using a nonlinear model. The source of the non-linearity in the aircraft model usually comes from the coupling effects arising in the EoM as a result of the kinematic and inertia coupling, as well as from nonlinear aerodynamic representation of the coefficients. For the HARV models, it was seen that the aerodynamic characteristics from different sources have nonlinear properties at high AoA as referred to Section 3.3.

A common approach to studying a nonlinear system is by means of piecewise linearization. The advantage of a linear model is that the solutions are additive and underlying modes of motion can be identified. However, in some circumstances, this linear approach may

fail to portray the nonlinear modes that may be observed in such a complex system. Therefore, it is best to know the degree of non-linearity in the system prior to the analysis so a suitable tool for nonlinear analysis may be chosen.

## 5.2 Nonlinearity Index: Theoretical Background

The non-linearity index is a tool to quantify the non-linearity of a system at a specific condition defined by an index. The larger the index value, the stronger non-linearity is. However, methods of estimating the index found in the literature vary from one application to another. Among the earliest application of the index quantification was applied to a system modelling based upon the input and output signals. In Reference [50], a multilayer perceptron concept, a type of artificial neural network, was proposed in estimating the degree of system non-linearity tested on a parametric nonlinear system. A computer simulation had validated the result showing the index was increased as the system parameter was increased. Later the method was adapted by Mizuta et. al. [92] for a system output with additive exogenous noise. The adaptive algorithm was implemented in tracking the degree of non-linearity of the output signal in a real time, which is suitable for the application of mobile or network communication systems for monitoring the signal distortion.

In a recent application of the non-linearity index, an approach based on computing the largest variation found in a linearized matrix over a set of extreme points was introduced by Junkins in [51, 52] for the application of orbital mechanics. In this method, the nonlinear system is represented by an approximate set of linear systems around some operating points. While Reference [51] provides the ground breaking of the theory, Reference [52] applied the theory to rigorously measure the non-linearity of a system within four different test cases of attitude kinematic representation; Euler Angle Representation, Classical Rodrigues Parameter Representation, Modified Rodrigues Parameter Representation, and Quaternion Representation. The non-linearity was found to be consistent with the error from the linear and nonlinear simulation. The index has indicated highest value of non-linearity for Euler Angle Representation.

While the application of the non-linearity index by Junkins was only restricted to the initial value sensitivity, Omran and Newman [46] extended the study by analysing input excitation sensitivity and applied it to aircraft flight mechanics. In combination with Junkins approach, four expressions were generated in Reference [46] which were applied to measure non-linearity strength over the entire flight envelope of F-16 and T-38. The index was high in two regions, a lower speed region where the AoA were high and in the transonic region where the compressibility effect cannot be ignored. The tools provide a visual indicative together with the index, a specific region for probability of nonlinear behaviour to occur; hence a proper control strategy may be designed. On the other hand, specific flight conditions were chosen by Tapolcai et. al. in [54] and [55] to assess the non-linearity strength by considering stall phenomena for the T-2C in the longitudinal flight and spin phenomena for the F-18 HARV in the lateral-directional flight respectively. In both instances, the authors managed to demonstrate that a nonlinear activity such as limit cycle is likely to occur when the indices were at maximum and then linked each condition to the source of the non-linearity.

The non-linearity index used in this thesis was based on the combination of the method introduced by junkins and Singla [52] and Omran and Newman [46]. While the non-



linearity index as approached by Tapolcai et al. [54, 55] was implemented on the reduced analytical expression for longitudinal and lateral-directional flight and limited to the initial state excitation only. In this thesis, a similar approach will be proposed but applied on a full numerical aircraft model built in a Simulink, and also the application of the non-linearity index will be extended into analysing other inputs shape into the system such as impulse and doublet with a very high input to drive the system to go unstable. Then, the index can be used to study their effects on the behaviour of the aircraft model.

The general dynamical system for flight dynamics application with the time varying model for a nonlinear state and output model are given by:

$$\dot{x} = f(t, x, u) \quad (5.1)$$

$$y = g(t, x, u) \quad (5.2)$$

where  $f$  and  $g$  are the functions denote the non-linearities of the model. Given at time,  $t = 0$ , the initial condition of  $x$  is known as  $x(t_0) = x_0$ . In applying the concept into a flight mechanics application, a parameterized aircraft model is considered. Therefore, it is easy to understand the effects of parameter changes in the dynamics model. The time varying characteristics in Equation 5.1, are indirectly incorporated through parameter dependence, which can be replaced by linear parameter varying (LPV) system as:

$$\dot{x} = A(\lambda(t))x + B(\lambda(t))u \quad (5.3)$$

$$y = C(\lambda(t))x + D(\lambda(t))u \quad (5.4)$$

where  $A(\lambda(t))$  is the state dynamics matrix,  $B(\lambda(t))$  is the input distribution matrix,  $C(\lambda(t))$  is the output distribution matrix, and  $D(\lambda(t))$  is the direct input - output matrix. The matrices are Jacobian in form and are varied according to a scheduling parameter,  $\lambda$ , that can be chosen from the state variables.

The non-linearity index approach has been divided into two criteria: static non-linearity indices and dynamic non-linearity indices. Each index is generalized for two options, one is based on the initial value sensitivity and the other is based on the input excitation sensitivity. The initial value sensitivity is addressed by the state and output matrix while the input excitation sensitivity is addressed by the input and direct matrix. However, in certain flight mechanics applications, the output and direct matrices are not really considered as they are often identity and zeros matrix respectively.

### 5.2.1 Static Non-linearity Indices

Static non-linearity is captured as the departure of linearized models from being constant over a family of worst case variations as a parameter is changed. The worst case variations or sometimes the sub-region is defined to be the region that any change in the system properties is expected to influence the behaviour of the system for a given operating point.

Thus the index can be used as a tool in identifying the operating point where nonlinear behaviour is likely to occur. As a result, the region can narrow the area into detecting the source of non-linearity as well as providing a base to discover any non-linearity type that may specifically exist during the flight condition.

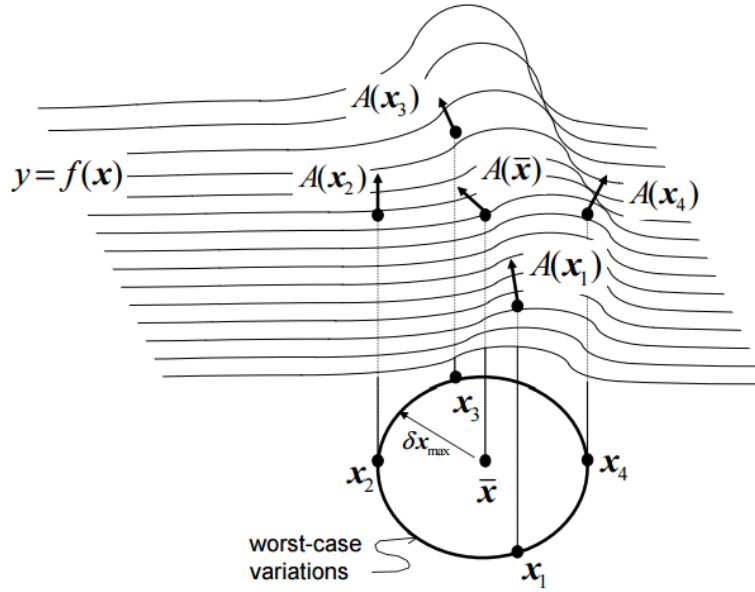


Figure 5.1: Schematic Diagram showing the worst case variations extracted from [51].

Static non-linearity measure the variation of the state space matrix across the local sub-region. The indices are given by:

$$\nu_s^A(\lambda_i) = \sup_{j=1, \dots, N} \frac{\|A(\lambda_j) - \bar{A}(\lambda_i)\|}{\|\bar{A}(\lambda_i)\|} \quad (5.5)$$

$$\nu_s^B(\lambda_i) = \sup_{j=1, \dots, N} \frac{\|B(\lambda_j) - \bar{B}(\lambda_i)\|}{\|\bar{B}(\lambda_i)\|} \quad (5.6)$$

where  $\bar{A}(\lambda_i)$  and  $\bar{B}(\lambda_i)$  are the state and input matrices evaluated at a nominal condition or operating point,  $i$ , of  $x(t_0) = \bar{x}_0$ . Similarly,  $A(\lambda_j)$  and  $B(\lambda_j)$  are the state and input matrices evaluated within a sub region of the given operating point,  $j$ , of  $x(t_0) = x_0$ . While  $N$  is determined by the maximum and minimum band of the scheduling parameter within the sub-region.

Static indices are used to observe any deviation between the linearized matrix given at particular condition,  $\bar{x}_0$ , and any generated linear model within the neighbouring sub-region,  $x_0$ . The Equations in 5.5 and 5.6 measure the maximum relative deviation of Jacobian matrix taken at the operating point over a set of extreme operating points within the sub-region. This non-dimensional measure of the indices can be an indicator of the linearized matrix variations due to changes in the system variables. The static state index,  $\nu_s^A$ , represents the non-linearity associated to initial state sensitivity and the static input index,  $\nu_s^B$ , represents the non-linearity associated to input excitation sensitivity.

### 5.2.2 Dynamic Non-linearity Indices

Dynamics non-linearity is a measure of the variation of the state transition matrix through time,  $\Phi(t)$ , by which propagation of the linearized model defines the trajectory of the point  $x(t_0)$  based on the mean point  $\bar{\Phi}$  or on the point itself  $\Phi$ . A same trajectory indicates the system is linear whereas for a nonlinear will show some deviation. The idea is interpreted in Figure 5.2

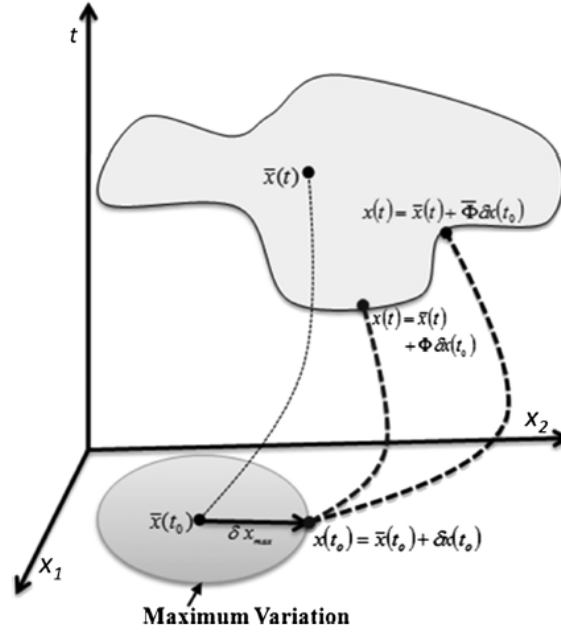


Figure 5.2: Interpretation of dynamic non-linearity extracted from [53].

Dynamic indices are generalized from the combination of the state transition matrix with other system matrices. These indices are given by:

$$\nu_d^x(t, \lambda_i) = \sup_{j=1, \dots, N} \frac{\| \Phi(t, \lambda_j) - \bar{\Phi}(t, \lambda_i) \|}{\| \bar{\Phi}(t, \lambda_i) \|} \quad (5.7)$$

$$\nu_d^u(t, \lambda_i) = \sup_{j=1, \dots, N} \frac{\| \Phi(t, \lambda_j) B(\tau) - \bar{\Phi}(t, \lambda_i) \bar{B}(\lambda_j) \|}{\| \bar{\Phi}(t, \lambda_j) \bar{B}(\lambda_i) \|} \quad (5.8)$$

where  $\bar{\Phi}(t, \lambda_i)$  is a state transition matrix that is obtained at the nominal condition or operating point  $i$  and  $\Phi(t, \lambda_j)$  is a state transition matrix that is obtained within the sub-region of the given operating point,  $j$ , which is  $x_0 = \bar{x}_0 + \delta x_0$ . The state transition matrix is a function of both time and scheduling parameters. Thus, the dynamics indices also measure the propagation of state non-linearity with time.

The deviation of the system transmission paths, either state-to-state or input-to-state, is captured through these indices from Equations 5.7 and 5.8 which indicates the sensitivity of the aircraft dynamics to any change in initial condition over the local sub-region. The dynamic state index,  $\nu_d^x$ , represents the sensitivity of the state propagation across the local sub-region and the dynamic input index,  $\nu_d^u$ , represents the influence of input signal on the linear approximation deviation. They not only quantify the strength of the non-linearity, but also indicate source of that non-linearity.

### 5.3 Non-linearity Index within a Region of Flight Envelope

The non-linearity index was set up by obtaining the state and input matrix respectively. MATLAB code has been developed to generalize the calculation of the non-linearity index for all three aerodynamic models. For each model, the trimming and analytical linearized models were used to determine the index.

Using the developed code, each model of the F-18 HARV, represented by a different aerodynamic model was linearized to generate sets of linear models within range of AoA, in this case  $5^\circ < \alpha_i < 30^\circ$  with  $1^\circ$  increment step, to obtain the state matrix,  $\bar{A}(\lambda_i)$ , and input matrix  $\bar{B}(\lambda_i)$ . Then, the sub-region size,  $N$ , is considered at about a 5% difference of maximum and minimum band within each operating point  $i$ . These give the sub-region operating point of  $\alpha_{j_{min}} = \alpha_i - (5\% * 30^\circ)$  and  $\alpha_{j_{max}} = \alpha_i + (5\% * 30^\circ)$  with the state matrix within the sub-region,  $A(\lambda_j)$ , and input matrix  $B(\lambda_j)$ . Applying the non-linearity index from Equations 5.5 - 5.8, a plot of the index can be generated as a result of varying the scheduling parameter.

The process is summarized by the pseudocode in Figure 5.3. The algorithm includes two loops: the first loop is to find the trimmed angles of attack and speeds across the flight envelope denoted by  $i$ , before passing them to the second loop for the consideration of a smaller sub-region around the the selected trimmed point denoted by  $j$ . The number of cycles in the first loop is determined by the range of the selected flight envelope and the step increment, while the number of cycles in the second loop,  $N$ , is determined at least by 5% of the maximum and minimum band scheduling parameter,  $\lambda$ . Once the loop in the sub-region is finished, the maximum deviation is recorded to represent the non-linearity index at the operating condition  $i$ .

```

Initialization
  Loop 1: Operating point across the flight envelope
    Trimming and linearization at  $i$ 
    Find norm for each  $i$  condition
    Get transition matrix for each  $i$  condition
    Passing the trimmed condition to Loop 2
    Determine  $N$ , sub-region range
    Loop 2: Sub-region with  $N$  loops
      Trimming and linearization at point  $j$ 
      Find norm for each  $j$  condition
      Get transition matrix for each  $j$  condition
      Calculate the deviation to speculate the nonlinearity
    End loop
  Find the supreme of the matrix deviation
End Loop
Plot the index against  $\lambda$ 

```

Figure 5.3: Non-linearity index algorithm within the trimming and linearization processes.

AoA has been chosen as the scheduling parameter,  $\lambda$ , to be varied across the flight envelope. The variation is from  $5^\circ$  for the minimum band to  $30^\circ$  for the maximum band due to the limitation of the Mach number specified by each model (3.3). This is because at very low, the trim speed of the model yields Mach number,  $M > 0.6$ . Also, such a range of AoA is chosen in order to set the differences in the characteristics of each model to the same highest angle of attack that is suitable for trimming (refer Table 4.2). The models did not trim at same AoA for a specific trim speed,  $V_T$ , also that the Chakraborty model cannot be trimmed at  $\alpha > 30^\circ$  as the throttle trim position,  $\tau_T$ , will be bigger than 1.

The static and dynamics indices with the variation of AoA for all the three models were plotted for both numerical and analytical results (see Figure 5.4). The indices were determined for both numerical and analytical methods so that the numerical results can be compared with the analytical results for validation. It is also means to show the sensitivity of each numerical and analytical for the HARV models (Cao, Chak and

NASA). The analytical results were obtained from the linearized matrix as in Table 4.3 and 4.4. The analytical method is preferred due to the mathematical expressions that it contains, thus relating the stability and control derivatives definition to the aerodynamic properties. So at least it can be compared with the numerical results and explained the pattern of the results. In Figure 5.4, some of the numerical and analytical results seem not to have similar pattern. Disparity of the analytical and numerical are obviously seen in static and dynamics non-linearities due to input excitation for the Cao model and in dynamic non-linearity for the NASA model.

In Section 4.3, the eigenvalue trajectories for both numerical and analytical methods did not coincide with each other. However, the results for the non-linearity index have indicated that some of them show common curves, especially for the Chakraborty model (see Figure 5.4). The index was calculated based on the ratio of the differences in the state or input matrix due to change of dynamic properties to the state or input matrix at a particular flight condition. Thus, the differences in the eigenvalue trajectories are not indicative of the differences in the non-linearity index. However, it is expected that the numerical and analytical results behave in similar patterns, regardless if the matrix does not predict similar elements.

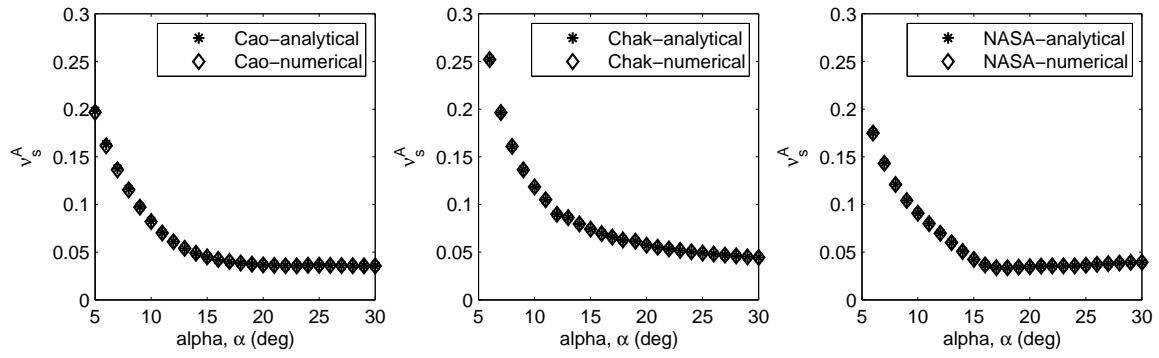
Considering the Cao model, the initial value excitation on the model is appears to cause some changes in the dynamics properties in the input matrices,  $\nu_s^B$  and  $\nu_d^u$ , at certian AoA between  $6^\circ < \alpha < 10^\circ$  and  $21^\circ < \alpha < 24^\circ$  in the numerical results. From the inspection, it was found that there was sudden change in third entry of the input matrix, which is pitch moment due to the horizontal stabilator,  $m_{\delta_h}$ , which represents the principal measure of pitch control power. The changes of  $m_{\delta_h}$  across the sub-region,  $\alpha_j$  causes the departure of the linearized input matrix to vary greatly (see Figure 5.5) in the numerical results. According to the direct definition of the element, it can be linked to the graph of  $C_{m_{\delta_h}}$ . However, there is no peculiar change of  $C_{m_{\delta_h}}$  with AoA for ranges of AoA of  $6^\circ < \alpha < 10^\circ$  and  $21^\circ < \alpha < 24^\circ$  that can be associated with the change of the strength of the non-linearity. Therefore, it is difficult to explain why the numerical results caused some drastic changes in the indices apart from any numerical error that may exist in the model.

In contrast to the Cao models, differences in the strength of non-linearities found in the NASA model were experienced by both of the dynamics non-linearities, as plotted for the numerical results. There is no specific pattern regarding the dynamics non-linearity index, but the numerical results seem to match the pattern for the analytical results. However, the inconsistency in the plot for numerical results may be due to the uneven propagation of the state matrix within the sub-region that is sensitive to the changes of the matrix's elements.

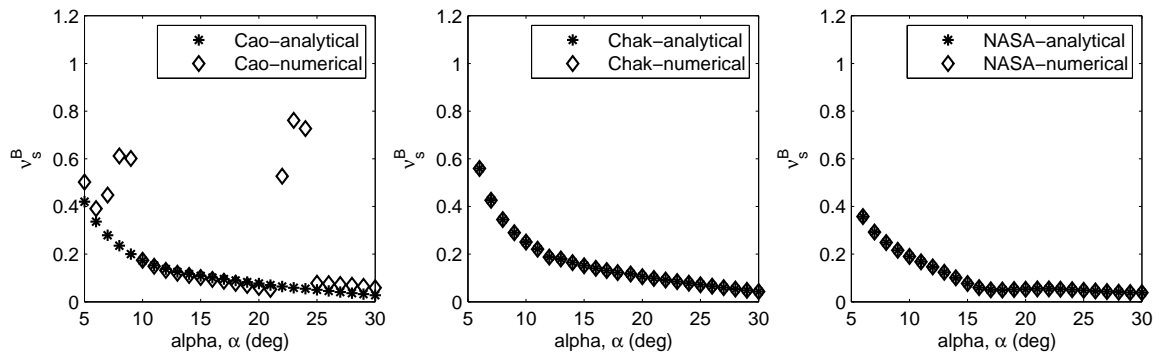
It is obvious that the indices were high at lower AoA which is not as expected. Given the matrix  $A_{long}$  as defined in Equation 4.10, taken at  $\alpha = 8^\circ$  with trim speed of  $V_T = 408.25 ft/s$  when applying to the Chakraborty model, the following matrix is yield:

$$A_{longana} = \begin{bmatrix} 0.000843 & 0.0014921 & -56.818 & -31.861 \\ -0.082981 & -0.53107 & 404.28 & -4.4778 \\ 0.00037589 & -0.0024352 & -0.20055 & 0 \\ 0 & 0 & 1 & 0 \end{bmatrix} \quad (5.9)$$

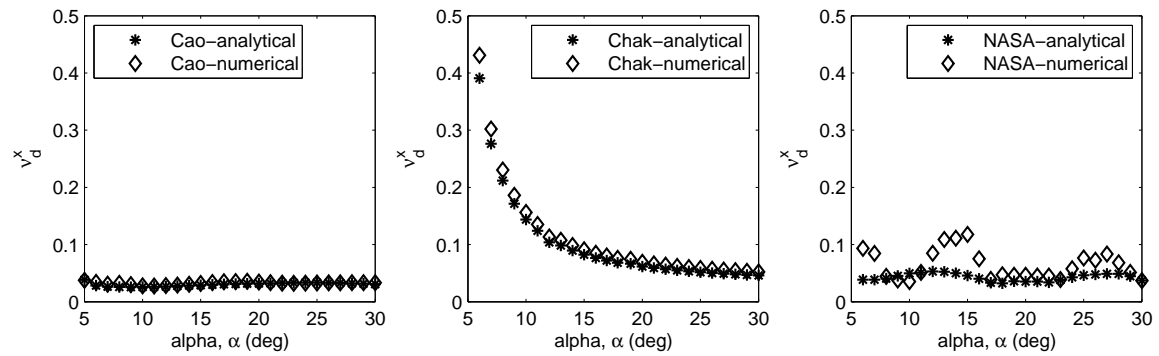
If the norm of matrix in 5.9 is calculated, it returns the value of 408.26, which actually corresponds to the trim speed. The domination of the speed in  $A_{long}$  matrix is traced



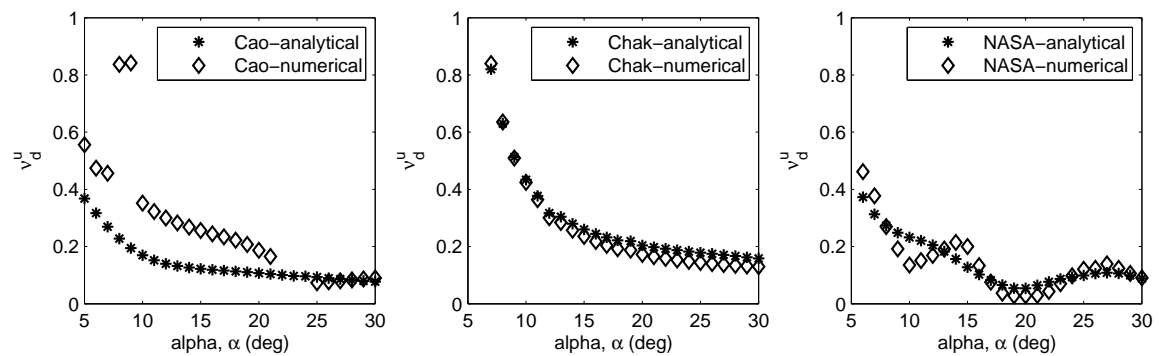
(a) Static nonlinearity due to initial value excitation.



(b) Static nonlinearity due to input excitation.



(c) Dynamic nonlinearity due to initial value excitation.



(d) Dynamic nonlinearity due to input excitation.

Figure 5.4: Plots of the nonlinearity index for all the models numerically and analytically.

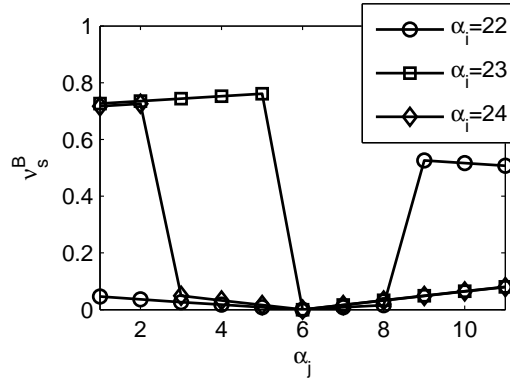


Figure 5.5: Sudden change in input matrix across the sub-region.

out due to the component  $z_q$  as highlighted. The condition is demonstrated in Table 5.1 showing at each  $i$  iteration the highest speed is seen to appear at lowest  $\alpha$ . Therefore, the change in the indices reflect the change in speed rather than the non-linearity itself.

Table 5.1: Trim speeds in each  $i$  and  $j$  loop as  $\alpha$  is increased.

	$V_{\alpha_{j1}}$	$V_{\alpha_{j2}}$	$V_{\alpha_{j3}}$	$V_{\alpha_{j4}}$	$V_{\alpha_{j5}}$	$V_{\alpha_{j6}}$
$i_1$	472.12	442.69	418.69	397.52	381.63	365.40
$i_2$	365.40	353.08	342.69	332.55	323.42	315.16
$i_3$	315.16	307.63	300.64	294.37	288.49	283.04
$i_4$	283.04	277.95	273.19	268.73	264.54	260.59

## 5.4 Non-linearity Index with respect to Different Input Excitation Shape

The non-linearity index analysis found in [54] and [55] have focused on the effect of the nonlinear flight region given at specific flight condition, in order to understand the effect of the index on the dynamics models. This was conducted by determining the initial condition perturbation throughout the flight envelope region. However in this section, it is important to understand the effects of input excitation on the behaviour of the aircraft model. Hence, three different input shapes with large perturbation are considered and tested on each model to investigate whether the model will experience nonlinear behaviour or return to its initial condition. In this case, larger perturbations will force the model to respond based on the given aerodynamic data range whether it will drive the model to go beyond its limit. For example, based on the graphs of aerodynamic derivatives in Section 3.3, the changes of the aerodynamic derivatives with respect to AoA can be quite drastic and sudden. Thus, it is important to know whether these sudden will influence the nonlinear behaviour of the model.

To begin with, a trim condition at approximately  $\alpha \approx 23^\circ$  was chosen to demonstrate the effect of large perturbation in input excitation response of each model. The different shapes of input perturbations and magnitude are shown in Figure 5.6. These input shapes were chosen mainly to excite the models so they go beyond the safe limit of AoA. It starts with a simple pulse input with  $10^\circ$  input to a distressing triplet pulse to see how sensitive the model would correspond to such disturbances.

Each input shape was excited to each model at the trim condition, which will be the reference initial condition in order to assess the non-linearity strength. The influence of differing types of input would most likely change the indicated behaviour observed.

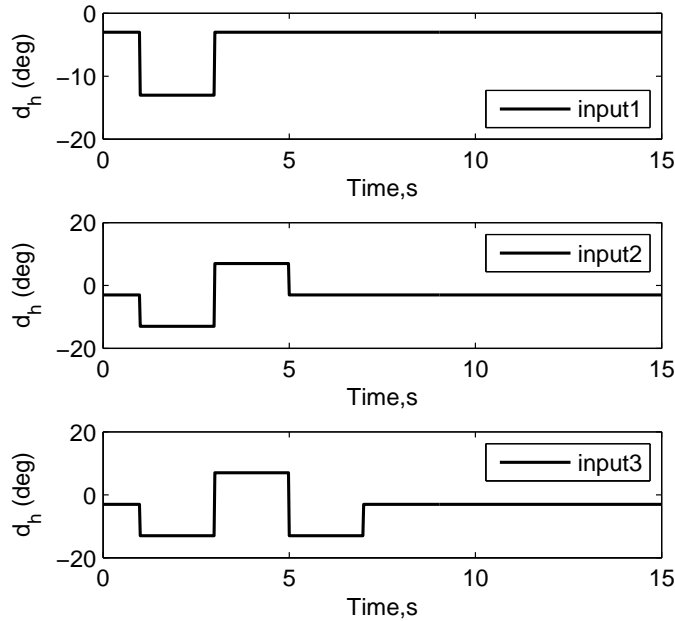


Figure 5.6: Input shapes used to excite the model aircraft.

The responses of the state variables are plotted in Figure 5.7 - 5.9. For each input shape, the state variables responses are also plotted together with the non-linearity indices to show the changes in response due to the input perturbation. Therefore, at each maximum non-linearity index, the corresponding AoA is traced to specific aerodynamics properties at such condition recognizing it as the source of the non-linearity. In this manner, it is possible to observe whether each model will correspond to a similar source of the non-linearity behaviour.

Among all three models, the Cao model has shown the highest magnitude in response to the input shapes perturbation from the trim condition while the Chakraborty model does not show obvious changes in response as it is seen to be more damped. Whereas the NASA model almost shows similar responses to the Cao model except with smaller magnitude. Due to sensitive responses of the Cao model to the input shapes perturbation, the highest non-linearity indices are also recorded by the Cao model.

The indices actively fluctuate once the input shapes are excited and relax after certain time. The highest non-linearity indices for each non-linearity type in the same input shape excitation do not correspond to similar AoA. However, the dynamic non-linearity in the input matrix,  $\nu_d^u$ , has shown the highest index compared to other non-linearity indices. The product of the propagation of the state non-linearity with the input matrix shoot the non-linearity strength to exceed 1 based on the Cao model results. It can therefore be concluded that the input signals have a strong influence on the linear approximation deviation when input excitation is considered. Input shape 3 has the most influential signal in the dynamic non-linearity compared to input shape 1 and input shape 2.

If the  $\nu_d^u$  is considered particularly for the Cao model at each input shape, the highest non-linearity index is spotted at AoA approximately reaching  $60^\circ$  for input shape 1 and



input shape 2. While the input shape 3, the highest non-linearity index is spotted at AoA approximately  $30^\circ$ . These situations may be due to the sudden changes seen in the basic airframe moment coefficients and moment coefficients due to horizontal stabilator deflections,  $(C_{m_0}, C_{m_{\delta_h}})$ , and lift coefficients due to pitch rate,  $C_{L_q}$ , respectively. Similarly, for the Chakraborty and the NASA models, the highest index of  $\nu_d^u$  can be traced out for each input shape which summarized in Table 5.2.

Table 5.2: Summary of the influence of aerodynamic data to the highest nonlinearity index for each input shape.

Model	Input shape	$\alpha$ ( $^\circ$ )	Correspond aero data
Cao	Input 1	60	$C_{m_0}, C_{m_{\delta_h}}$
	Input 2	60	$C_{m_0}, C_{m_{\delta_h}}$
	Input 3	30	$C_{L_q}$
Chak	Input 1	35	$C_{D_{\delta_h}}, C_{L_q}, C_{m_q}$
	Input 2	35	$C_{D_{\delta_h}}, C_{L_q}, C_{m_q}$
	Input 3	35	$C_{D_{\delta_h}}, C_{L_q}, C_{m_q}$
NASA	Input 1	55	$C_{L_{\delta_h}}, C_{m_0}$
	Input 2	40	$C_{m_q}$
	Input 3	55	$C_{L_{\delta_h}}, C_{m_0}$

From Table 5.2, each maximum  $\nu_d^u$  seems to be traced to certain aerodynamic properties. Though the maximum  $\nu_d^u$  for the Chakraborty model are traced to similar AoA, the corresponding aerodynamic characteristics were also traced to three critical conditions of the aerodynamic characteristics. Therefore, for each input excitation shape, there may be one or more factors that affect the non-linearity. Overall, the three different models do not predict the same source of non-linearities.

## 5.5 Conclusion

For this chapter, a non-linearity strength was assessed on different aerodynamics models: the Cao model, the Chakraborty model, and the NASA model, which is quantified by an index. the index has two forms: a static non-linearity index and a dynamic non-linearity index. For each form, it can be assessed by initial value excitation and input excitation. The non-linearity index as approached by Tapolcai et. al. [54], [55] has focused on the initial value excitation. Sets of linear approximation matrices were determined to find the deviation from the nominal trim conditions in order to inspect for the highest non-linearity strength exist within the sub-region. the sub-region is determined by the flight envelope for a given flight condition.

A similar approach was performed on the three aerodynamic models but the results have shown that it is not suitable to be implemented on the numerical model such as the one built in Simulink. The reduced 4 by 4 matrix for the longitudinal flight was found to be dominated by the trim speed at the specific flight condition; does the changes of the trim speed itself are actually computed in the assessment of the non-linearity, not the deviation of the state matrix. Therefore, for such an application to be implemented, it is best to have an even distribution within the matrix elements so no bias in the matrix norm would be given.

A further investigation was conducted on the input excitation on the static and dynamics non-linearity of the models by considering three different shapes of input excitation with

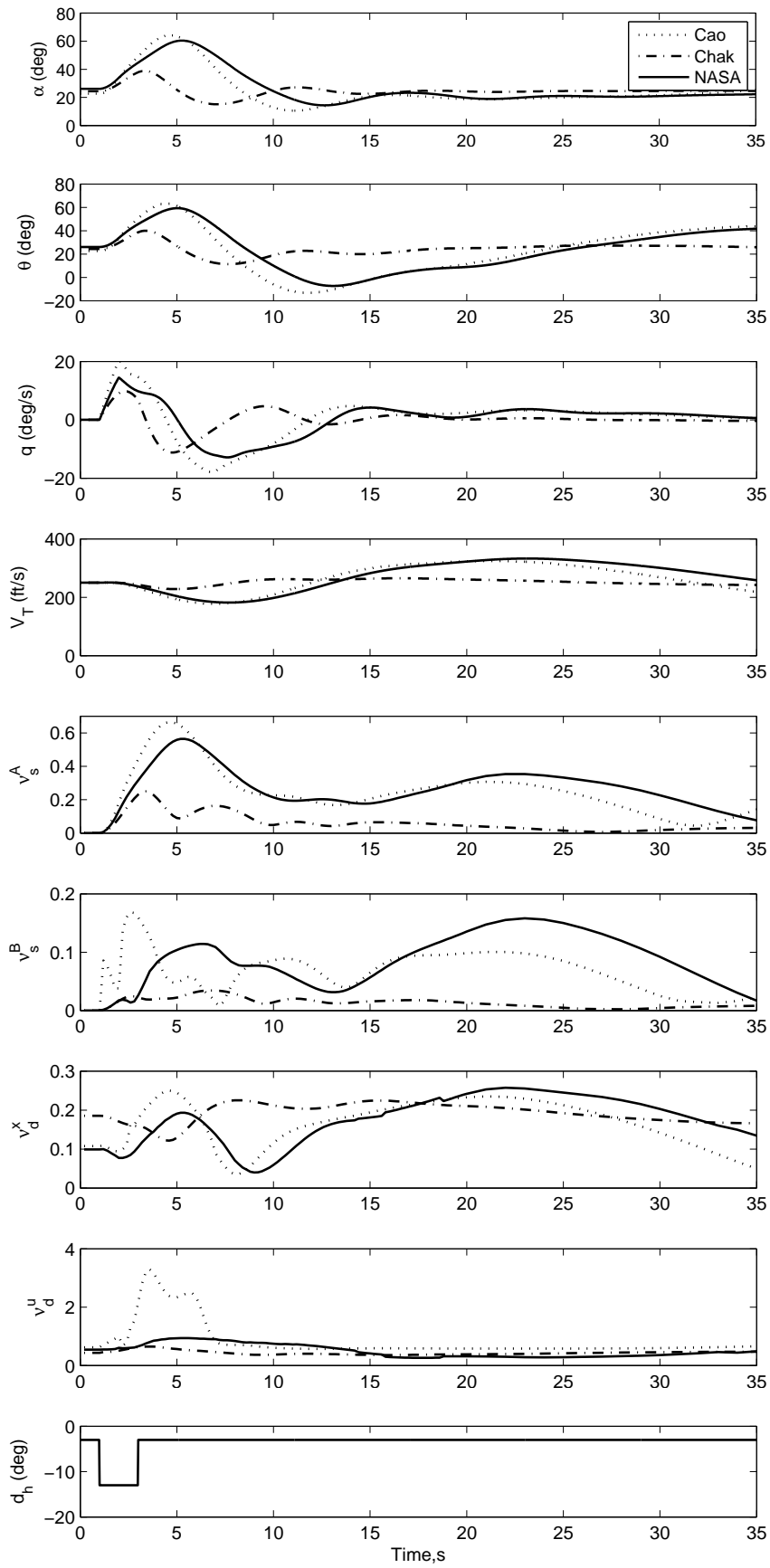


Figure 5.7: Simulation with time of the non-linearity index for input 1.

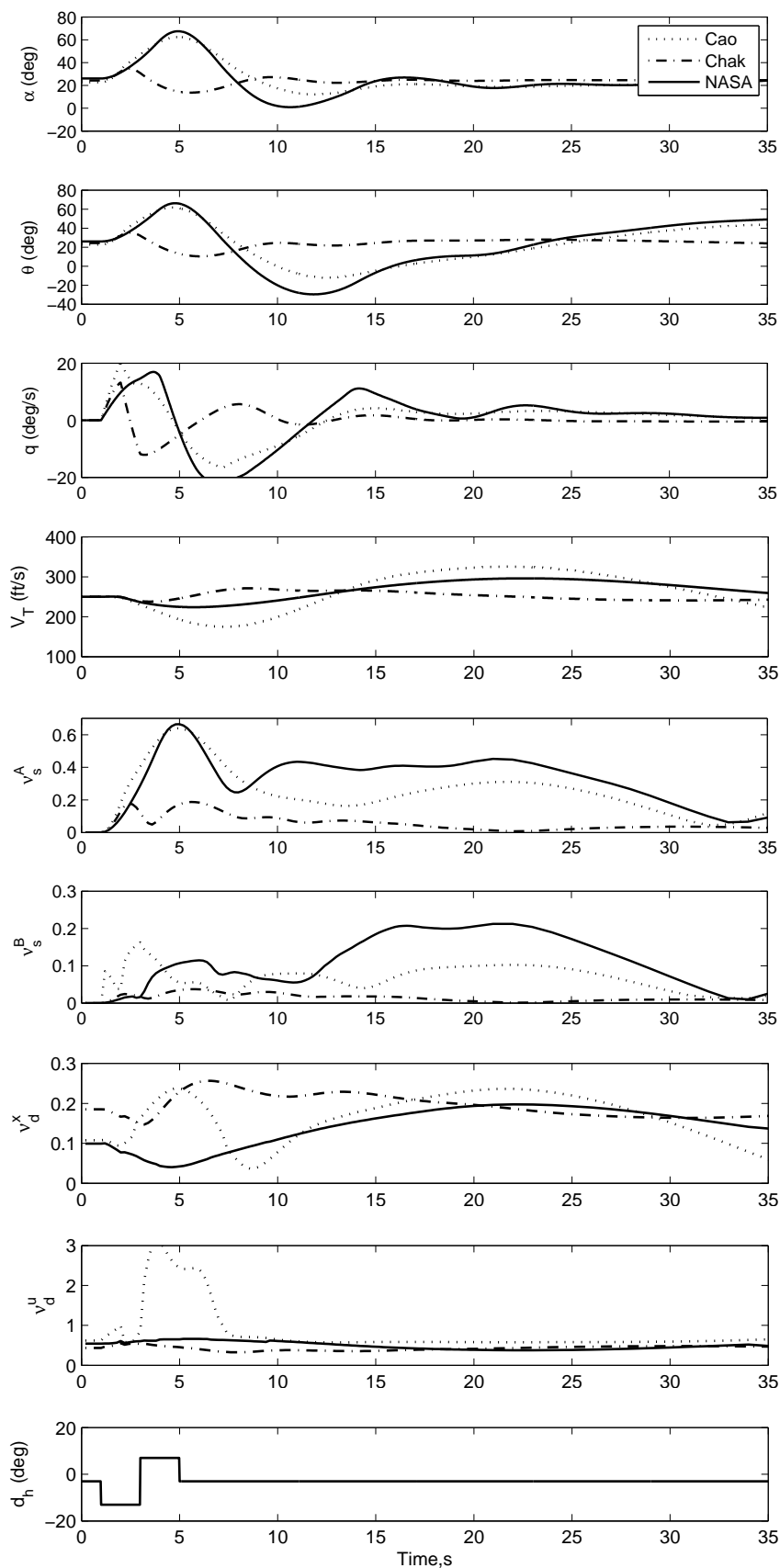


Figure 5.8: Simulation with time of the non-linearity index for input 2.

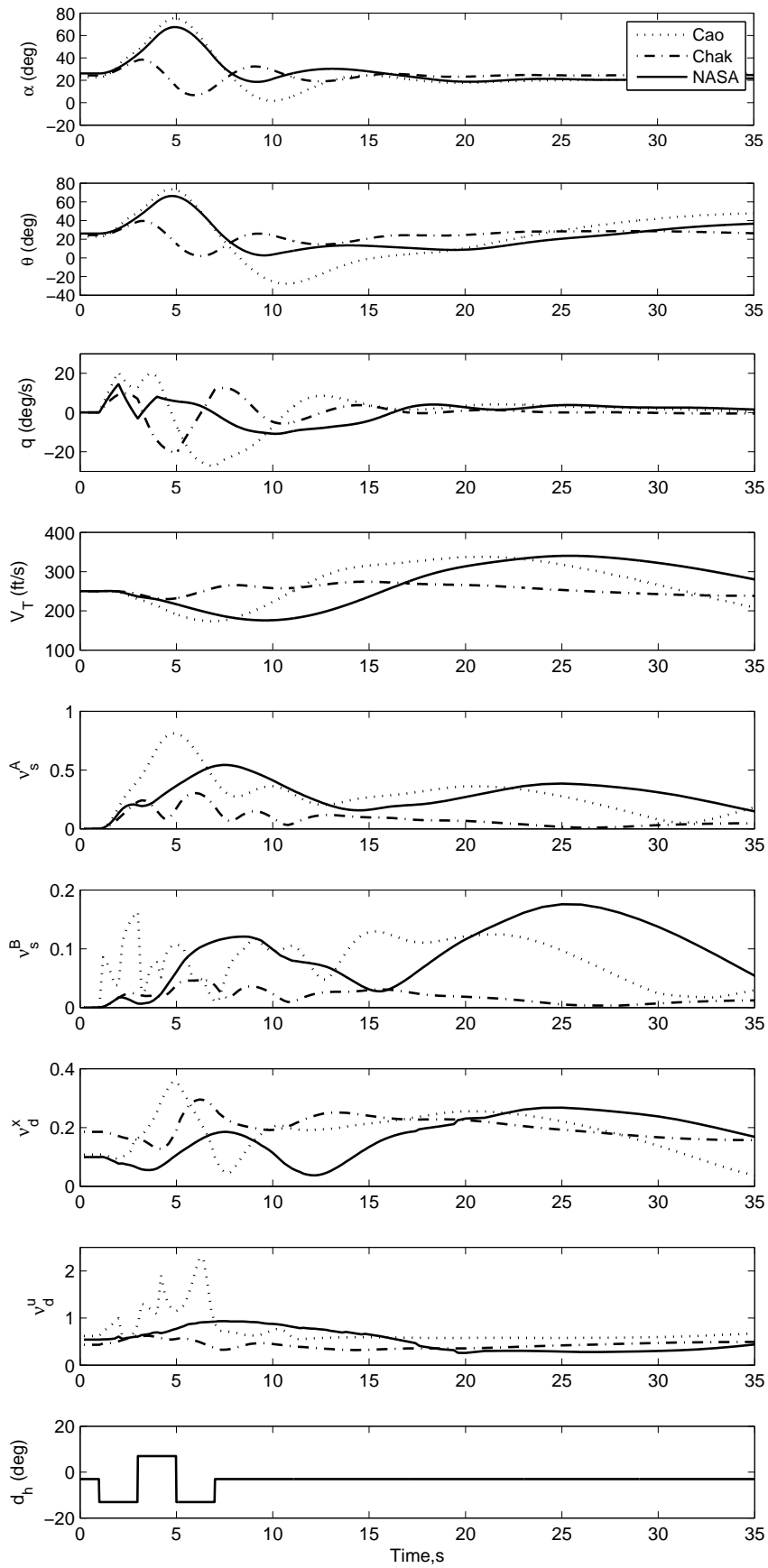


Figure 5.9: Simulation with time of the non-linearity index for input 3.

large perturbation tested on the model. Then, the non-linearity index was used to study their effects on the aerodynamic properties of the aircraft model. Basically, each model shows that all the state variables return to the initial position after a certain time once the input was perturbed regardless of the input shapes. Eigenvalues at this flight condition also indicating that the model is stable. In contrast, to the nonlinear simulations demonstrated in Chapter 4, the models showed significance responses to large perturbation as been excited into the models. The Chakraborty model shows less sensitive in response while the Cao model shows the most sensitive response to the perturbation though the NASA model shows similar response to the Cao model but with less magnitude.

The changes of the indices with time is seen due to the changes in behaviour as showed by the state variables which oscillated due to the perturbation induced into the models. It can be seen that at the early stage after the input disturbance, the indices were fluctuated in the same way as spotted from other state variables and sometimes the highest indices were recorded when AoA was reaching the peak. Based on the information given regarding the maximum non-linearity strength, each model has predicted different sources of non-linearity, which corresponded to the sudden change when it is traced to the aerodynamic models respectively.

A new approach such as non-linearity index however, can expose specific non-linearities, as evaluation of eigenvalues alone was incapable of revealing hidden nonlinear behaviour as expected. It has proven to be a systematic search technique for assessing non-linearity strength and to identify the source of the non-linearity. Although the first part of the chapter did not justify the analysis methodology, the second part has highlighted the different sources of the non-linearities that occurred for each aerodynamic model. At the time of completion of this thesis, this approach is thought to be acceptable, although future analysis should consider a new scheme or an alternative method.

This page is intentionally left blank.

# Chapter 6

## Conclusion

In this thesis, the effects of the differences in aerodynamic data collected from different aerodynamic models of a same aircraft, the F-18 HARV, is reported. This chapter summarizes the main findings and contributions of the thesis. Future research directions are also proposed in the final section of the chapter.

### 6.1 Summary

Three different aerodynamic models for the F-18 HARV, which were collected from literature available in the public domain, were presented. It was first intended to develop a comprehensive aircraft model that is suitable for high AoA application, and to pursue a control design for the aircraft at such condition together with the integration of thrust vectoring. However, direct access to the aircraft data was impossible, hence the effort to collect the available data from the public domain. Findings on the aerodynamic models for this aircraft vary from a simple model presented with several linearized matrices to a complex model formulated into indicial form. Some of the models were provided with both longitudinal and lateral-directional flights data, whilst some others only considered the longitudinal flight data. This is because longitudinal flight is an important criterion in achieving trim flight. The effects from flight parameters also might be varied from one aerodynamic model to another.

However, in this thesis the sources are narrow to three different aerodynamic models for the F-18 HARV. All three models were selected due to the comprehensive data they possessed. But they are basically differentiated by the methods of presenting the data, which by arc-tangent approximation function for the Cao model, polynomial function for the Chakraborty model, and LUT for the NASA model. While analysing the data from the Cao model, it was recognized that some of the published data from the formulation did not match the wind tunnel test data, as had been claimed. Thus modifications of affected formulations were performed to at least match the wind tunnel data. The differences in aerodynamic characteristics of the Cao, the Chakraborty and the NASA models were studied by comparing data from these models at various AoA. The Cao and the NASA models were found to closely share the aerodynamic properties though no information was provided concerning the origin of the NASA data.

A nonlinear six DoF Simulink model based on the F-18 HARV was developed to accommodate the three aerodynamic models separately. The trim conditions of the models

were obtained for different combinations of AoA and airspeed, and the models were linearized in each case. Then the eigenvalues were evaluated in order to investigate the longitudinal dynamics of each model. Poles of the eigenvalues were mapped to determine the trajectory of the eigenvalues as one of the flight parameters was varied, that being AoA. Numerical and analytical approaches were used to validate the eigenvalues but large differences were evident between them. It was suspected that this was due to the approximation of the concise derivative for pitch moment due to pitch rate,  $m_q$ , in the analytical expression which was derived directly from lift due to stabilator deflection,  $C_{L_{\delta_h}}$ . However, it is still not enough to explain why the Chakraborty model showed good approximation between both approaches which remained unanswered in this thesis. However, simpler polynomial models may be desirable for improved numerical performance and faster simulation as this does not require costly interpolation operations used in the LUT or arc-tangent evaluation at each flight condition.

A non-linearity index algorithm has been developed based on [46] and [54] to be applied to the numerical aircraft models built using MATLAB and Simulink. A range of flight envelope from low AoA to high AoA was tested based on the algorithm, but it was found that the state matrix was dominated by the trim speed,  $V_T$ . Thus, the uneven contributions of the state matrix in computing the matrix norm causes the index to indicate highest non-linearity at lower AoA. This is unfortunately not the case as it is expected that some non-linearity behaviour be detected at high AoA. However, this condition was not really portrayed when the index was computed for different shapes of input excitations. The highest non-linearity at least was detected at each peak of AoA as it changes with time, which links to different sources of non-linearity for each aerodynamic model. Interestingly, the Chakraborty model did not predict the same simulation as demonstrated by the Cao and the NASA models, but shows a more relaxed simulation after some disturbances were imposed to the Cao and the NASA models.

Last but not least, the significance of the differences in aerodynamic models were interpreted into the eigenvalue trajectories and the assessment of the non-linearity index of each model. Both methods showed variational results towards the characterization of the aerodynamic properties. Though the differences were obviously seen in the poles mapping, the time response however did not show a significant effect in the nonlinear simulation. The differences as reflected in the poles mapping may be due to the formulation type of aerodynamic models. While implementation of the non-linearity index on the different shapes, at least predicted different sources of non-linearity linked to each aerodynamic model. However, further exploration on the effect of nonlinear behaviour should be conducted.

## 6.2 Contributions to Knowledge

The contributions to knowledge which have comprised part of this thesis work are highlighted below:

- Compilation of different aerodynamic models of the F-18 HARV collected from open literature into one source which includes characterization of the differences in each model.
- Development of six DoF simulation models in Simulink for the F-18 HARV aircraft that couples the nonlinear equations of motion with the nonlinear aerodynamic and



engine performance for use in analysis. It requires minimal changes to accommodate the three aerodynamic models respectively.

- Modification to the aerodynamic model provided by Cao which some mismatches of the generated formulation were found after comparing them with the wind tunnel test results. All the curves were regenerated in Appendix B with the modification are highlighted with red fonts.
- Presentation of the properties differences on the selected aerodynamic models which highlights the properties of each model and accomplishment of detail on dynamic properties for the models analysis numerically and analytically by pole mapping.
- Assessment of non-linearity index based on the effects of different input shapes provide a new insight into the application of the theory.

### 6.3 Recommendations for Future Study

The following list summarizes the primary areas of concern which may be addressed for future work:

- Improve the trimming function at high AoA by implementing additional controller of thrust vectoring.
- The approximate expression for the dimensionless aerodynamic stability and control derivatives in Chapter 4 were taken from [89] which are derived from conventional aircraft. A new analytical expression for the derivatives of an all moving tailplane such as the F-18 HARV may be derived to see if it will affect the new trajectories for pole mapping.
- Extending the present work by implementing robust high AoA controller that has to cope with demonstrable model uncertainty.
- Adopting the bifurcation analysis in identifying the significant of the models' differences in predicting the results, so the robustness of the technique when faced with model differences and rapidly changing aerodynamic properties can be studied.
- Normalization of the state matrix for the assessment of the non-linearity so the effect of trim speed,  $V_T$ , can be negated so each element in the matrix would contribute evenly.

This page is intentionally left blank.

# References

- [1] D. Enns. Robustness of dynamic inversion vs mu synthesis- lateral-directional flight control example. In *AIAA Guidance, Navigation and Control Conference, Portland, OR*, number 3338, pages 210–222, 1990. doi: 10.2514/6.1990-3338.
- [2] S. A. Snell, D. F. Enns, and W. L. Arrard. Nonlinear inversion flight control for a supermaneuverable aircraft. *Journal of Guidance, Control, and Dynamics*, 15(4):976–984, 1992. doi: 10.2514/3.20932.
- [3] D. J. Bugajski and D. F. Enns. Nonlinear control law with application to high angle-of-attack flight. *Journal of Guidance, Control, and Dynamics*, 15(3):761–767, 1992. doi: 10.2514/3.20902.
- [4] Ö. Atesoglu and M. K. Özgören. Control and robustness analysis for a high  $\alpha$  maneuverable thrust vectoring fighter aircraft. *Journal of Guidance, Control, and Dynamics*, 32(5):1483–1496, September - October 2009. doi: 10.2514/1.42989.
- [5] R. M. Hall, D. W. Banks, D. F. Fisher, F. Ghaffari, D. G. Murri, J. C. Ross, and W. R. Lanser. A status report on high alpha technology program (HATP) ground test to flight comparisons. Technical Report N95-14230, NASA Ames Research Center, 1995.
- [6] A. H. Bowers, J. W. Pahle, R. J. Wilson, B. C. Flick, and R. L. Rood. An overview of the nasa f-18 high alpha research vehicle. Technical Report NASA TM 4772, National Aeronautics and Space Administration, Dryden Flight Research Center, California, October 1996.
- [7] S. Thomas. *Reconfiguration and Bifurcation in Flight Controls*. PhD thesis, Drexel University, 2004.
- [8] A. Chakraborty. Linear and nonlinear analysis of susceptibility of F/A-18 flight control laws to the falling leaf mode. Master’s thesis, University of Minnesota, 2010.
- [9] NASA. Nasa dryden fact sheet - F-18 high angle-of-attack (alpha) research vehicle. <http://www.nasa.gov/centers/dryden/news/FactSheets/FS-002-DFRC.html>. Last retrieved: 12 March 2013.
- [10] F. J. Lallman, J. B. Davidson, and P. C. Murphy. A method for integrating thrust-vectoring and actuated forebody strakes with conventional aerodynamic controls on a high-performance fighter airplane. Technical Report NASA/TP-1998-208464, NASA Langley Research Center, 1998.
- [11] J. D. Anderson. *Fundamentals of aerodynamics*. McGraw-Hill, 1991. ISBN: 0071254080.

- [12] Anon. Volume II. flying qualities flight testing phase. chapter 10: High angle of attack. Technical report, DTIC Document, May 1991. Last retrieved on February 2013.
- [13] H. Ashley. On the Feasibility of Low - Speed Aircraft Maneuvers Involving Extreme Angles of Attack. *Journal of Fluids and Structures*, 1:319 – 335, 1987.
- [14] B. Dickinson. *Aircraft Stability and Control for Pilots and Engineers*. Sir Isaac Pitman & Sons Ltd, Kingsway, London, 1968. SBN: 273 43910 3.
- [15] R. F. Stengel. *Flight Dynamics*. Princeton University Press, Princeton, New Jersey, 2004. ISBN 0-691-11407-2.
- [16] C. A. Martin. Flight behaviour of highly manoeuvrable aircraft. In *The Australian Aeronautical Conference*, 1989.
- [17] W. H. Mason. High angle of attack aerodynamics. Course Note: AOE 4124, Aerospace and Ocean Engineering, Virginia Tech, 2010.
- [18] N. K. Sinha and N. Ananthkrishnan. *Elementary Flight Dynamics with an Introduction to Bifurcation and Continuation Methods*. CRC Press, 2013. ISBN 9781439886021.
- [19] M. H. Lowernberg. Bifurcation methods - a practical methodology for implementation by flight dynamicists. In *Proceedings of International Council of the Aeronautical Sciences (ICAS)*, 1990.
- [20] F. B. J. Macmillen and J. M. T. Thompson. Bifurcation analysis in the flight dynamics design process? a view from the aircraft industry. *Philosophical Transactions of the Royal Society of London. Series A: Mathematical, Physical and Engineering Sciences*, 356(1745):2321 – 2333, 1998. A theme compile in J. M. T. Thompson and F. B. J. Macmillen., Nonlinear flight dynamics of high-performance aircraft, doi: 10.1098/rsta.1998.0276.
- [21] J. V. Carroll and R. K. Mehra. Bifurcation analysis of nonlinear aircraft dynamics. *Journal of Guidance, Control and Dynamics*, 5(5):529–536, 1982. doi: 10.2514/3.56198.
- [22] G. I. Zagaynov and M. G. Goman. Bifurcation analysis of critical aircraft flight regimes. In *Proceedings of International Council of the Aeronautical Sciences (ICAS)*, 1984.
- [23] C. C. Jahnke and F. E. C. Culick. Application of bifurcation theory to the high-angle-of-attack dynamics of the F-14. *Journal of Aircraft*, 31(1):26 – 34, 1994. doi: 10.2514/3.46451.
- [24] N. Ananthkrishnan, N. K. Gupta, and N. K. Sinha. Computational bifurcation analysis of multiparameter dynamical systems. *Journal of Guidance, Control and Dynamics*, 32(5):1651–1653, 2009. doi: 10.2514/1.44173.
- [25] N. Ananthkrishnan and N. K. Sinha. Level flight trim and stability analysis using extended bifurcation and continuation procedure. *Journal of Guidance, Control and Dynamics*, 24(6):1225–1228, 2001. doi: 10.2514/3.22620.
- [26] P. Wang and Z. Shi. Study of deep-stall characteristics and longitudinal special phenomena of t-tail aircraft. In *International Conference on Mechatronics and Automation (ICMA)*, pages 59–64. IEEE, 2010. doi: 10.1109/ICMA.2010.5588718.

- [27] D. C. Liaw and C. C. Song. Analysis of longitudinal flight dynamics: A bifurcation - theoretic approach. *Journal of Guidance, Control and Dynamics*, 24(1):109 – 116, Jan-Feb 2001. doi: 10.2514/2.4682.
- [28] P. Guicheteau. Bifurcation theory: A tool for nonlinear flight dynamics. *Philosophical Transactions of the Royal Society of London. Series A:Mathematical, Physical and Engineering Sciences*, 356(1745):2181–2201, 1998. A theme compile in J. M. T. Thompson and F. B. J. Macmillen., Nonlinear flight dynamics of high-performance aircraft, doi: 10.1098/rsta.1998.0269.
- [29] C. C. Jahnke and F. E. C. Cullick. Application of dynamical system theory to nonlinear aircraft dynamics. In *AIAA Atmospheric Flight Conference*, 1988.
- [30] P. A. Cummings. Continuation methods for qualitative analysis of aircraft dynamics. Technical Report NASA/CR-2004-213035, National Institutes of Aerospace, Hampton, Virginia, July 2004.
- [31] K. S. Sibilski and R. Roziecki. The continuation design framework for nonlinear aircraft control. In *Collection of Technical Papers - 44th AIAA Aerospace Sciences Meeting*, number AIAA 2006-426, Reno, Nevada, 2006. doi: 10.2514/6.2006-426.
- [32] A. Paranjape, N. K. Sinha, and N. Ananthkrishnan. Use of bifurcation and continuation methods for aircraft trim and stability analysis—a state-of-the-art. *Journal of Aerospace Sciences and Technologies*, 60(2):85, 2008.
- [33] M. G. Goman and A. V. Khrantsovsky. Application of continuation and bifurcation methods to the design of control systems. *Philosophical Transactions of the Royal Society of London. Series A: Mathematical, Physical and Engineering Sciences*, 356(1745):2277–2295, 1998. A theme compile in J. M. T. Thompson and F. B. J. Macmillen., Nonlinear flight dynamics of high-performance aircraft, doi: 10.1098/rsta.1998.0274.
- [34] M. A. Savi. Chaos and order in biomedical rhythms. *Journal of the Brazilian Society of Mechanical Sciences and Engineering*, 27(2):157–169, 2005. doi.org/10.1590/S1678-58782005000200008.
- [35] P. K. Raghavendra, T. Sahai, P. A. Kumar, M. Chauhan, and N. Ananthkrishnan. Aircraft spin recovery, with and without thrust vectoring, using nonlinear dynamic inversion. *Journal of Aircraft*, 42(6):1492–1503, 2005. doi: 10.2514/1.12252.
- [36] S. Thomas, H. G. Kwatny, and Bor-Chin Chang. Bifurcation-induced limits of a controller-reconfigured f-16 subject to actuator failures. In *Proceedings of 2005 IEEE Conference on Control Applications*, pages 165 –170, Toronto, Ohio, Aug. 2005. IEEE. doi: 10.1109/CCA.2005.1507119.
- [37] B.S. Liebst. The dynamics, prediction, and control of wing rock in high-performance aircraft. *Philosophical Transactions of the Royal Society of London. Series A:Mathematical, Physical and Engineering Sciences*, 356(1745):2257–2276, 1998. A theme compile in J. M. T. Thompson and F. B. J. Macmillen., Nonlinear flight dynamics of high-performance aircraft, doi: 10.1098/rsta.1998.0274.
- [38] S. J. Pauck and J. A. A. Engelbrecht. Bifurcation analysis of the generic transport model with a view to upset recovery. In *AIAA Atmospheric Flight Mechanics Conference*, number AIAA-2012-4646, Minneapolis, Minnesota, 2012. doi: 10.2514/6.2012-4646.

- [39] S. J. Gill, M. H. Lowenberg, Simon A. Neild, B. Krauskopf, G. Puyou, and E. Coetsee. Upset dynamics of an airliner model: a nonlinear bifurcation analysis. *Journal of Aircraft*, 50(6):1832 – 1842, 2013. doi: 10.2514/1.C032221.
- [40] D Wang. Algebraic analysis of stability and bifurcation for nonlinear flight dynamics. *Aeronautical Journal*, 115(1168):345 – 349, June 2011.
- [41] Z. Shi and L. Fan. Bifurcation analysis of polynomial models for longitudinal motion at high angle of attack. *Chinese Journal of Aeronautics*, 26(1):151 – 160, 2013. doi: 10.1016/j.cja.2012.12.019.
- [42] E. Doedel. *AUTO 07 Software for Continuation and Bifurcation Problems in Ordinary Differential Equations*, 2007.
- [43] A. Dhooge, W. Govaerts, and Y.A. Kuznetsov. MATCONT: A MATLAB package for numerical bifurcation analysis of ODEs. *ACM Transactions on Mathematical Software (TOMS)*, 29(2):141–164, 2003.
- [44] E. Coetsee, P. Thota, and R. Rankin. Dynamical system toolbox. <https://github.com/ecoetsee/Dynamical-Systems-Toolbox>. Last retrieved: 23 April 2013.
- [45] H. Stalford, W. T. Baumann, F. J.E. Garret, and T. L. Herman. Accurate modelling of nonlinear system using volterra series submodels. In *Proceedings of the 6th American Control Conference*, volume 2, pages 886 –891. IEEE, July 1987.
- [46] A. Omran and B. Newman. Piecewise global volterra nonlinear modeling and characterization for aircraft dynamics. *Journal of Guidance, Control, and Dynamics*, 32(3):749–759, May - June 2009. doi: 10.2514/1.40655.
- [47] E. N. Abdulwahab and C. Hongquan. Characterization of state variables in post-stall dynamics of high performance aircraft. *Proceedings of the Institution of Mechanical Engineers, Part G: Journal of Aerospace Engineering*, 222(3):369 – 378, March 2008. doi: 10.1243/09544100JAERO277.
- [48] E. N. Abdulwahab and C. Hongquan. Periodic motion suppression based on control of wing rock in aircraft lateral dynamics. *Aerospace Science and Technology*, 12(4):295 – 301, June 2008. doi: 10.1016/j.ast.2007.07.003.
- [49] A. Maqsood and T. H. Go. Multiple time scale analysis of aircraft longitudinal dynamics with aerodynamic vectoring. *Nonlinear Dynamics*, 69(3):731–742, August 2012. doi: 10.1007/s11071-011-0300-3.
- [50] H. Yoshida, M. Kiomai, and K. Yana. An index of system nonlinearity and its estimation. In *Proceedings of 1993 International Conference on Neural Networks*, volume 2, pages 2021 – 2024. IEEE, 1993. doi: 10.1109/IJCNN.1993.717055.
- [51] J. L. Junkins. Adventure on the interface of dynamics and control. *Journal of Guidance, Control and Dynamics*, 20(6):1058–1071, 1997. doi: 10.2514/2.4176.
- [52] J. L. Junkins and P. Singla. How nonlinear is it? a tutorial on nonlinearity of orbit and attitude dynamics. *The Journal of the Astronautical Sciences*, 52(1 & 2):7–60, 2004.
- [53] A. Omran and B. Newman. Nonlinearity index theory for aircraft dynamic assessment. *Journal of Guidance, Control and Dynamics*, 36(1):293–303, 2012. doi: 10.2514/1.53906.

- [54] D. P. Tapolcai, A. Omran, and B. Newman. Aircraft stall phenomenon analysis using nonlinearity index theory. In *AIAA Atmospheric Flight Mechanics Conference*, AIAA 2012-4403, August 2012 2012.
- [55] D. P. Tapolcai, A. Omran, and B. Newman. Aircraft spin phenomenon analysis using nonlinearity index theory. In *AIAA Atmospheric Flight Mechanics Conference*, AIAA 2012-4401, August 2012 2012.
- [56] A. Abdallah, B. Newman, and A. Omran. Measuring aircraft nonlinearity across aerodynamic attitude flight envelope. In *AIAA Atmospheric Flight Mechanics Conference*, number AIAA 2013-4985, August 2013. doi: 10.2514/6.2013-4985.
- [57] D. J. Diston. Modelling and simulation. *Encyclopedia of Aerospace Engineering*, 2010. doi: 10.1002/9780470686652.eae479.
- [58] J. R. Chambers and S. B. Grafton. Aerodynamic characteristics of airplanes at high angles of attack. Technical Report NASA TM 74097, Langley Research Center, Virginia, 1977.
- [59] J. F. Whidborne and A. K. Cooke. *Course Notes: Air Vehicle Modelling and Simulation*. Cranfield University, January 2010.
- [60] M. Sadraey and R. Colgren. UAV flight simulation: credibility of linear decoupled vs. nonlinear coupled equations of motion. In *AIAA Modeling and Simulation Technologies Conference and Exhibit*, number AIAA-2005-6425, San Francisco, California, 2005. doi: 10.2514/6.2005-6425.
- [61] S Zhongke and F Li. Bifurcation analysis of polynomial model for longitudinal motion at high angles of attack. *Chinese Journal of Aeronautics*, 26(1):151–160, 2013. doi: 10.1016/j.cja.2012.12.019.
- [62] U. Ozdemir and M. S. Kavsoglu. Linear and nonlinear simulations of aircraft dynamics using body axis system. *Aircraft Engineering and Aerospace Technology*, 80(6):638 – 648, 2008. doi: 10.1108/00022660810911581.
- [63] K. E. Boyum, M. Pachter, and C. H. Houppis. High angle of attack velocity vector rolls. *Control Engineering Practice*, 3(8):1087 – 1093, August 1995. doi: 10.1016/0967-0661(95)00101-Y.
- [64] J. Kalviste. Use of rotary balance and forced oscillation test data in a six degrees of freedom simulation. In *AIAA Atmospheric Flight Mechanics Conference*, number AIAA-82-1364, San Diego, California, 1982. doi: 10.2514/6.1982-1364.
- [65] M. R. Napolitano, A. C. Paris, and B. A. Seanor. Estimation of the longitudinal aerodynamic parameters from flight data for the NASA F/A-18 HARV. In *AIAA Atmospheric Flight Mechanics Conference*, number AIAA-96-3419 in -CP, pages 469–478, 1996. doi: 10.2514/6.1996-3419.
- [66] M. R. Napolitano, A. C. Paris, B. A. Seanor, and A. H. Bowers. Estimation of the lateral-directional aerodynamic parameters from flight data for the NASA F/A-18 HARV. In *AIAA Atmospheric Flight Mechanics Conference*, number AIAA-96-3420 in CP, pages 479–489, July 1996. doi: 10.2514/6.1996-3420.
- [67] J. M. Brandon and J. V. Foster. Recent dynamic measurements and considerations for aerodynamic modeling of fighter airplane configurations. *AIAA Paper*, pages 98–4447, 1998.

- [68] J. M. Brandon. Dynamical effects and application to high performance aircraft. Technical Report AGARD Report No. 776, April 1991.
- [69] G. Leng. Reduced-order nonlinear analysis of aircraft dynamics. *Journal of Guidance, Control and Dynamics*, 18(2):361–364, March - April 1995. doi: 10.2514/3.21392.
- [70] E. A. Morelli. Global nonlinear aerodynamic modelling using multivariate orthogonal functions. *Journal of Aircraft*, 32(2):270 – 277, March - April 1995. doi: 10.2514/3.46712.
- [71] P. D. Bruce and M. G. Kellett. Modelling and identification of non-linear aerodynamic functions using b-splines. *Proceedings of the Institution of Mechanical Engineers, Part G: Journal of Aerospace Engineering*, 214(1):27 – 40, January 2000. doi: 10.1243/0954410001531890.
- [72] G. Leng. Compression of aircraft aerodynamic database using multivariable Chebyshev polynomials. *Advances in Engineering Software*, 28(2):133 – 141, March 1997. doi: 10.1016/S0965-9978(96)00043-9.
- [73] A. Chakraborty, P. Seiler, and G.J. Balas. Susceptibility of F/A-18 flight controllers to the falling-leaf mode: Linear analysis. *Journal of Guidance, Control and Dynamics*, 34(1):57–72, 2011. doi: 10.2514/1.50674.
- [74] J. Cao, F. J. Garret, E. Hoffman, and H. Stalford. Analytical aerodynamic model of high alpha research vehicle wind tunnel model. Technical Report NASA CR 187469, Georgia Institute of Technology, Atlanta, Georgia, September 1990.
- [75] A. Chakraborty, P. Seiler, and G.J. Balas. Susceptibility of F/A-18 flight controllers to the falling-leaf mode: Nonlinear analysis. *Journal of Guidance, Control and Dynamics*, 34(1):73–85, 2011. doi: 10.2514/1.50675.
- [76] Anon. F/A-18 stability and control data report, vol i: Low angle of attack. Technical Report MDC A7247, McDonnell Aircraft Company, August 1981.
- [77] C. Butrill, P. Arbuckle, and K. Hoffer. Simulation model of a twin-tail, high performance airplane. Technical Report NASA TM 107601, Langley Research Center, Hampton, Virginia, 1992.
- [78] K. W. Iliff and K. S. C. Wang. Extraction of lateral-directional stability and control derivatives for the basic F-18 aircraft at high angles of attack. Technical Report NASA TM 4786, National Aeronautics and Space Administration, 1997.
- [79] B. R. Carter. Time-optimization of high performance combat maneuvers. Master’s thesis, Naval Postgraduate School, Monterey, California, 2005.
- [80] Anon. F/A-18 stability and control data report, vol ii: High angle of attack. Technical Report MDC A7247, McDonnell Aircraft Company, August 1981.
- [81] S. Cho and K. Cho. Nonlinear adaptive control for high angle of attack flight. *Journal of Mechanical Science and Technology*, 9:147–155, 1995. doi: 10.1007/BF02953616.
- [82] P. Granasy, P. G. Thomasson, C. B. Srensen, and E. Mosekilde. Nonlinear flight dynamics at high angles-of-attack. *Aeronautical Journal*, 102(1016):337 – 343, 1998.
- [83] B. L. Stevens and F. L. Lewis. *Aircraft Control and Simulation*. John Wiley & Sons, Inc., 2003. ISBN 0-471-37145-9.



- [84] NASA. Documentation for a dynamic inversion control law proposed for rfc. <http://www.nasa.gov/centers/dryden/history/pastprojects/HARV/Work/NASA2/nasa2.html>. Last retrieved: February 2013.
- [85] K. Ghosh, A. Paranjape, and N. Ananthkrishnan. Effect of thrust vectoring on aircraft post-stall trims, stability, and maneuvers. In *AIAA Atmospheric Flight Mechanics Conference and Exhibit*, number AIAA - 2006 - 6486, 2006. doi: 10.2514/6.2006-6486.
- [86] M. G. Goman and E. N. Khramtsovsky, A. V. and Kolesnikov. Evaluation of aircraft performance and maneuverability by computation of attainable equilibrium sets. *Journal of Guidance, Control and Dynamics*, Vol. 31(2):329 – 339, 2008. doi: 10.2514/1.29336.
- [87] V. Klein and E. A. Morelli. *Aircraft System Identification Theory and Practice*. AIAA Education Series, Blacksburg, Virginia, 2006. ISBN 1-56347-832-3.
- [88] K. J. Orlik-Ruckemann. Aerodynamic aspects of aircraft dynamics at high angle of attack. In *AIAA 9th Atmospheric Flight Conference*, number AIAA-82-1363, Ontario, Canada, 1982. National Aeronautical Establishment. doi: 10.2514/6.1982-1363.
- [89] M. V. Cook. *Flight dynamics principles: a linear systems approach to aircraft stability and control*. Butterworth-Heinemann, Oxford, UK, 2007. ISBN: 978-0-08-098242-7.
- [90] J. M. Cooke. NPSNET: Flight simulation dynamic modeling using quaternions. Master’s thesis, Naval Postgraduate School, 1992.
- [91] R.C. Nelson. *Flight stability and automatic control*. McGraw-Hill New York, Singapore, 1998. ISBN 0-07-046273-9.
- [92] H. Mizuta, M. Jibu, and K. Yana. Adaptive estimation of the degree of system nonlinearity. In *Adaptive Systems for Signal Processing, Communications and Control Symposium*, pages 352 – 356, Lake Louise, Alta, 2000. IEEE. doi: 10.1109/ASSPCC.2000.882499.
- [93] L.T. Nguyen, M.E. Ogburn, W.P. Gilbert, K.S. Kibler, P.W. Brown, and P.L. Deal. Simulator study of stall/post-stall characteristics of a fighter airplane with relaxed longitudinal static stability. Technical Report NASA -TP-1538, NASA, 1979.
- [94] E. J. Cornelisse. Six degrees of freedom simulation of the F-16 fighter aircraft in MATLAB Simulink. Master’s thesis, Cranfield University, 2005.
- [95] J. D. Mattingly, W. H. Heiser, and D. T. Pratt. *Aircraft Engine Design*. AIAA Education Series, Reston, Virginia, 1987. ISBN 1-56347-538-3.
- [96] McDonnell Douglas F/A-18 Hornet. [http://en.wikipedia.org/wiki/F/A-18\\_Hornet](http://en.wikipedia.org/wiki/F/A-18_Hornet). Last retrieved: July 2013.
- [97] M. D. Messina, M. E. Strickland, K. D. Hoffler, S. W. Carzoo, W. T. Bundick, J. C. Yeager, and F. L. Beissner Jr. Simulation model of the F/A-18 high angle of attack research vehicle utilized for the design of advanced control laws. Technical Report NASA TM-110216, National Aeronautics and Space Administration (NASA), Langley Research Center, May 1996.

This page is intentionally left blank.

# Appendix A

## Mathematical Model Development

A model for the analysis of the nonlinear motion of an aircraft at high angles of attack is presented. Objectives of this section is to review all the necessary theoretical background in developing the mathematical model of the aircraft and to present list of equations used to describe the components used to obtain the state and control matrix of the aircraft.

### A.1 Generalized Nonlinear Model of Aircraft

For a given aircraft, the dynamics can be represented by:

$$\dot{x}(t) = f(x(t), u(t)) \quad (\text{A.1})$$

where, the state vector  $x$  is given by

$$x(t) = [U \ V \ W \ h \ P \ Q \ R \ \Phi \ \Theta \ \Psi]^T \quad (\text{A.2})$$

and the control input,  $u$  is given by

$$u(t) = [\delta_h \ \delta_a \ \delta_r \ \tau]^T \quad (\text{A.3})$$

$x$  and  $u$  denote the state matrix and control vector while  $f$  denotes the nonlinear functions from the analytic expressions. The full state vector for the six degree-of-freedom (DOF) is obtained by determining forces and moments from the aerodynamics characteristics and thrust elements, and then incorporated with the kinematics equations. This was achieved by using body axes frame assuming that the aircraft is a rigid body and symmetric with origin at the center of mass. Full development can be found in [89].

### Force Equations

From the Newton's Law, the force equations are determined from the summation of all forces acting on the aircraft in which during the flight usually consist of aerodynamic (i.e.  $X_{aero}, Y_{aero}, Z_{aero}$ ), thrust (i.e.  $X_{th}, Y_{th}, Z_{th}$ ) and gravitational forces.

$$\dot{u} = \frac{1}{m} [X_{aero} + X_{th} - mg \sin \Theta] + RV - QW \quad (\text{A.4})$$

$$\dot{v} = \frac{1}{m} [Y_{aero} + Y_{th} + mg \cos \Theta \sin \Phi] + PW - RU \quad (\text{A.5})$$

$$\dot{w} = \frac{1}{m}[Z_{aero} + Z_{th} + mg \cos \Theta \cos \Phi] + QU - PV \quad (\text{A.6})$$

The above equations can be transformed in terms of wind axes variables  $V$ ,  $\alpha$ , and  $\beta$ . These variables have a direct relationship to the aerodynamic forces and moments and are more convenient in studying dynamic behaviour.

$$V_0 = \sqrt{u^2 + v^2 + w^2} \quad (\text{A.7})$$

$$\alpha = \tan^{-1}(w/u) \quad (\text{A.8})$$

$$\beta = \sin^{-1}(v/V) \quad (\text{A.9})$$

By differentiating the above equations on both sides, and using Eq. A.4 to A.6, thus, we can write the derivatives of  $V$ ,  $\beta$ , and  $\alpha$  as;

$$\begin{aligned} \dot{V} &= \frac{1}{m} \{ [X_{aero} + X_{th}] \cos \alpha \cos \beta + [Y_{aero} + Y_{th}] \sin \beta + [Z_{aero} + Z_{th}] \sin \alpha \cos \beta \} \\ &\quad + g_0 (\cos \theta \cos \phi \sin \alpha \cos \beta + \cos \theta \sin \phi \sin \beta - \sin \theta \cos \alpha \cos \beta) \end{aligned} \quad (\text{A.10})$$

$$\begin{aligned} \dot{\beta} &= \frac{1}{mV} \{ -[X_{aero} + X_{th}] \cos \alpha \sin \beta + [Y_{aero} + Y_{th}] \cos \beta - [Z_{aero} + Z_{th}] \sin \alpha \sin \beta \} \\ &\quad + \frac{g_0}{V_0} (\cos \theta \cos \phi \sin \alpha \sin \beta + \cos \theta \sin \phi \cos \beta - \sin \theta \cos \alpha \sin \beta) + p \sin \alpha \\ &\quad - r \cos \alpha \end{aligned} \quad (\text{A.11})$$

$$\begin{aligned} \dot{\alpha} &= \frac{1}{mV \cos \beta} \{ -[X_{aero} + X_{th}] \sin \alpha + [Z_{aero} + Z_{th}] \cos \alpha \} - \tan \beta (p \cos \alpha + r \sin \alpha) \\ &\quad + \frac{g_0}{V_0 \cos \beta} (\cos \theta \cos \phi \cos \alpha - \sin \theta \sin \alpha) + q \end{aligned} \quad (\text{A.12})$$

## Moment Equations

Assuming the gravity field is uniform, thus there is no gravity moment acting on the aircraft but only the aerodynamic (i.e.  $L_{aero}$ ,  $M_{aero}$ ,  $N_{aero}$ ) and thrust (i.e.  $L_{th}$ ,  $M_{th}$ ,  $N_{th}$ ) moments.

$$\dot{p} = \frac{I_z}{I_D} [(l_{aero} + l_{th}) + I_{xz}pq + (I_y - I_z)qr] + \frac{I_{xz}}{I_D} [(n_{aero} + n_{th}) - I_{xz}qr + (I_x - I_y)pq] \quad (\text{A.13})$$

$$\dot{q} = \frac{1}{I_y} [(m_{aero} + m_{th}) - (I_x - I_z)pr - I_{xz}(p^2 - r^2)] \quad (\text{A.14})$$

$$\dot{r} = \frac{I_{xz}}{I_D} [(l_{aero} + l_{th}) + I_{xz}pq + (I_y - I_z)qr] + \frac{I_{xx}}{I_D} [(n_{aero} + n_{th}) - I_{xz}qr + (I_x - I_y)pq] \quad (\text{A.15})$$

where  $I_D = I_x I_z - I_x^2$ . Similarly, the external moments are considered from both aerodynamics ( $L_{aero}$ ,  $M_{aero}$ ,  $N_{aero}$ ) and thrust ( $L_{th}$ ,  $M_{th}$ ,  $N_{th}$ ) elements which details can be found in Section A.2 and A.3.

## Kinematic Equations

The orientation of the aircraft with respect to earth can be defined from the Euler's angle determination which is given as follows;

$$\dot{\phi} = p + q \sin \phi \tan \theta + r \cos \phi \tan \theta \quad (\text{A.16})$$

$$\dot{\theta} = q \cos \phi - r \sin \phi \quad (\text{A.17})$$

$$\dot{\psi} = q \sin \phi \sec \theta + r \cos \phi \sec \theta \quad (\text{A.18})$$

## Quaternion Transformation

For high  $\alpha$  simulation purposes, the quaternion transformation is considered in avoiding the singularities when the angles reached  $90^\circ$ . Therefore, the quaternion transformation is used rather than direct determination of the Euler's angles from the kinematic relation. The quaternion variables are given as follows;

$$\begin{bmatrix} \dot{e}_0 \\ \dot{e}_1 \\ \dot{e}_2 \\ \dot{e}_3 \end{bmatrix} = \frac{1}{2} \begin{bmatrix} 0 & -p & -q & -r \\ p & 0 & r & -q \\ q & -r & 0 & p \\ r & q & -p & 0 \end{bmatrix} \begin{bmatrix} e_0 \\ e_1 \\ e_2 \\ e_3 \end{bmatrix} \quad (\text{A.19})$$

The initial value for each quaternion variables are defined as;

$$\begin{aligned} e_0 &= \cos \frac{\psi}{2} \cos \frac{\theta}{2} \cos \frac{\phi}{2} + \sin \frac{\psi}{2} \sin \frac{\theta}{2} \sin \frac{\phi}{2} \\ e_1 &= \cos \frac{\psi}{2} \cos \frac{\theta}{2} \sin \frac{\phi}{2} - \sin \frac{\psi}{2} \sin \frac{\theta}{2} \cos \frac{\phi}{2} \\ e_2 &= \cos \frac{\psi}{2} \sin \frac{\theta}{2} \cos \frac{\phi}{2} + \sin \frac{\psi}{2} \cos \frac{\theta}{2} \sin \frac{\phi}{2} \\ e_3 &= \sin \frac{\psi}{2} \cos \frac{\theta}{2} \cos \frac{\phi}{2} - \cos \frac{\psi}{2} \sin \frac{\theta}{2} \sin \frac{\phi}{2} \end{aligned} \quad (\text{A.20})$$

## Navigation Equations

The navigation equations are used in determining the position of the aircraft with respect to earth axes (i.e. x-axis pointing north, y-axis pointing east, and z-axis pointing down). They are described as the change of aircraft position with respect to time. Thus, the  $\dot{x}$ ,  $\dot{y}$  and  $\dot{z}$  can be defined by applying the axis transformation to the velocity components of the aircraft which are defined in the body axes. The axis transformation from earth axes to body axes can be performed by applying the direction cosine matrix which is given as:

$$DCM = \begin{bmatrix} \cos \theta \cos \psi & \cos \theta \sin \psi & -\sin \theta \\ \sin \phi \sin \theta \cos \psi - \cos \phi \sin \psi & \sin \phi \sin \theta \sin \psi + \cos \phi \cos \psi & \sin \phi \cos \theta \\ \cos \phi \sin \theta \cos \psi + \sin \phi \sin \psi & \cos \phi \sin \theta \sin \psi - \sin \phi \cos \psi & \cos \phi \cos \theta \end{bmatrix} \quad (\text{A.21})$$

Whereas the transformation from body axes to earth axes is performed by using the inverse of the matrix of Equation A.21;

$$V_e = DCM^{-1}V_b \quad (\text{A.22})$$

which the results are given as follows;

$$\begin{bmatrix} \dot{x} \\ \dot{y} \\ \dot{h} \end{bmatrix} = \begin{bmatrix} u \cos \psi \cos \theta + v(\cos \psi \sin \theta \sin \phi - \sin \psi \cos \phi) + w(\cos \psi \sin \theta \cos \phi + \sin \psi \sin \theta) \\ u \sin \psi \cos \theta + v(\sin \psi \sin \theta \sin \phi + \cos \psi \cos \phi) + w(\sin \psi \sin \theta \sin \phi - \cos \psi \sin \theta) \\ u \sin \theta - v \sin \phi \cos \theta - w \cos \phi \cos \theta \end{bmatrix} \quad (\text{A.23})$$

Here the notation for  $\dot{h}$  is much preferable than the  $\dot{z}$  in order to present the altitude. However, the emphasize is put on the  $\dot{h}$  since the aerodynamic model for the Cao model depended on the altitude.

## A.2 Aerodynamic Modeling

The aerodynamic model calculates the nondimensional force and moment coefficients, which are then used to calculate the total forces and moments. The details of the aerodynamic models used in the thesis for the F-18 HARV were based from different models which are given in Chapter 3. Three aerodynamic models were obtained from different sources, with each model was presented by arc-tangent function, polynomial function and look up tables (LUT). The models depend on the aerodynamics angles ( $\alpha$  and  $\beta$ ), angular rates ( $p$ ,  $q$ , and  $r$ ), and control surfaces deflections ( $\delta_h$ ,  $\delta_h$ , and  $\delta_h$ ).

The aerodynamic forces consist of axial force ( $X_{aero}$ ), sideforce ( $Y_{aero}$ ), and normal force ( $Z_{aero}$ ), in which the lift and drag force are resolved into  $x$  and  $z$  axes which modelled as:

$$\begin{bmatrix} X_{aero} \\ Y_{aero} \\ Z_{aero} \end{bmatrix} = \begin{bmatrix} \bar{q}SC_L \sin \alpha - \bar{q}SC_D \cos \alpha \\ \bar{q}SC_Y \\ -\bar{q}SC_L \cos \alpha - \bar{q}SC_D \sin \alpha \end{bmatrix} \quad (\text{A.24})$$

The aerodynamic moments are described by the pitching moment, ( $M_{aero}$ ), rolling moment ( $L_{aero}$ ), and yawing moment, ( $N_{aero}$ ). Similarly, the moments due to aerodynamic forces are detained as:

$$\begin{bmatrix} L_{aero} \\ M_{aero} \\ N_{aero} \end{bmatrix} = \begin{bmatrix} \bar{q}SbC_l + (l_y Z_{aero} - l_z Y_{aero}) \\ \bar{q}S\bar{c}C_m + (l_z X_{aero} - l_x Z_{aero}) \\ \bar{q}SbC_n + (l_x Y_{aero} - l_y X_{aero}) \end{bmatrix} \quad (\text{A.25})$$

## A.3 Thrust Modeling

The modified engines for the NASA F-18 HARV are fitted with 3 paddle vanes to provide additional pitch and yaw moments during high  $\alpha$  maneuvering. To model the vectoring thrust, a constant thrust value is determined from a simple model that is controlled by a throttle setting and deviated by the vanes' paddle deflection angle which provide the pitch vectoring angle,  $\theta_{TV}$  and yaw vectoring angle,  $\psi_{TV}$ .

The constant thrust is estimated from available thrust provided by engine model, F404-GE-400, whereas the dynamics of the engines were adopted from the F16 model as described in [93] and [94]. However, the application of the model has been slightly modified to match the HARV's engine performance. Since the aircraft is fitted with two after-burning turbofan engines, the same model is used for both engines with modification in the thrust magnitude. Due to lacking of information data for the specified engine type,

instead of using a table look up to determine the thrust available at a specific flight condition, a simple thrust lapse relation is assumed to match the installed thrust by considering the effect of density changing, as given by [95];

$$T = aT_{SL} \quad (\text{A.26})$$

For a low bypass ratio turbofan engine,  $a$  will be depending on the Mach number, altitude and the operating condition of the afterburner in which when it is operating is referred as  $max$  whereas when it is not is referred as  $mil$ . The estimated value for both operating conditions are respectively given by following relations;

$$a_{mil} = 0.72[0.88 + 0.245(|M - 0.6|)^{1.4}]\sigma^{0.7} \quad (\text{A.27})$$

$$a_{max} = [0.94 + 0.38(M - 0.4)^2]\sigma^{0.7} \quad (\text{A.28})$$

For the F404-GE-400 type of engine, it is given that at sea level, the thrust without afterburner,  $T_{SL_{mil}}$ , is 11000 lbf, and with afterburner,  $T_{SL_{max}}$ , is 17750 lbf [96]. By applying Eq.A.26 and Eq.A.27, the variation of the thrusts according to the afterburner operation can be estimated which then illustrated in Figure A.1.

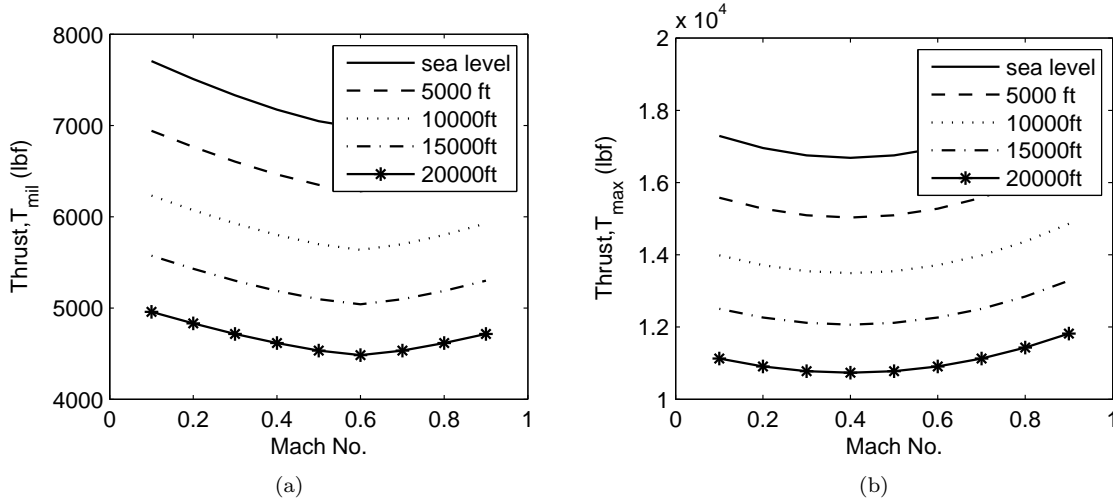


Figure A.1: Variation of the thrust with Mach no. and altitude (a) Without afterburner and (b) With afterburner

The amount of thrust is controlled by the position of the throttle travel,  $\tau$ . Using the similar function of throttle command gearing as depicted in [93], at a given throttle position, traveling from 0 to 1, the commanded power is computed from the following:

$$P_a = \begin{cases} 64.94\tau & \text{if } \tau \leq 0.77 \\ 217.38\tau - 117.38 & \text{if } \tau > 0.77 \end{cases} \quad (\text{A.29})$$

Thus, for each engine, the total thrust response to the throttle and afterburner effect is estimated using the modified Eq.A.30 which the original relation is given in [93] to match the  $max$  and  $mil$  thrust available for the engine type. Figure A.2 illustrated the example of the total thrust calculated at altitude of 15000 ft and Mach number of 0.6 when the throttle level is changed.

$$T_{total} = \begin{cases} T_{mil} + (T_{max} - T_{mil})((P_a - 62)/38) & \text{if } P_a < 62 \\ T_{mil}(P_a/62) & \text{if } P_a \geq 62 \end{cases} \quad (\text{A.30})$$

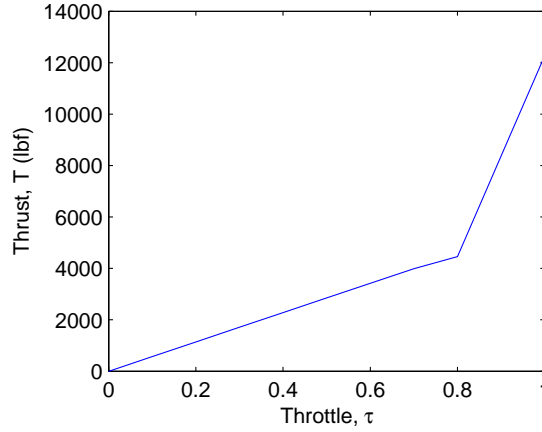


Figure A.2: Example of thrust response as a function of throttle setting with account to the afterburner effect.

Once the total thrust available by the engines are known, the magnitude of the vectoring thrust forces component provided by the left and right engines can be calculated by considering the engine orientation illustrated in Figure A.3(a). The engine's canted angle,  $\delta$ , is given  $1.98^\circ$  from the center line of the aircraft. The vectoring angles configuration of the are determined based on the configuration illustrated in Figure A.3.

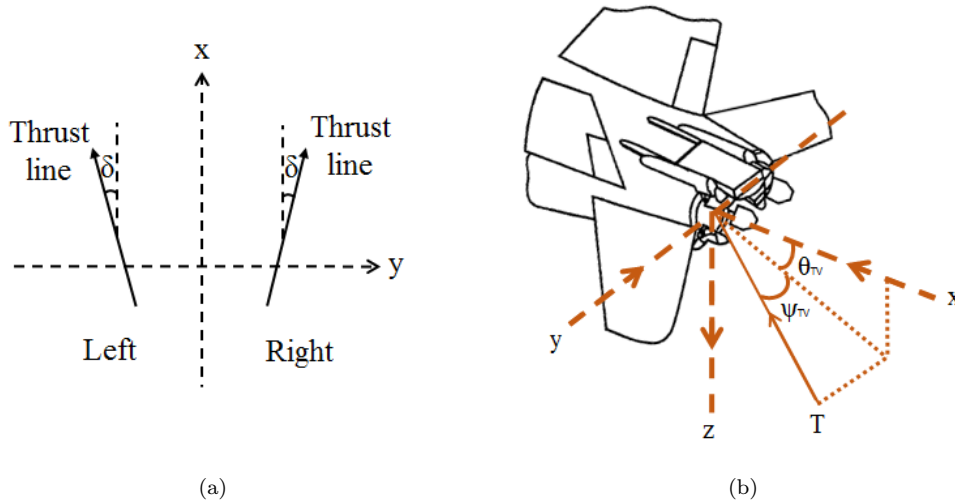


Figure A.3: Thrust line and orientation.

$$\begin{bmatrix} X_{th} \\ Y_{th} \\ Z_{th} \end{bmatrix} = \begin{bmatrix} T_L \cos \theta_{TV} \cos \psi_{TV} \cos -1.98^\circ + T_R \cos \theta_{TV} \cos \psi_{TV} \cos 1.98^\circ \\ T_L \sin \psi_{TV} \sin -1.98^\circ + T_R \sin \psi_{TV} \sin 1.98^\circ \\ -T_L \sin \theta_{TV} \cos \psi_{TV} - T_R \sin \theta_{TV} \cos \psi_{TV} \end{bmatrix} \quad (\text{A.31})$$

The determination of the resultant thrust deviation angles of pitch,  $\theta_{TV}$ , and yaw,  $\psi_{TV}$ , are based on the jet turning envelope for the HARV as shown in Figure A.4 from the three deflected vanes, taken from [4]. The thrust vectoring vanes are modeled as devices capable of deflecting the thrust within a  $30^\circ$ . In mathematical term, the vectoring angles



are simplified as:

$$\begin{bmatrix} \theta_{TV} \\ \psi_{TV} \end{bmatrix} = \begin{bmatrix} -(30/30) & (1/2)(30/30) & (1/2)(30/30) \\ 0 & (20/30) & -(20/30) \end{bmatrix} \begin{bmatrix} \delta_1 \\ \delta_2 \\ \delta_3 \end{bmatrix} \quad (\text{A.32})$$

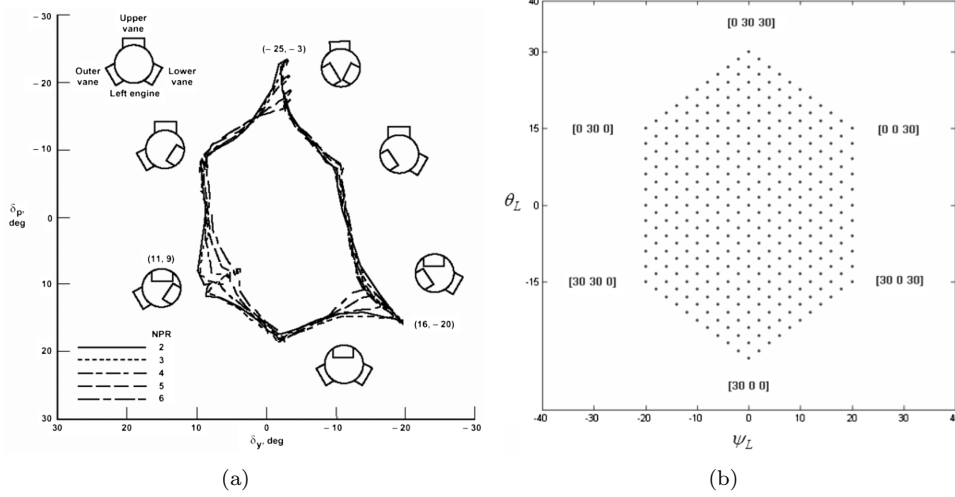


Figure A.4: (a) Maximum jet turning envelope for HARV and (b) Jet turning model for the study extracted from [4].

The induced thrust moments then can be calculated from the thrust forces knowing the moment arm of each components to the center of gravity of the aircraft respectively:

$$\begin{bmatrix} L_{th} \\ M_{th} \\ N_{th} \end{bmatrix} = \begin{bmatrix} l_{ye}Z_{th} - l_{ze}Y_{th} \\ l_{ze}X_{th} - l_{xe}Z_{th} \\ l_{xe}Y_{th} - l_{ye}X_{th} \end{bmatrix} \quad (\text{A.33})$$

## A.4 Actuator Dynamics

The actuator dynamics though has not been included in the analysis of this thesis, could be included where necessary in the model. The delayed input signal from the actuator can have a significant effect on the simulation. Thus, actuator modeling has been taken into consideration by including a simple second order including the rate limit and position limit of each controller. These data was determined directly from [97] and presented in Table A.1. However, the positive value for position limit given for aileron is not the same since the data as provided by Cao is valid up to  $25^\circ$  only whereas the actual value is given at  $45^\circ$ .

## A.5 Nonlinear Simulink Model of F-18 HARV

In summary, taking into consideration for the whole aircraft, a revised nonlinear model for F-18 HARV can be rewritten by following:

$$\mathbf{x}(t) = [U \ V \ W \ h \ P \ Q \ R \ \Phi \ \Theta \ \Psi]^T \quad (\text{A.34})$$

Table A.1: F18 HARV control surface position and rate limits [6].

Actuator	Position Limits (deg)	Rate Limits (deg/s)	Transfer Function
Aileron	+25, -25	$\pm 100$	$\frac{75^2}{s^2 + 2(0.59)(75)s + 75^2}$
Stabilator	+10.5, -24	$\pm 40$	$\frac{30.74^2}{s^2 + 2(0.509)(30.74)s + 30.74^2}$
Rudder	$\pm 30$	$\pm 82$	$\frac{72.1^2}{s^2 + 2(0.59)(72.1)s + 72.1^2}$

and the control input,  $u$  is given by

$$\mathbf{u}(t) = [\delta_h \ \delta_a \ \delta_r \ \tau \ \delta_1 \ \delta_2 \ \delta_3]^T \tag{A.35}$$

followed by the output vector;

$$\mathbf{y}(t) = [V_T \ \beta \ \gamma \ h]^T \tag{A.36}$$

where  $\delta_1, \delta_2, \delta_3$  are the additional controller from the engine paddle if the vectored thrust is considered. Therefore in case the vectoring effect is neglected, the values should be replaced by 0.

The open-loop SIMULINK model is shown in Figure A.5. The primary use for this model is for further analysis in the coming chapters as to establish a trim point and linear model for selected flight conditions and evaluate the open-loop aircraft responses to initial conditions, control inputs, or disturbances.

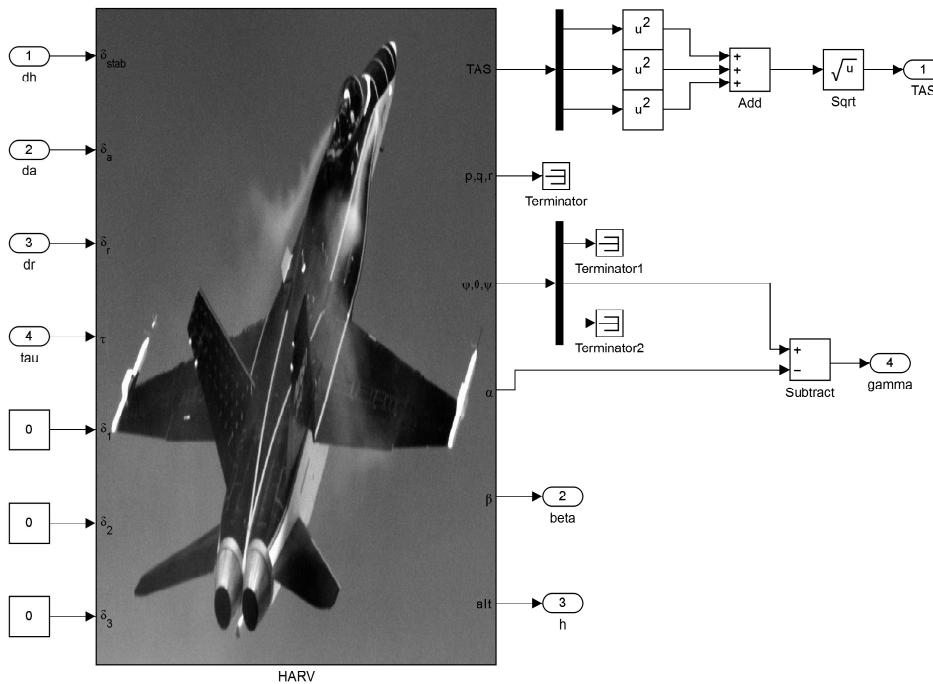


Figure A.5: Open loop simulink model of HARV.

# Appendix B

## F-18 HARV Aerodynamic Data

### B.1 Cao Aerodynamic Data

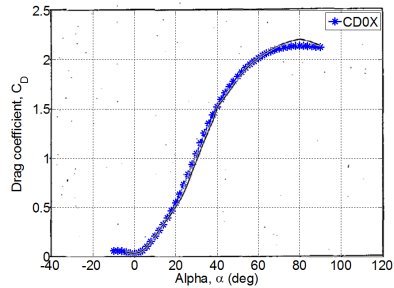
#### Analytical Formulation for Drag Coefficients

The drag coefficients,  $C_D$ , as presented in Cao's report only consider for the flight condition at  $M = 0.6$  and  $h = 15000ft$ . The variations of the drag coefficients are depending on the deflection angles of the stabilator at  $\delta_h = 10.5^\circ, 0^\circ, -5^\circ$  and  $-24^\circ$  as tabulated in Table B.1. The  $10.5^\circ$  and  $-24^\circ$  are taken at the extreme deflections of the stabilator. The notations of each drag can be referred to Table B.1.

Table B.1: Drag coefficients,  $C_D$ , notation.

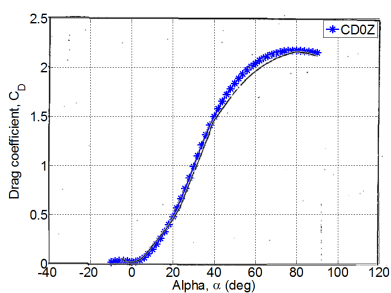
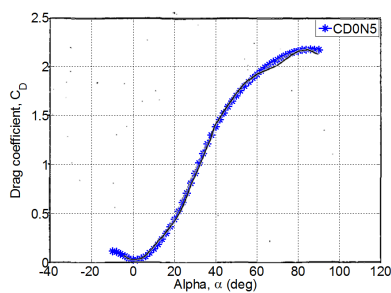
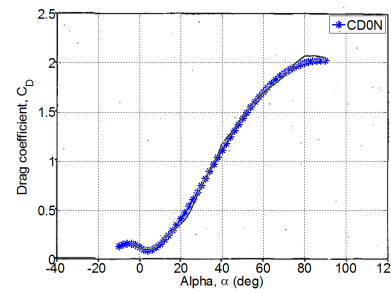
$\delta_h$ ( $^\circ$ )	$C_D$
10.5	CD0X
0	CD0Z
-5	CD0N5
-24	CD0N

Table B.2: Compared formulation from Cao's report: Drag Coefficients.

Curve	Formulation
	$  \begin{aligned}  CD0X = & (.4/2.75) \arctan(((78/80)\alpha + 7)/30) + \dots \\  & (.6/2.75) \arctan(-((78/80)\alpha + 2)/8) + \dots \\  & (-.3/2.75) \arctan(-((78/80)\alpha + 5)/90) + \dots \\  & (-.2/2.75) \arctan(-((78/80)\alpha - 6)/5) + \dots \\  & (1.95/2.75) \arctan(((78/80)\alpha - 28)/15) + \dots \\  & (2.2/2.75) \arctan(((78/80)\alpha - 58)/40) + \dots \\  & (1.4/2.75) \arctan(-((78/80)\alpha - 73)/30) + \dots \\  & (2.3/2.75) \arctan(-((78/80)\alpha - 138)/20) - 0.147  \end{aligned}  $

*Continued on next page*

Table B.2 – Continued from previous page

Curve	Formulation
	$CD0Z = (2.17/2.10) * ((.6/2.75) \arctan(((77/80)\alpha + 6)/30) + \dots$ $(.6/2.75) \arctan(-((77/80)\alpha + 1)/8) + \dots$ $(-.3/2.75) \arctan(-((77/80)\alpha + 4)/90) + \dots$ $(-.2/2.75) \arctan(-((77/80)\alpha - 7)/10) + \dots$ $(1.95/2.75) \arctan(((77/80)\alpha - 29)/15) + \dots$ $(2.2/2.75) \arctan(((77/80)\alpha - 59)/40) + \dots$ $(1.55/2.75) \arctan(-((77/80)\alpha - 74)/30) + \dots$ $(2.3/2.75) \arctan(-((77/80)\alpha - 139)/20) - .2837) + .0199$
	$CD0N5 = (.32/2.75) \arctan(((80/85)\alpha + 8)/30) + \dots$ $(.6/2.75) \arctan(-((80/85)\alpha + 3.5)/6.5) + \dots$ $(-.3/2.75) \arctan(-((80/85)\alpha + 7)/90) + \dots$ $(-.2/2.75) \arctan(-((80/85)\alpha - 4)/15) + \dots$ $(1.95/2.75) \arctan(((80/85)\alpha - 28)/15) + \dots$ $(2.25/2.75) \arctan(((80/85)\alpha - 68)/40) + \dots$ $(1.664/2.75) \arctan(-((80/85)\alpha - 90)/30) + \dots$ $(2.35/2.75) \arctan(-((80/85)\alpha - 140)/20) - 0.246$
	$CD0N = (.5/2.75) \arctan((\alpha + 5)/30) + \dots$ $(.6/2.75) \arctan(-(\alpha - 0)/6) + \dots$ $(-.25/2.75) \arctan(-(\alpha + 3)/90) + \dots$ $(-.15/2.75) \arctan(-(\alpha - 4)/40) + \dots$ $(1.85/2.75) \arctan((\alpha - 30)/28) + \dots$ $(2.3/2.75) \arctan((\alpha - 60)/40) + \dots$ $(1.15/2.75) \arctan(-(\alpha - 85)/30) + \dots$ $(2.3/2.75) \arctan(-(\alpha - 140)/20) - 0.2425$

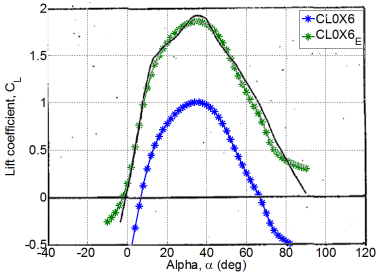
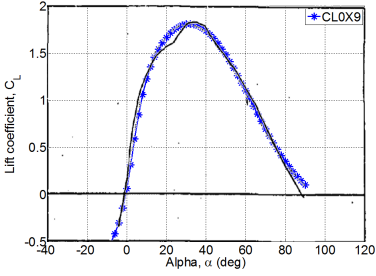
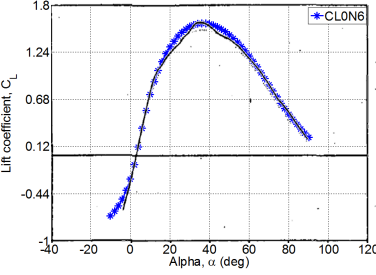
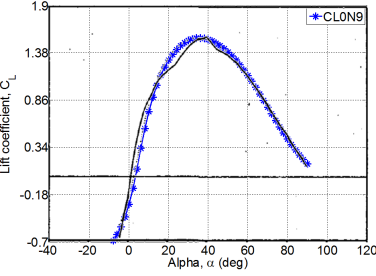
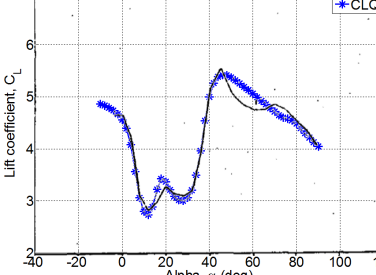
### Analytical Formulation for Lift Coefficients

The formulations for lift coefficients,  $C_L$ , were given at the extreme deflection angles of  $\delta_h$ , with varying M at 0.6 and 0.9 as given in Table B.3. The effect of pitch rate, q, is given as CLQ. However, there is an additional effect of the unsteady aerodynamics due to time rate of change of angle of attack,  $\dot{\alpha}$ , given in the formulations which is notated as CLAD. The reproduced curves were tabulated in Table B.4 for comparison.

Table B.3: Lift coefficients,  $C_{L0}$ , notation.

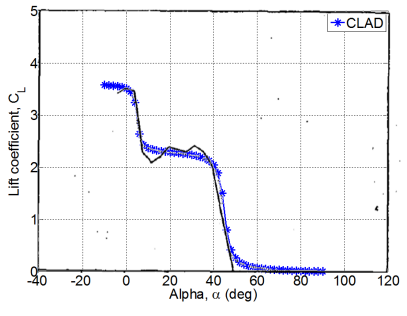
$\delta_h$ (°)	M	
	0.6	0.9
10.5	CL0N6	CL0N9
-24.0	CL0X6	CL0N9

Table B.4: Compared formulation from Cao's report: Lift Coefficients.

Curve	Formulation
	$CL0X6 = (.86/2.75) \arctan(-(\alpha + 5)/100) + \dots$ $(2.19/2.75) \arctan((\alpha - 5)/7) + \dots$ $(.9/2.75) \arctan((\alpha - 24)/17) + \dots$ $(1.71/2.75) \arctan(-(\alpha - 53)2/25) + \dots$ $(.41/2.75) \arctan(-(\alpha - 70)2/7) - .95$ $CL0X6_E = (.86/2.75) \arctan(-(\alpha + 5)/100) + \dots$ $(2.19/2.75) \arctan((\alpha - 5)/7) + \dots$ $(.9/2.75) \arctan((\alpha - 24)/17) + \dots$ $(1.71/2.75) \arctan(-(\alpha - 53)2/25) + \dots$ $(.41/2.75) \arctan(-(\alpha - 70)2/7) - .095$
	$CL0X9 = (.86/2.75) \arctan(-(\alpha + 5)/100) + \dots$ $(2.59/2.75) \arctan((\alpha - 3)/7) + \dots$ $(1.6/2.75) \arctan((\alpha - 20)/22) + \dots$ $(3.41/2.75) \arctan(-(\alpha - 57)/30) + \dots$ $(0.41/2.75) \arctan(-(\alpha - 70)/20) - .65$
	$CL0N6 = (1.06/2.75) \arctan(-(\alpha + 5)/100) + \dots$ $(1.79/2.75) \arctan((\alpha - 5)/7) + \dots$ $(2.5/2.75) \arctan((\alpha - 15)/22) + \dots$ $(2.71/2.75) \arctan(-(\alpha - 59)/50) + \dots$ $(1.21/2.75) \arctan(-(\alpha - 70)/20) - .72$
	$CL0N9 = (1.06/2.75) \arctan(-(\alpha + 5)/100) + \dots$ $(1.79/2.75) \arctan((\alpha - 5)/7) + \dots$ $(2.5/2.75) \arctan((\alpha - 13)/22) + \dots$ $(2.71/2.75) \arctan(-(\alpha - 59)/50) + \dots$ $(1.21/2.75) \arctan(-(\alpha - 70)/20) - .80$
	$CLQ = (.262/2.75) \arctan(-(\alpha - 5)/10) + \dots$ $(-2.39/2.75) \arctan((\alpha - 6)/3) + \dots$ $(2.4/2.75) \arctan((\alpha - 15.5)/3) + \dots$ $(2.0/2.75) \arctan(-(\alpha - 20)/5) + \dots$ $(4.3/2.75) \arctan((\alpha - 37)/4.5) + \dots$ $(2.2/2.75) \arctan(-(\alpha - 45)/15) + \dots$ $(2.2/2.75) \arctan(-(\alpha - 80)/15) + \dots$ $(-.45/2.75) \arctan(-(\alpha - 76)/3.5) + 4.2$

Continued on next page

Table B.4 – Continued from previous page

Curve	Formulation
	$CLAD = (1.32/\pi) \arctan(-(\alpha - 5) * 5 * \pi/18) + \dots$ $(-.75) \arctan((\alpha - 45)/2) + 1.8$

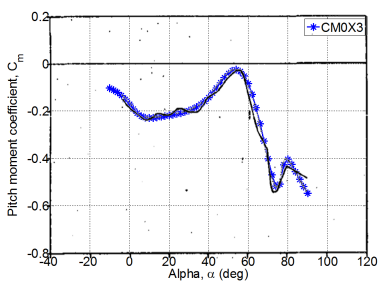
### Analytical Formulation for Pitch Moment Coefficients

As for the pitch moment coefficients,  $C_m$ , the formulations were given at various  $\delta_h$ , corresponding to M ranging from 0.3 to 0.9. The notation of the effects on  $\delta_h$  and M are given in Table B.5. It was notified that some formulations for the M = 0.3 exhibited similar wind tunnel pattern for M = 0.6 at  $\delta_h = -5.0^\circ, 0^\circ, 2^\circ$  and  $5^\circ$ . Thus, they used same the formulation in approximating the wind tunnel distributions for both M at the specified  $\delta_h$ . Likewise the lift coefficients model, the pitch moment coefficients also include the effect of the unsteady aerodynamics due to  $\dot{\alpha}$ , in its mathematical structure which is given as CMAD. While the effect of pitch rate is given as CMQ notation. All the curves are then compared with the original curves as shown in Table B.6.

Table B.5: Notation used for the pitch moment coefficients,  $C_{M_0}$ .

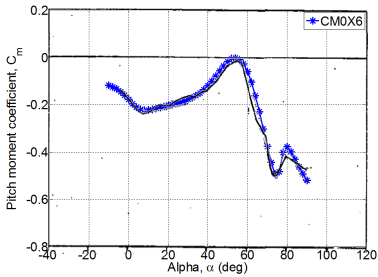
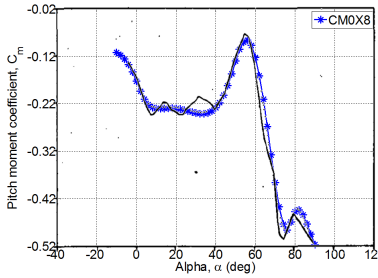
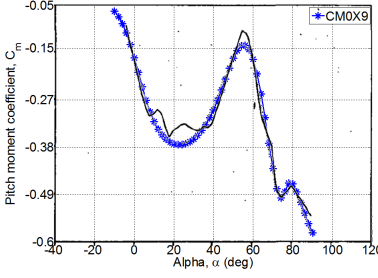
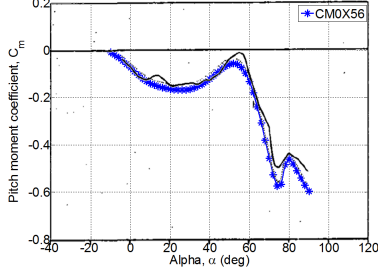
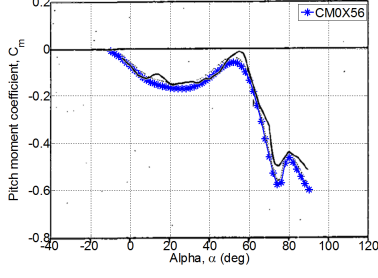
M	$\delta_h$ ( $^\circ$ )						
	-24.0	-12.5	-5.0	0.0	2.0	5.0	10.5
0.3	CM0N3	CM0NZ3	CM0N56	CM006	CM0X26	CM0X56	CM0X3
0.6	CM0N6	CM0Z6	CM0N56	CM006	CM0X26	CM0X56	CM0X6
0.8	CM0N8	CM0NZ8	CM0N58	CM0X08	CM0X28	CM0X58	CM0X8
0.9	CM0N9	CM0NZ9	CM0N59	CM0X09	<b>CM0X29</b>	CM0X59	CM0X9

Table B.6: Compared formulation from Cao’s Report: Pitching Moment.

Curve	Formulation
	$CM0X3 = (.26/2.75) \arctan(-(\alpha - 5)/10) + \dots$ $(-.39/2.75) \arctan((\alpha - 1)/8) + \dots$ $(.75/2.75) \arctan((\alpha - 5)/13) + \dots$ $(.7/2.75) \arctan(-(\alpha - 10)/65) + \dots$ $(1.2/2.75) \arctan((\alpha - 49)/15) + \dots$ $(2.1/2.75) \arctan(-(\alpha - 69)/15) + \dots$ $(-.45/2.75) \arctan(-(\alpha - 77)/2) - .398$

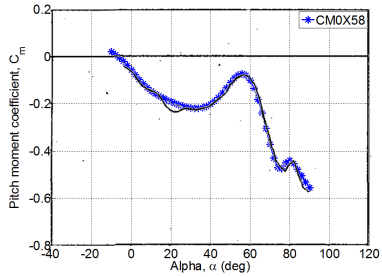
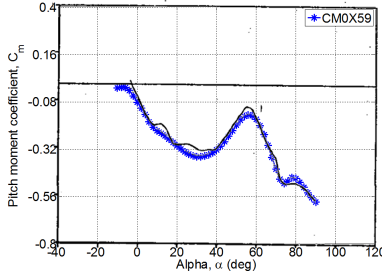
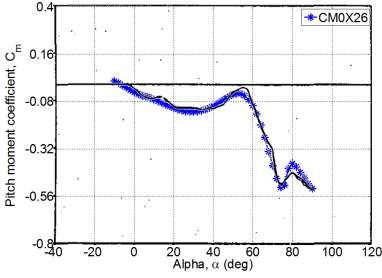
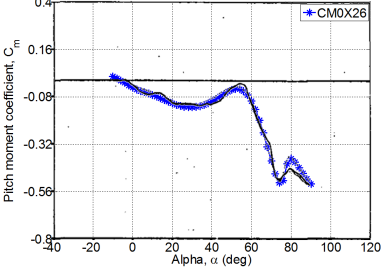
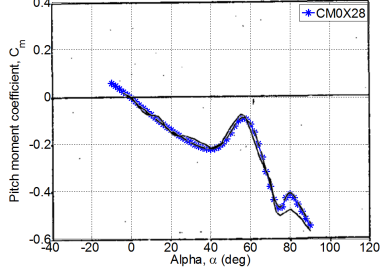
Continued on next page

Table B.6 – Continued from previous page

Curve	Formulation
	$  \begin{aligned}  CM0X6 = & (.26/2.75) \arctan(-(\alpha - 5)/10) + \dots \\  & (-.39/2.75) \arctan((\alpha - 1)/8) + \dots \\  & (.8/2.75) \arctan((\alpha - 5)/13) + \dots \\  & (.7/2.75) \arctan(-(\alpha - 10)/65) + \dots \\  & (1.2/2.75) \arctan((\alpha - 49)/15) + \dots \\  & (2.1/2.75) \arctan(-(\alpha - 69)/15) + \dots \\  & (-.45/2.75) \arctan(-(\alpha - 77)/2) - .398  \end{aligned}  $
	$  \begin{aligned}  CM0X8 = & (.26/2.75) \arctan(-(\alpha - 5)/15) + \dots \\  & (-.33/2.75) \arctan((\alpha - 1)/7) + \dots \\  & (.72/2.75) \arctan((\alpha - 5)/15) + \dots \\  & (.7/2.75) \arctan(-(\alpha - 35)/75) + \dots \\  & (1.13/2.75) \arctan((\alpha - 51)/11) + \dots \\  & (2.08/2.75) \arctan(-(\alpha - 67)/17) + \dots \\  & (-.45/2.75) \arctan(-(\alpha - 78)/4) - .44  \end{aligned}  $
	$  \begin{aligned}  CM0X9 = & (.26/2.75) \arctan(-(\alpha - 5)/10) + \dots \\  & (-.39/2.75) \arctan((\alpha - 0)/10) + \dots \\  & (1/2.75) \arctan((\alpha - 3)/25) + \dots \\  & (.70/2.75) \arctan(-(\alpha - 7)/25) + \dots \\  & (1.3/2.75) \arctan((\alpha - 50)/16) + \dots \\  & (2.1/2.75) \arctan(-(\alpha - 69)/15) + \dots \\  & (-.45/2.75) \arctan(-(\alpha - 76)/3.5) - .433  \end{aligned}  $
	$  \begin{aligned}  CM0X56 = & (.26/2.75) \arctan(-(\alpha - 5)/10) + \dots \\  & (-.39/2.75) \arctan((\alpha - 1)/12) + \dots \\  & (.9/2.75) \arctan((\alpha - 5)/15) + \dots \\  & (.85/2.75) \arctan(-(\alpha - 10)/30) + \dots \\  & (1.35/2.75) \arctan((\alpha - 49)/19) + \dots \\  & (2.2/2.75) \arctan(-(\alpha - 69)/15) + \dots \\  & (-.45/2.75) \arctan(-(\alpha - 77)/2) - .368  \end{aligned}  $
	$  \begin{aligned}  CM0X56 = & (.26/2.75) \arctan(-(\alpha - 5)/10) + \dots \\  & (-.39/2.75) \arctan((\alpha - 1)/12) + \dots \\  & (.9/2.75) \arctan((\alpha - 5)/15) + \dots \\  & (.85/2.75) \arctan(-(\alpha - 10)/30) + \dots \\  & (1.35/2.75) \arctan((\alpha - 49)/19) + \dots \\  & (2.2/2.75) \arctan(-(\alpha - 69)/15) + \dots \\  & (-.45/2.75) \arctan(-(\alpha - 77)/2) - .368  \end{aligned}  $

Continued on next page

Table B.6 – Continued from previous page

Curve	Formulation
	$  \begin{aligned}  \text{CM0X58} = & (.26/2.75) \arctan(-(\alpha - 5)/10) + \dots \\  & (-.39/2.75) \arctan((\alpha - 1)/12) + \dots \\  & (.7/2.75) \arctan((\alpha - 5)/15) + \dots \\  & (.85/2.75) \arctan(-(\alpha - 20)/40) + \dots \\  & (1.45/2.75) \arctan((\alpha - 52)/15) + \dots \\  & (2.2/2.75) \arctan(-(\alpha - 69)/15) + \dots \\  & (-.45/2.75) \arctan(-(\alpha - 77)/3.4) - .33  \end{aligned}  $
	$  \begin{aligned}  \text{CM0X59} = & (.26/2.75) \arctan(-(\alpha - 5)/4) + \dots \\  & (-.39/2.75) \arctan((\alpha + 2)/5) + \dots \\  & (1/2.75) \arctan((\alpha - 1)/15) + \dots \\  & (.6/2.75) \arctan(-(\alpha - 18)/13) + \dots \\  & (1.3/2.75) \arctan((\alpha - 51)/14) + \dots \\  & (2.15/2.75) \arctan(-(\alpha - 69)/15) + \dots \\  & (-.45/2.75) \arctan(-(\alpha - 76)/3.5) - .49  \end{aligned}  $
	$  \begin{aligned}  \text{CM0X26} = & (.26/2.75) \arctan(-(\alpha - 2)/10) + \dots \\  & (-.39/2.75) \arctan((\alpha - 1)/10) + \dots \\  & (1/2.75) \arctan((\alpha - 3)/11) + \dots \\  & (.85/2.75) \arctan(-(\alpha - 7)/20) + \dots \\  & (1.35/2.75) \arctan((\alpha - 51)/19) + \dots \\  & (2.2/2.75) \arctan(-(\alpha - 69)/15) + \dots \\  & (-.45/2.75) \arctan(-(\alpha - 77)/2) - .31  \end{aligned}  $
	$  \begin{aligned}  \text{CM0X26} = & (.26/2.75) \arctan(-(\alpha - 2)/10) + \dots \\  & (-.39/2.75) \arctan((\alpha - 1)/10) + \dots \\  & (1/2.75) \arctan((\alpha - 3)/11) + \dots \\  & (.85/2.75) \arctan(-(\alpha - 7)/20) + \dots \\  & (1.35/2.75) \arctan((\alpha - 51)/19) + \dots \\  & (2.2/2.75) \arctan(-(\alpha - 69)/15) + \dots \\  & (-.45/2.75) \arctan(-(\alpha - 77)/2) - .31  \end{aligned}  $
	$  \begin{aligned}  \text{CM0X28} = & (.36/2.75) \arctan(-(\alpha - 5)/35) + \dots \\  & (-.29/2.75) \arctan((\alpha - 1)/30) + \dots \\  & (1/2.75) \arctan((\alpha - 15)/90) + \dots \\  & (.75/2.75) \arctan(-(\alpha - 48)/110) + \dots \\  & (.9/2.75) \arctan((\alpha - 52)/9) + \dots \\  & (2.1/2.75) \arctan(-(\alpha - 69)/17) + \dots \\  & (-.45/2.75) \arctan(-(\alpha - 77)/3) - .387  \end{aligned}  $

Continued on next page



Table B.6 – Continued from previous page

Curve	Formulation
	$CM0X29 = (.26/2.75) \arctan(-(\alpha - 5)/10) +$ $(-.39/2.75) \arctan((\alpha + 4)/7) + \dots$ $(1.33/2.75) \arctan((\alpha - 1)/40) +$ $(.6/2.75) \arctan(-(\alpha - 19)/17) + \dots$ $(1.9/2.75) \arctan((\alpha - 51)/9) +$ $(2.05/2.75) \arctan(-(\alpha - 69)/15) + \dots$ $(-.45/2.75) \arctan(-(\alpha - 76)/3.5) - .45$ $CM0X29_E = (.26/2.75) \arctan(-(\alpha - 5)/10) +$ $(-.39/2.75) \arctan((\alpha + 4)/7) + \dots$ $(1.33/2.75) \arctan((\alpha - 1)/40) +$ $(.6/2.75) \arctan(-(\alpha - 19)/17) + \dots$ $(0.9/2.75) \arctan((\alpha - 51)/9) +$ $(2.11/2.75) \arctan(-(\alpha - 69)/15) + \dots$ $(-.45/2.75) \arctan(-(\alpha - 76)/3.5) - .45$
	$CM006 = (.36/2.75) \arctan(-(\alpha - 5)/30) + \dots$ $(-.29/2.75) \arctan((\alpha - 1)/15) + \dots$ $(.9/2.75) \arctan((\alpha - 5)/35) + \dots$ $(.8/2.75) \arctan(-(\alpha - 48)/75) + \dots$ $(.9/2.75) \arctan((\alpha - 52)/10) + \dots$ $(2.1/2.75) \arctan(-(\alpha - 69)/15) + \dots$ $(-.45/2.75) \arctan(-(\alpha - 77)/2) - .457$
	$CM006 = (.36/2.75) \arctan(-(\alpha - 5)/30) + \dots$ $(-.29/2.75) \arctan((\alpha - 1)/15) + \dots$ $(.9/2.75) \arctan((\alpha - 5)/35) + \dots$ $(.8/2.75) \arctan(-(\alpha - 48)/75) + \dots$ $(.9/2.75) \arctan((\alpha - 52)/10) + \dots$ $(2.1/2.75) \arctan(-(\alpha - 69)/15) + \dots$ $(-.45/2.75) \arctan(-(\alpha - 77)/2) - .457$
	$CM0X08 = (.36/2.75) \arctan(-(\alpha - 5)/35) + \dots$ $(-.29/2.75) \arctan((\alpha - 1)/30) + \dots$ $(1/2.75) \arctan((\alpha - 15)/90) + \dots$ $(.8/2.75) \arctan(-(\alpha - 48)/90) + \dots$ $(.9/2.75) \arctan((\alpha - 52)/9) + \dots$ $(2.1/2.75) \arctan(-(\alpha - 69)/17) + \dots$ $(-.45/2.75) \arctan(-(\alpha - 77)/3) - .387$

Continued on next page

Table B.6 – Continued from previous page

Curve	Formulation
	$  \begin{aligned}  \text{CM0X09} = & (.26/2.75) \arctan(-(\alpha - 5)/10) + \dots \\  & (-.39/2.75) \arctan((\alpha + 2)/10) + \dots \\  & (1.3/2.75) \arctan((\alpha - 1)/40) + \dots \\  & (.6/2.75) \arctan(-(\alpha - 19)/15) + \dots \\  & (.9/2.75) \arctan((\alpha - 51)/9) + \dots \\  & (2.11/2.75) \arctan(-(\alpha - 69)/15) + \dots \\  & (-.45/2.75) \arctan(-(\alpha - 76)/3.5) - .49  \end{aligned}  $
	$  \begin{aligned}  \text{CM0N56} = & (.26/2.75) \arctan(-(\alpha - 5)/30) + \dots \\  & (-.39/2.75) \arctan((\alpha - 1)/30) + \dots \\  & (1.2/2.75) \arctan((\alpha - 5)/40) + \dots \\  & (.6/2.75) \arctan(-(\alpha - 8)/23) + \dots \\  & (1.3/2.75) \arctan(-(\alpha - 60)/65) + \dots \\  & (2.8/2.75) \arctan((\alpha - 72)/55) + \dots \\  & (2.3/2.75) \arctan(-(\alpha - 73)/19) + \dots \\  & (-.45/2.75) \arctan(-(\alpha - 77)/2) - .188  \end{aligned}  $
	$  \begin{aligned}  \text{CM006} = & (.26/2.75) \arctan(-(\alpha - 5)/30) + \dots \\  & (-.39/2.75) \arctan((\alpha - 1)/30) + \dots \\  & (1.2/2.75) \arctan((\alpha - 5)/40) + \dots \\  & (.6/2.75) \arctan(-(\alpha - 8)/23) + \dots \\  & (1.3/2.75) \arctan(-(\alpha - 60)/65) + \dots \\  & (2.8/2.75) \arctan((\alpha - 72)/55) + \dots \\  & (2.3/2.75) \arctan(-(\alpha - 73)/19) + \dots \\  & (-.45/2.75) \arctan(-(\alpha - 77)/2) - .188  \end{aligned}  $
	$  \begin{aligned}  \text{CM0N58} = & (.36/2.75) \arctan(-(\alpha - 5)/35) + \dots \\  & (-.29/2.75) \arctan((\alpha - 1)/30) + \dots \\  & (1.3/2.75) \arctan((\alpha - 15)/95) + \dots \\  & (.8/2.75) \arctan(-(\alpha - 47)/35) + \dots \\  & (1/2.75) \arctan((\alpha - 53)/10) + \dots \\  & (2.15/2.75) \arctan(-(\alpha - 69)/18) + \dots \\  & (-.45/2.75) \arctan(-(\alpha - 78)/2) - .367  \end{aligned}  $
	$  \begin{aligned}  \text{CM0N59} = & (.26/2.75) \arctan(-(\alpha - 5)/11) + \dots \\  & (-.39/2.75) \arctan((\alpha + 2)/10) + \dots \\  & (1.5/2.75) \arctan((\alpha - 1) * 1.1/48) + \dots \\  & (.6/2.75) \arctan(-(\alpha - 19)/15) + \dots \\  & (.8/2.75) \arctan((\alpha - 51)/10) + \dots \\  & (2.32/2.75) \arctan(-(\alpha - 70)/20) + \dots \\  & (-.45/2.75) \arctan(-(\alpha - 78)/3.5) - .49  \end{aligned}  $

Continued on next page

Table B.6 – Continued from previous page

Curve	Formulation
	$  \begin{aligned}  CM0NZ3 = & (.26/2.75) \arctan(-(\alpha - 5)/60) + \dots \\  & (-.39/2.75) \arctan((\alpha - 1)/14) + \dots \\  & (.85/2.75) \arctan((\alpha - 5)/42) + \dots \\  & (.8/2.75) \arctan(-(\alpha - 50)/60) + \dots \\  & (1.8/2.75) \arctan((\alpha - 70)/54) + \dots \\  & (2.4/2.75) \arctan(-(\alpha - 69)/25) + \dots \\  & (-.45/2.75) \arctan(-(\alpha - 79)/2) - .158  \end{aligned}  $
	$  \begin{aligned}  CM0Z6 = & (.26/2.75) \arctan(-(\alpha - 5)/60) + \dots \\  & (-.39/2.75) \arctan((\alpha - 1)/14) + \dots \\  & (.8/2.75) \arctan((\alpha - 5)/42) + \dots \\  & (.8/2.75) \arctan(-(\alpha - 20)/55) + \dots \\  & (1.8/2.75) \arctan((\alpha - 65)/60) + \dots \\  & (2.4/2.75) \arctan(-(\alpha - 69)/20) + \dots \\  & (-.45/2.75) \arctan(-(\alpha - 79)/2) - .158  \end{aligned}  $
	$  \begin{aligned}  CM0NZ8 = & (.36/2.75) \arctan(-(\alpha - 5)/35) + \dots \\  & (-.29/2.75) \arctan((\alpha - 1)/30) + \dots \\  & (1.25/2.75) \arctan((\alpha - 15)/95) + \dots \\  & (.8/2.75) \arctan(-(\alpha - 47)/28) + \dots \\  & (1/2.75) \arctan((\alpha - 53)/10) + \dots \\  & (2.25/2.75) \arctan(-(\alpha - 69)/18) + \dots \\  & (-.45/2.75) \arctan(-(\alpha - 78)/2) - .317  \end{aligned}  $
	$  \begin{aligned}  CM0NZ9 = & (.26/2.75) \arctan(-(\alpha - 5)/7) + \dots \\  & (-.39/2.75) \arctan((\alpha - 0)/10) + \dots \\  & (1.6/2.75) \arctan((\alpha - 5)/50) + \dots \\  & (.6/2.75) \arctan(-(\alpha - 32)/11) + \dots \\  & (.8/2.75) \arctan((\alpha - 51)/11) + \dots \\  & (2.23/2.75) \arctan(-(\alpha - 69)/19) + \dots \\  & (-.45/2.75) \arctan(-(\alpha - 78)/3.5) - .41  \end{aligned}  $
	$  \begin{aligned}  CM0N3 = & (.26/2.75) \arctan(-(\alpha - 5)/60) + \dots \\  & (-.39/2.75) \arctan((\alpha - 1)/30) + \dots \\  & (.8/2.75) \arctan((\alpha - 5)/45) + \dots \\  & (.8/2.75) \arctan(-(\alpha - 10)/65) + \dots \\  & (1.8/2.75) \arctan((\alpha - 49)/40) + \dots \\  & (2.8/2.75) \arctan(-(\alpha - 69)/23) + \dots \\  & (-.45/2.75) \arctan(-(\alpha - 79)/2) - .138  \end{aligned}  $

Continued on next page

Table B.6 – Continued from previous page

Curve	Formulation
	$CM06 = (.26/2.75) \arctan(-(\alpha - 5)/60) + \dots$ $(-.39/2.75) \arctan((\alpha - 1)/30) + \dots$ $(.8/2.75) \arctan((\alpha - 5)/45) + \dots$ $(.8/2.75) \arctan(-(\alpha - 10)/65) + \dots$ $(1.8/2.75) \arctan((\alpha - 51)/45) + \dots$ $(2.8/2.75) \arctan(-(\alpha - 69)/23) + \dots$ $(-.45/2.75) \arctan(-(\alpha - 79)/2) - .148$
	$CM08 = (.26/2.75) \arctan(-(\alpha - 5)/40) + \dots$ $(-.45/2.75) \arctan((\alpha - 4)/30) + \dots$ $(.7/2.75) \arctan((\alpha - 2)/40) + \dots$ $(.8/2.75) \arctan(-(\alpha - 37)/25) + \dots$ $(1.9/2.75) \arctan((\alpha - 52)/25) + \dots$ $(2.7/2.75) \arctan(-(\alpha - 69)/20) + \dots$ $(-.45/2.75) \arctan(-(\alpha - 79)/2) - .198$
	$CM09 = (.16/2.75) \arctan(-(\alpha - 5)/40) + \dots$ $(-.39/2.75) \arctan((\alpha - 3)/8) + \dots$ $(1.2/2.75) \arctan((\alpha - 15)/120) + \dots$ $(.7/2.75) \arctan(-(\alpha - 25)/50) + \dots$ $(2/2.75) \arctan((\alpha - 52)/75) + \dots$ $(2/2.75) \arctan(-(\alpha - 69)/20) + \dots$ $(-.42/2.75) \arctan(-(\alpha - 79)/4) - .068$
	$CMQ = (-.82/\pi) \arctan(-(\alpha - 5)2\pi/18) + \dots$ $2 \arctan(-(\alpha - 32)/6) + \dots$ $4.55 \arctan((\alpha - 43)3.5) + \dots$ $(-3.5) \arctan((\alpha - 57)/5) - 5.8$
	$CMAD = -.02/\pi \arctan(-(\alpha - 1)5\pi/18) + \dots$ $.5 \arctan((\alpha - 6)5) + \dots$ $(-.8) \arctan((\alpha - 18)/2) + \dots$ $.9 \arctan((\alpha - 45)/2) - .9$

### Analytical Formulation for Side Force Coefficients

The analytical formulations for side force coefficients,  $C_Y$ , were constructed at  $\beta = 0^\circ$  and  $20^\circ$ ,  $\delta_r = \pm 30^\circ$ , and  $\delta_a = \pm 25^\circ$ . However it was only specified at  $M = 0.6$ . All the notations used in defining the side force coefficients are given in Table B.7. Whereas the contributions of p, r, and  $\beta$ , are given as  $C_{yP}$ ,  $C_{yR}$  and  $C_{yB}$  respectively as can be found in Table B.8. The comparison curves are demonstrated in Table B.8.

Table B.7: Notation used for side force coefficient,  $C_{Y_0}$ .

		$\delta_r = -30^\circ$	$\delta_r = 30^\circ$
$\beta = 20^\circ$	$\delta_a = 25^\circ$	<b>Cy0XNB2</b>	<b>Cy0XXB2</b>
	$\delta_a = -25^\circ$	<b>Cy0NNB2</b>	<b>Cy0NXB2</b>
$\beta = 0^\circ$	$\delta_a = 25^\circ$	Cy0XNB0	Cy0XXB0
	$\delta_a = -25^\circ$	Cy0NNB0	Cy0NXB0

Table B.8: Compared formulation from Cao's report: Side Force.

Curve	Formulation
	$C_{y0XNB2} = (.232/\pi) \arctan((\alpha - 16)(110\pi/180) - .394$ $C_{y0XNB2E} = (.132/\pi) \arctan((\alpha - 18)(11\pi/180) + \dots$ $(.05/\pi) \arctan((\alpha - 9).098) - .2735$
	$C_{y0NNB2} = (.219544/\pi) \arctan((\alpha - 21)5/56 + \dots$ $(.0636375/\pi) \arctan(-(\alpha - 74)/4) + \dots$ $(.0709125/\pi) \arctan((\alpha - 85)3/10) - .36444$ $C_{y0NNB2E} = (.07344/\pi) \arctan((\alpha - 17)7/56 + \dots$ $(.0636375/\pi) \arctan((\alpha - 74)/14) + \dots$ $(.0636375/\pi) \arctan((\alpha - 13)/4) - .2495$

*Continued on next page*

Table B.8 – Continued from previous page

Curve	Formulation
	$Cy0XXB2 = (.06/\pi) \arctan((\alpha/3) + \dots$ $(.09/\pi) \arctan((\alpha - 31)5/8) + \dots$ $(.06/\pi) \arctan(-(\alpha - 46)3/10) + \dots$ $(.03/\pi) \arctan((\alpha - 65)3/7) + \dots$ $(.09/\pi) \arctan((75 - \alpha)3/5) + \dots$ $(.04/\pi) \arctan((\alpha - 85)4/5) - .285$ $Cy0XXB2_E = (.04/\pi) \arctan((\alpha/3) + \dots$ $(.05/\pi) \arctan((\alpha - 18)5/15) + \dots$ $(.07/\pi) \arctan(-(\alpha - 52)3/12) + \dots$ $(.03/\pi) \arctan((\alpha - 65)3/9) + \dots$ $(.03/\pi) \arctan((74 - \alpha)3/7) - .1612$
	$Cy0NXB2 = (.047/\pi) \arctan(\alpha/2) + \dots$ $(.021/\pi) \arctan(-(\alpha - 17)5/4) + \dots$ $(.037/\pi) \arctan((\alpha - 32)5/3) + \dots$ $(.043/\pi) \arctan(\alpha - 85) + \dots$ $(.06/\pi) \arctan(-(\alpha - 76)5/4) - .248;$
	$Cy0XNB0 = (.029624) \arctan((\alpha - 20)4/25) + \dots$ $(-.0020868) \arctan((12 - \alpha)5) + \dots$ $6.99 \exp(-(\alpha + 17.6)) - .075535;$
	$Cy0XXB0 = (.01216/2.75) \arctan(\alpha/4) + \dots$ $(.03247/2.75) \arctan(-(\alpha - 13)/4) + \dots$ $(.00891/2.75) \arctan((\alpha - 29.5)2/3) + \dots$ $(.03058/2.75) \arctan(-(\alpha - 46)2/5) + \dots$ $(.02759/2.75) \arctan(-(\alpha - 75)3/40) + .03477$

Continued on next page

Table B.8 – Continued from previous page

Curve	Formulation
	$C_{yP} = (.086/\pi) \arctan(\alpha)10\pi/18) + \dots$ $(.09/\pi) \arctan((-\alpha + 23)100\pi/180) + \dots$ $(.20/\pi) \arctan((-\alpha + 45)100\pi/180) + \dots$ $(.256/\pi) \arctan((\alpha - 54)100\pi/180) - .047$ $C_{yP_E} = (.099/\pi) \arctan(\alpha - 1)(4\pi/18) + \dots$ $(.11/\pi) \arctan((-\alpha + 25)3\pi/18) + \dots$ $(.23/\pi) \arctan((-\alpha + 45.5)3\pi/18) + \dots$ $(.28/\pi) \arctan((\alpha - 54.5)3\pi/14) - .0451$
	$C_{yR} = (.17/\pi) \arctan(\alpha - 4)10\pi/18) + \dots$ $(.55/\pi) \arctan((-\alpha - 20)10\pi/18) + \dots$ $(.54/\pi) \arctan((\alpha - 45)10\pi/18) + \dots$ $(.26/\pi) \arctan(-(\alpha - 61)10\pi/18) + .07$ $C_{yR_E} = (.4/\pi) \arctan(\alpha - 4)\pi/18) + \dots$ $(.75/\pi) \arctan((-\alpha - 19)2\pi/20) + \dots$ $(.64/\pi) \arctan((\alpha - 44)5\pi/20) + \dots$ $(.36/\pi) \arctan(-(\alpha - 61)\pi/18) + .03$

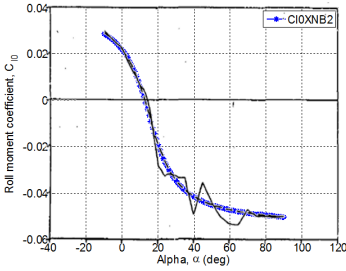
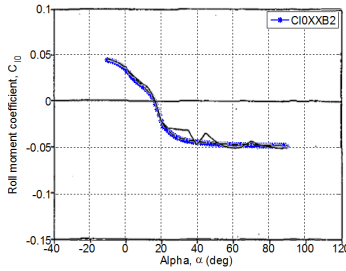
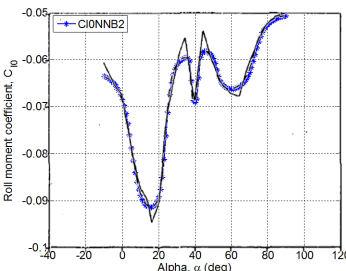
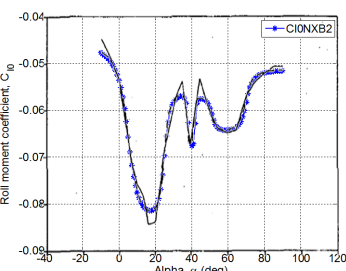
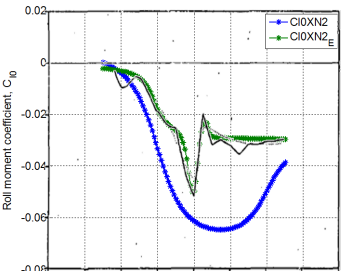
### Analytical Formulation for Rolling Moment Coefficients

Similar to  $C_Y$ , the formulations for rolling moment coefficients,  $C_l$ , were also given at same flight conditions for  $C_Y$  with an additional M at 0.9. The notations used for the different flight conditions are as summarized in Table B.9. The derivatives HCIP and LCIP are due to p at M = 0.9 and M = 0.6 respectively, while CIR is due to r and CIB is the contribution from  $\beta$ . All the curves were reproduced and compared with the original curves in Table B.10.

Table B.9: Notation used for rolling moment coefficient,  $C_{l_0}$ .

		$\delta_r = -30^\circ$	$\delta_r = 30^\circ$
$M = 0.6$	$\beta = 20^\circ$	$\delta_a = 25^\circ$ C10XNB2	C10XXB2
		$\delta_a = -25^\circ$ C10NNB2	C10NXB2
	$\beta = 0^\circ$	$\delta_a = 25^\circ$ C10XNB0	C10XXB0
		$\delta_a = -25^\circ$ C10NNB0	C10NXB0
$M = 0.9$	$\beta = 20^\circ$	$\delta_a = 25^\circ$ <b>C10XN2</b>	<b>C10XX2</b>
		$\delta_a = -25^\circ$ C10NN2	<b>C10NX2</b>
	$\beta = 0^\circ$	$\delta_a = 25^\circ$ C10XN0	C10XX0
$\delta_a = -25^\circ$ -C10XX0		-C10XN0	

Table B.10: Compared formulation from Cao's report: Rolling Moment.

Curve	Formulation
	$C_{l0XNB2} = (.085/2.75) \arctan(-(\alpha - 15)8/92) - .0065$
	$C_{l0XXB2} = (.02771/2.75) \arctan(-(\alpha - 2)/5) + \dots$ $(.06763/2.75) \arctan(-(\alpha - 19)/4) + \dots$ $(.006/2.75) \arctan((\alpha - 22)2) + .00081$
	$C_{l0NNB2} = (.0344/2.75) \arctan(-(\alpha - 5)3/13) + \dots$ $(.037/2.75) \arctan((\alpha - 24)2/5) + \dots$ $(.011/2.75) \arctan(-(\alpha - 38)2) + \dots$ $(.012/2.75) \arctan((\alpha - 42)7/4) + \dots$ $(.011/2.75) \arctan(-(\alpha - 52)3/8) + \dots$ $(.0176/2.75) \arctan((\alpha - 73)3/13) - .0553$
	$C_{l0NXB2} = (.0395/2.75) \arctan(-(\alpha - 5)3/13) + \dots$ $(.0295/2.75) \arctan((\alpha - 25)3/7) + \dots$ $(.0126/2.75) \arctan(-(\alpha - 38)4/3) + \dots$ $(.0114/2.75) \arctan((\alpha - 42)2) + \dots$ $(.0082/2.75) \arctan(-(\alpha - 51)/2) + \dots$ $(.0132/2.75) \arctan(\alpha - 70)2/5) - .0479$
	$C_{l0XN2} = (.048/2.75) \arctan(-(\alpha - 18)8/92) + \dots$ $(.03/2.75) \arctan(-(\alpha - 23)8/92) + \dots$ $(.045/2.75) \arctan((\alpha - 80)8/92) - .0105$ $C_{l0XN2E} = (.024/2.75) \arctan(-(\alpha - 18)8/42) + \dots$ $(.04/2.75) \arctan(-(\alpha - 37)8/18) + \dots$ $(.048/2.75) \arctan((\alpha - 42)8/15) + \dots$ $(.01/2.75) \arctan((48 - \alpha)8/9) - .0155$

Continued on next page

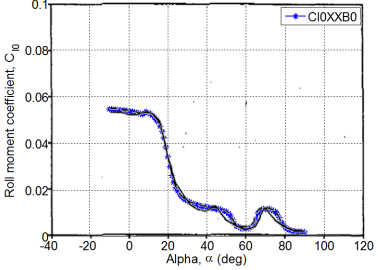
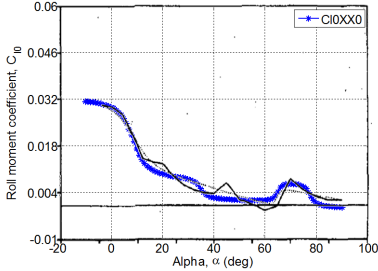
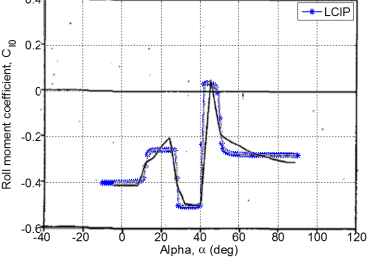
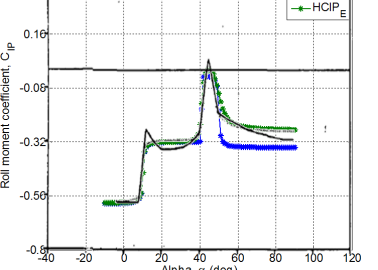
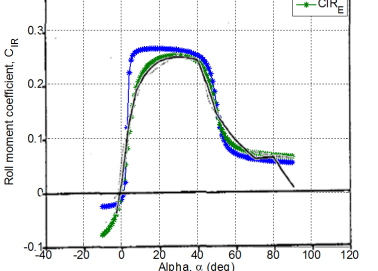


Table B.10 – Continued from previous page

Curve	Formulation
	$C_{l0XX2} = (.085/2.75) \arctan(-(\alpha - 15)8/92) - .0198$ $C_{l0XX2E} = (.035/2.75) \arctan(-(\alpha - 10)8/52) + \dots$ $(.04/2.75) \arctan(-(\alpha - 35)8/25) + \dots$ $(.038/2.75) \arctan((\alpha - 42)8/10) + \dots$ $(.01/2.75) \arctan((50 - \alpha)8/62) - .0075$
	$C_{l0NN2} = - (.0544/2.75) \arctan(-(\alpha - 7)3/13) + \dots$ $(.087/2.75) \arctan((\alpha - 17)2/7) + \dots$ $(.008/2.75) \arctan(-(\alpha - 25)2) + \dots$ $(.019/2.75) \arctan((\alpha - 28)7/4) + \dots$ $(.051/2.75) \arctan(-(\alpha - 42)3/8) + \dots$ $(.0096/2.75) \arctan((\alpha - 55)3/13) - .0553/2.6$ $- .074$
	$C_{l0NX2} = (.0295/2.75) \arctan(-(\alpha - 25)3/13) + \dots$ $(.0295/2.75) \arctan((\alpha - 42.5)3/7) + \dots$ $(.0086/2.75) \arctan(-(\alpha - 15)4/3) + \dots$ $(.0014/2.75) \arctan((\alpha - 42)2) + \dots$ $(.0162/2.75) \arctan(-(\alpha - 51)/2) + \dots$ $(.0012/2.75) \arctan((\alpha - 70)2/5) - .0466$ $C_{l0NX2E} = (.099/2.75) \arctan(-(\alpha - 38)3/17) + \dots$ $(.0895/2.75) \arctan((\alpha - 41.5)3/8) + \dots$ $(.016/2.75) \arctan(-(\alpha - 15)4/10) + \dots$ $(.0094/2.75) \arctan((\alpha - 70)2/6) + \dots$ $(.0162/2.75) \arctan(-(\alpha - 46)/2) + \dots$ $(.022/2.75) \arctan((\alpha - 25)2/10) - .0266$
	$C_{l0XNB0} = (.0041/2.75) \arctan(-(\alpha - 4)2/3) + \dots$ $(.003/2.75) \arctan(-(\alpha - 20)/3) + \dots$ $(.011/2.75) \arctan(-(\alpha - 59)2/5) + \dots$ $(-.00144/2.75) \arctan(-(\alpha + 1)8) + .01793$ $C_{l0XNB0E} = (.0261/2.75) \arctan(-(\alpha - 20)2/5) + \dots$ $(.003/2.75) \arctan(-(\alpha - 20)/3) + \dots$ $(.011/2.75) \arctan(-(\alpha - 59)2/5) + \dots$ $(-.00544/2.75) \arctan(-(\alpha)8/35) + .01783$

Continued on next page

Table B.10 – Continued from previous page

Curve	Formulation
	$C10XXB0 = (.04226/2.75) \arctan(-(\alpha - 20)2/7) + \dots$ $(.00831/2.75) \arctan(-(\alpha - 53)4/7) + \dots$ $(.00997/2.75) \arctan((\alpha - 65)4/5) + \dots$ $(.0101/2.75) \arctan(-(\alpha - 77.5)8/15) + \dots$ $(-.002/\pi) \arctan(-(\alpha - 8)10) + .0286$
	$C10XX0 = (.04226/2.75) \arctan(-(\alpha - 8.5)2/7) + \dots$ $(.01031/2.75) \arctan(-(\alpha - 35)4/7) + \dots$ $(.00997/2.75) \arctan((\alpha - 65)4/5) + \dots$ $(.0131/2.75) \arctan(-(\alpha - 77.5)8/15) + \dots$ $(-.002/\pi) \arctan(-(\alpha - 8)10) + .0286/1.8$
	$LCIP = (.15/\pi) \arctan((\alpha - 12)10\pi/18) + \dots$ $(.25/\pi) \arctan(-(\alpha - 28)100\pi/18) + \dots$ $(.55/\pi) \arctan((\alpha - 41)100\pi/18) + \dots$ $(.33/\pi) \arctan(-(\alpha - 50)10\pi/18) - .341$
	$HCIP = (.28/\pi) \arctan((\alpha - 10)10\pi/18) + \dots$ $(.25/\pi) \arctan(-(\alpha - 41)100\pi/18) + \dots$ $(.55/\pi) \arctan((\alpha - 41)100\pi/18) + \dots$ $(.33/\pi) \arctan(-(\alpha - 50)10\pi/18) - .471$ $HCIP_E = (.28/\pi) \arctan((\alpha - 10)10\pi/18) + \dots$ $(.25/\pi) \arctan(-(\alpha - 41)100\pi/18) + \dots$ $(.65/\pi) \arctan((\alpha - 41)10\pi/18) + \dots$ $(.36/\pi) \arctan(-(\alpha - 50)\pi/9) - .431$
	$CIR = (.304/\pi) \arctan((\alpha - 3)10\pi/18) + \dots$ $(.22/\pi) \arctan(-(\alpha - 50)2\pi/18) + \dots$ $(-.026/\pi) \exp((\alpha - 85)/100) + .018$ $CIR_E = (.404/\pi) \arctan((\alpha - 3)\pi/13) + \dots$ $(.22/\pi) \arctan(-(\alpha - 49)2\pi/28) + \dots$ $(-.026/\pi) \exp((\alpha - 85)/100) - .018$

Continued on next page

Table B.10 – Continued from previous page

Curve	Formulation
	$C_{lB} = .0001((6.32/\pi) \arctan(-(\alpha - 13)100\pi/18) + 3.2621)$ $C_{lB_E} = .0001((6.0/\pi) \arctan(-(\alpha - 13)100\pi/18) + 2.9821)$

### Analytical Formulation for Yawing Moment Coefficients

The yawing moment coefficients,  $C_n$ , formulations have included the effect of  $\delta_h$  as well instead of  $M$ ,  $\beta$ ,  $\delta_r$ , and  $\delta_a$ , as used in  $C_n$  and  $C_Y$ . Each flight condition is notated as in Table B.11. The CnP, CnR and CnB are the derivatives for yawing moment due to p, r, and  $\beta$ . While the improved formulation of the deviated curves are shown in Table B.12 whenever they are applicable.

Table B.11: Notation used for yawing moment coefficient,  $C_{n0}$ .

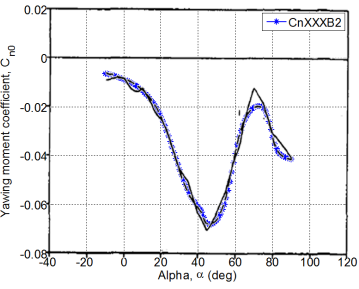
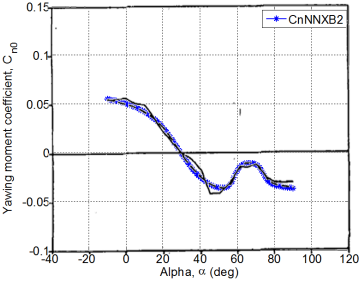
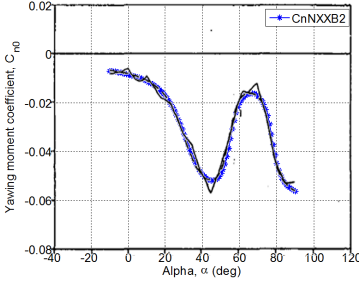
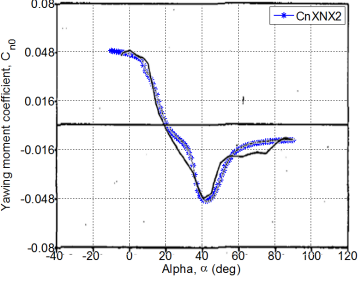
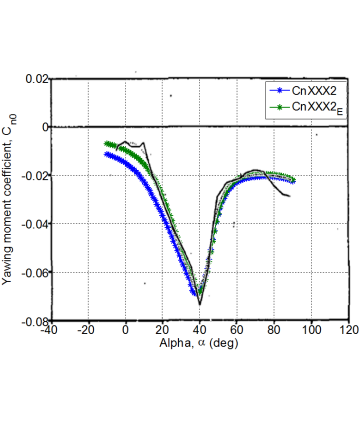
			$\delta_h = -24^\circ$		$\delta_h = 10.5^\circ$	
			$\delta_r = -30^\circ$	$\delta_r = 30^\circ$	$\delta_r = -30^\circ$	$\delta_r = 30^\circ$
$M = 0.6$	$\beta = 20^\circ$	$\delta_a = 25^\circ$	CnXNNB2	CnXXNB2	CnXNXB2	CnXXXB2
		$\delta_a = -25^\circ$	CnNNNB2	CnNXNB2	CnNNXB2	CnNXXB2
$M = 0.6$	$\beta = 0^\circ$	$\delta_a = 25^\circ$	CnXNNB0	CnXXNB0	CnXNXB0	CnXXXB0
		$\delta_a = -25^\circ$	-CnXXNB0	-CnXNNB0	-CnXXXB0	-CnXNXB0
$M = 0.9$	$\beta = 20^\circ$	$\delta_a = 25^\circ$	CnXNN2	<b>CnXXN2</b>	CnXNX2	<b>CnXXX2</b>
		$\delta_a = -25^\circ$	CnNNN2	<b>CnNXN2</b>	CnNNX2	<b>CnNXX2</b>
$M = 0.9$	$\beta = 0^\circ$	$\delta_a = 25^\circ$	CnXNN0	<b>CnXXN0</b>	<b>CnXNX0</b>	CnXXX0
		$\delta_a = -25^\circ$	-CnXXN0	-CnXNN0	-CnXXX0	-CnXNX0

Table B.12: Compared formulation from Cao’s report: Yawing Moment.

Curve	Formulation
	$C_{nXNXB2} = (.06482/2.75) \arctan(-(\alpha - 20)3/14) + \dots$ $(.04937/2.75) \arctan(-(\alpha - 41)5/14) + \dots$ $(.053/2.75) \arctan((\alpha - 60)/6) + \dots$ $(.005/2.75) \arctan(-(\alpha - 8)4) + .0211$

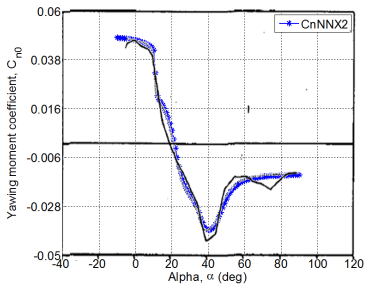
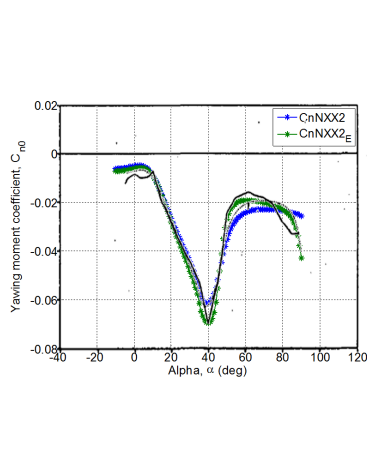
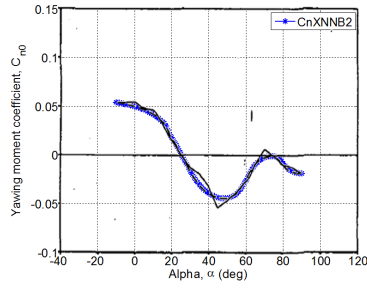
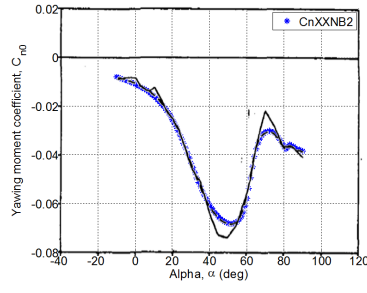
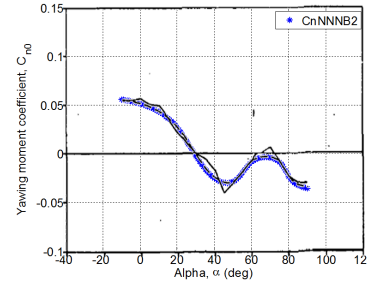
Continued on next page

Table B.12 – Continued from previous page

Curve	Formulation
	$CnXXXB2 = (.077832/2.75) \arctan(-(\alpha - 27.5)4/45) + \dots$ $(.0744/2.75) \arctan((\alpha - 58.5)4/25) + \dots$ $(.02885/2.75) \arctan(-(\alpha - 79)7/20) + \dots$ $(.006/2.75) \arctan(-(\alpha - 43)) - .022$
	$CnNXXB2 = (.11977/2.75) \arctan(-(\alpha - 28.5)3.5/51) + \dots$ $(.04303/2.75) \arctan((\alpha - 58.5)4/13) + \dots$ $(.02532/2.75) \arctan(-(\alpha - 74)2/5) + .01184$
	$CnNXXB2 = (.06132/2.75) \arctan(-(\alpha - 31)/10) + \dots$ $(.05521/2.75) \arctan((\alpha - 55)2/9) + \dots$ $(.04659/2.75) \arctan(-(\alpha - 77.5)4/15) - .03235$
	$CnNXX2 = (.05428/2.75) \arctan(-(\alpha - 16)3/14) + \dots$ $(.05037/2.75) \arctan(-(\alpha - 36)5/14) + \dots$ $(-.003/2.75) \arctan((\alpha - 45)/6) + \dots$ $(.06/2.75) \arctan((\alpha - 50)/6) + \dots$ $(.005/2.75) \arctan(-(\alpha - 8)4) + .0211$
	$CnXXX2 = (.067832/2.75) \arctan(-(\alpha - 30)4/45) + \dots$ $(.065/2.75) \arctan(-(\alpha - 14)4/45) + \dots$ $(-.04/2.75) \arctan(-(\alpha - 14)4/45) + \dots$ $(.0844/2.75) \arctan((\alpha - 46)4/25) + \dots$ $(.04085/2.75) \arctan(-(\alpha - 100)7/20) + \dots$ $(.006/2.75) \arctan(-(\alpha - 35)) - .0352$ $CnXXX2_E = (.067832/2.75) \arctan(-(\alpha - 32)4/45) + \dots$ $(.065/2.75) \arctan(-(\alpha - 22)4/45) + \dots$ $(-.03/2.75) \arctan(-(\alpha - 22)4/45) + \dots$ $(.0944/2.75) \arctan((\alpha - 46)4/25) + \dots$ $(.045085/2.75) \arctan(-(\alpha - 100)7/20) + \dots$ $(.009/2.75) \arctan(-(\alpha - 38)) - .0352$

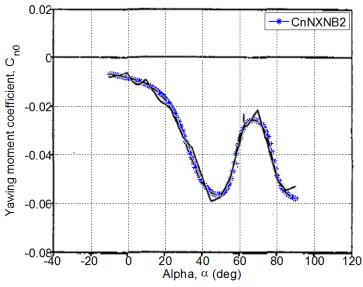
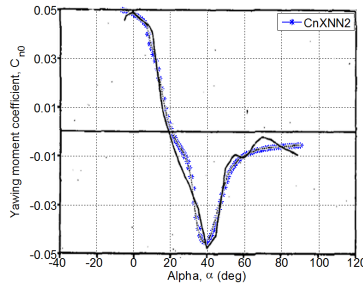
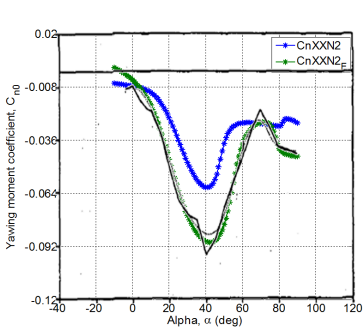
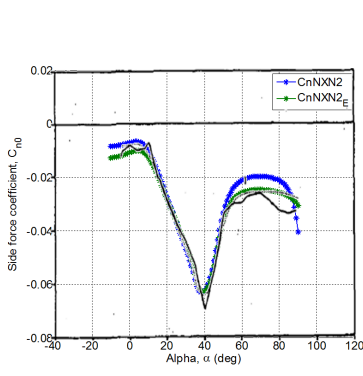
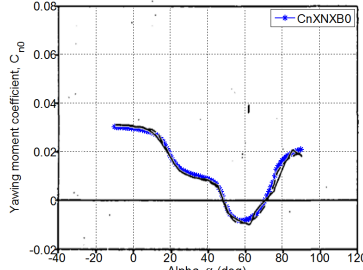
Continued on next page

Table B.12 – Continued from previous page

Curve	Formulation
	$CnNXX2 = (.05428/2.75) \arctan(-(\alpha - 22)3/14) + \dots$ $(.02037/2.75) \arctan(-(\alpha - 36)5/14) + \dots$ $(-.003/2.75) \arctan((\alpha - 45)/6) + \dots$ $(.042/2.75) \arctan((\alpha - 47)/6) + \dots$ $(.020/2.75) \arctan(-(\alpha - 11)4) + .0181$
	$CnNXX2 = (.067832/2.75) \arctan(-(\alpha - 35)4/45) + \dots$ $(.070/2.75) \arctan(-(\alpha - 14)4/45) + \dots$ $(-.04/2.75) \arctan(-(\alpha - 4)4/45) + \dots$ $(.0844/2.75) \arctan((\alpha - 46)4/25) + \dots$ $(.04085/2.75) \arctan(-(\alpha - 100)7/20) + \dots$ $(.006/2.75) \arctan(-(\alpha - 35)) - .0362$ $CnNXX2_E = (.067832/2.75) \arctan(-(\alpha - 35)4/45) + \dots$ $(.070/2.75) \arctan(-(\alpha - 15)4/45) + \dots$ $(-.04/2.75) \arctan(-(\alpha - 4)4/45) + \dots$ $(.0844/2.75) \arctan((\alpha - 46)7/25) + \dots$ $(.04085/2.75) \arctan(-(\alpha - 90)7/20) + \dots$ $(.006/2.75) \arctan(-(\alpha - 35)) - .0362$
	$CnXNNB2 = (.11857/2.75) \arctan(-(\alpha - 26.5)4/45) + \dots$ $(.07065/2.75) \arctan((\alpha - 60.5)4/25) + \dots$ $(.02518/2.75) \arctan(-(\alpha - 80)3/10) + \dots$ $(.005/2.75) \arctan(-(\alpha - 18)2) + .020265$
	$CnXXNB2 = (.080916/2.75) \arctan(-(\alpha - 30)3/42) + \dots$ $(.056/2.75) \arctan((\alpha - 62)/4) + \dots$ $(.02085/2.75) \arctan(-(\alpha - 79)/5) + \dots$ $(-.005/2.75) \arctan(-(\alpha - 82)2) - .02221$
	$CnNNNB2 = (.120543/2.75) \arctan(-(\alpha - 28)3/40) + \dots$ $(.05707/2.75) \arctan((\alpha - 55.5)4/25) + \dots$ $(.03650/2.75) \arctan(-(\alpha - 78.5)4/15) + .01202$

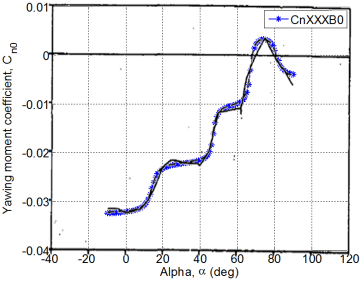
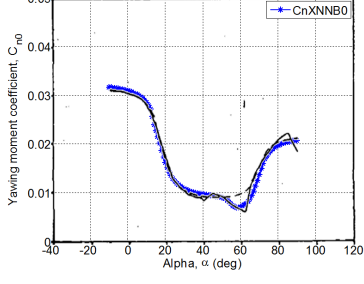
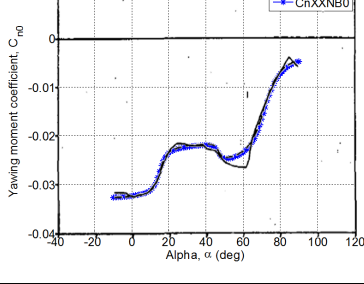
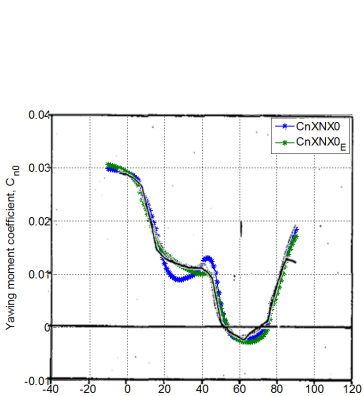
Continued on next page

Table B.12 – Continued from previous page

Curve	Formulation
	$CnNXNB2 = (.063768/2.75) \arctan(-(\alpha - 32)/10) + \dots$ $(.04788/2.75) \arctan((\alpha - 57.5)6/25) + \dots$ $(.03829/2.75) \arctan(-(\alpha - 77.5)4/15) - .03288$
	$CnXNN2 = (.05428/2.75) \arctan(-(\alpha - 15)3/14) + \dots$ $(.05037/2.75) \arctan(-(\alpha - 33)5/14) + \dots$ $(-.003/2.75) \arctan((\alpha - 45)/6) + \dots$ $(.062/2.75) \arctan((\alpha - 46)/6) + \dots$ $(.005/2.75) \arctan(-(\alpha - 8)4) + .0241$
	$CnXXN2 = (.11091/2.75) \arctan(-(\alpha - 25)3/42) + \dots$ $(-.025/2.75) \arctan(-(\alpha - 8)3/42) + \dots$ $(.05600/2.75) \arctan((\alpha - 48)/4) + \dots$ $(.03385/2.75) \arctan(-(\alpha - 100)/5) + \dots$ $(-.005/2.75) \arctan(-(\alpha - 82)2) - .03125$ $CnXXN2_E = (.16091/2.72) \arctan(-(\alpha - 20)3/45) + \dots$ $(-.025/2.75) \arctan(-(\alpha - 8)3/42) + \dots$ $(.09600/2.75) \arctan((\alpha - 54.5)5/30) + \dots$ $(.02085/2.75) \arctan(-(\alpha - 78)2/4) - .01525$
	$CnNXN2 = (.067832/2.75) \arctan(-(\alpha - 32)4/45) + \dots$ $(.063/2.75) \arctan(-(\alpha - 14)4/45) + \dots$ $(-.04/2.75) \arctan(-(\alpha - 4)4/45) + \dots$ $(.0844/2.75) \arctan((\alpha - 46)4/25) + \dots$ $(.04085/2.75) \arctan(-(\alpha - 90)7/20) + \dots$ $(.006/2.75) \arctan(-(\alpha - 35)) - .0352$ $CnNXN2_E = (.070832/2.75) \arctan(-(\alpha - 35)4/45) + \dots$ $(.063/2.75) \arctan(-(\alpha - 14)4/45) + \dots$ $(-.042/2.75) \arctan(-(\alpha - 4)4/45) + \dots$ $(.0844/2.75) \arctan((\alpha - 46)4/25) + \dots$ $(.04885/2.75) \arctan(-(\alpha - 96)7/20) + \dots$ $(.006/2.75) \arctan(-(\alpha - 35)) - .0452$
	$CnNXNB0 = (.02026/2.75) \arctan(-(\alpha - 19)3/14) + \dots$ $(.022/2.75) \arctan(-(\alpha - 49)2/7) + \dots$ $(.03393/2.75) \arctan((\alpha - 73)/7) + \dots$ $(.002/2.75) \arctan(-(\alpha - 14)/2) + \dots$ $(.003/2.75) \arctan((\alpha - 76)2) + .02769$

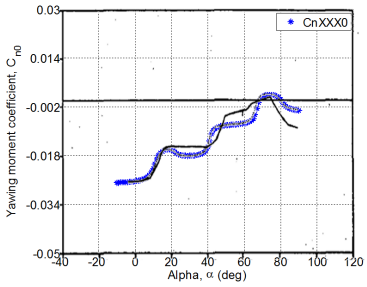
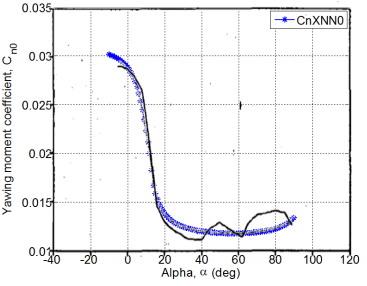
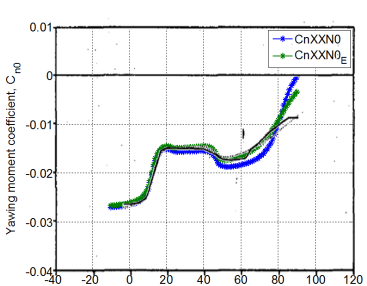
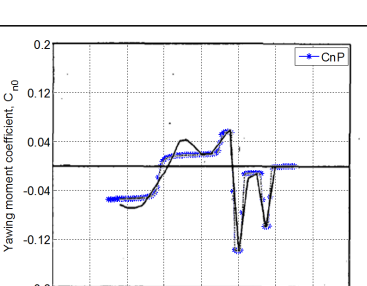
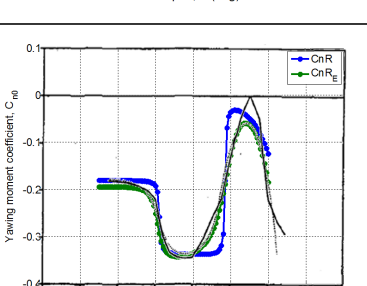
Continued on next page

Table B.12 – Continued from previous page

Curve	Formulation
	$CnXXXB0 = (.00952/2.75) \arctan((\alpha - 14)3/8) + \dots$ $(.01056/2.75) \arctan((\alpha - 47)2/3) + \dots$ $(.01395/2.75) \arctan((\alpha - 67)9/14) + \dots$ $(.00899/2.75) \arctan(-(\alpha - 81)3/8) - .01862$
	$CnXNNB0 = (.02037/2.75) \arctan(-(\alpha - 17.5)8/43) + \dots$ $(.00389/2.75) \arctan(-(\alpha - 54.5)6/17) + \dots$ $(.01623/2.75) \arctan((\alpha - 69.5)5/23) + \dots$ $(.002/2.75) \arctan(-(\alpha - 13)2) + .02711$
	$CnXXNB0 = (.00953/2.75) \arctan((\alpha - 15)3/8) + \dots$ $(.00411/2.75) \arctan(-(\alpha - 46.5)8/15) + \dots$ $(.02222/2.75) \arctan((\alpha - 71.5)4/25) - .01781$
	$CnXNX0 = (.01026/2.75) \arctan(-(\alpha - 13)3/14) + \dots$ $(-.009/2.75) \arctan(-(\alpha - 40)2/7) + \dots$ $(.010/2.75) \arctan(-(\alpha - 18)2/7) + \dots$ $(-.002/2.75) \arctan(-(\alpha - 30)2/7) + \dots$ $(.022/2.75) \arctan(-(\alpha - 49)2/7) + \dots$ $(.02543/2.75) \arctan((\alpha - 83)/7) + \dots$ $(.002/2.75) \arctan(-(\alpha - 7)2) + \dots$ $(.003/2.75) \arctan((\alpha - 76)2) + .02769$ $CnXNX0_E = (.01026/2.75) \arctan(-(\alpha - 13)3/14) + \dots$ $(-.008/2.75) \arctan(-(\alpha - 42)2/7) + \dots$ $(.009/2.75) \arctan(-(\alpha - 12)/10) + \dots$ $(-.001/2.75) \arctan(-(\alpha - 18)2/3) + \dots$ $(.025/2.75) \arctan(-(\alpha - 48)2/12) + \dots$ $(.02543/2.75) \arctan((\alpha - 83)/7) + \dots$ $(.002/2.75) \arctan(-(\alpha - 7)2) + \dots$ $(.003/2.75) \arctan((\alpha - 76)2) + .02769$

Continued on next page

Table B.12 – Continued from previous page

Curve	Formulation
	$CnXXX0 = (.01452/2.75) \arctan((\alpha - 11)3/8) + \dots$ $(-.005/2.75) \arctan((\alpha - 22)3/8) + \dots$ $(.01156/2.75) \arctan((\alpha - 41)2/3) + \dots$ $(.01205/2.75) \arctan((\alpha - 67)9/14) + \dots$ $(.00769/2.75) \arctan(-(\alpha - 81)3/8) - .01862/1.21$
	$CnXNN0 = (.01637/2.75) \arctan(-(\alpha - 10)8/43) + \dots$ $(.00559/2.75) \arctan(-(\alpha - 180)6/17) + \dots$ $(.01623/2.75) \arctan((\alpha - 100)5/23) + \dots$ $(.002/2.75) \arctan(-(\alpha - 13)2) + .0271$
	$CnXXN0 = (.01253/2.75) \arctan((\alpha - 12)3/8) + \dots$ $(-.002/2.75) \arctan((\alpha - 22)3/8) + \dots$ $(.00411/2.75) \arctan(-(\alpha - 46.5)8/15) + \dots$ $(.02222/2.75) \arctan((\alpha - 81.5)4/25) - .01161$ $CnXXN0_E = (.01253/2.75) \arctan((\alpha - 12)3/8) + \dots$ $(-.002/2.75) \arctan((\alpha - 22)3/8) + \dots$ $(.00411/2.75) \arctan(-(\alpha - 46.5)8/15) + \dots$ $(.02222/2.75) \arctan((\alpha - 81.5)4/50) - .01181$
	$CnP = (.075/\pi) \arctan((\alpha - 17)5\pi/18) + \dots$ $(.04/\pi) \arctan((\alpha - 50)10\pi/18) + \dots$ $(.2/\pi) \arctan(-(\alpha - 57)100\pi/18) + \dots$ $(.13/\pi) \arctan((\alpha - 62)100\pi/18) + \dots$ $(.09/\pi) \arctan(-(\alpha - 73)100\pi/18) + \dots$ $(.1/\pi) \arctan((\alpha - 77)100\pi/18) - .028$
	$CnR = (.16/\pi) \arctan(-(\alpha - 22)10\pi/18) + \dots$ $(.34/\pi) \arctan((\alpha - 57)10\pi/18) - \dots$ $(.1) \exp((\alpha - 78)/10) - .09$ $CnR_E = (.01026/2.75) \arctan(-(\alpha - 13)3/14) + \dots$ $(.19/\pi) \arctan(-(\alpha - 21)3\pi/25) + \dots$ $(.5/\pi) \arctan((\alpha - 58)\pi/21) + \dots$ $- (.1) \exp((\alpha - 71)/10) - .05$

Continued on next page



Table B.12 – Continued from previous page

Curve	Formulation
	$CnB = .000001((12.7/\pi) \arctan(-(\alpha - 13)100\pi/18) - 11.7)$ $CnB_E = .000001((3.4/\pi) \arctan(-(\alpha - 13)7\pi/18) - .017)$

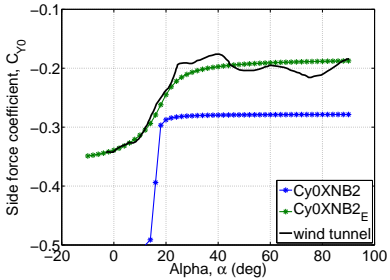
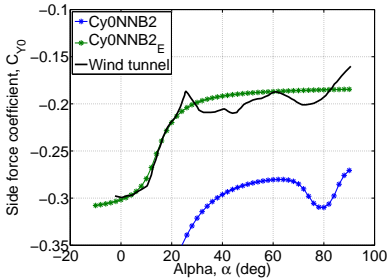
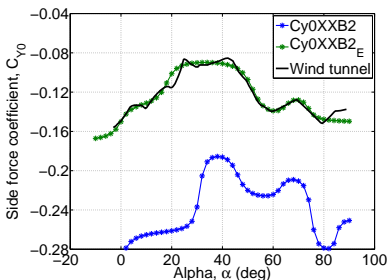
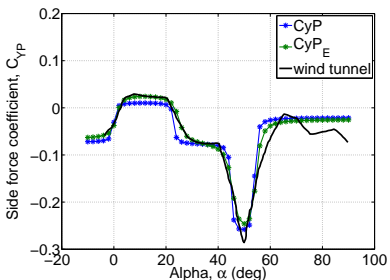
All the curves were regenerated in MATLAB environment with blue line represents the original formulation taken from the original report [74], green line represents the adjusted curves, and the black solid line represents the data curve from the wind tunnel test. The modified formulation were presented with a red font to highlight the effected variables from the original formulations.

Table B.13: List of some curves which have been modified.

Curve	Formulation
	$CLOX6 = (.86/2.75) \arctan(-(\alpha + 5)/100) + \dots$ $(2.19/2.75) \arctan((\alpha - 5)/7) + \dots$ $(.9/2.75) \arctan((\alpha - 24)/17) + \dots$ $(1.71/2.75) \arctan(-(\alpha - 53)2/25) + \dots$ $(.41/2.75) \arctan(-(\alpha - 70)2/7) - .95$ $CLOX6_E = (.86/2.75) \arctan(-(\alpha + 5)/100) + \dots$ $(2.19/2.75) \arctan((\alpha - 5)/7) + \dots$ $(.9/2.75) \arctan((\alpha - 24)/17) + \dots$ $(1.71/2.75) \arctan(-(\alpha - 53)2/25) + \dots$ $(.41/2.75) \arctan(-(\alpha - 70)2/7) - .095$
	$CM0X29 = (.26/2.75) \arctan(-(\alpha - 5)/10) + \dots$ $(-.39/2.75) \arctan((\alpha + 4)/7) + \dots$ $(1.33/2.75) \arctan((\alpha - 1)/40) + \dots$ $(.6/2.75) \arctan(-(\alpha - 19)/17) + \dots$ $(1.9/2.75) \arctan((\alpha - 51)/9) + \dots$ $(2.05/2.75) \arctan(-(\alpha - 69)/15) + \dots$ $(-.45/2.75) \arctan(-(\alpha - 76)/3.5) - .45$ $CM0X29_E = (.26/2.75) \arctan(-(\alpha - 5)/10) + \dots$ $(-.39/2.75) \arctan((\alpha + 4)/7) + \dots$ $(1.33/2.75) \arctan((\alpha - 1)/40) + \dots$ $(.6/2.75) \arctan(-(\alpha - 19)/17) + \dots$ $(0.9/2.75) \arctan((\alpha - 51)/9) + \dots$ $(2.11/2.75) \arctan(-(\alpha - 69)/15) + \dots$ $(-.45/2.75) \arctan(-(\alpha - 76)/3.5) - .45$

Continued on next page

Table B.13 – Continued from previous page

Curve	Formulation
 <p>A line graph showing the side force coefficient <math>C_{y0}</math> versus the angle of attack <math>\alpha</math> (in degrees) for three data series: <math>C_{y0XNB2}</math> (blue dashed line with square markers), <math>C_{y0XNB2E}</math> (green dashed line with square markers), and wind tunnel data (black solid line). The x-axis ranges from -20 to 100 degrees, and the y-axis ranges from -0.5 to -0.1. All curves show a sharp increase in <math>C_{y0}</math> between 0 and 20 degrees, followed by a plateau or slight decrease. <math>C_{y0XNB2}</math> plateaus at approximately -0.28, while <math>C_{y0XNB2E}</math> and the wind tunnel data reach approximately -0.2.</p>	$C_{y0XNB2} = (.232/\pi) \arctan((\alpha - 16)(110\pi/180)) - .394$ $C_{y0XNB2E} = (.132/\pi) \arctan((\alpha - 18)(11\pi/180)) + \dots$ $(.05/\pi) \arctan((\alpha - 9).098) - .2735$
 <p>A line graph showing the side force coefficient <math>C_{y0}</math> versus the angle of attack <math>\alpha</math> (in degrees) for three data series: <math>C_{y0NNB2}</math> (blue dashed line with square markers), <math>C_{y0NNB2E}</math> (green dashed line with square markers), and Wind tunnel data (black solid line). The x-axis ranges from -20 to 100 degrees, and the y-axis ranges from -0.35 to -0.1. <math>C_{y0NNB2}</math> shows a peak around 60 degrees before decreasing. <math>C_{y0NNB2E}</math> and the wind tunnel data show a similar trend to the first row, with a sharp increase at low angles and a plateau thereafter.</p>	$C_{y0NNB2} = (.219544/\pi) \arctan((\alpha - 21)5/56) + \dots$ $(.0636375/\pi) \arctan(-(\alpha - 74)/4) + \dots$ $(.0709125/\pi) \arctan((\alpha - 85)3/10) - .36444$ $C_{y0NNB2E} = (.07344/\pi) \arctan((\alpha - 17)7/56) + \dots$ $.0636375/\pi \arctan((\alpha - 13)/4) - .2495$
 <p>A line graph showing the side force coefficient <math>C_{y0}</math> versus the angle of attack <math>\alpha</math> (in degrees) for three data series: <math>C_{y0XXB2}</math> (blue dashed line with square markers), <math>C_{y0XXB2E}</math> (green dashed line with square markers), and Wind tunnel data (black solid line). The x-axis ranges from -20 to 100 degrees, and the y-axis ranges from -0.28 to -0.04. <math>C_{y0XXB2}</math> shows a complex, oscillatory behavior with multiple peaks and troughs. <math>C_{y0XXB2E}</math> and the wind tunnel data show a similar trend, with a peak around 40 degrees and a subsequent dip.</p>	$C_{y0XXB2} = (.06/\pi) \arctan((\alpha/3)) + \dots$ $(.09/\pi) \arctan((\alpha - 31)5/8) + \dots$ $(.06/\pi) \arctan(-(\alpha - 46)3/10) + \dots$ $(.03/\pi) \arctan((\alpha - 65)3/7) + \dots$ $(.09/\pi) \arctan((75 - \alpha)3/5) + \dots$ $(.04/\pi) \arctan((\alpha - 85)4/5) - .285$ $C_{y0XXB2E} = (.04/\pi) \arctan((\alpha/3)) + \dots$ $(.05/\pi) \arctan((\alpha - 18)5/15) + \dots$ $(.07/\pi) \arctan(-(\alpha - 52)3/12) + \dots$ $(.03/\pi) \arctan((\alpha - 65)3/9) + \dots$ $(.03/\pi) \arctan((74 - \alpha)3/7) - .1612$
 <p>A line graph showing the side force coefficient <math>C_{yP}</math> versus the angle of attack <math>\alpha</math> (in degrees) for three data series: <math>C_{yP}</math> (blue dashed line with square markers), <math>C_{yPE}</math> (green dashed line with square markers), and wind tunnel data (black solid line). The x-axis ranges from -20 to 100 degrees, and the y-axis ranges from -0.3 to 0.2. <math>C_{yP}</math> shows a sharp negative peak around 50 degrees. <math>C_{yPE}</math> and the wind tunnel data show a similar trend, with a positive peak around 10 degrees and a sharp negative peak around 50 degrees.</p>	$C_{yP} = (.086/\pi) \arctan(\alpha)10\pi/18) + \dots$ $(.09/\pi) \arctan((-\alpha + 23)100\pi/180) + \dots$ $(.20/\pi) \arctan((-\alpha + 45)100\pi/180) + \dots$ $(.256/\pi) \arctan((\alpha - 54)100\pi/180) - .047$ $C_{yPE} = (.099/\pi) \arctan(\alpha - 1)(4\pi/18) + \dots$ $(.11/\pi) \arctan((-\alpha + 25)3\pi/18) + \dots$ $(.23/\pi) \arctan((-\alpha + 45.5)3\pi/18) + \dots$ $(.28/\pi) \arctan((\alpha - 54.5)3\pi/14) - .0451$

Continued on next page

Table B.13 – Continued from previous page

Curve	Formulation
	$C_{yR} = (.17/\pi) \arctan(\alpha - 4)10\pi/18) + \dots$ $(.55/\pi) \arctan((-\alpha - 20)10\pi/18) + \dots$ $(.54/\pi) \arctan((\alpha - 45)10\pi/18) + \dots$ $(.26/\pi) \arctan(-(\alpha - 61)10\pi/18) + .07$ $C_{yR_E} = (.4/\pi) \arctan(\alpha - 4)\pi/18) + \dots$ $(.75/\pi) \arctan((-\alpha - 20)2\pi/20) + \dots$ $(.68/\pi) \arctan((\alpha - 46)5\pi/20) + \dots$ $(.39/\pi) \arctan(-(\alpha - 62)\pi/18) + .03$
	$C_{10XN2} = (.048/2.75) \arctan(-(\alpha - 18)8/92) + \dots$ $(.03/2.75) \arctan(-(\alpha - 23)8/92) + \dots$ $(.045/2.75) \arctan((\alpha - 80)8/92) - .0105$ $C_{10XN2_E} = (.024/2.75) \arctan(-(\alpha - 18)8/42) + \dots$ $(.04/2.75) \arctan(-(\alpha - 37)8/18) + \dots$ $(.048/2.75) \arctan((\alpha - 42)8/15) + \dots$ $(.01/2.75) \arctan((48 - \alpha)8/9) - .0155$
	$C_{10XX2} = (.085/2.75) \arctan(-(\alpha - 15)8/92) - .0198$ $C_{10XX2_E} = (.035/2.75) \arctan(-(\alpha - 10)8/52) + \dots$ $(.04/2.75) \arctan(-(\alpha - 35)8/25) + \dots$ $(.038/2.75) \arctan((\alpha - 42)8/10) + \dots$ $(.01/2.75) \arctan((50 - \alpha)8/62) - .0075$
	$C_{10NX2} = (.0295/2.75) \arctan(-(\alpha - 25)3/13) + \dots$ $(.0295/2.75) \arctan((\alpha - 42.5)3/7) + \dots$ $(.0086/2.75) \arctan(-(\alpha - 15)4/3) + \dots$ $(.0014/2.75) \arctan((\alpha - 42)2) + \dots$ $(.0162/2.75) \arctan(-(\alpha - 51)/2) + \dots$ $(.0012/2.75) \arctan((\alpha - 70)2/5) - .0466$ $C_{10NX2_E} = (.099/2.75) \arctan(-(\alpha - 38)3/17) + \dots$ $(.0895/2.75) \arctan((\alpha - 41.5)3/8) + \dots$ $(.016/2.75) \arctan(-(\alpha - 15)4/10) + \dots$ $(.0094/2.75) \arctan((\alpha - 70)2/6) + \dots$ $(.0162/2.75) \arctan(-(\alpha - 46)/2) + \dots$ $(.022/2.75) \arctan((\alpha - 25)2/10) - .0266$

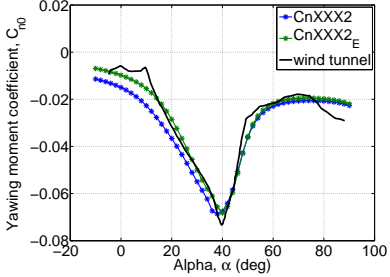
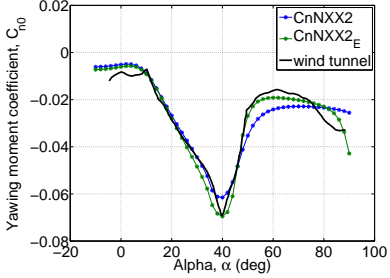
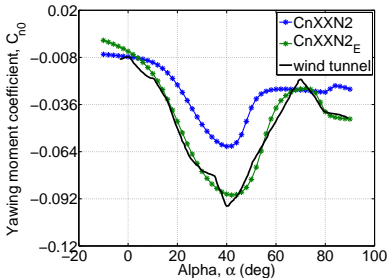
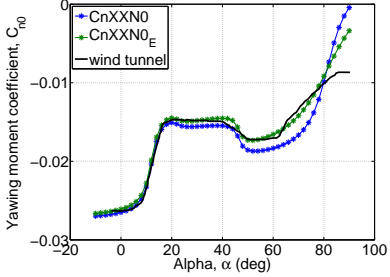
Continued on next page

Table B.13 – Continued from previous page

Curve	Formulation
	$C_{l0XNB0} = (.0041/2.75) \arctan(-(\alpha - 4)2/3) + \dots$ $(.003/2.75) \arctan(-(\alpha - 20)/3) + \dots$ $(.011/2.75) \arctan(-(\alpha - 59)2/5) + \dots$ $(-.00144/2.75) \arctan(-(\alpha + 1)8) + .01793$ $C_{l0XNB0E} = (.0261/2.75) \arctan(-(\alpha - 20)2/5) + \dots$ $(.003/2.75) \arctan(-(\alpha - 20)/3) + \dots$ $(.011/2.75) \arctan(-(\alpha - 59)2/5) + \dots$ $(-.00544/2.75) \arctan(-(\alpha)8/35) + .01783$
	$HClP = (.28/\pi) \arctan((\alpha - 10)10\pi/18) + \dots$ $(.25/\pi) \arctan(-(\alpha - 41)100\pi/18) + \dots$ $(.55/\pi) \arctan((\alpha - 41)100\pi/18) + \dots$ $(.33/\pi) \arctan(-(\alpha - 50)10\pi/18) - .471$ $HClPE = (.28/\pi) \arctan((\alpha - 10)10\pi/18) + \dots$ $(.25/\pi) \arctan(-(\alpha - 41)100\pi/18) + \dots$ $(.65/\pi) \arctan((\alpha - 41)10\pi/18) + \dots$ $(.36/\pi) \arctan(-(\alpha - 50)\pi/9) - .431$
	$ClR = (.304/\pi) \arctan((\alpha - 3)10\pi/18) + \dots$ $(.22/\pi) \arctan(-(\alpha - 50)2\pi/18) + \dots$ $(-.026/\pi) \exp((\alpha - 85)/100) + .018$ $ClRE = (.404/\pi) \arctan((\alpha - 3)\pi/13) + \dots$ $(.22/\pi) \arctan(-(\alpha - 49)2\pi/28) + \dots$ $(-.026/\pi) \exp((\alpha - 85)/100) - .018$
	$ClB = .0001((6.32/\pi) \arctan(-(\alpha - 13)100\pi/18) + 3.2621)$ $ClBE = .0001((6.0/\pi) \arctan(-(\alpha - 13)100\pi/18) + 2.9821)$

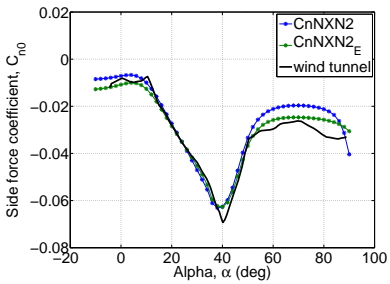
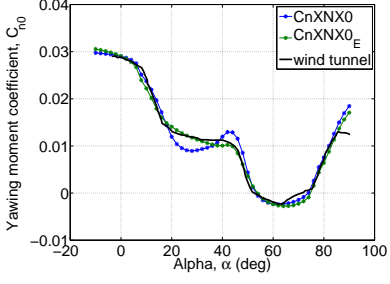
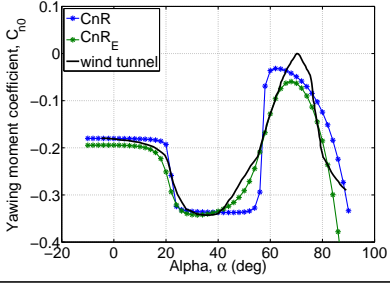
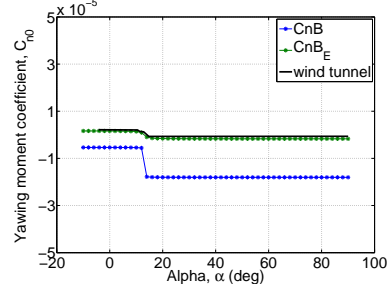
Continued on next page

Table B.13 – Continued from previous page

Curve	Formulation
	$\begin{aligned} CnXXX2 &= (.067832/2.75) \arctan(-(\alpha - 30)4/45) + \dots \\ & \quad (.065/2.75) \arctan(-(\alpha - 14)4/45) + \dots \\ & \quad (-.04/2.75) \arctan(-(\alpha - 14)4/45) + \dots \\ & \quad (.0844/2.75) \arctan((\alpha - 46)4/25) + \dots \\ & \quad (.04085/2.75) \arctan(-(\alpha - 100)7/20) + \dots \\ & \quad (.006/2.75) \arctan(-(\alpha - 35)) - .0352 \end{aligned}$ $\begin{aligned} CnXXX2_E &= (.067832/2.75) \arctan(-(\alpha - 32)4/45) + \dots \\ & \quad (.065/2.75) \arctan(-(\alpha - 22)4/45) + \dots \\ & \quad (-.03/2.75) \arctan(-(\alpha - 22)4/45) + \dots \\ & \quad (.0944/2.75) \arctan((\alpha - 46)4/25) + \dots \\ & \quad (.045085/2.75) \arctan(-(\alpha - 100)7/20) + \dots \\ & \quad (.009/2.75) \arctan(-(\alpha - 38)) - .0352 \end{aligned}$
	$\begin{aligned} CnNXX2 &= (.067832/2.75) \arctan(-(\alpha - 35)4/45) + \dots \\ & \quad (.070/2.75) \arctan(-(\alpha - 14)4/45) + \dots \\ & \quad (-.04/2.75) \arctan(-(\alpha - 4)4/45) + \dots \\ & \quad (.0844/2.75) \arctan((\alpha - 46)4/25) + \dots \\ & \quad (.04085/2.75) \arctan(-(\alpha - 100)7/20) + \dots \\ & \quad (.006/2.75) \arctan(-(\alpha - 35)) - .0362 \end{aligned}$ $\begin{aligned} CnNXX2_E &= (.067832/2.75) \arctan(-(\alpha - 35)4/45) + \dots \\ & \quad (.070/2.75) \arctan(-(\alpha - 15)4/45) + \dots \\ & \quad (-.04/2.75) \arctan(-(\alpha - 4)4/45) + \dots \\ & \quad (.0844/2.75) \arctan((\alpha - 46)7/25) + \dots \\ & \quad (.04085/2.75) \arctan(-(\alpha - 90)7/20) + \dots \\ & \quad (.006/2.75) \arctan(-(\alpha - 35)) - .0362 \end{aligned}$
	$\begin{aligned} CnXXN2 &= (.11091/2.75) \arctan(-(\alpha - 25)3/42) + \dots \\ & \quad (-.025/2.75) \arctan(-(\alpha - 8)3/42) + \dots \\ & \quad (.05600/2.75) \arctan((\alpha - 48)4) + \dots \\ & \quad (.03385/2.75) \arctan(-(\alpha - 100)/5) + \dots \\ & \quad (-.005/2.75) \arctan(-(\alpha - 82)2) - .03125 \end{aligned}$ $\begin{aligned} CnXXN2_E &= (.16091/2.72) \arctan(-(\alpha - 20)3/45) + \dots \\ & \quad (-.025/2.75) \arctan(-(\alpha - 8)3/42) + \dots \\ & \quad (.09600/2.75) \arctan((\alpha - 54.5)5/30) + \dots \\ & \quad (.02085/2.75) \arctan(-(\alpha - 78)2/4) - .01525 \end{aligned}$
	$\begin{aligned} CnXXN0 &= (.01253/2.75) \arctan((\alpha - 12)3/8) + \dots \\ & \quad (-.002/2.75) \arctan((\alpha - 22)3/8) + \dots \\ & \quad (.00411/2.75) \arctan(-(\alpha - 46.5)8/15) + \dots \\ & \quad (.02222/2.75) \arctan((\alpha - 81.5)4/25) - .01161 \end{aligned}$ $\begin{aligned} CnXXN0_E &= (.01253/2.75) \arctan((\alpha - 12)3/8) + \dots \\ & \quad (-.002/2.75) \arctan((\alpha - 22)3/8) + \dots \\ & \quad (.00411/2.75) \arctan(-(\alpha - 46.5)8/15) + \dots \\ & \quad (.02222/2.75) \arctan((\alpha - 81.5)4/50) - .01181 \end{aligned}$

Continued on next page

Table B.13 – Continued from previous page

Curve	Formulation
 <p>Side force coefficient, <math>C_{n0}</math></p> <p>Alpha, <math>\alpha</math> (deg)</p> <p>Legend: <math>C_{nNXN2}</math> (blue dashed), <math>C_{nNXN2E}</math> (green dashed), wind tunnel (black solid)</p>	$C_{nNXN2} = (.067832/2.75) \arctan(-(\alpha - 32)4/45) + \dots$ $(.063/2.75) \arctan(-(\alpha - 14)4/45) + \dots$ $(-.04/2.75) \arctan(-(\alpha - 4)4/45) + \dots$ $(.0844/2.75) \arctan((\alpha - 46)4/25) + \dots$ $(.04085/2.75) \arctan(-(\alpha - 90)7/20) + \dots$ $(.006/2.75) \arctan(-(\alpha - 35)) - .0352$ $C_{nNXN2E} = (.070832/2.75) \arctan(-(\alpha - 35)4/45) + \dots$ $(.063/2.75) \arctan(-(\alpha - 14)4/45) + \dots$ $(-.042/2.75) \arctan(-(\alpha - 4)4/45) + \dots$ $(.0844/2.75) \arctan((\alpha - 46)4/25) + \dots$ $(.04885/2.75) \arctan(-(\alpha - 96)7/20) + \dots$ $(.006/2.75) \arctan(-(\alpha - 35)) - .0452$
 <p>Yawing moment coefficient, <math>C_{n0}</math></p> <p>Alpha, <math>\alpha</math> (deg)</p> <p>Legend: <math>C_{nXNX0}</math> (blue dashed), <math>C_{nXNX0E}</math> (green dashed), wind tunnel (black solid)</p>	$C_{nXNX0} = (.01026/2.75) \arctan(-(\alpha - 13)3/14) + \dots$ $(-.009/2.75) \arctan(-(\alpha - 40)2/7) + \dots$ $(.010/2.75) \arctan(-(\alpha - 18)2/7) + \dots$ $(-.002/2.75) \arctan(-(\alpha - 30)2/7) + \dots$ $(.022/2.75) \arctan(-(\alpha - 49)2/7) + \dots$ $(.02543/2.75) \arctan((\alpha - 83)/7) + \dots$ $(.002/2.75) \arctan(-(\alpha - 7)2) + \dots$ $(.003/2.75) \arctan((\alpha - 76)2) + .02769$ $C_{nXNX0E} = (.01026/2.75) \arctan(-(\alpha - 13)3/14) + \dots$ $(-.008/2.75) \arctan(-(\alpha - 42)2/7) + \dots$ $(.009/2.75) \arctan(-(\alpha - 12)/10) + \dots$ $(-.001/2.75) \arctan(-(\alpha - 18)2/3) + \dots$ $(.025/2.75) \arctan(-(\alpha - 48)2/12) + \dots$ $(.02543/2.75) \arctan((\alpha - 83)/7) + \dots$ $(.002/2.75) \arctan(-(\alpha - 7)2) + \dots$ $(.003/2.75) \arctan((\alpha - 76)2) + .02769$
 <p>Yawing moment coefficient, <math>C_{n0}</math></p> <p>Alpha, <math>\alpha</math> (deg)</p> <p>Legend: <math>C_{nR}</math> (blue dashed), <math>C_{nRE}</math> (green dashed), wind tunnel (black solid)</p>	$C_{nR} = (.16/\pi) \arctan(-(\alpha - 22)10\pi/18) + \dots$ $(.34/\pi) \arctan((\alpha - 57)10\pi/18) - \dots$ $(.1) \exp((\alpha - 78)/10) - .09$ $C_{nRE} = (.01026/2.75) \arctan(-(\alpha - 13)3/14) + \dots$ $(.19/\pi) \arctan(-(\alpha - 21)3\pi/25) + \dots$ $(.5/\pi) \arctan((\alpha - 58)\pi/21) + \dots$ $(-.1) \exp((\alpha - 71)/10) - .05$
 <p>Yawing moment coefficient, <math>C_{n0}</math></p> <p>Alpha, <math>\alpha</math> (deg)</p> <p>Legend: <math>C_{nB}</math> (blue dashed), <math>C_{nBE}</math> (green dashed), wind tunnel (black solid)</p>	$C_{nB} = .000001((12.7/\pi) \arctan(-(\alpha - 13)100\pi/18) - 11.7)$ $C_{nBE} = .000001((3.4/\pi) \arctan(-(\alpha - 13)7\pi/18) - .017)$

## B.2 Chakraborty Aerodynamic Data

The aerodynamic coefficients presented here are taken from Reference [8]. It was extracted from various papers [65, 66, 78] based on the flight test data. However, some of the data were artificially introduced due to the lacking of data at low  $\alpha$  for example at  $0^\circ < \alpha < 10^\circ$ . The data were presented in least square fit as shown in the following subsections.

### Lift Coefficient, $C_L$

$$C_{L_{Chak}} = (1.1645\alpha^3 - 5.4246\alpha^2 + 5.6770\alpha - 0.0204) \cos(2\beta/3) + \dots \quad (\text{B.1})$$

$$(2.1852\alpha^3 - 2.6975\alpha^2 + 0.4055\alpha + 0.5725)\delta_h;$$

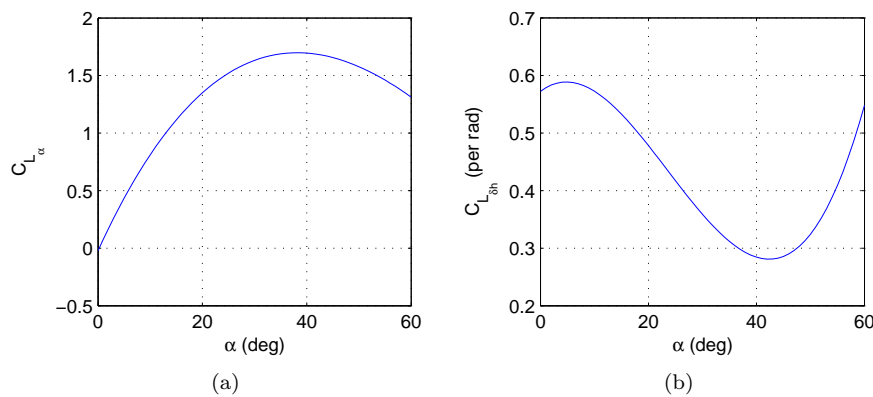


Figure B.1: Lift coefficient for (a) basic airframe and (b) stabilator deflection.

**Drag Coefficient,  $C_D$** 

$$CD_{Chak} = (1.4610\alpha^4 - 5.7341\alpha^3 + 6.3971\alpha^2 - 0.1995\alpha - 1.4994) \cos(\beta) + \dots \quad (\text{B.2})$$

$$1.5036 + (-3.8578\alpha^3 + 4.2360\alpha^2 - 0.2739\alpha + 0.0366)\delta_h;$$

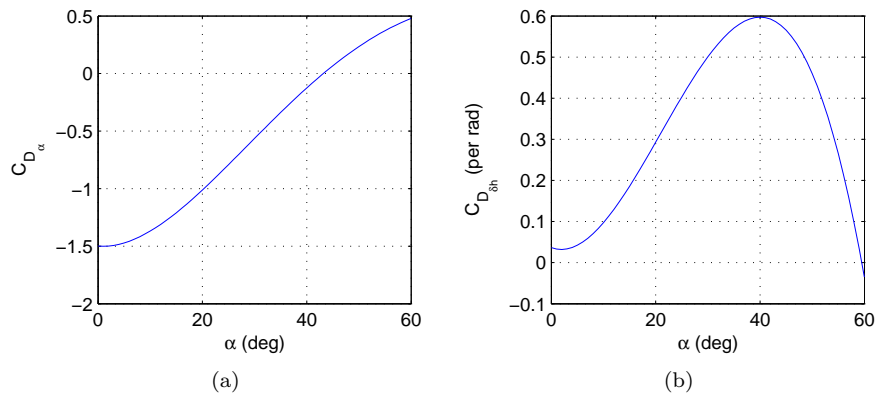


Figure B.2: Drag coefficient for (a) basic airframe and (b) stabilator deflection.

**Pitching Moment Coefficient,  $C_m$** 

$$CM_{Chak} = (-1.2897\alpha^2 + 0.5110\alpha - 0.0866) + (0.9338\alpha^2 - 0.3245\alpha - 0.9051)\delta_h + \dots$$

$$\bar{c}/(2V)(64.7190\alpha^3 - 68.5641\alpha^2 + 10.9921\alpha - 4.1186)q; \quad (\text{B.3})$$



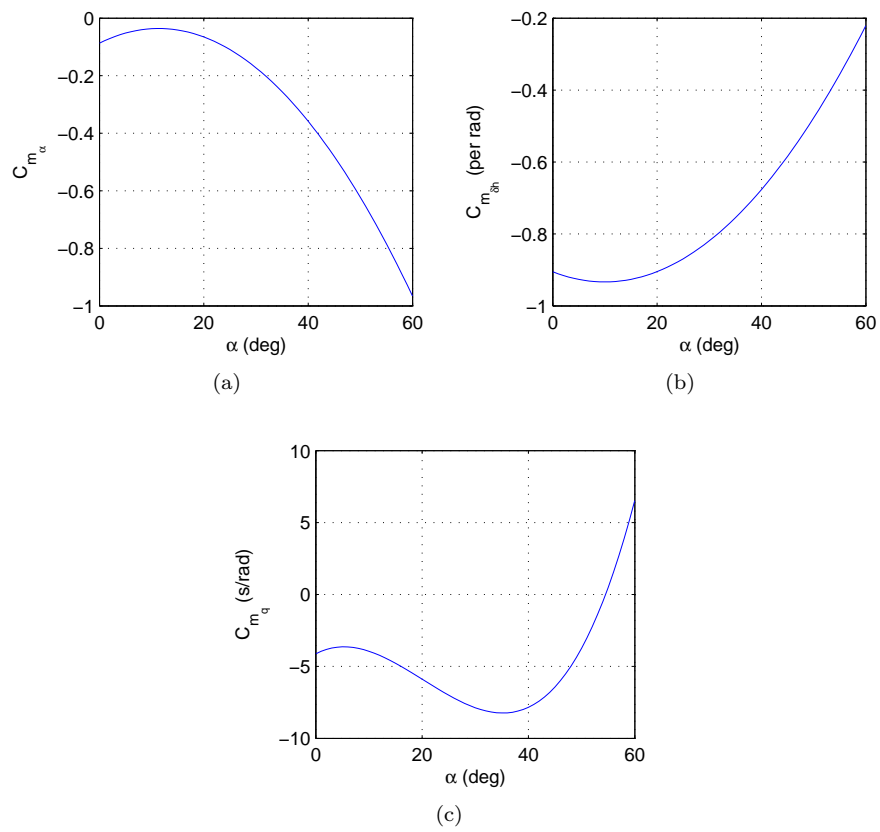


Figure B.3: Pitching moment coefficient for (a) basic airframe, (b) stabilator deflection and (c) pitch rate.

Side Force Coefficient,  $C_Y$ 

$$\begin{aligned}
 CY_{Chak} = & (-0.1926\alpha^2 + 0.2654\alpha - 0.7344)\beta + \dots \\
 & (-0.8500\alpha^3 + 1.5317\alpha^2 - 0.2403\alpha - 0.1656)\delta_a + \dots \\
 & (0.9351\alpha^3 - 1.6921\alpha^2 + 0.4082\alpha + 0.2054)\delta_r;
 \end{aligned}
 \tag{B.4}$$

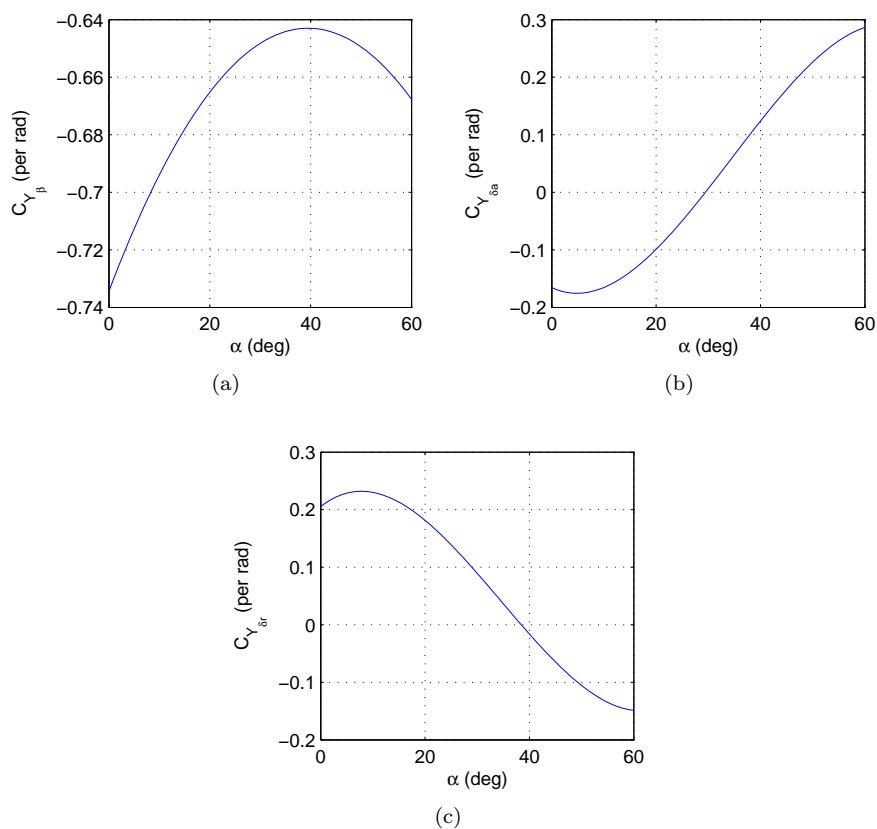


Figure B.4: Side force coefficient for (a) basic airframe, (b) aileron deflection and (c) rudder deflection.

Rolling Moment Coefficient,  $C_l$ 

$$\begin{aligned}
Cl_{Chak} = & (-1.6196\alpha^4 + 2.3843\alpha^3 - 0.3620\alpha^2 - 0.4153\alpha - 0.0556)\beta + \dots \\
& (0.1989\alpha^3 - 0.2646\alpha^2 - 0.0516\alpha + 0.1424)\delta_a + \dots \\
& (-0.0274\alpha^3 - 0.0083\alpha^2 - 0.0014\alpha + 0.0129)\delta_r + \dots \\
& b/(2V)(0.2377\alpha - 0.3540)p + \dots \\
& b/(2V)(-1.0871\alpha^2 - 0.7804\alpha + 0.1983)r;
\end{aligned} \tag{B.5}$$

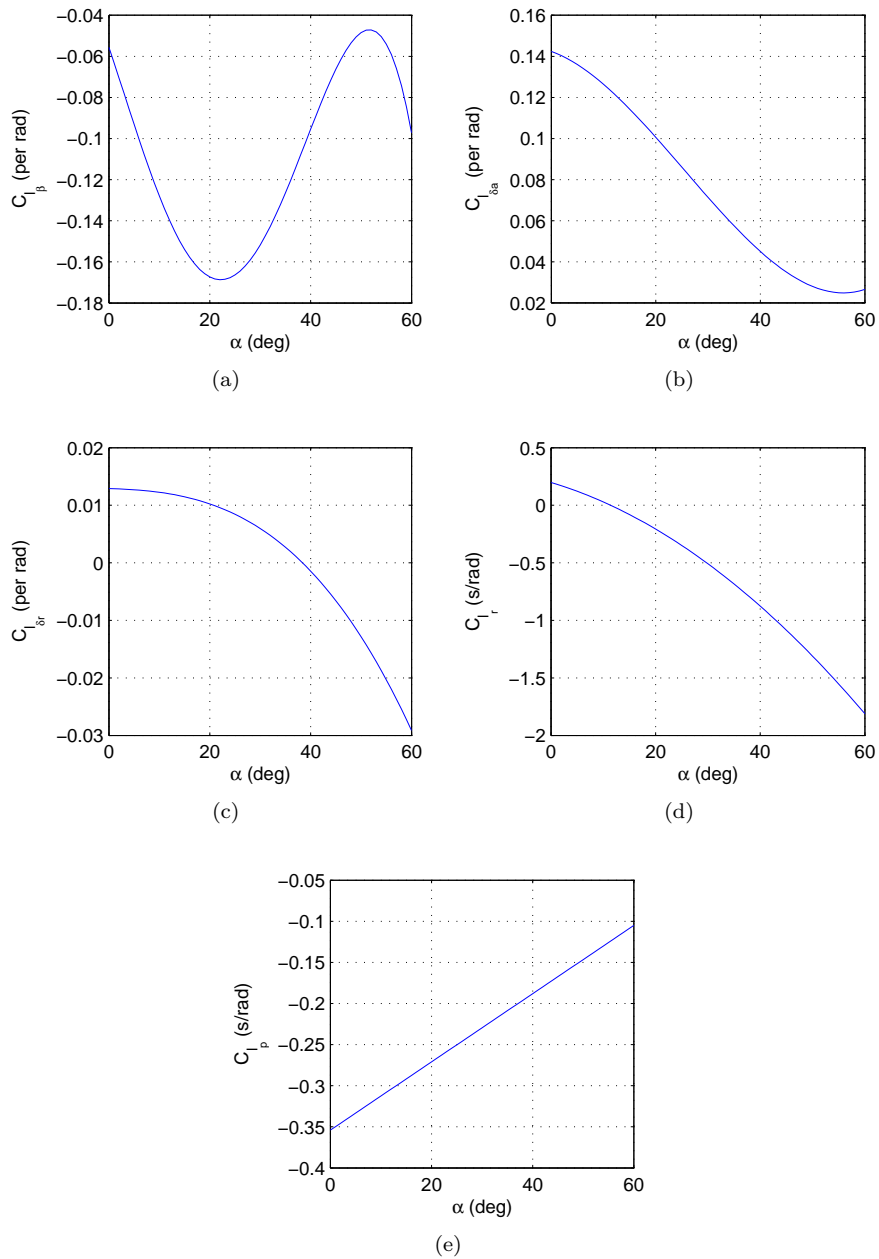


Figure B.5: Rolling moment coefficient for (a) basic airframe, (b) aileron deflection, (c) rudder deflection, (d) yaw rate and (e) roll rate.

Yawing Moment Coefficient,  $C_n$ 

$$\begin{aligned}
C_{n_{Chak}} = & (-0.3816\alpha^2 + 0.0329\alpha + 0.0885)\beta + \dots \\
& (0.3899\alpha^4 - 0.8980\alpha^3 + 0.5564\alpha^2 - 0.0176\alpha - 0.0780)\delta_r + \dots \\
& (0.2694\alpha^3 - 0.3413\alpha^2 + 0.0584\alpha + 0.0104)\delta_a + \dots \\
& b/(2V)(-0.0881\alpha + 0.0792)p + \dots \\
& b/(2V)(-0.1307\alpha - 0.4326)r;
\end{aligned} \tag{B.6}$$

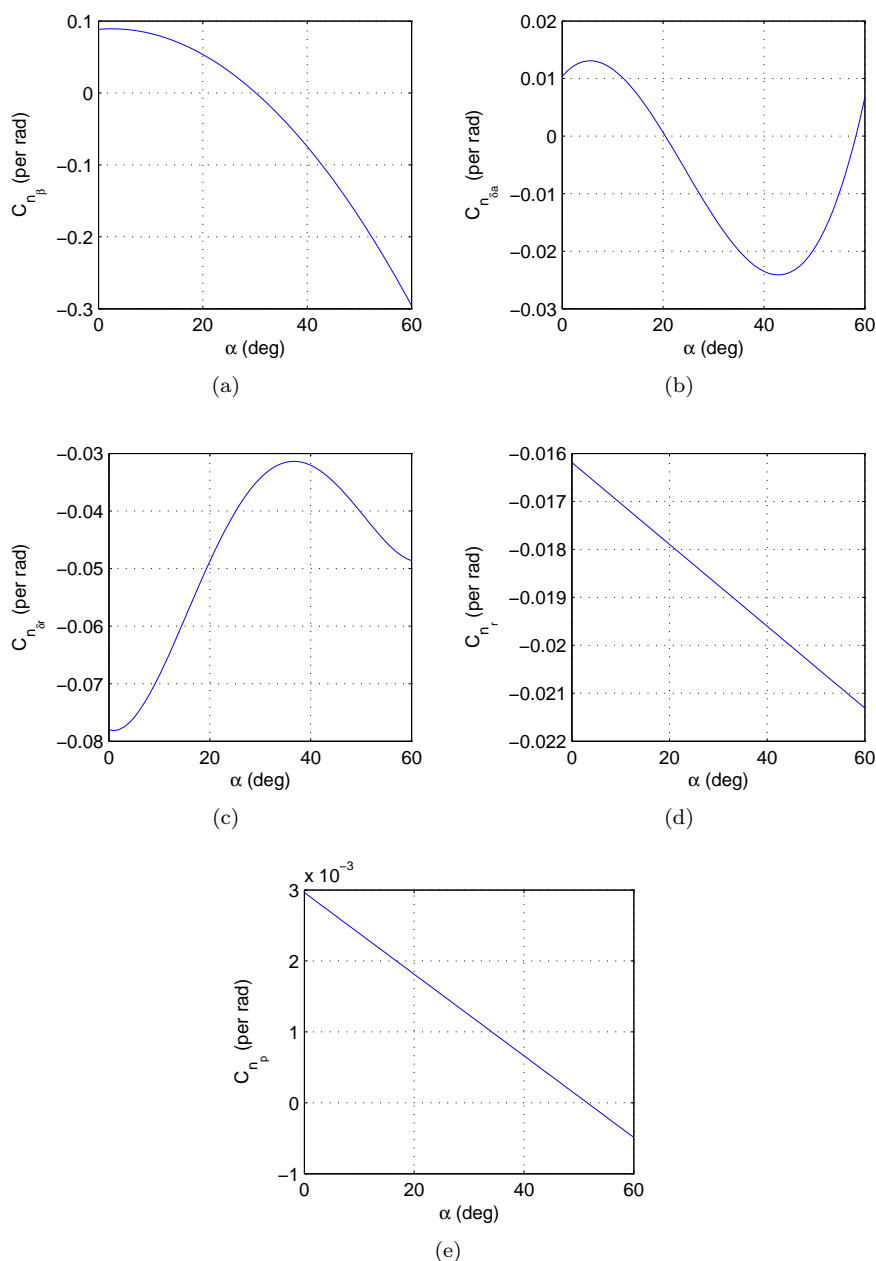


Figure B.6: Yawing moment coefficient for (a) basic airframe, (b) aileron deflection, (c) rudder deflection, (d) yaw rate and (e) roll rate.

## B.3 NASA Aerodynamic Data

% Database for F18 HARV aeodynamics data look up table. All derivatives  
% are in per degree unit.

```
alpha = [ -14.0000 -10.00000 -6.00000 -2.00000 2.00000 6.00000 ...
          10.00000 14.0000 18.0000 22.0000 26.0000 30.0000 34.0000 ...
          38.0000 42.0000 46.0000 50.0000 54.0000 58.0000 62.0000 ...
          66.0000 70.0000 74.0000 78.0000 82.0000 86.0000 90.0000]';
```

% Longitudinal derivative

% Drag

```
cd0 = [ 0.227325 0.170673 7.47685E-02 3.20977E-02 2.79305E-02 ...
        6.13288E-02 0.154023 0.261263 0.363863 0.486635 0.643989 0.863792 ...
        1.08558 1.27900 1.47638 1.61911 1.74604 1.84448 1.92402 ...
        1.98384 2.02834 2.06708 2.11362 2.15514 2.17363 2.16283 ...
        2.12822]';
```

% Drag due to pitch rate

```
cd.q = [ 1.48740E-16 -2.21604E-16 -8.70391E-05 -7.79330E-04 -8.31959E-04 ...
         -6.60720E-05 1.33279E-03 1.67685E-04 5.84481E-06 -9.59697E-17 ...
         -6.48262E-17 -2.05428E-16 -2.53047E-16 2.02363E-16 3.51664E-16 ...
         8.52635E-16 5.44982E-16 -5.45460E-16 1.14528E-15 -2.50755E-16 ...
         8.43503E-16 -8.45493E-16 -2.54842E-15 -7.66583E-16 -3.79368E-16 ...
         9.11688E-16 9.07194E-16]';
```

% Drag due to left stabilator deflection

```
cd.del = [-2.63851E-03 -2.42289E-03 -2.00960E-03 -1.61668E-03 -1.11178E-03 ...
          -4.31951E-04 4.33892E-04 1.11520E-03 1.97203E-03 2.82682E-03 ...
          3.59917E-03 4.29851E-03 4.93824E-03 5.55955E-03 5.88711E-03 ...
          5.82388E-03 5.49440E-03 5.22574E-03 5.15071E-03 5.18088E-03 ...
          5.20101E-03 5.06911E-03 3.65306E-03 2.50369E-03 1.69598E-03 ...
          1.25007E-03 1.13131E-03]';
```

% Drag due to right stabilator deflection

```
cd.der = [-2.63851E-03 -2.42289E-03 -2.00960E-03 -1.61668E-03 -1.11178E-03 ...
          -4.31951E-04 4.33892E-04 1.11520E-03 1.97203E-03 2.82682E-03 ...
          3.59917E-03 4.29851E-03 4.93824E-03 5.55955E-03 5.88711E-03 ...
          5.82388E-03 5.49440E-03 5.22574E-03 5.15071E-03 5.18088E-03 ...
          5.20101E-03 5.06911E-03 3.65306E-03 2.50369E-03 1.69598E-03 ...
          1.25007E-03 1.13131E-03]';
```

% Lift

```
clift0 = [ -1.03860 -0.880907 -0.551318 -0.216206 0.154461 0.560857 ...
           0.951575 1.24168 1.39786 1.53103 1.64110 1.77724 1.88652 ...
           1.88940 1.80975 1.68556 1.57524 1.46011 1.31884 1.17117 ...
           1.02151 0.858875 0.685334 0.529482 0.378268 0.229349 ...
           9.10933E-02 ]';
```

% Lift due to pitch rate

```
clift.q = [7.87143E-02 7.87143E-02 7.87144E-02 7.88452E-02 7.64891E-02 ...
           6.91587E-02 6.33554E-02 5.99084E-02 5.89049E-02 6.05629E-02 ...
           6.28755E-02 6.91587E-02 8.89245E-02 0.119991 0.147829 0.159698 ...
           0.131772 1.03847E-01 9.21534E-02 8.79646E-02 8.63938E-02 ...
           8.63938E-02 8.49975E-02 8.25541E-02 7.97615E-02 7.66200E-02 ...
           7.24312E-02]';
```

% Lift due to left stabilator deflection

```
clift.del = [5.03735E-03 5.30820E-03 5.80124E-03 6.25003E-03 6.76123E-03 ...
            7.18902E-03 7.15986E-03 6.87948E-03 6.62941E-03 6.28904E-03 ...
            5.97515E-03 5.90878E-03 5.86386E-03 5.55871E-03 4.76025E-03 ...
            3.56060E-03 2.26618E-03 1.55859E-03 1.04476E-03 5.88013E-04 ...
            1.18163E-04 -3.68531E-04 -1.10325E-03 -1.79305E-03 -2.27413E-03 ...
            -2.48706E-03 -2.47676E-03]';
```

% Lift due to right stabilator deflection

```
clift.der = [5.03735E-03 5.30820E-03 5.80124E-03 6.25003E-03 6.76123E-03 ...
            7.18902E-03 7.15986E-03 6.87948E-03 6.62941E-03 6.28904E-03 ...
            5.97515E-03 5.90878E-03 5.86386E-03 5.55871E-03 4.76025E-03 ...
            3.56060E-03 2.26618E-03 1.55859E-03 1.04476E-03 5.88013E-04 ...
            1.18163E-04 -3.68531E-04 -1.10325E-03 -1.79305E-03 -2.27413E-03 ...
            -2.48706E-03 -2.47676E-03]';
```

## % Moment

```
cm0 = [9.62520E-02  8.07290E-02  5.54066E-02  2.80686E-02  5.08503E-03 ...
      -6.61034E-03  -1.64371E-02  -1.60245E-02  -5.86329E-02  -8.42348E-02 ...
      -8.52663E-02  -0.105573  -0.117061  -0.110115  -0.114069  -0.118398...
      -1.01818E-01  -0.146057  -0.228343  -0.351592  -0.426319  -0.476887...
      -0.601749  -0.563499  -0.547688  -0.570013  -0.588038]';
```

## % Moment due to pitch rate

```
cm_q = [-8.68301E-02  -8.68301E-02  -8.68301E-02  -8.65683E-02  -8.53902E-02 ...
      -8.08524E-02  -7.57473E-02  -7.23875E-02  -7.56600E-02  -8.29032E-02 ...
      -8.81828E-02  -1.02364E-01  -0.147655  -0.205556  -0.132732  1.80642E-02 ...
      4.31969E-02  1.80642E-02  -1.96350E-02  -6.50135E-02  -1.00967E-01 ...
      -9.81748E-02  -9.53822E-02  -9.25897E-02  -8.90991E-02  -8.52593E-02 ...
      -8.24668E-02]';
```

## % Moment due to left stabilator deflection

```
cm_del = [-6.46703E-03  -6.58967E-03  -6.83004E-03  -7.09553E-03  -7.45696E-03 ...
      -7.82965E-03  -8.00920E-03  -8.04445E-03  -8.05054E-03  -8.00358E-03 ...
      -7.99808E-03  -7.98872E-03  -7.79706E-03  -7.35454E-03  -6.39032E-03 ...
      -5.05660E-03  -3.75061E-03  -3.37707E-03  -3.03092E-03  -2.32363E-03 ...
      -1.37503E-03  -8.13315E-04  -7.80549E-04  -1.77291E-03  -2.35148E-03 ...
      -2.35499E-03  -2.89985E-03]';
```

## % Moment due to right stabilator deflection

```
cm_der = [-6.46703E-03  -6.58967E-03  -6.83004E-03  -7.09553E-03  -7.45696E-03 ...
      -7.82965E-03  -8.00920E-03  -8.04445E-03  -8.05054E-03  -8.00358E-03 ...
      -7.99808E-03  -7.98872E-03  -7.79706E-03  -7.35454E-03  -6.39032E-03 ...
      -5.05660E-03  -3.75061E-03  -3.37707E-03  -3.03092E-03  -2.32363E-03 ...
      -1.37503E-03  -8.13315E-04  -7.80549E-04  -1.77291E-03  -2.35148E-03 ...
      -2.35499E-03  -2.89985E-03]';
```

## % Lateral-directional derivative

## % Side force due to beta

```
cy_b = [-1.71957E-02  -1.71957E-02  -1.77407E-02  -1.82857E-02  -1.84197E-02 ...
      -1.84159E-02  -1.87763E-02  -1.77142E-02  -1.55057E-02  -1.40980E-02 ...
      -1.28732E-02  -1.26852E-02  -1.25160E-02  -1.35594E-02  -1.40314E-02 ...
      -1.33128E-02  -1.19496E-02  -1.30678E-02  -1.37112E-02  -1.37528E-02 ...
      -1.33426E-02  -1.29076E-02  -1.33076E-02  -1.38320E-02  -1.37811E-02 ...
      -1.31714E-02  -1.27360E-02]';
```

## % Side force due to roll rate

```
cy_p = [-1.06465E-03  -1.06465E-03  -1.06465E-03  -8.63938E-04  -2.09440E-04 ...
      4.14516E-04  5.80322E-04  5.32325E-04  4.53786E-04  2.22529E-04 ...
      -1.74533E-04  -5.49779E-04  -9.42478E-04  -1.35699E-03  -2.60752E-03 ...
      -4.39823E-03  -5.23599E-03  -3.00197E-03  -1.65806E-03  -7.85399E-04 ...
      -2.96706E-04  -4.36332E-04  -9.25024E-04  -9.94838E-04  -9.25024E-04 ...
      -9.77384E-04  -1.39626E-03]';
```

## % Side force due to yaw rate

```
cy_r = [2.69653E-03  2.69653E-03  2.69653E-03  2.89725E-03  3.36412E-03 ...
      3.94444E-03  4.45932E-03  3.82227E-03  1.22609E-03  -1.61443E-03 ...
      -3.46448E-03  -4.66876E-03  -5.36689E-03  -5.67232E-03  -3.89208E-03 ...
      3.49069E-05  5.06146E-03  5.06145E-03  4.11898E-03  2.79253E-03 ...
      1.60570E-03  1.04720E-03  8.37758E-04  6.28319E-04  4.88692E-04 ...
      4.18879E-04  3.49066E-04]';
```

## % Side force due to aileron deflection

```
cy_da = [-5.77397E-04  -5.77397E-04  -5.77397E-04  -5.46240E-04  -4.60488E-04 ...
      -4.06750E-04  -4.16183E-04  -3.70449E-04  -1.95515E-04  4.51627E-05 ...
      2.63830E-04  4.73923E-04  6.38852E-04  7.09741E-04  6.50343E-04 ...
      1.99345E-04  -1.00616E-04  -1.48179E-04  -1.74477E-04  -1.95743E-04 ...
      -2.18725E-04  -2.40677E-04  -2.78179E-04  -3.06420E-04  -3.28602E-04 ...
      -3.47581E-04  -3.65875E-04]';
```

## % Side force due to rudder deflection

```
cy_dr = [3.46480E-03  3.46480E-03  3.46480E-03  3.52987E-03  3.66813E-03 ...
      3.73320E-03  3.66813E-03  3.46480E-03  3.08253E-03  2.57827E-03 ...
      2.11467E-03  1.79747E-03  1.59413E-03  1.47213E-03  1.50955E-03 ...
      1.59771E-03  1.48189E-03  1.25806E-03  1.04497E-03  9.72747E-04 ...
      1.04790E-03  1.15331E-03  1.10125E-03  1.01504E-03  1.04757E-03 ...
      1.15266E-03  1.08499E-03]';
```

## % Side force due to left stabilator deflection

```

cy_del = [-1.21826E-03  -1.21826E-03  -1.21826E-03  -1.18543E-03  -1.08596E-03  ...
-9.69152E-04  -8.62255E-04  -7.02810E-04  -4.98886E-04  -2.88800E-04  ...
-4.99497E-05  2.06273E-04  4.27489E-04  5.91445E-04  7.25571E-04  ...
8.56568E-04  1.00528E-03  1.13120E-03  1.22832E-03  1.30397E-03  ...
1.29672E-03  1.07641E-03  5.04952E-04  -4.54204E-05  -5.69973E-04  ...
-1.00132E-03  -1.20941E-03]';

```

% Side force due to right stabilator deflection

```

cy_der = [1.21826E-03  1.21826E-03  1.21826E-03  1.18543E-03  1.08596E-03  ...
9.69152E-04  8.62255E-04  7.02810E-04  4.98886E-04  2.88800E-04  ...
4.99497E-05  -2.06273E-04  -4.27489E-04  -5.91445E-04  -7.25571E-04  ...
-8.56568E-04  -1.00528E-03  -1.13120E-03  -1.22832E-03  -1.30397E-03  ...
-1.29672E-03  -1.07641E-03  -5.04952E-04  4.54205E-05  5.69973E-04  ...
1.00132E-03  1.20941E-03]';

```

% Roll moment due to beta

```

croll_b = [-3.70196E-05  -3.70196E-05  -4.41520E-04  -8.46019E-04  -1.27065E-03  ...
-1.70123E-03  -2.11290E-03  -2.77077E-03  -3.37291E-03  -3.47757E-03  ...
-3.16486E-03  -2.35754E-03  -1.22554E-03  -1.14567E-03  -1.63756E-03  ...
-2.22957E-03  -2.45882E-03  -2.47686E-03  -2.44493E-03  -2.51646E-03  ...
-2.70976E-03  -2.90803E-03  -2.82658E-03  -2.75756E-03  -2.70552E-03  ...
-2.67292E-03  -2.66024E-03]';

```

% Roll moment due to roll rate

```

croll_p = [-7.05113E-03  -7.05113E-03  -7.05113E-03  -7.05113E-03  -7.05113E-03  ...
-7.05113E-03  -6.24828E-03  -5.25344E-03  -4.62512E-03  -3.85718E-03  ...
-5.38434E-03  -7.94125E-03  -8.68301E-03  -8.72665E-03  -4.88692E-03  ...
3.49064E-05  -3.31613E-03  -3.73500E-03  -4.04916E-03  -4.36332E-03  ...
-4.67748E-03  -4.88692E-03  -5.02655E-03  -5.16617E-03  -5.30580E-03  ...
-5.41052E-03  -5.41052E-03]';

```

% Roll moment due to roll rate

```

croll_r = [2.14676E-04  2.14676E-04  2.14676E-04  5.85558E-04  1.52804E-03  ...
2.57087E-03  3.39117E-03  3.84496E-03  3.98895E-03  4.11549E-03  ...
4.43401E-03  5.18886E-03  5.68192E-03  5.06669E-03  4.07360E-03  ...
3.28122E-03  2.56214E-03  2.18515E-03  1.86052E-03  1.58127E-03  ...
1.33692E-03  1.11352E-03  1.12748E-03  1.13097E-03  9.28515E-04  ...
5.34071E-04  1.71042E-04]';

```

% Roll moment due to aileron deflection

```

croll_da = [1.16543E-03  1.16543E-03  1.16543E-03  1.16686E-03  1.17021E-03  ...
1.17426E-03  1.14013E-03  1.04034E-03  8.40294E-04  6.31892E-04  ...
5.23513E-04  4.56671E-04  3.86010E-04  3.20124E-04  2.81594E-04  ...
2.56481E-04  2.33946E-04  2.11792E-04  1.97660E-04  1.86966E-04  ...
1.74839E-04  1.56123E-04  9.61564E-05  5.02267E-05  1.77607E-05  ...
-6.65660E-23  -7.15216E-23]';

```

% Roll moment due to left stabilator deflection

```

croll_del = [5.65136E-04  5.65136E-04  5.65136E-04  5.80368E-04  6.12176E-04  ...
6.47732E-04  6.78982E-04  6.89279E-04  6.85958E-04  6.90546E-04  ...
6.99129E-04  6.97942E-04  6.82421E-04  6.50934E-04  5.94802E-04  ...
5.18515E-04  4.32725E-04  3.44090E-04  2.67459E-04  2.01739E-04  ...
1.42504E-04  8.19937E-05  2.43887E-05  -5.32750E-06  -2.92725E-05  ...
-5.58400E-05  -7.97000E-05]';

```

% Roll moment due to right stabilator deflection

```

croll_der = [-5.65136E-04  -5.65136E-04  -5.65136E-04  -5.80368E-04  -6.12176E-04  ...
-6.47732E-04  -6.78982E-04  -6.89279E-04  -6.85958E-04  -6.90546E-04  ...
-6.99129E-04  -6.97942E-04  -6.82421E-04  -6.50934E-04  -5.94802E-04  ...
-5.18515E-04  -4.32725E-04  -3.44090E-04  -2.67459E-04  -2.01739E-04  ...
-1.42504E-04  -8.19937E-05  -2.43887E-05  5.32750E-06  2.92725E-05  ...
5.58400E-05  7.97000E-05]';

```

% Roll moment due to rudder deflection

```

croll_dr = [2.86293E-04  2.86293E-04  2.86293E-04  2.69213E-04  2.39120E-04  ...
2.18787E-04  2.10653E-04  2.07400E-04  1.80560E-04  1.24440E-04  ...
6.91333E-05  3.49733E-05  1.87067E-05  4.88000E-06  -3.44528E-05  ...
-8.67339E-05  -1.08661E-04  -7.83403E-05  -2.63520E-05  3.68277E-05  ...
9.48021E-05  1.25253E-04  9.58432E-05  7.66811E-05  6.73115E-05  ...
6.47088E-05  6.32773E-05]';

```

% Yawing moment due to beta

```

cn_b = [1.42071E-03  1.42071E-03  1.52521E-03  1.62971E-03  1.65089E-03  ...

```

```

1.67084E-03  1.80024E-03  1.46016E-03  9.91781E-04  6.82316E-04 ...
1.75902E-04 -1.09086E-03 -1.11070E-03 -1.59428E-03 -1.88776E-03 ...
-1.76721E-03 -1.35917E-03 -1.52852E-03 -1.63273E-03 -1.59147E-03 ...
-1.44456E-03 -1.34440E-03 -1.47796E-03 -1.60891E-03 -1.69618E-03 ...
-1.72843E-03 -1.73807E-03]';

% Yawing moment due to roll rate
cn_p = [-1.26406E-03 -1.26406E-03 -1.26406E-03 -1.23533E-03 -1.17787E-03 ...
-1.12041E-03 -9.39611E-04 -6.36739E-04 -2.47236E-04 1.00356E-04 ...
3.70882E-04 4.58149E-04 3.97062E-04 2.48709E-04 2.33874E-04 ...
4.18879E-04 6.98132E-04 9.77384E-04 -1.04720E-03 -1.60570E-03 ...
-3.24631E-04 -2.26893E-04 -1.44164E-03 -6.98132E-04 -8.81388E-14 ...
-9.39512E-14 -9.97960E-14]';

% Yawing moment due to yaw rate
cn_r = [-3.11978E-03 -3.11978E-03 -3.11978E-03 -3.11105E-03 -3.10669E-03 ...
-3.12850E-03 -3.17650E-03 -3.27686E-03 -3.46448E-03 -3.97935E-03 ...
-4.62949E-03 -5.14872E-03 -5.53269E-03 -5.63741E-03 -5.53706E-03 ...
-5.23162E-03 -4.53349E-03 -3.97499E-03 -2.89288E-03 -1.70606E-03 ...
-6.93768E-04 4.36324E-06 -6.93769E-04 -2.64854E-03 -4.18443E-03 ...
-4.81274E-03 -5.23162E-03]';

% Yawing moment due to aileron deflection
cn_da = [-8.69999E-06 -8.69999E-06 -8.69999E-06 -2.06625E-05 -3.45825E-05 ...
-3.93675E-05 -4.78500E-05 -6.15525E-05 -7.74300E-05 -1.02660E-04 ...
-1.32240E-04 -1.55512E-04 -1.72042E-04 -1.80090E-04 -1.97403E-04 ...
2.05320E-04 -2.40120E-04 -2.69352E-04 -2.87796E-04 -3.02644E-04 ...
-1.09272E-04 2.45624E-12 8.35200E-05 1.59210E-04 2.21850E-04 ...
2.43600E-04 1.74000E-04]';

% Yawing moment due to left stabilator deflection
cn_del = [4.45020E-04 4.45020E-04 4.45020E-04 4.36729E-04 4.17690E-04 ...
3.94303E-04 3.58695E-04 2.82299E-04 1.66782E-04 6.38125E-05 ...
-7.86875E-06 -9.12188E-05 -2.04675E-04 -3.33137E-04 -4.30339E-04 ...
-4.76974E-04 -4.53709E-04 -5.23318E-04 -6.41640E-04 -7.97428E-04 ...
-9.85781E-04 -1.20466E-03 -1.53810E-03 -1.97276E-03 -2.31246E-03 ...
-2.51679E-03 -2.70661E-03]';

% Yawing moment due to right stabilator deflection
cn_der = [-4.45020E-04 -4.45020E-04 -4.45020E-04 -4.36729E-04 -4.17690E-04 ...
-3.94303E-04 -3.58695E-04 -2.82299E-04 -1.66782E-04 -6.38125E-05 ...
7.86875E-06 9.12188E-05 2.04675E-04 3.33137E-04 4.62771E-04 ...
5.89670E-04 7.57910E-04 8.80937E-04 1.03114E-03 1.17862E-03 ...
1.32721E-03 1.51793E-03 1.84599E-03 2.19195E-03 2.41929E-03 ...
2.53951E-03 2.70661E-03]';

% Yawing moment due to rudder deflection
cn_dr = [-1.15493E-03 -1.15493E-03 -1.15493E-03 -1.16632E-03 -1.18177E-03 ...
-1.18259E-03 -1.15656E-03 -1.08336E-03 -9.58920E-04 -8.03573E-04 ...
-6.80760E-04 -6.18947E-04 -5.90480E-04 -5.80720E-04 -5.15533E-04 ...
-4.17092E-04 -3.72355E-04 -3.86914E-04 -3.85538E-04 -3.51603E-04 ...
-3.00387E-04 -2.75612E-04 -2.70873E-04 -3.22200E-04 -3.84710E-04 ...
-4.23059E-04 -4.16915E-04]';

```



# Appendix C

## Linearized Matrix

This section presents the plots of the selected elements in the longitudinal state matrix for numerical and analytical results. The elements of the state matrix is given as follows:

$$A_{long} = \begin{bmatrix} x_u & x_w & x_q & x_\theta \\ z_u & z_w & z_q & z_\theta \\ m_u & m_w & m_q & m_\theta \\ 0 & 0 & 1 & 0 \end{bmatrix} \quad (C.1)$$

The selected elements are  $x_u$ ,  $x_w$ ,  $z_u$ ,  $m_w$  and  $m_q$  since other elements which are not mentioned do not show significant differences.

### C.1 State Matrix from the Cao Model

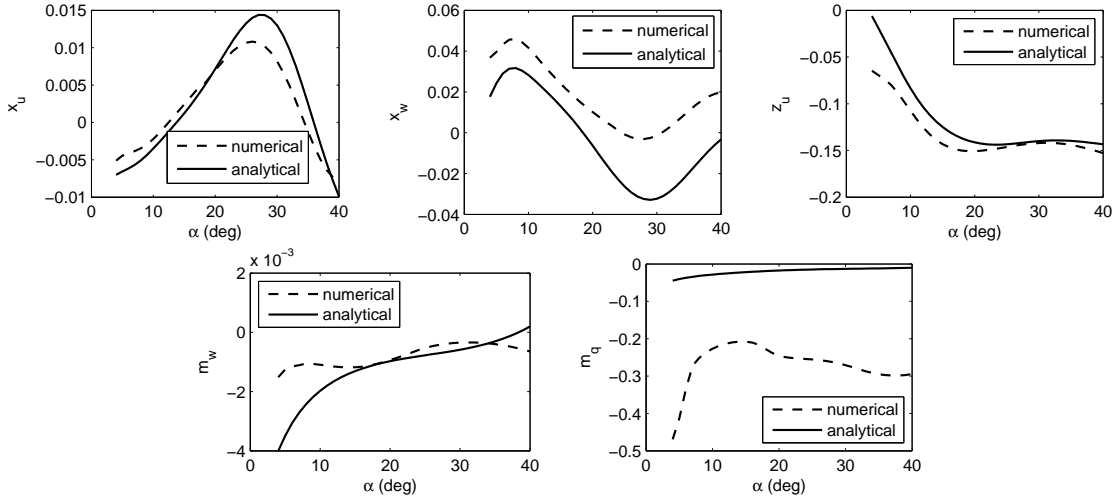


Figure C.1: Variations of the state matrix's elements with AoA for the Cao model.

## C.2 State Matrix from the Chakraborty Model

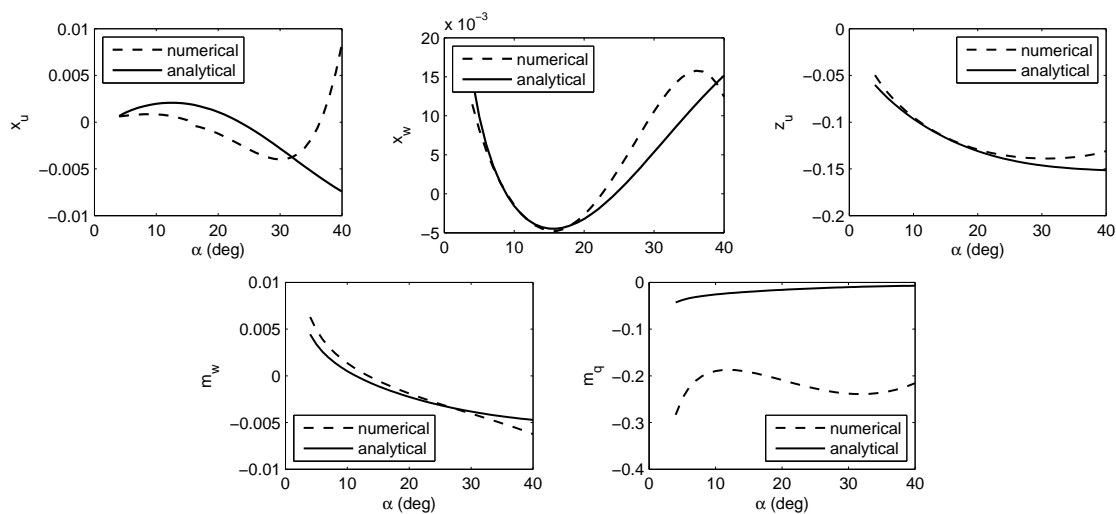


Figure C.2: Variations of the state matrix's elements with AoA for the Chakraborty model.

## C.3 State Matrix from the NASA Model

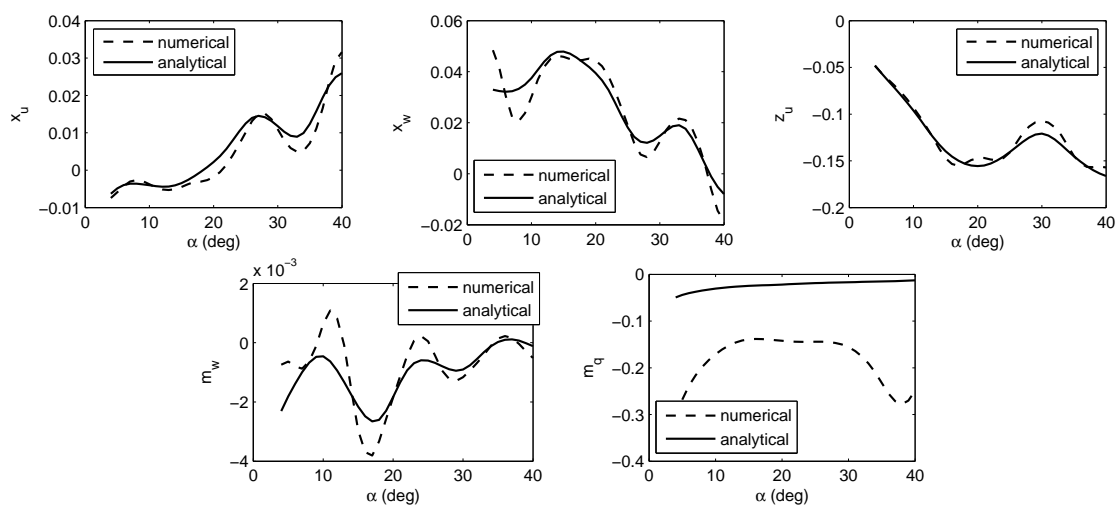


Figure C.3: Variations of the state matrix's elements with AoA for the NASA model.